

# **RADIOISOTOPE AND NUCLEAR TECHNOLOGIES FOR SPACE EXPLORATION**

Submitted by

**Robert C. O'Brien**

For the Degree of  
Ph.D. Physics Research  
In the Department of Physics and Astronomy  
University of Leicester

2010

# Abstract

Radioisotope heat sources and power systems, traditionally fuelled by  $^{238}\text{Pu}$ , have been developed and used for spacecraft thermal management and to provide electrical power during many deep space and planetary science missions. The use of fission reactors in space, however, has been limited to high power applications in Earth orbit. Previous ground based research programs conducted by the U.S. Atomic Energy Commission demonstrated the principal of nuclear thermal rocket propulsion but to date, flight heritage of nuclear propulsion has been limited to nuclear-electric propulsion. The development of space nuclear systems and tributary components that are capable of meeting the rigors of space flight is of paramount importance. Performance, lifetime and operational safety under all foreseeable conditions are essential considerations that must be made. The selection of appropriate materials and environmental compatibility is vital to the success of any given design. The ability for radioisotope heat sources to survive the extreme temperatures and mechanical loads associated with launch related accidents, is both legally mandated and necessary for the protection of life and the Earth's environment. Nuclear fuels for fission systems must provide equal protection during accidents while the integral design ensures that a reactor remains in a safe configuration. A historical overview of nuclear systems for space is presented. Traditional and modern system designs and fabrication techniques are discussed. Applicable solid state and mechanical power conversion methods are described and their performances are evaluated. Consideration is made for the effect of radioisotope selection and heat source encapsulation architecture upon radiation safety. The identification of  $^{241}\text{Am}$  as an alternative isotope fuel is made. Other candidate isotopes such as  $^{210}\text{Po}$ ,  $^{242}\text{Cm}$  and  $^{244}\text{Cm}$  are assessed.

The development of encapsulation methods that are resistant to the extraction and dispersion of the radioactive materials enclosed is increasingly attractive for security reasons. Spark Plasma Sintering (SPS) processes are presented as novel, simple and rapid techniques for the encapsulation of radioisotopic materials within tungsten ceramic-metallic or cermet matrices. Computational modelling via Monte-Carlo simulation has shown that the encapsulation of radioisotopes within heterogeneous tungsten cermet matrices may reduce the neutron, X-ray and Gamma-ray radiation dose delivered to the localised environment. The prevention of fabrication related volatilisation of radioisotopic compounds is fundamental to the success of the encapsulation process. SPS is empirically demonstrated via the use of  $\text{CeO}_2$  as an inert simulant for radioisotopic compounds such as  $\text{PuO}_2$ ,  $\text{AmO}_2$  and  $\text{UO}_2$ . The chemical compatibility of americium oxides within a tungsten matrix is also demonstrated through pressureless sintering within a Differential Scanning Calorimetric furnace. The techniques developed for radioisotope encapsulation are also demonstrated in context of cermet fuel fabrication for high temperature space power and propulsion reactor systems. The use of tungsten cermet fuels may eliminate material incompatibilities and failures experienced by historical nuclear thermal propulsion programs.

Finally, three novel concept applications of nuclear energy as an enabling technology for planetary exploration are presented. Melt penetration of icy surfaces and long range mobility on planetary surfaces is proposed via the use of pulsed high power heat capacitive radioisotope sources. In-situ resource utilization is considered for propellant production. The use of  $\text{CO}_2$  is proposed as a propellant for a radioisotope thermal rocket in the context of a 'Mars Hopper'. A  $\text{CO}_2$  propellant is also considered in the context of a high temperature (3000 °C) nuclear thermal propulsion system for a single stage surface ascent vehicle under a Mars sample return mission.

# Acknowledgments

This thesis is written under a 3 year research program funded by the Engineering and Physical Sciences Research Council.

The author wishes to thank his advisors Dr. N.P Bannister and Dr. R.M. Ambrosi for their encouragement, support, and for granting the freedom to pursue this research.

The extensive assistance provided by the staff at the Idaho National Laboratory granted the author with the ability to drive theoretical concept to practical demonstration. Particularly, the author sincerely acknowledges the support of Dr. W.E. Windes, Mr. J.E. Werner, Dr. J.R. Kennedy, Dr. T.P. O'Holleran, Mr. M.A. Henry, Ms. C.A. Papesch and Mr. B. Foresman.

The author is greatly appreciative of the kind support provided by Dr. C. Deeley and Mr. N. Bennett of REVISS Services UK LTD through the supply of radioisotopic materials used during his experimental work.

Finally, the author wishes to thank Dr. S.D. Howe, Director of the Center for Space Nuclear Research at the Idaho National Laboratory, whose friendship and steadfast support from the inception of this project was greatly needed and is eternally appreciated.

## **Dedication**

To my Mother and Father who taught me to aspire to my dreams, and my Wife Sarah for her support and understanding.

This thesis is also dedicated to the memory of colleague and friend Prof. M.J.L. Turner whose encouragement and teachings helped to shape my passion for rocketry and space technology into a sound scientific understanding.

# Contents

<b>i</b>	<b><i>Abstract</i></b>	
<b>ii</b>	<b><i>Acknowledgements</i></b>	
<b>iii</b>	<b><i>Dedication</i></b>	
<b>Chapter 1</b>	<b><i>Introduction</i></b>	Page 1
<b>Chapter 2</b>	<b><i>An overview of radioisotope and nuclear technologies for space</i></b>	Page 8
<b>2.1</b>	<i>Power conversion</i>	Page 11
<b>2.2</b>	<i>The U.S. SNAP and early space nuclear systems program</i>	Page 15
<b>2.3</b>	<i>Russian space nuclear power systems</i>	Page 20
<b>2.4</b>	<i>Current U.S. space radioisotope power technology</i>	Page 26
<b>2.5</b>	<i>The Plutonium climate</i>	Page 29
<b>2.6</b>	<i>The Multi-Mission RTG (MMRTG) &amp; Advanced Stirling Radioisotope Generator (ASRG)</i>	Page 30
<b>2.7</b>	<i>The European Space Agency</i>	Page 35
<b>2.8</b>	<i>Summary of space RTG systems built to date</i>	Page 36
<b>2.9</b>	<i>Introduction to Nuclear Thermal Propulsion</i>	Page 41
<b>2.10</b>	<i>Tungsten core power and propulsion reactors</i>	Page 48
<b>2.11</b>	<i>Thermal analysis of Nuclear Thermal Propulsion</i>	Page 54
<b>2.12</b>	<i>References</i>	Page 59
<b>Chapter 3</b>	<b><i>Current radioisotope heat source encapsulation technology</i></b>	Page 62
<b>3.1</b>	<i>The General Purpose Heat Source</i>	Page 63
<b>3.2</b>	<i>The Light Weight Radioisotope Heater Unit</i>	Page 75
<b>3.3</b>	<i>The Angel RHU</i>	Page 76
<b>3.4</b>	<i>Helium evolution and its effect upon the encapsulation of radioisotopic materials</i>	Page 77
<b>3.5</b>	<i>References</i>	Page 81
<b>Chapter 4</b>	<b><i>Alternative and reduced radiation isotope power sources</i></b>	Page 83
<b>4.1</b>	<i><sup>238</sup>Pu and Alternative Radioisotopes</i>	Page 85
<b>4.2</b>	<i>Monte Carlo radiation environment modelling and shielding criteria</i>	Page 103
<b>4.3</b>	<i>Reduced radiation isotope sources</i>	Page 114
<b>4.4</b>	<i>Mixed Am-Cm isotope heat sources</i>	Page 119
<b>4.5</b>	<i>Summary of radioisotope heat source solutions</i>	Page 130
<b>4.6</b>	<i>References</i>	Page 131
<b>Chapter 5</b>	<b><i>The encapsulation of radioisotopes and nuclear fuels within a tungsten matrix</i></b>	Page 135
<b>5.1</b>	<i>Tungsten encapsulation of radioisotopic material</i>	Page 135
<b>5.2</b>	<i>Traditional sintering technologies for tungsten cermet production</i>	Page 136
<b>5.3</b>	<i>Introduction and overview of the Spark Plasma Sintering Process</i>	Page 138
<b>5.4</b>	<i>Experimental demonstration of SPS cermet fabrication</i>	Page 144
<b>5.5</b>	<i>Encapsulation of oxide pellets and cermets within a metallic cladding via spark plasma sintering</i>	Page 151
<b>5.6</b>	<i>Tungsten alloy clad GPHS architecture</i>	Page 154
<b>5.7</b>	<i>Fabrication of high temperature NTP fuels by Spark Plasma Sintering</i>	Page 156
<b>5.8</b>	<i>Conclusions and future work</i>	Page 160
<b>5.10</b>	<i>References</i>	Page 164

<b>Chapter 6</b>	<b><i>Experimental cermet encapsulation of americium oxides in tungsten</i></b>	Page 167
<b>6.1</b>	<i>Calculation of the AmO<sub>2</sub> Gibbs free energies and the W/Am oxide Ellingham diagram</i>	Page 168
<b>6.2</b>	<i>Sample preparation for DSC, XRD and SEM analysis of W-AmO<sub>2</sub> systems</i>	Page 170
<b>6.3</b>	<i>Evaluation and SEM analysis of AmO<sub>2</sub> experimental feedstock material</i>	Page 172
<b>6.4</b>	<i>DSC analysis of W-Am<sub>x</sub>O<sub>x</sub> systems</i>	Page 174
<b>6.5</b>	<i>XRD analysis of sintered AmO<sub>2</sub> and W-Am<sub>x</sub>O<sub>x</sub> systems</i>	Page 184
<b>6.6</b>	<i>SEM analysis of sintered AmO<sub>2</sub> and W-Am<sub>x</sub>O<sub>x</sub> systems</i>	Page 191
<b>6.7</b>	<i>Estimation of feedstock specific thermal power</i>	Page 195
<b>6.8</b>	<i>Discussion and conclusions</i>	Page 196
<b>6.9</b>	<i>References</i>	Page 199
<b>Chapter 7</b>	<b><i>Potential applications and mission architectures enabled by nuclear power and propulsion systems</i></b>	Page 200
<b>7.1</b>	<i>Melt Penetration Missions</i>	Page 201
<b>7.2</b>	<i>A Mars Hopper</i>	Page 215
<b>7.3</b>	<i>Mars sample return via a single stage Nuclear Thermal Rocket</i>	Page 228
<b>7.4</b>	<i>References</i>	Page 231
<b>Chapter 8</b>	<b><i>Summary</i></b>	Page 234
<b>Appendix A</b>	<b><i>Power conversion mechanisms</i></b>	Page 241
<b>A.1</b>	<i>Thermoelectric power conversion</i>	Page 241
<b>A.2</b>	<i>Thermionic Conversion</i>	Page 253
<b>A.3</b>	<i>Direct Energy Conversion</i>	Page 259
<b>A.4</b>	<i>Free-Piston Stirling Generators</i>	Page 260
<b>A.5</b>	<i>Thermoacoustic &amp; Thermoacoustic MHD Power Conversion</i>	Page 268
<b>A.6</b>	<i>The Brayton Cycle</i>	Page 270
<b>A.7</b>	<i>The Rankine Cycle</i>	Page 277
<b>A.9</b>	<i>References</i>	Page 281
<b>Appendix B</b>	<b><i>Decay chains for radioisotopes considered for space applications</i></b>	Page 383

# 1

## Introduction

Efficient power production has always been one of the challenges for the exploration of space and the solar system. The challenge is even greater at increasing distance from the Sun or beneath planetary surfaces, where solar light intensity levels and extreme temperatures could preclude the use of solar power and chemical power generation systems. Figure 1.1 illustrates solar intensity as a function of orbital radius from the sun. When in orbit around Mars, a spacecraft is illuminated by 60 % less sunlight than when in an Earth orbit. The same spacecraft would receive only 5 % of the sunlight it receives at Earth at an orbit of equal radius to Jupiter. High efficiency photovoltaic (PV) cells are reported up to 40% efficiency [1] but for flagship class missions where electrical power budgets are typically several hundred to kilowatts [2], PV arrays become large for orbits beyond Jupiter. The presence of a large PV array on a deep space craft is likely to introduce rotational torques that must be constantly countered, and flight through regions of elevated debris content such as in the Kuiper belt presents an elevated probability of mechanical damage to the cells. Damage to solar cells by natural background radiation such as protons and electrons with energies of the order of keV to GeV [3, 4] is significantly limiting on the lifetime of a solar array, especially in orbits around planets such as Jupiter which possess magnetic fields that typically trap charged particles similar to the Earth's Van Allen belts [5]. Additional power burdens on the budgets available for certain missions may be imposed by systems that have specific operating temperatures and temperature control requirements.

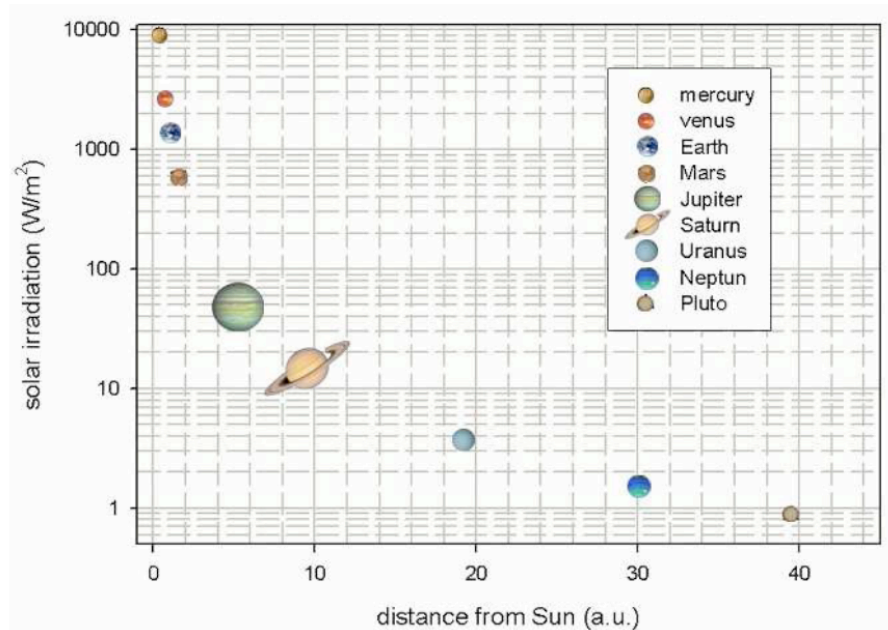


**Figure 1.1:** Solar irradiation power per unit area as a function of orbital radius. Image courtesy of NASA.

Radioisotope power systems have been used to provide energy for thermal management and up to hundreds of Watts of electrical power over long lifetime missions in regions where solar illumination is greatly reduced or where background radiation is elevated [6]. Most recently, the NASA New Horizons mission to Pluto, launched in 2006, is powered by a single Radioisotope Thermoelectric Generator (RTG) [7]. Reducing the mass, maximising the efficiency, and improving the physical safety and security of radioisotope power sources will have a positive impact on the overall mass budgets of science payloads and the range of mission scenarios for a specific project.

Nuclear fission reactors have also been developed that are capable of delivering kilowatts of electrical power for power intensive applications. To date, spaceflight heritage of reactor systems has been confined to missions in Earth orbit such as under the U.S. SNAPSHOT [6] and Russian Cosmos missions [8]. Adaptation of nuclear fission technologies have been applied to the field of spacecraft propulsion, leading to the development and ground testing of Nuclear Thermal Propulsion (NTP) systems. The limitation and restriction of the use of nuclear power and NTP up to the present day is significantly attributed to safety concerns amidst the challenge of nuclear fuel encapsulation and its impact upon launch safety.

A historical overview of international nuclear power and propulsion systems developed for space applications is presented in chapter 2 of this thesis. The power conversion mechanisms that may be adopted by radioisotope and nuclear power systems are evaluated and presented in Appendix A.

Isotope Selection is of great importance to the overall performance, specific mass, radiation safety and lifetime of a radioisotope power system. The modes of decay, half-lives and origin of radioisotopes are most significant to the isotope selection process.  $^{238}\text{Pu}$  has been most widely adopted for radioisotope power systems. An evaluation of the performance of alternative radioisotopes is presented in chapter 4 and comparison is made to that of  $^{238}\text{Pu}$ . Specifically, Monte Carlo analysis was performed for the substitution of  $^{238}\text{Pu}$  fuel within the U.S. General Purpose Heat Source (GPHS) {Bennett, 2006 #14} architecture (see chapters 3 & 4) by  $^{208}\text{Po}$ ,  $^{210}\text{Po}$ ,  $^{241}\text{Am}$  and  $^{90}\text{Sr}$  and the comparison of radiation dose rates delivered to the local environment is made. As a consequence of this study, the use of  $^{241}\text{Am}$  is proposed.  $^{241}\text{Am}$  is attractive due to

its abundance in the commercial nuclear power fuel cycle and commercial availability in addition to its reduced impact upon the local radiation environment when combined within an appropriate encapsulation scheme.

The extraction of radioisotopes from discharged commercial reactor fuels is also evaluated in chapter 4 with particular attention given to the extraction of composite blends of americium and curium isotopes. Such composite isotopic compounds may be used to fuel RTG systems where the production of  $^{238}\text{Pu}$  is uneconomical while delivering a similar specific thermal power ( $W_{\text{th}}/\text{g}$ ).

For radioisotope power systems, the encapsulation mechanisms and architectures adopted are essential for launch safety and handling of the systems during assembly. Traditionally, such schemes must provide physical retention and isolation of the hazardous materials while providing ventilation for radiogenic gases generated by the radioactive decay of the encapsulated materials. Thermal protection must be provided so as to ensure intact atmospheric re-entry of radioisotope heat sources while providing efficient thermal conductivity to power conversion systems during normal operation. The traditional encapsulation architectures discussed in chapter 3 require concentric assembly of cladding and aeroshell structures, thus occupying volumes much greater than that occupied by the isotopic materials. As an alternative to the traditional encapsulation mechanisms adopted by radioisotope power systems, the encapsulation of isotopic materials within a tungsten matrix is proposed (see chapter 5). Tungsten matrices are proposed and evaluated for radiation shielding characteristics and reduction in delivered dose to the localised environment throughout chapter 4. It is anticipated that matrices based on tungsten and alloys of tungsten are capable of

surviving the high temperatures, in excess of 2000 K [9], which are typically experienced during atmospheric re-entry, such as in the event of launch related accidents [10, 11]. Methods of tungsten encapsulate production are proposed and demonstrated in chapter 5. Specifically, Spark Plasma Sintering (SPS) is proposed and evaluated for its capability to process tungsten ceramic-metallic matrices (cermets) at temperatures of around 40% of its melting temperature [10]. Such temperatures are typically below those at which significant volatilization of ceramic isotopic compounds occurs [10].

An experimental demonstration of americium oxide encapsulation within a tungsten cermet matrix was performed by the author and is discussed in chapter 6. Here an  $^{241}\text{AmO}_2$  powdered feedstock was mixed with tungsten powder (3 - 6  $\mu\text{m}$ ) and sintered via pressureless sintering in a differential scanning calorimetric (DSC) furnace. In doing so, validation of reaction kinetics for the theoretical system was performed. Estimation of the specific thermal power for the  $^{241}\text{AmO}_2$  feedstock was also made via measurement of the bulk cermet temperature and DSC analysis. This was found to be approximately  $0.094 \text{ W}_{\text{th}}/\text{g}$ .

Further development of SPS processing capabilities has led to the development of tungsten cermet nuclear fuel elements with integrated coolant channels [12]. It is anticipated that the adaptation of tungsten matrices for space power and NTP reactor fuels may present a solution to the problems such as propellant compatibility that gave rise to the physical failure of fuel elements during ground tests performed under the U.S. Rover and NERVA NTP programs (see chapters 2 and 5). In addition, the high melting temperatures of tungsten and tungsten alloys will allow for the operation of

space reactors at temperatures up to 3000 °C and hence for an improvement in overall system efficiency. Improvements in the physical safety and security through the use of tungsten based reactor cores is also presented in chapters 2 and 5.

Clearly, the adaptation of nuclear technologies allows for the advancement of mission capabilities. As such, these technologies may provide key enabling strategies and systems for missions that would be excessively mass intensive, uneconomical or too complex through the use of conventional power production and propulsion. Three examples of missions that may be enabled by radioisotope and nuclear technologies are proposed and discussed in Chapter 7.

The findings of this research and proposed future work are summarised in the final chapter of this thesis.

## References

- [1] R.R. King, D.C. Law, K.M. Edmonson, et al., "40% efficient metamorphic GaInP/GaInAs/Ge multijunction solar cells". *Applied Physics Letters*. 90 (2007) 183516.
- [2] California Institute of Technology Jet Propulsion Lab (JPL). "*Cassini Program environmental impact study Volume 2: Alternate Mission and Power Supply*". JPL Publication No. D-11777. Cassini document No. 699-070-2. 1994.
- [3] J. Feynman, T.P. Armstron, L. Dao-Gibner, S. Silverman, "New interplanetary proton and fluence model". *J. Spacecraft*. 27 (1992) 403.
- [4] C. Tranquille, E.J. Daley, "An evaluation of solar proton event models for ESA missions". *ESTEC Working Paper*. 1647 (1992).
- [5] R.L. Crabb, "Solar Cell Radiation Damage". *Radiat. Phys. Chem.* 43 (1994) 99-103.
- [6] J. A. Angelo, D. Burden, "*Space Nuclear Power*". Krieger Publishing, Malabar, FL.; 1985. ISBN: 0-89464-000-3.

[7] Science Mission Directorate. "*Final Environmental Impact Statement For The New Horizons Mission, Volume 1*". NASA, Washington D.C. 2005.

[8] M. Wade. "Encyclopedia Astronautica".  
<http://www.astronautix.com/project/rorsat.htm>.

[9] A. Schock. "*Design Evolution and verification of the General-Purpose Heat Source*". Fairchild Space and Electronics Company, Germantown, Maryland. 1983.

[10] R.C. O'Brien, R.M. Ambrosi, N.P. Bannister, S.D. Howe, H.V. Atkinson, "Spark Plasma Sintering of simulated radioisotope materials in tungsten cermets". *Journal of Nuclear Materials*. 393 (2009) 108-113. DOI: [10.1016/j.jnucmat.2009.05.012](https://doi.org/10.1016/j.jnucmat.2009.05.012).

[11] R.C. O'Brien, R.M. Ambrosi, N.P. Bannister, S.D. Howe, H.V. Atkinson, "Safe radioisotope thermoelectric generators and heat sources for space applications". *Journal of Nuclear Materials*. 377 (2008) 506-521.

[12] R.C. O'Brien, R.M. Ambrosi, S.D. Howe, N.P. Bannister, H.V. Atkinson. "Fabrication of prismatic fuel elements for space power and nuclear thermal propulsion reactors by spark plasma sintering". Proceedings of: Nuclear and Emerging Technologies for Space (NETS-2009), Paper Number 206153; June 14-19, 2009; Atlanta, GA.

# 2

## An overview of radioisotope and nuclear technologies for space

Radioisotope Heating Units (RHUs) and Radioisotope Power Sources (RPSs) are devices that are capable of producing thermal energy for thermal control purposes, or electrical energy respectively by harnessing the energy released by the radioactive decay of radioisotope materials. These technologies have been successfully employed on a number of space missions and used extensively in terrestrial applications. Russian built ‘Beta-M’ Radioisotope Thermoelectric Generators (RTGs) fuelled with Strontium-90 were deployed in unmanned lighthouses, coastal beacons and remote weather and environment monitoring stations and had a typical power output of around 230 Watts electrical ( $W_e$ ) [1]. The original network of Automatic Weather Stations (AWSs) built by the United States in Antarctica was powered by RTGs; however, by the early 1990s safety concerns led to the removal of these power sources [2]. Today, RTG devices have become safer in design due to advances in material fabrication techniques.



**Figure 2.1:** Disused  $^{90}\text{Sr}$  fuelled Beta-M RTGs used for remote power operations. Image courtesy of Finnmark Region Government.

To date,  $^{238}\text{Pu}$  has been the most commonly used radioisotope fuel for RTGs and RHUs for space applications, although other isotopes have had some laboratory and flight history. The main rationale for the use of the plutonium isotope was primarily economic due to the existence in the U.S. of the large infrastructure that was established after the Manhattan project to produce plutonium for nuclear weapons. The use of these existing facilities allowed for the production of  $^{238}\text{Pu}$  with very minor alterations to production and extraction lines.  $^{238}\text{Pu}$  decays primarily by alpha emission, where the kinetic energy of the alpha particle is approximately 5 MeV.  $^{238}\text{Pu}$  can also decay by spontaneous fission with a very low probability [3]. The absorption of the alpha particles (and any fission products) by the source material matrix will result in the conversion of kinetic energy into heat that can be exploited to generate electricity by means of a power conversion system, in the form of thermoelectric junctions or other power conversion mechanisms.

The power budgets for modern flagship missions often call for the use of a significant number of radioisotope power systems that in some cases imposes limitation on system availability for subsequent missions (see section 2.5 below). The use of nuclear fission power sources in space is highly desirable given the availability of nuclear fuels. Through consideration for specific power density, fission power sources can be scaled between hundreds of watts to megawatts of electrical power generation. Through careful design and selection of power conversion mechanisms, a system of high reliability, safety and long operational lifetime can be conceived. The controllability of fission power reactors allows for a system to be started, shutdown and regulated at any given moment during a mission and unlike radioisotope power systems, are not driven by the decay rate and radiological inventory at production.

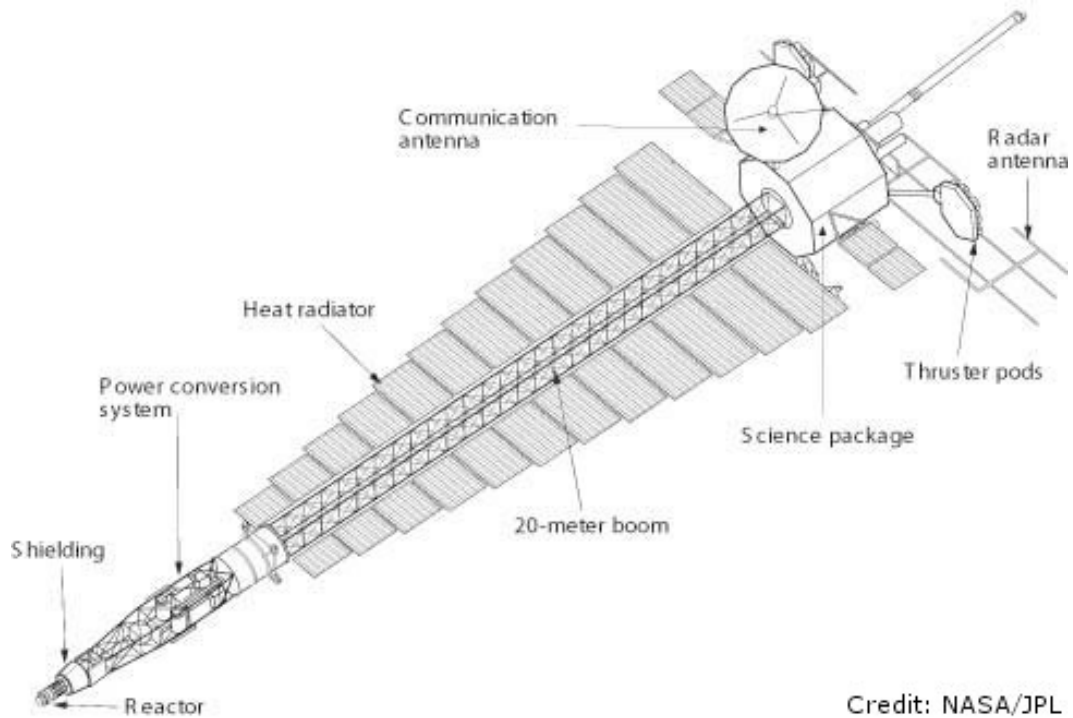


**Figure 2.2:** Schematic of the cancelled Jupiter Icy Moons Orbiter (JIMO). Image courtesy of NASA/JPL.

In modern mission concept design, the use of fission reactors in space is often coupled to the provision of electrical power for both instrumentation and propulsion via plasma or ion engines. Early reactor systems were often based on fuel forms that could not achieve high temperatures. As such, Nuclear Electric Propelled (NEP) spacecraft designs such as the Jupiter Icy Moons Orbiter (JIMO) required large radiators for heat rejection from the power conversion mechanism. See Figure 2.2. By driving reactor systems to higher operational temperatures, the surface area of a radiator can be reduced. Such operation will require the use of advanced high temperature reactor fuels and the careful selection of materials and processing of the fuel forms. Advances in such techniques are proposed and discussed by the author (see chapter 5) in the context of high temperature reactors for nuclear thermal rocket propulsion.

## **2.1 Power conversion**

The overall efficiency of any given radioisotope or nuclear power system is limited most fundamentally by the efficiency of the power conversion mechanism or series of mechanisms employed. Commonly, the production of electrical power is achieved most efficiently through the conversion of heat via a mechanical intermediate stage. For space applications requiring nuclear or radioisotopic power generation, the added complexity and mass of mechanical power conversion systems was historically unacceptable given the already significant probability of mission failure due to propulsion and guidance systems alone. Instead, solid state and direct energy conversion mechanisms were developed so as to minimise space mission failure probabilities attributed to spacecraft power supply. Significant development of thermoelectric conversion was made for lower temperature applications (primarily radioisotopic power) while thermionic power conversion was developed for space fission reactor systems.

The optimistic pro-nuclear future outlook of the 1950s and 1960s in which an abundant supply of radioisotopic materials would be produced allowed for the historical adoption of the somewhat inefficient power conversion technologies for use within radioisotope power systems in order to maximise reliability and lifetime. At the time of writing, space agencies are faced with the converse global situation in which economic and political restrictions have led to a shortfall in supply of radioisotopic materials while the number of civilian missions alone demand more material than can currently be produced. For this reason alternative power conversion mechanisms to thermoelectric generation should be, and are under consideration.

Many contributing parameters must be considered when selecting a given power conversion mechanism for a specific application. Consideration of the operational lifetime, local environmental influences and complexity of a power conversion mechanism are vital in mission specific selection. It is apparent that although several conversion mechanisms exist that are suitable for nuclear power systems, all must be considered on merit for each target application. Clearly, no single general-purpose mechanism can be applied to all conceivable applications. The power conversion methods and mechanisms that have been considered and developed for space applications include:

- Thermoelectric conversion
- Thermionic conversion
- Direct energy conversion
- Thermoacoustic conversion
- Stirling cycle
- Brayton cycle
- Rankine cycle

A detailed discussion of the above power conversion mechanisms is presented in Appendix A of this thesis.

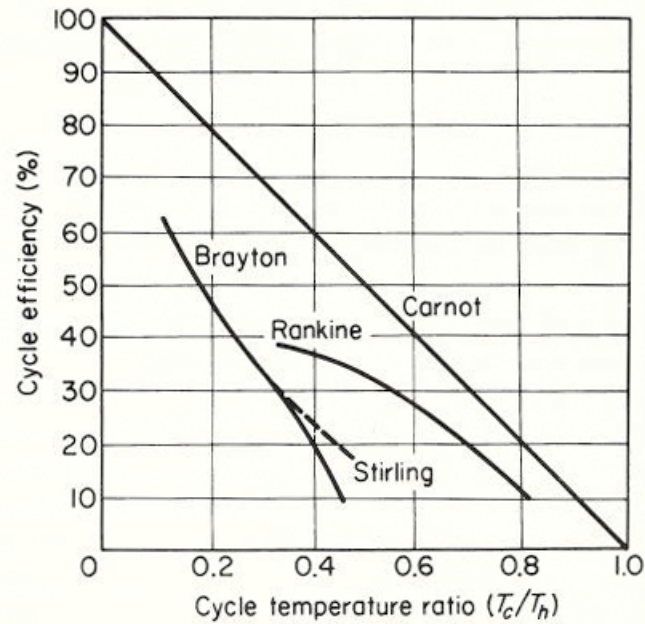


**Figure 2.3:** Comparison of dynamic power conversion cycle typical efficiencies verses the temperature ratio between the cold and hot sides of the cycle [4].

Examination of dynamic power conversion cycles (see Figure 2.3) indicates that for small and low power applications where the temperature ratios between the cold and hot sides of the cycle are particularly large, the Rankine cycle is highly suitable. Under the same conditions of large  $T_c/T_h$  ratios, the Stirling cycle is favoured over the Brayton cycle. Below a  $T_c/T_h$  ratio of the order of 0.23, the Brayton and Stirling cycles are equally favoured in efficiency over the Rankine cycle. The very nature of dynamic power conversion technologies require moving components. It is essential therefore that space system design is a highly motivational factor in converter design such that vibrations and rotational torques be minimised.

Engineering challenges that must be addressed during the qualification of any dynamic power converter are creep and structural fatigue effects and in the case of rotating or sliding components, the replacement of mechanical bearings with contactless gas bearings is critical.

Similarly, thermionic power conversion has substantial spaceflight heritage but the high temperatures required for efficient operation place the requirement on suitable materials selection. Thermionic converters are typically sensitive to large temperature transients due to CTE mismatches between differing electrode materials. Behaviour of this nature may be intolerable by certain missions where variations in the temperature and control of heat rejection surface may be lost or difficult such as missions that use an inner solar orbit for a series of gravity assists prior to departure to colder outer and extra-solar orbits.

Although thermoelectric power conversion efficiency is significantly lower than dynamic power conversion cycles, its simplicity and predictable characteristics are well suited to applications where no maintenance and longevity of the operational life of a system is crucial. In addition, some instances of low power system design ( $\sim 1 \text{ W}_e$ ) may present significant challenge for the engineer when manufacturing an equivalent dynamic converter, In such cases, the density of the overall thermoelectric system is likely to be lower than that of dynamic systems.

Thus, the selection of power converter technologies must be facilitated by definition of the operating parameters of the hot and cold sides of the nuclear system including throughput power, heat rejection capacity and energy availability from the nuclear heat source. Also of extreme significance for space nuclear power systems is the specific power density of a conversion system and the system as a whole, determined by the temperature regime and associated compatible materials, modern engineering and manufacturing capabilities and the heat rejection technologies used.

## 2.2 The U.S. SNAP and early space nuclear systems programs

Under the Systems Nuclear Auxiliary Power (SNAP) program, a range of RTGs and small reactors were developed in the United States for space and military use. The RTGs developed were successfully flown on several satellite and space exploration missions [5]. The efficiencies of some of the early devices were between 4% and 5% [6]. This was due to limitations in the power conversion process and losses within the system. Later devices such as the Multi Hundred Watt (MHW) power sources flown on the Voyager missions and the General Purpose Heat Source RTGs (GPHS-RTG) as flown on board Galileo & Cassini missions have efficiencies of the order of 6.6% [6].



**Figure 2.4:** Presentation and demonstration of the  $^{210}\text{Po}$  fuelled SNAP 3 RTG to U.S. President Eisenhower on the 16<sup>th</sup> of January 1959. Image courtesy of the United States Department of Energy.

Early iterations of the SNAP-19A design examined the use of  $^{238}\text{Pu}$ ,  $^{90}\text{Sr}$  and  $^{210}\text{Po}$  but were never fuelled. SNAP-19B devices fuelled by  $^{238}\text{Pu}$  were successfully used on the Nimbus B1 and Nimbus III meteorological satellites. A later derivation of the device named SNAP-19 was used onboard the Pioneer 10 and 11 [5] and were also included in the Viking 1 and 2 Mars lander missions (two  $35\text{W}_e$  units per lander) [7].

The SNAP-19 devices were loaded with  $^{238}\text{PuO}_2\text{-Mo}$  fuel cermet with a total activity ranging from 34.4 kCi to 80 kCi [6] depending on the mission and application. The casing for the SNAP-19 design was fabricated from Magnesium metal so as to provide a secure but lightweight structure suitable for integration with mass constrained missions such as the Viking landings on Mars.

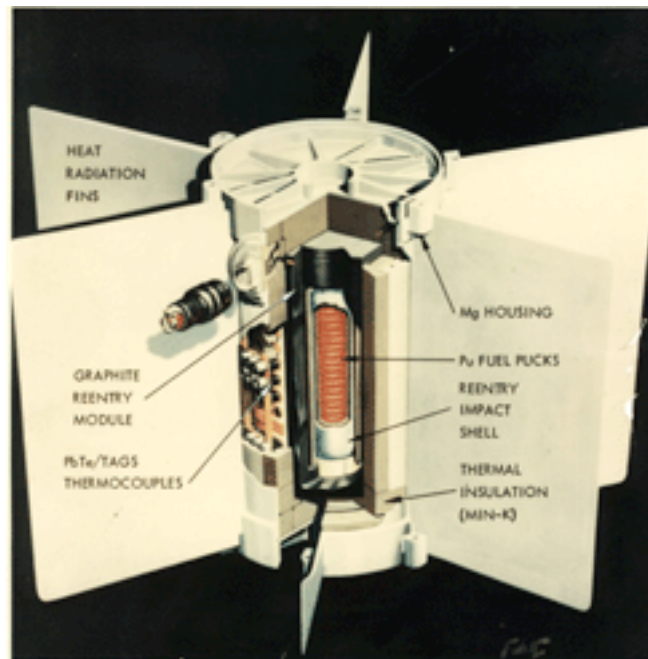


**Figure 2.5:** The SNAP-19 RTG design Image courtesy of NASA.

The SNAP-27 devices that were landed on the moon during the Apollo 12, 14, 15, 16 and 17 missions were designed to provide a beginning of life (BOL) output power of  $63.5\text{W}_e$  (Electrical Power in Watts) and a specific power density of  $3.2\text{W}_e/\text{kg}$  [6]. The SNAP-27 devices were used under these missions as power sources for lunar surface science experiments with life spans ranging from 4 to 8 years. The total activity of the SNAP-27 fuel source was 44.5 kCi and consisted of microspheres of  $^{238}\text{PuO}_2$  ceramic [6]. These devices had a power conversion system with a 5% efficiency based

on PbSnTe junctions. The output voltages of the SNAP-27 devices were between 14 V and 16 V D.C.

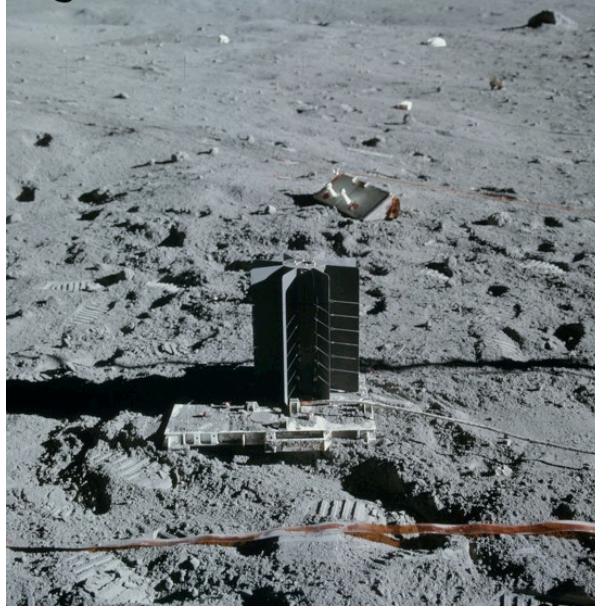


**Figure 2.6:** SNAP-27 RTG deployed on the lunar surface during the Apollo 16 mission [7].

Prior to the SNAP-19 design, the radioisotope heat sources for RTG systems were designed to completely burn up and disperse over a large trajectory in the event of launch or orbit failure of host spacecraft. After concerns about the safety of the dispersal mechanism in relation to exposure of the biosphere to plutonium or other radioisotope materials from what were becoming increasingly larger heat sources, it was decided that all heat sources should be encased within a heat shield and impact shell so as to minimise the risks of radiological exposure during accident scenarios by ensuring that fuel containment is completely maintained upon re-entry into the Earth's atmosphere and impact at the Earth's surface. Today, all designs for radioisotope power sources for space applications must comply with resolution 47/68 of the United Nations General Assembly regarding the use of nuclear power sources in space. This resolution was passed on the 14<sup>th</sup> of December 1992 and states that RTGs and RHUs can be used

in space provided that the physical form of the radioactive materials used and a system of protective shells are employed so as to guarantee non-dispersal of radioactive matter into the Earth's environment during nominal use and conditions attributed to all possible accident situations.

The failure of the Apollo 13 mission inadvertently enabled the testing of the integrity of the SNAP-27 design during the re-entry of its lunar module into the Earth's atmosphere. The lunar module splashed down in the Tonga Trench in the Pacific Ocean. No contamination has been detected to date and it is assumed that the SNAP-27 fuel capsule is intact at a depth of 6.5 km below the surface of the ocean. Even though the integrity of the SNAP design during re-entry is not in question, the additional mass of the separate aeroshell and cask used by this system reduced the overall system power density which could be improved today by the adoption of alternative encapsulation techniques.

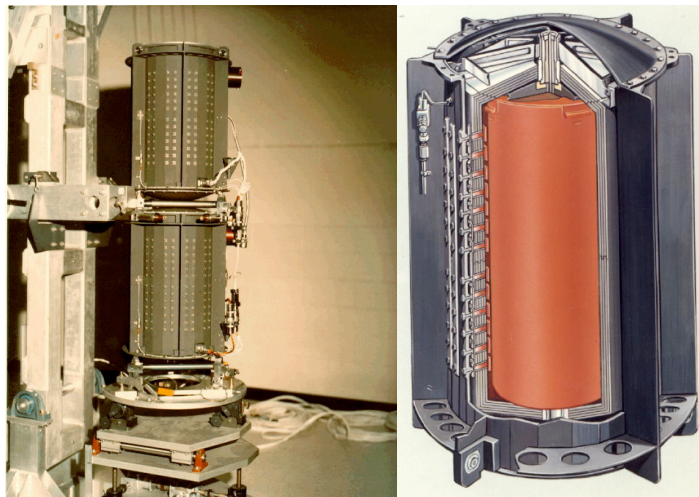


**Figure 2.7:** *(Left)* A stack of two Multi-Hundred Watt (MHW) RTGs as flown on the LES 8 spacecraft seen here at checkout at the Department of Energy's Mound facility. *(Right)* Cut away of the MHW RTG. Images courtesy of NASA.



**Figure 2.8:** Image of the author holding a single Multi-Hundred Watt RTG heat source engineering model.

Following the SNAP programmes, the U.S. developed the Multi-hundred Watt (MHW) RTG systems to provide power to the Lincoln Experimental Satellites LES 8 and 9 and Voyager 1 and 2 spacecraft. These devices were fuelled by 24 pressed spheres of  $^{238}\text{PuO}_2$ , each with an activity of 3.2 kCi. Each sphere was encapsulated within a cladding of iridium alloy and housed individually within a filament wound carbon-carbon impact shell. All 24 assembled spheres were housed within a cylindrical POCO graphite aeroshell for re-entry protection [6]. The thermoelectric conversion was performed using SiGe junctions [8] with an efficiency of 6.7% [6]. The MHW RTGs had a beginning of mission power level of  $2.4 \text{ kW}_{\text{th}}$  [8] or  $160.8 \text{ W}_e$ . The overall beginning of mission system power density was  $4.2 \text{ W/kg}$  [8].

Despite extensive ground based research into space reactor systems under the SNAP program, only one reactor, SNAP-10A, was flown by the United States aboard the SNAPSHOT spacecraft. SNAPSHOT was launched on the 3<sup>rd</sup> of April 1965 and operated successfully for 43 days until a fault occurred within a voltage regulator causing the premature shutdown of the SNAP-10A reactor. At the end of the mission, the reactor was placed into an orbital altitude of 1300 km at which it is expected to

reside for approximately 4000 years. Unlike the BES-5 reactor designs from the Soviet Union (see below), the SNAP-10A reactor operated with a thermal neutron spectrum. This was facilitated by the use of a uranium-zirconium hydride fuel form. The thermal power output of the SNAP-10A was 42 kW, and through transfer of thermal energy to PbTe thermoelectric converters via a sodium potassium (NaK) coolant loop, the electrical power output of the system was around 650 W<sub>e</sub> at the beginning of life, and 535 W<sub>e</sub> after 43 days [6].



**Figure 2.9:** Photograph of the SNAP-10A during ground based testing. Image courtesy of NASA.

### 2.3 Russian space nuclear power systems

To date, the vast majority of Russian flight heritage of nuclear power systems in space has stemmed from an extensive research and development program for space reactor systems and hence very few missions have been augmented by RTG power. The RORSAT ocean surveillance missions flown by the Soviet Union between 1971 and 1988 resulted in the launch of a total of 33 reactors in space, 30 of which successfully reached orbit and were operated beyond start up.

The first known reactor to have been flown by the Soviet Union was the BES-5 Buk design, launched on October 3<sup>rd</sup> 1970 under the Cosmos 367 mission. It is understood that a total of 31 BES-5 Buk reactors were launched between 1970 and 1988 [9] although 3 units failed to launch successfully or failed after achieving orbit [9]. Widespread public awareness of the Soviet space nuclear program was first made on the 24<sup>th</sup> of January 1978 when fragments of the Cosmos 954 spacecraft and its BES-5 reactor re-entered and crashed in the Alberta and Saskatchewan regions of northwest Canada [10].

The BES-5 Buk reactor design was based around a core operating in the fast neutron spectrum and fuelled by a highly enriched (95 Wt %)  $^{235}\text{U}$ -Mo alloy that was cooled by a Sodium-potassium NaK loop. The NaK coolant was used to transfer the thermal energy from the core to SiGe thermoelectric converters [11] and for heat rejection to a conical radiator shroud below a shadow radiation shield [9]. Control of the reactor was facilitated through the displacement of Beryllium control rods, which served as both reflector and control mechanism. The electrical power output of the BES-5 design was up to 3 kWe and had an operational lifetime of up to 6 months.

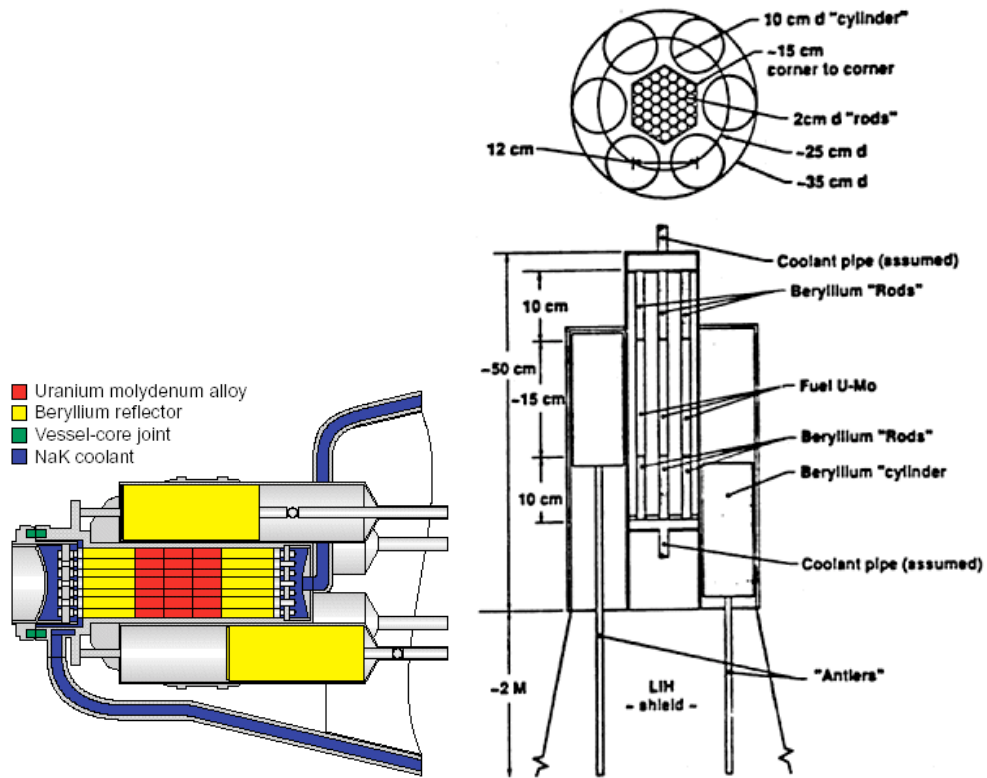


**Figure 2.10:** Schematic diagrams of the BES-5 Buk reactor core design [9].

A later reactor design, TOPAZ addressed issues of safety and performance over the BES-5 design. Fundamentally, the operation of the reactor was in the epithermal neutron spectrum and the control system for the TOPAZ design utilized rotating Beryllium control drums that were partially segmented with  $B_4C$  to reduce the system to a subcritical condition when rotated fully into the core. This control design change reduced the risk of the system achieving criticality in the event of accidental impact. The third major design change from the BES-5 design was that power conversion was performed via in-core thermionic converters. A total of two TOPAZ reactors were flown, the first was launched on the 1<sup>st</sup> of February 1987 on Cosmos 1818, the second on the 10<sup>th</sup> of July 1987 onboard Cosmos 1867 [12].

The TOPAZ design had a 5.5 kWe design output for up to 1 year, limited mainly by the supply of caesium used in vapour form to neutralize inter electrode space charge within the thermionic converters. The thermionic converters formed an integral component of the fuel element structure, connected in series arrangements of 5 cells, each surrounding individual highly enriched (96 wt%)  $^{235}\text{UO}_2$  fuel pellets. For this reason, the fuel assemblies were referred to as Thermionic Fuel Elements (TFEs). A total of 79 TFEs were arranged within the core, 60 of which provided power to the spacecraft bus while 19 were used to power a linear electromagnetic induction pump that was used to circulate NaK coolant from the core to a conical radiator. The structure of the TOPAZ core consisted of 4 moderator disks composed of zirconium hydride that were stacked axially and surrounded by a Be reflector and control drums. Channels within the core structure allowed the TFEs to be loaded.

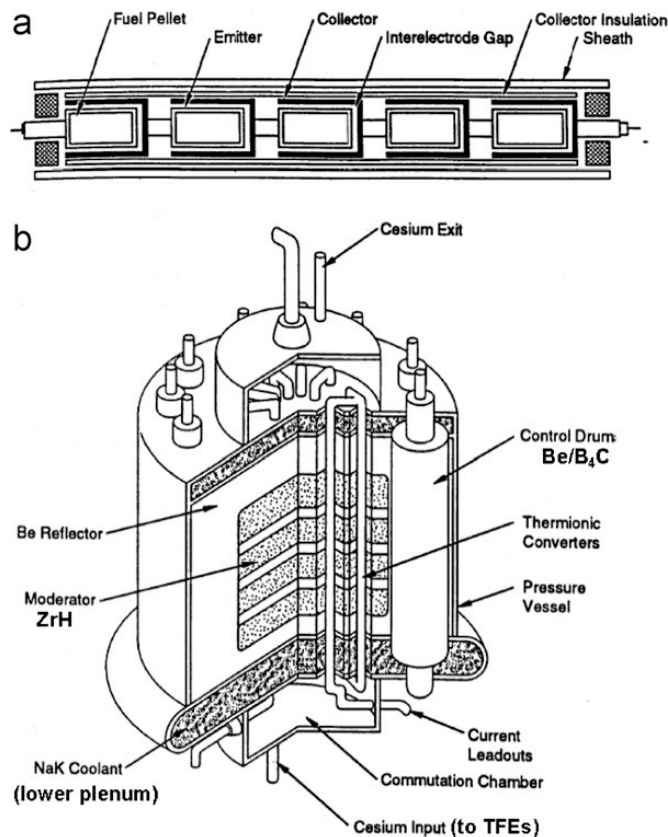


**Figure 2.11:** (a) Schematic of the TOPAZ Thermionic Fuel Elements (TFEs). (b) Cross-section of the TOPAZ reactor design.

A second variation of the TOPAZ design (TOPAZ-II / YENISEI) was produced and although successfully ground tested, has not seen flight [13]. Several units were sold to the United States for testing and evaluation but due to concern regarding launch abort criticality issues with oceanic impacts, it was determined that NASA would not fly the units.

The first Russian flights of RTG systems took place in 1965 and 1971 onboard the Cosmos 84 and Cosmos 90 missions [14]. These initial devices named Orion-1 and Orion-2 were fuelled by  $^{210}\text{Po}$  and provided 20 Watts of electrical power. In 1969 and 1971, two lunar rovers were launched by Russia under the Lunochod missions [14]. Both Lunochod rovers were heated by RHUs fuelled by a  $^{210}\text{Po}$  heat source with an initial thermal loading of around 800 Watts each [14]. An RTG system was also developed in 1978, again fuelled by a  $^{210}\text{Po}$  heat source, with a thermal loading of 600  $\text{W}_{\text{th}}$  and an electrical power output of 40  $\text{W}_{\text{e}}$ , but was never launched.

On the 16<sup>th</sup> of November 1996 the ill-fated Mars 96 mission began with a launch from the Russian Baikonur facility. Mars 96 was an ambitious mission that set out to land two surface science stations (soft landers) and two surface penetrators at separate locations in the northern hemisphere of Mars. Both surface science stations were powered by two RTGs fuelled by  $^{238}\text{Pu}$ . The Mars 96 spacecraft successfully achieved an Earth parking orbit but after an anomalously short burn of the fourth stage of the proton launch vehicle, the autonomous firing of the ‘Fregat’ transfer module occurred, placing the spacecraft into an orbit that resulted in its re-entry into the earth’s atmosphere over South America.

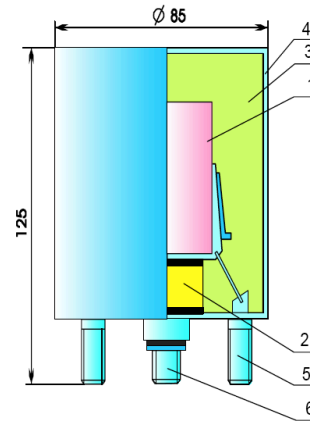


**Figure 2.12:** 8.5 W<sub>th</sub> ANGEL RHU/RTG

The RTGs flown on the Mars 96 mission were built around heat sources named Angel units. These Angel RTG devices, built by BIOPAS under contract to the Red Star Company, are the current design that is exploited by Russian space mission designers and to date, some interest in their use has been generated within the European Space Agency. The Angel RHUs have a thermal power output of 8.5 Watts and when used as an RTG, provide an electrical power output of 0.15 Watts at 15 volts D.C. [15]. Since very little electrical power is generated by the Angel RTGs, it is implied that for power production purposes, they should be used in conjunction with electrical batteries as a trickle charge source.

## 2.4 Current U.S. space radioisotope power technology

The general-purpose heat source radioisotope thermoelectric generator (GPHS-RTG) is an electrical power source that features an integrated modular heat source design [16] (see Figure 3.2). Originally designed for and flown on the NASA Galileo spacecraft, the GPHS-RTG was successfully used for the NASA Cassini mission and more recently, the New Horizons Kuiper belt mission. The GPHS-RTG was originally built by the US Department of Energy (DOE) at the Mound Laboratory in Miamisburg, Ohio. As a result of increased security requirements and costs, the DOE closed the Mound site. The responsibility for assembling RTGs was transferred to a new facility at the Idaho National Laboratory (INL) Materials and Fuels Complex (MFC). This was completed prior to the production of the GPHS-RTG for the NASA New Horizons mission that was launched in 2006.

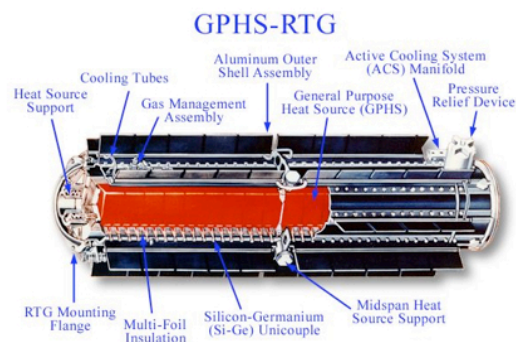


**Figure 2.13:** *Top:* pre-flight checkout of the Cassini GPHS-RTGs - Courtesy NASA/KSC. *Bottom:* A cutaway schematic of the GPHS RTG - Courtesy NASA/JPL-Caltech.

A general purpose heat source (GPHS) module is a composite carbon based body that houses a total of four fuel pellets and as a whole acts as an aero-impact shell and hence conforms to the UN resolution 47/68. The isotope fuel for the GPHS-RTG is in the form of plutonium dioxide ( $^{238}\text{PuO}_2$ ) at approximately 80% density. The fuel is pressed into pellets with an approximate length and diameter of 27.6 mm [16]. Each pellet has approximately 0.55 mm of iridium alloy (DOP-26) cladding [16] that is used to maintain the structural integrity of the pellet both under normal operating conditions and under impact. The iridium cladding also prevents the interaction of the source alpha particles with materials with low atomic masses, which could produce neutrons via a-n reactions. The internal structure of the GPHS module consists of two composite impact shells covered by a carbon-bonded carbon sleeve. Each internal impact shell contains two fuel pellets separated by a floating membrane [16]. The thermal power output of a single fuel pellet is approximately  $62.5 \text{ W}_{\text{th}}$  [16]. GPHS Modules can be stacked together and thermally coupled. The required electrical output power levels are achieved through the appropriate selection of a number of GPHS modules incorporated in a RTG system. The number of modules required is directly related to the power conversion efficiency of the system. The current GPHS-RTG systems have a power conversion efficiency of 6.5% to 7% and an overall system power density of  $5.2 \text{ W}_e \text{ kg}^{-1}$  [6] if a stack of 18 GPHS modules is used [16]. The thermoelectric junctions used for power conversion by the GPHS-RTG are SiGe type junctions.

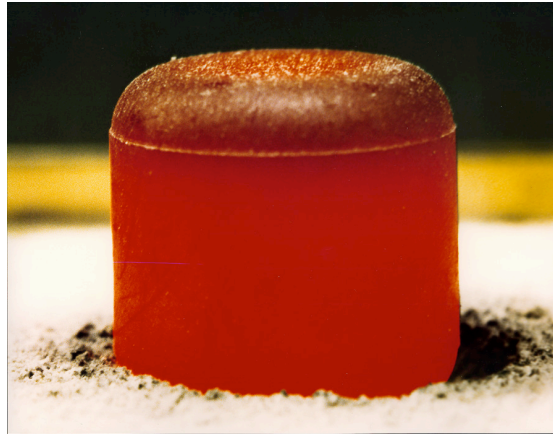


**Figure 2.14:** An un-clad pressed  $^{238}\text{PuO}_2$  GPHS fuel pellet. The image shows the pellet glowing caused by its 62.5 W thermal power output as a result of the  $\alpha$  decay of  $^{238}\text{Pu}$ . Image Courtesy of the U.S. Department of Energy.

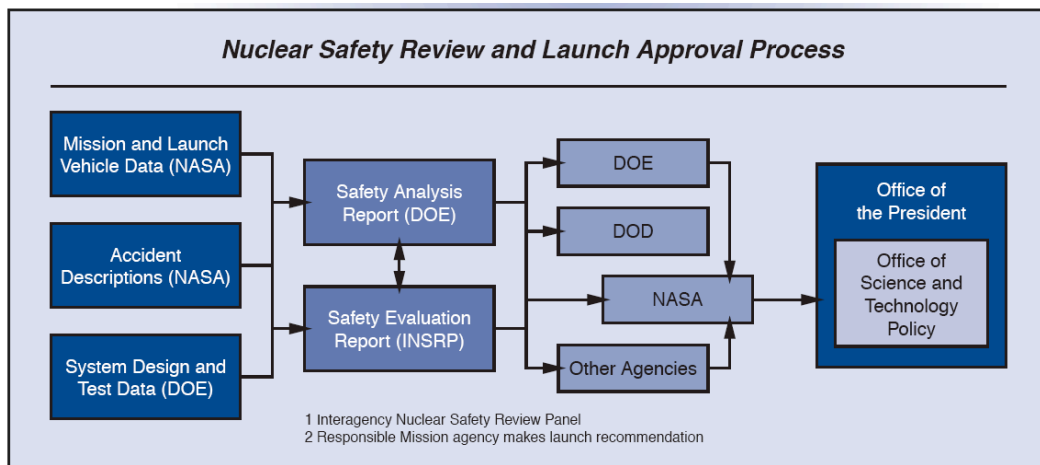


**Figure 2.15:** Launch safety and approval process undertaken by inter-agency panels prior to the launch of any U.S. space nuclear system. Image courtesy of the United States Department of Energy.

Prior to any launch of a nuclear system or subsystem from the United States of America, an established launch safety review and approval process must be undertaken. It is the role of an interagency final review to make recommendations to the Office of Science and Technology in the Office of the President of the United States. It is anticipated that this procedure will remain effective throughout the foreseeable future NPS programs.

## 2.5 The plutonium climate

Much of the  $^{238}\text{Pu}$  fuel that is used within the GPHS-RTG systems is currently supplied to the U.S. Department of Energy (DOE) by Russia in the form of  $^{238}\text{PuO}_2$  powder with an activity of between  $12.6 \text{ Ci g}^{-1}$  and  $15.1 \text{ Ci g}^{-2}$ .  $^{238}\text{Pu}$  is manufactured by the proton irradiation of  $^{237}\text{Np}$  or more industrially via the neutron irradiation of  $^{237}\text{Np}$  in a high flux reactor. The latter is the more commonly used method and results in the production of  $^{238}\text{Np}$  (half-life of 2.117 days), which decays via beta emission into  $^{238}\text{Pu}$ . Current concerns over the availability of  $^{238}\text{Pu}$  [17, 18] that is of sufficient purity for space applications have prompted the DOE to investigate the feasibility of establishing a new production line in the US in order to meet the future needs of NASA [19]. One proposal that has been established by Idaho National Laboratory has suggested the use of the Advanced Test Reactor for the neutron irradiation of  $^{237}\text{Np}$  targets followed by the chemical separation of the  $^{238}\text{Pu}$  via solvent extraction [20]. Other methods of production suggested include the irradiation of neptunium targets in commercial power reactors, but this presents lower production efficiencies and challenges in facility licensing.

In 1976, President Ford issued a presidential directive to cease all reprocessing of nuclear materials in the United States amidst a tense political climate regarding nuclear proliferation after a successful Indian demonstration of weapons capabilities derived from reprocessing technologies. President Carter reviewed and reaffirmed this directive in 1977. In 1981, the U.S. ban on reprocessing was lifted by President Regan but due to a lack of financial support from his government, restarting a reprocessing program within the U.S. was not commercially viable. For this reason, a finite inventory

of materials produced in the U.S. was created and through an agreement between the U.S. and Russian governments, a limited supply of  $^{238}\text{Pu}$  to the U.S. was established. Current concerns over the limited availability of suitably pure materials and the cost of restarting the production of  $^{238}\text{Pu}$  [17] has increased the need to explore alternative isotopes for these applications. Several alternative radioisotopes that are possible solutions to the limited supply of  $^{238}\text{Pu}$  are presented and discussed throughout this thesis. These include  $^{241}\text{Am}$ ,  $^{208}\text{Po}$  and  $^{210}\text{Po}$  and  $^{90}\text{Sr}$ .

## **2.6 The Multi Mission RTG & Advanced Stirling Radioisotope Generator**

In attempt to address the shortage of  $^{238}\text{Pu}$  in the short term, NASA, the U.S. Department of Energy and their subcontractors have invested in the development of two smaller, more versatile and efficient power source designs for space applications. These designs, called the Multi-Mission Radioisotope Thermoelectric Generator (MMRTG) and the Advanced Stirling Radioisotope Generator (ASRG), are both designed around the currently serviced and approved GPHS module design but essentially use fewer numbers of modules in each system to provide the desired output power.

The MMRTG for all intents and purposes is a smaller, more versatile derivation of the GPHS-RTG that is capable of operating both in the vacuum of space and within an atmosphere such as on the surface of planetary bodies. The heat source for the system consists of a total of 8 GPHS modules developing a total of 2000 Watts of thermal power and operate at 538 °C. These modules are surrounded by Pb-Te

thermoelectric junctions which yield a total electrical power output of approximately 125 Watts. The remaining 1875 Watts of thermal power is rejected to the operating environment or space via fins held at 210°C on the outside of the MMRTG casing. The efficiency of the thermoelectric conversion for the MMRTG is dependant upon the working pressure of the system, which in turn is selected to be compatible with the operating environment. For use in deep space (vacuum), the MMRTG has a conversion efficiency of 6.3 % and for operation on the surface of Mars, its efficiency is approximately 6.2 %. Although these figures indicate a lower efficiency and lower electrical output power than the GPHS-RTG, it is much more versatile in its application and requires 55.6% less plutonium to be fully fuelled.

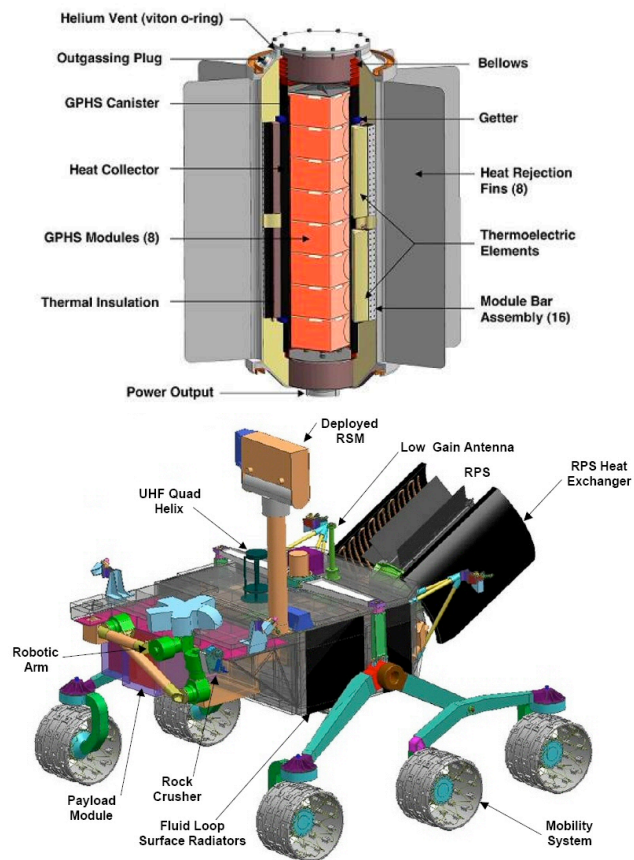


**Figure 2.16:** *Top:* schematic of the Multi-Mission RTG (MMRTG). *Bottom:* Schematic of the Mars Science Laboratory rover powered by a single MMRTG. Images Courtesy of NASA/JPL.

The first flight of an MMRTG system will be on board the NASA Mars Science Laboratory (MSL) mission where a single unit will provide the required electrical power for long duration operation of its rover on Mars. The use of an active heat exchanger in the vicinity of the MMRTG outer casing which operates at around 210 °C, allows for the radiated rejected heat from the power source to be used to maintain electronic and mechanical subsystems at their required operational temperatures. The MMRTG is currently in the final stages of flight qualification in preparation for the launch of the MSL mission in 2011.

The Advanced Stirling Radioisotope generator (ASRG) is currently under the development stages leading to a fully integrated engineering unit (EU) that is capable of generating electrical power from electrically simulated nuclear decay heat input. The final system will be based around two free piston Stirling converters produced under contract for NASA by Sunpower incorporated, each thermally coupled via a mechanical heat collector to an individual GPHS module and a common cold end heat rejection chassis (see Figure 2.16) which uses fins to radiate heat away from the system. The temperature difference of 580 degrees exists across the Stirling engine which results from a heat source operating temperature of 640 °C and a heat rejection side temperature of 60 °C. Under this thermal operating regime, each Stirling converter produces approximately 73 Watts of electrical power resulting in a total system electrical power output of approximately 145 Watts. The free piston Stirling converters operate linearly and resonate at around 105 Hz, and so as to minimize the effect of this motion and hence dampen the system, both converters operate in phase but are mechanically mounted at 180° to one another for mutual opposition of motion (see Figure 2.16 *Top*).

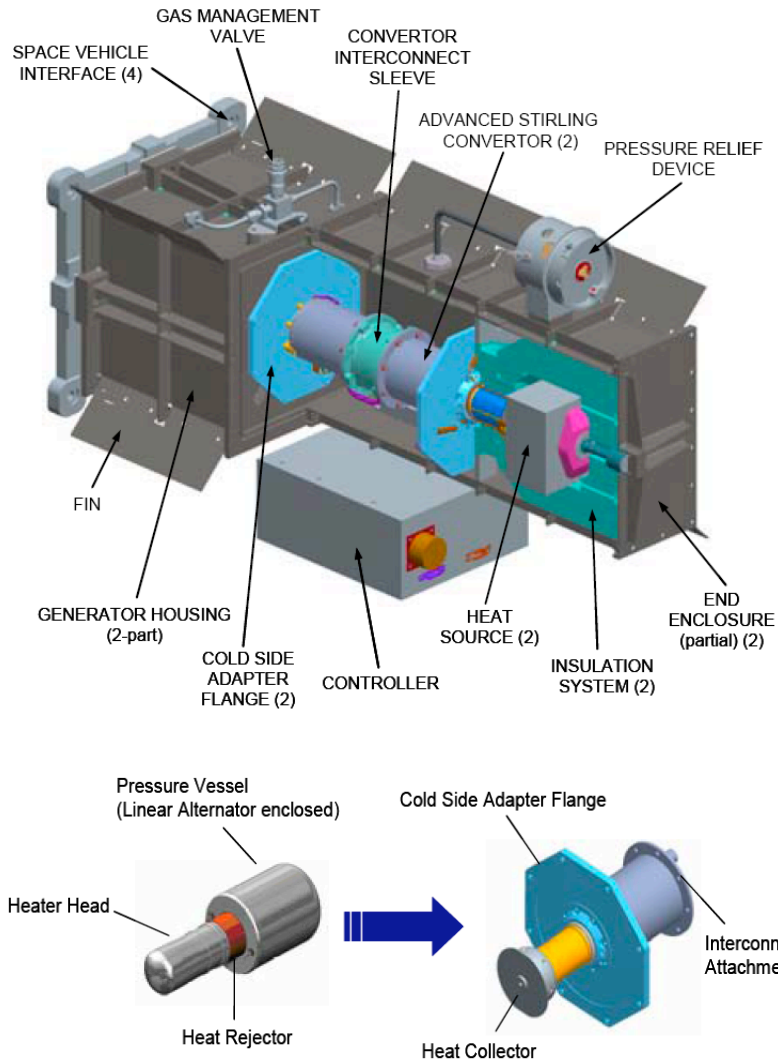


**Figure 2.17:** *Top:* Schematic of the Advanced Stirling Radioisotope Generator. *Bottom Left:* Sunpower inc. free piston Stirling engine. *Bottom Right:* Thermo-mechanical interface for free piston Stirling engine. Images courtesy of NASA.

The efficiency of the free piston Stirling converter engine is limited to the Carnot efficiency and the efficiency of the linear dynamo that is integral to the converter design. The overall efficiency of each converter is between 27 % - 30 %. Little can be done to improve on these figures but thermal losses throughout the system can be combated to result in a system that is close to its theoretical efficiency.

Ongoing work conducted by the NASA Glenn Research Center and Sunpower inc. is establishing the life expectancy for the ASRG. Given that the ASRG has several high frequency moving components that are subjected to physical wear and thermal stress, it is expected that the lifetime of such units may not match those of RTG systems. For this reason, it is reasonable to accept the necessity for both types of system where an acceptable trade-off between efficiency and lifetime cannot be made by mission planners. Table 2.1 below highlights the comparison between both the ASRG and the MMRTG.

	<b>MMRTG</b>	<b>ASRG</b>
Beginning of mission electrical output power ( $W_E$ ):	115-125	145
Beginning of mission thermal output power ( $W_T$ ):	2000	500
Number of $^{238}\text{PuO}_2$ fuelled GPHS modules used:	8	2
Heat source operating temperature ( $^{\circ}\text{C}$ ):	538	640
Heat rejection system operating temperature ( $^{\circ}\text{C}$ ):	210	60
Power Conversion efficiency (%):	~ 6.3	~ 30
Total Mass (kg):	44.2	~ 21
Specific electrical power ( $W_E / \text{kg}$ ):	2.8	~ 7
Operational Life expectancy (years):	> 14	10-14

**Table 2.1:** Performance comparison of the Multi-Mission Radioisotope Thermoelectric Generator (MMRTG) and the Advanced Stirling Radioisotope Generator (ASRG).

## 2.7 The European Space Agency

To date, the European Space Agency has not built or launched its own nuclear power or heating systems. Instead, through its involvement and partnership in NASA missions such as Cassini-Huygens the agency has had experience in space system design that has exploited RTG and RHU technologies. The Huygens probe schematic below depicts the use of a total of 34 Light Weight Radioisotope Heater Units (LWRHUs) [21, 22] that were provided to NASA by the U.S. Department of Energy for integration prior to launch at Cape Canaveral with the Huygens probe structure.

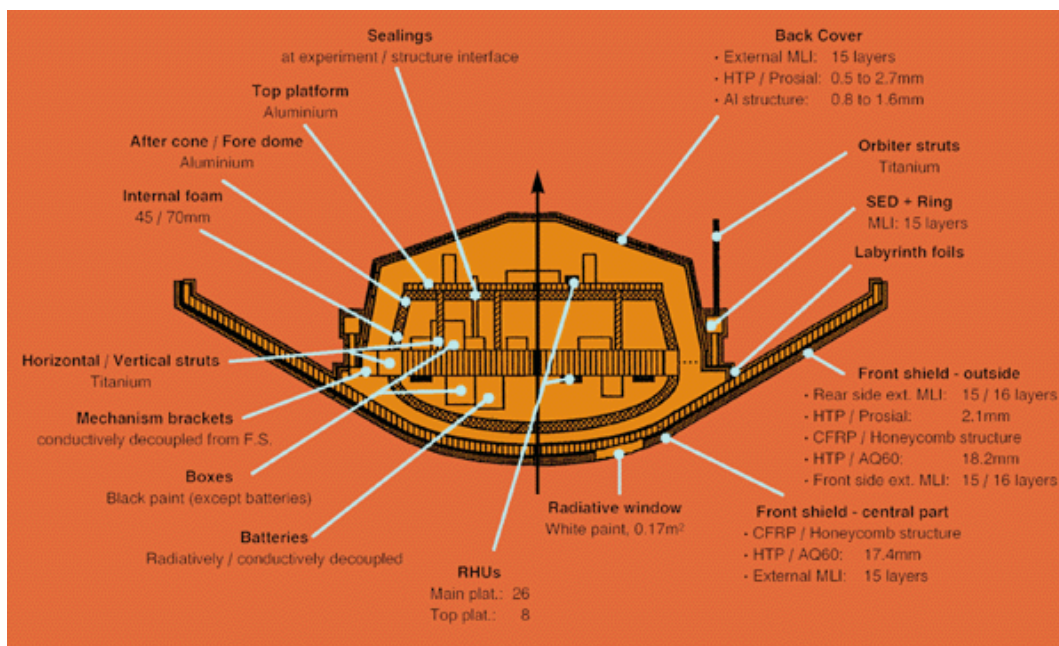


**Figure 2.18** – Schematic of the ESA's Huygen's Probe showing the location of all 34 LWRHUs/

During the mid 1990s, the European space agency explored the option of purchasing Angel RHUs and RTGs from the Russian government as part of a technology exchange program [15]. The discussions explored the purchase of flight qualified 8.5W<sub>th</sub> units in addition to the development of a 50 W<sub>th</sub> RHU but to date have

not been successful, despite recent interest in the use of 8.5 W<sub>th</sub> units under the ExoMars rover mission. At the time of writing, it is anticipated that the ExoMars rover will utilise between 3 and 8 Light Weight RHUs supplied by the U.S. Department of Energy under a technology transfer agreement between the European Space Agency and NASA.

In order to develop its own capability in RHU and RPS technologies, the European Space Agency has begun a series of technical evaluations and feasibility studies in related fields as the author completes this thesis. Through formal contributions and informal discussions with the ESA program staff, the results from this thesis and the author's related work is helping to answer key questions regarding radioisotope encapsulation, selection and availability that will be used to define the ESA strategy and developmental roadmap.

## **2.8 Summary of space RTG systems built to date**

Table 2.2 below outlines the chronological development of unclassified radioisotope power systems for space.

Device	Fuel	Application	Designed Electrical Power (W)	Mass (kg)	Design Life	Mission Status
SNAP-1	<sup>144</sup> Ce	USAF satellite	500	n/a	60 days	Superseded by SNAP-1A
SNAP-1A	<sup>144</sup> Ce	USAF satellite	125	91	1 year	Cancelled 1959
SNAP-3	<sup>210</sup> Po	Thermoelectric demonstration (AEC)	2.5	2	90 days	Shown to President Eisenhower in 1960 in the Oval Office.
SNAP-3B	<sup>238</sup> Pu	Transit 4A (U.S. Navy Navigation)	2.7	2	>1 year	Launched June 1961. Operation terminated 1976
	<sup>238</sup> Pu	Transit 4B (U.S. Navy Navigation)	2.7	2	>1 year	Launched Nov 1961. Operation terminated 1971
POODLE / SNAPOODLE	<sup>210</sup> Po	Radioisotope Thruster / RTG for various DOD applications	220		< 1 year	Development program ran 1961-1967
SNAP-9A	<sup>238</sup> Pu	Transit 5BN-1 (U.S. Navy Navigation)	25	12	>1 year	Launched 28 <sup>th</sup> Sept 1963 with 2.2-year life.
	<sup>238</sup> Pu	Transit 5BN-2 (U.S. Navy Navigation)	25	12	>1 year	Launched 5 <sup>th</sup> Dec 1963 with 2.2-year life.
	<sup>238</sup> Pu	Transit 5BN-3 (U.S. Navy Navigation)	25	12	>1 year	Destroyed during launch abort 21 <sup>st</sup> April 1964.
SNAP-11	<sup>242</sup> Cm	Surveyor Lunar Lander (NASA)	25	14	90 days	Requirement cancelled 1965
SNAP-13	<sup>242</sup> Cm	Thermionic demonstration (AEC)	12.5	2	90 days	Program completed at ORNL Nov 1965 to 1966.
Orion-1	<sup>210</sup> Po	Cosmos 84 (USSR)	20	-	-	Launched 1965
SNAP-17A & SNAP-17B	<sup>90</sup> Sr	Comms. Satellite (USAF)	30	14	>1 year	Design & component tests completed Nov 1965.

**Table 2.2:** Highlighted cells within the fuel column indicates if a device was fuelled.

Device	Fuel	Application	Designed Electrical Power (W)	Mass (kg)	Design Life	Mission Status
SNAP-19A	<sup>238</sup> Pu	Imp satellite (NASA)	20	8	>1 year	Component tests completed 1963. Not flown on Imp due to Radiation interference
	<sup>90</sup> Sr	Various Satellites (AEC)	250	n/a	>1 year	6 design studies (1964)
	<sup>238</sup> Pu	Surveyor Lunar Rover (NASA)	40	10	1 year	Design study (1964)
	<sup>210</sup> Po	Extended Apollo Missions (AEC)	1500	n/a	30-90 days	Design study (1964)
SNAP-19B	<sup>238</sup> Pu	Nimbus B-1 Meteorological satellite (NASA)	30	14	>1 year	Launch aborted 1968. fuel recovered and re-used in SNAP-19B3
SNAP-19B3	<sup>238</sup> Pu	Nimbus III Meteorological satellite (NASA)	30	14	>1 year	Launched 14 <sup>th</sup> April 1969.
SNAP-25	<sup>238</sup> Pu	Various satellites (AEC)	75	16	>1 year	Program cancelled
SNAP-27	<sup>238</sup> Pu	Apollo 12 Lunar Surface Experiment Packages (NASA)	63.5	31 + 11kg cask	1 year	1 <sup>st</sup> unit deployed on lunar surface. Launched 14 <sup>th</sup> November 1969.
	<sup>238</sup> Pu	Apollo 13, Lunar Surface Experiment Package (NASA)	63.5	31 + 11kg cask	1 year	Launched 11 <sup>th</sup> April 1970. Unit landed deep pacific ocean (Tonga Trench) after mission failure.
	<sup>238</sup> Pu	Apollo 14 Lunar Surface Experiment Package (NASA)	63.5	31 + 11kg cask	1 year	Launched 31 <sup>st</sup> January 1971
	<sup>238</sup> Pu	Apollo 15 Lunar Surface Experiment Package (NASA)	63.5	31 + 11kg cask	1 year	Launched 26 <sup>th</sup> July 1971
	<sup>238</sup> Pu	Apollo 16 Lunar Surface Experiment Package (NASA)	63.5	31 + 11kg cask	1 year	Launched 26 <sup>th</sup> April 1972
	<sup>238</sup> Pu	Apollo 17 Lunar Surface Experiment Package (NASA)	63.5	31 + 11kg cask	1 year	Launched 7 <sup>th</sup> December 1972
Orion-2	<sup>210</sup> Po	Cosmos 90 (USSR)	20	-	-	Launched 1971

**Table 2.2 continued:** Highlighted cells within the fuel column indicates if a device was fuelled.

Device	Fuel	Application	Designed Electrical Power (W)	Mass (kg)	Design Life	Mission Status
SNAP-29	<sup>238</sup> Pu <sup>90</sup> Sr <sup>244</sup> Cm	Various mission designs for NASA and the DOD	100 to 15,000	n/a	90 days to 5 years	Design & test program from 1967 to 1970
Transit RTG	<sup>238</sup> Pu	Navigation satellite (U.S. Navy)	30	14	5 years	Launched 1972
SNAP-19	<sup>238</sup> Pu	Pioneer 10 Jupiter flyby mission (NASA)	30	14	3 years	1973-2006 4 SNAP-19 units used
	<sup>238</sup> Pu	Pioneer 11 Jupiter flyby mission (NASA)	30	14	3 years	1973-1995 4 SNAP-19 units used
	<sup>238</sup> Pu	Viking 1 Mars Lander (NASA)	35	14	> 2 years	July 1976 – Nov 1982 2 SNAP-19 used
	<sup>238</sup> Pu	Viking 2 Mars Lander (NASA)	35	14	> 2 years	Sept 1975 – July 1978 2 SNAP-19 units used
Unknown	<sup>210</sup> Po	Unknown application (USSR)	40	-	-	Project initiated in 1978. Never launched. 600 Wth initial loading.
MHW-RTG	<sup>238</sup> Pu	Various Missions for the U.S. Department of Defence.	150	n/a	5 – 10 years	
	<sup>238</sup> Pu	Lincoln Experimental Satellite 8 (U.S. Air Force)	150	n/a	5 – 10 years	Launched 14 <sup>th</sup> March 1978 with LES 9 2 MHW-RTG units used
	<sup>238</sup> Pu	Lincoln Experimental Satellite 9 (U.S. Air Force)	150	n/a	5 – 10 years	Launched 14 <sup>th</sup> March 1978 with LES 8 2 MHW-RTG units used
	<sup>238</sup> Pu	Voyager 1 (NASA)	150	n/a	5 – 10 years	1977 – present 3 MHW-RTG units used
	<sup>238</sup> Pu	Voyager 2 (NASA)	150	n/a	5 – 10 years	1977 – present 3 MHW-RTG units used

**Table 2.2 continued:** Highlighted cells within the fuel column indicates if a device was fuelled.

Device	Fuel	Application	Designed Electrical Power (W)	Mass (kg)	Design Life	Mission Status
GPHS-RTG	<sup>238</sup> Pu	Various Missions for NASA and the DOD.	290	54	15 years	
	<sup>238</sup> Pu	Galileo (NASA)	290	54	15 years	1989-2003 2 GPHS-RTG units used
	<sup>238</sup> Pu	Ulysses (NASA)	290	54	15 years	1990-present 1 GPHS-RTG units used
	<sup>238</sup> Pu	Cassini (NASA)	290	54	15 years	1997 – present 3 GPHS-RTG units used
	<sup>238</sup> Pu	New Horizons (NASA)	290	54	15 years	2006 – present 1 GPHS-RTG unit used
Angel (8.5 W <sub>th</sub> )	<sup>238</sup> Pu	Mars 96 – 2 surface science stations (Russia)	0.15	0.5	10 years	Launched 16 <sup>th</sup> November 1996. 2 8.5W <sub>th</sub> Angel units used per surface science station. Failed Earth departure stage resulted in atmospheric re-entry.
MMRTG	<sup>238</sup> Pu	Various Missions for NASA and the U.S. Department of Defence.	125	44.2	> 14 years	
	<sup>238</sup> Pu	Mars Science Laboratory (NASA)	125	44.2	> 14 years	1 <sup>st</sup> flight Unit in storage for 2011 launch following MSL mission delay
ASRG	<sup>238</sup> Pu	Various Missions for NASA and the DOD.	145	21	-	Under Development

**Table 2.2 continued:** Highlighted cells within the fuel column indicates if a device was fuelled.

## 2.9 Nuclear thermal propulsion

In any rocket propulsion system, the thrust generated by a given engine design is related to the mass and velocity at which propellants are exhausted through a nozzle per unit time. This relationship is defined by Equation 2.1. In a chemical rocket engine, the heat of combustion results in the excitation of typically gaseous combustion products to a velocity referred to in the context of rocket propulsion as the characteristic velocity  $c^*$ . The physical design of a rocket engine is driven by its operating environment and most significantly, the nozzle is used to maximise the exhaust velocity. This optimisation is achieved through expansion of the exhaust down to a pressure as close to the external environmental pressure as is practically achievable. The gain in performance and thus exhaust velocity is represented by the introduction of a coefficient of thrust  $C_R$ . For derivation of the coefficient of thrust and its relationship to rocket nozzle design, the author directs the reader to the published works by Turner [23] and Sutton [24].

$$F_R = \dot{m} v_e \quad (2.1)$$

**Equation 2.1** Thrust generated by a rocket engine with a mass flow rate  $\dot{m}$  and exhaust velocity  $v_e$  [24].

$$v_e = c^* C_R \quad (2.2)$$

**Equation 2.2:** The exhaust velocity of a rocket engine as a function of the characteristic velocity  $c^*$  and the coefficient of thrust  $C_R$  [24].

Through conservation of energy, the characteristic velocity of the propellants obtained in a combustion chamber is related most fundamentally to the molecular mass and temperature of the exhaust [23]. This is defined in Equation 2.3. Clearly, for a fixed gas product, the greatest performance can be achieved through the maximisation of the operating temperature of the rocket engine and by using an exhaust product with a low molecular mass.

$$c^* = \left( \gamma \left( \frac{2}{\gamma + 1} \right)^{(\gamma+1)/(\gamma-1)} \frac{M}{R T_c} \right)^{-1/2} \quad (2.3)$$

**Equation 2.3:** Characteristic velocity of the exhaust from a rocket engine as a function of the exhaust molecular mass  $M$ , ratio of specific heats  $\gamma$ , gas constant  $R$  and the engine chamber temperature  $T_c$  [23].

When discussing the efficiency of a rocket propulsion system, the efficiency is often conveyed as a value called the specific impulse  $I_{sp}$ . The specific impulse is related to the exhaust velocity as derived in Equation 2.4. Thus, a system with a greater exhaust velocity will be more efficient in terms of  $I_{sp}$ . A word of caution is however offered by the author, since in practice one must consider losses in an orbital system due to gravity. For example, although a propulsion system may have a large exhaust velocity and hence a large  $I_{sp}$ , it may yield a very low thrust and therefore for some applications, its use may be precluded by large gravity losses due to extended propulsive operation to achieve a given velocity change. This may be illustrated by a typical electric propulsion system. For this reason, a propulsion system that is to be used for multiple applications, i.e. both on orbit or surface to orbit transfers, should deliver a suitable level of thrust while producing a suitably large specific impulse. In context, the best theoretical performance delivered by a chemical propulsion

system that uses Liquid oxygen and Liquid Hydrogen as propellants is a specific impulse of around 389.5 seconds [24].

$$I = F dt = \dot{m} v_e dt$$

$$I_{sp} = \frac{F dt}{\dot{m} g_0 dt} = \frac{\dot{m} v_e}{\dot{m} g_0} = \frac{v_e}{g_0}$$

$$I_{sp} = \frac{v_e}{g_0} = \frac{c^* C_R}{g_0} \tag{2.4}$$

**Equation 2.4:** The specific impulse of a rocket propulsion system with respect to the propellant characteristic velocity  $c^*$ , the thrust coefficient  $C_R$ , and the acceleration due to gravity  $g_0$  at the Earth's surface.

The Nuclear Thermal Rocket (NTR) engine was developed as a propulsion system that could achieve higher efficiencies ( $I_{sp}$ ) than can be achieved by chemical propulsion systems while being capable of delivering usable thrust for on orbit transfer in large fields of gravitational influence over short periods of time. The concept of NTP relies on the excitation of a propellant by provision of heat from the core of a nuclear fission reactor. Since the propellant characteristic velocity is related to both its molecular mass and operating temperature, a low mass propellant is highly desirable while the reactor core temperature should be driven to very high temperatures. The thermodynamic properties of the propellant should also be considered, in particular the ratio of specific heats since its magnitude is proportional to the magnitude of the characteristic velocity as described in Equation 2.3. It should of course be noted that non-combustible propellants can be selected for operation of NTP systems which may allow for a reduction in storage requirements, overall mass and mission cost. However, careful consideration must be made during propellant selection for material and chemical compatibility at high temperatures. As an example, oxidisers or pure

oxygen is not suitable for use as a propellant since this would be likely to cause combustion of the core structure. Table .1 identifies some potentially suitable propellants that can be used in a nuclear thermal propulsion system.

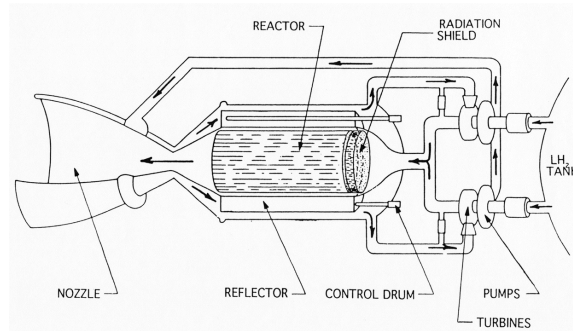


**Figure 2.19:** Basic components of a Nuclear Thermal Rocket (NTR) propulsion system [25].

Propellant	Ratio of specific heats ( $\gamma$ )	Molecular Mass (g/mol)	Characteristic velocity $c^*$ for an exit temperature of 2500 °C (m/s)	$I_{sp}$ at 2500 °C and $C_R=1.85$ (s)
Hydrogen (H <sub>2</sub> )	1.41	2	4946	933
Helium (He)	1.67	4	3304	623
Nitrogen (N <sub>2</sub> )	1.40	28	1325	250
Argon (Ar)	1.67	40	1044	197
Carbon Dioxide (CO <sub>2</sub> )	1.28	44	1091	206
Carbon Monoxide (CO)	1.40	28	1325	250
Ammonia (NH <sub>3</sub> )	1.32	17	1736	327
Methane (CH <sub>4</sub> )	1.32	16	1789	337
Sulphur Dioxide (SO <sub>2</sub> )	1.26	64	909	171

**Table 2.3:** Selected NTR propellants and their physical properties.  $\gamma = c_p/c_v$ . The characteristic velocity of the propellant is given for an NTR core temperature of 2500 °C.

Between 1955 and 1972, the United States built and performed in excess of twenty NTR engine tests under the Rover and NERVA programs. The Rover/NERVA tests demonstrated specific impulses of around 850 seconds and thrust levels between 111 kN and 1.11 MN [26]. The U.S. programs also demonstrated that operation in excess of two hours and the ability to execute multiple re-starts is achievable using reactors using the thermal neutron spectrum via self-moderating graphite based fuel designs [27]. Two fuel designs were developed and tested extensively for their lifetime and compatibility within the

NTR environments. The first fuels developed under the Rover program utilised a composite dispersion of metallic  $^{235}\text{U}$  within a graphite element matrix. Such fuels were found to be susceptible to migration of fuel at high temperatures through pores and voids within the matrix. In the second type, fuel particles coated within a pyro-carbon cladding were distributed within a graphite matrix in an attempt to prevent migration of fuel throughout the general matrix. These two fuel types are illustrated in Figure 2.20 below.

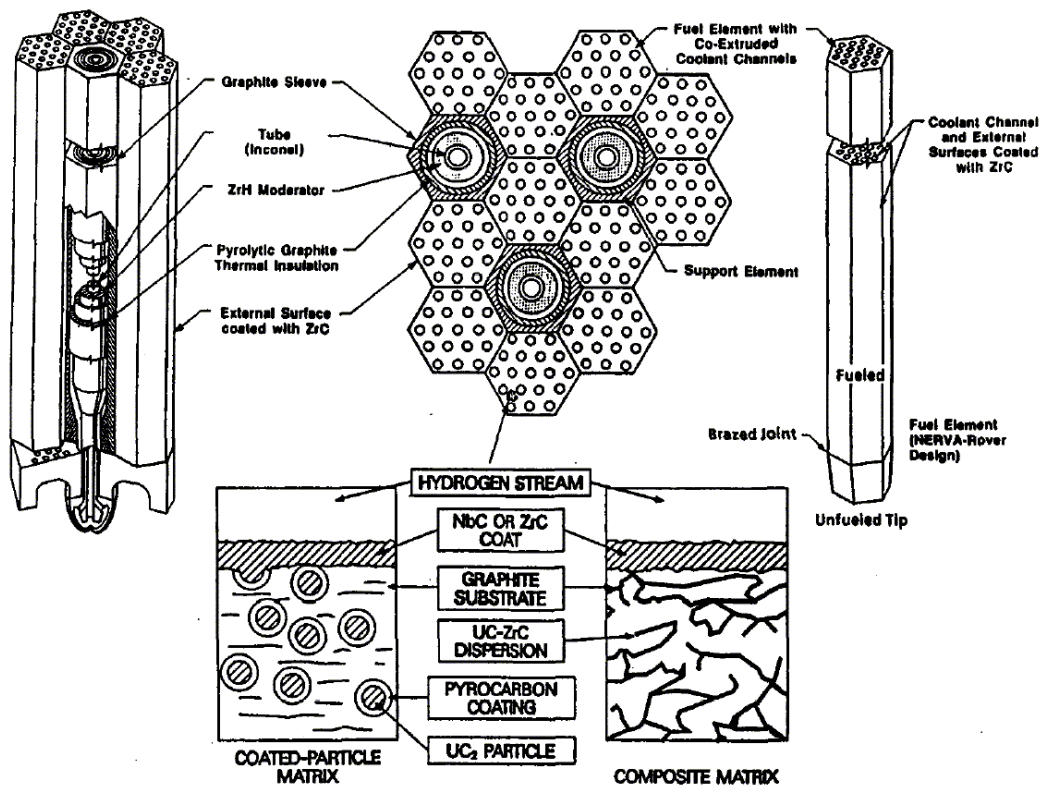


**Figure 2.20:** (Top) The Rover/NERVA fuel assembly design with 19 flow channels per fuel element. (Bottom) Composition of fuels developed and tested for the Rover/NERVA nuclear thermal rocket programs. [27]

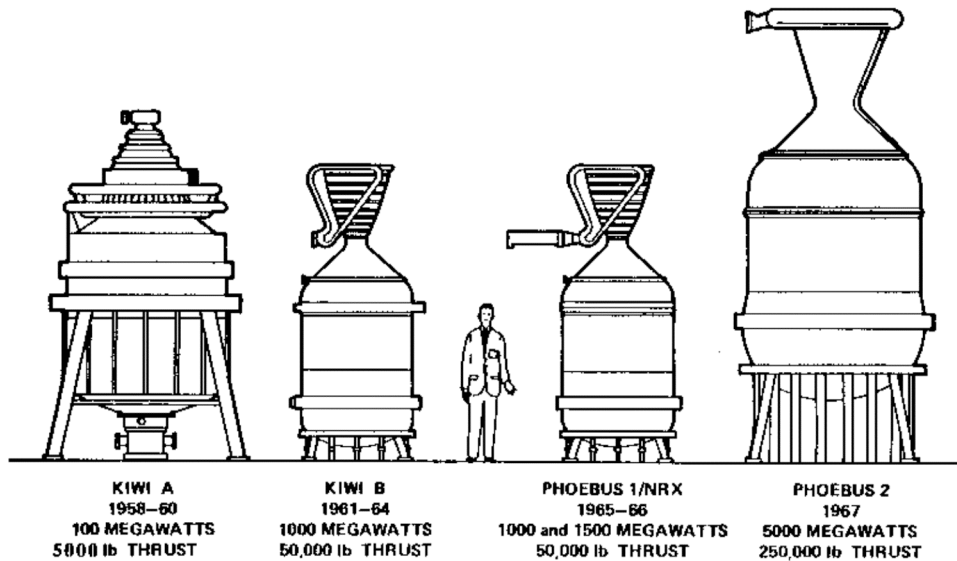


**Figure 2.21:** Approximate scale of reactors tested during the Rover Nuclear Thermal Rocket program [28].

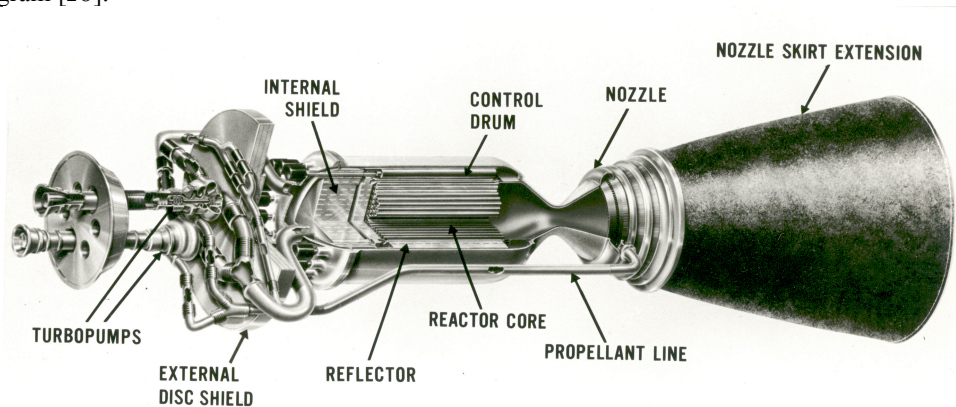


**Figure 2.22:** NERVA rocket engine design cross section. Image courtesy of NASA.

Building upon its extensive experience in space reactor design and operation, the Soviet Union also conducted a series of fuel tests for NTR systems within the IGR and EWG-1 research reactors in Kazakhstan. Figure 2.5 (right) illustrates in-core experimentation with UC-ZrC-NbC and UC-ZrC-C fuel forms within the EWG-1 reactor. The Soviet tests culminated in the operation of a 36 kN thruster of the RD-0140 design [29] (11B91 – IGRIT) on the 27<sup>th</sup> March 1978 [30]. A photograph of the IGRIT engine is illustrated Figure 2.5 (left). A design for a 392 kN thruster was also prepared during the Soviet research program [29] although production of a full scale prototypic unit is not confirmed.

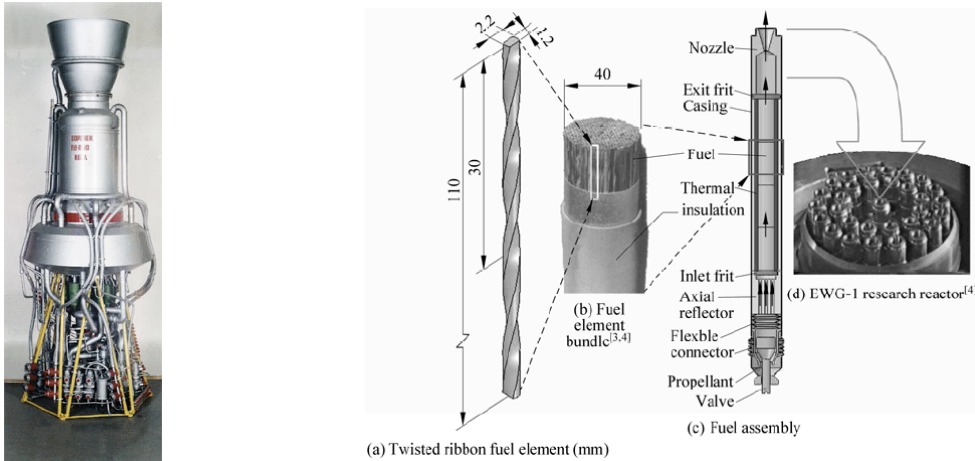


**Figure 2.23:** (Left) Russian 11B91 “IGRIT” NTR engine. (Right) Test assemblies of so called ‘Twisted-Ribbon’ fuel elements as tested within the EWG-1 research reactor [29].

In practice, propellant is injected into the reactor core at a velocity that is specific to the system design, typically via turbo machinery. Fundamentally, the injection velocity ( $v_{inj}$ ) is driven by mass flow rate ( $\dot{m}$ ), total cross sectional area of the flow channels ( $A_{CSF}$ ) and propellant injection density ( $\rho_{inj}$ ). Equation 2.5 expresses this relationship. In basic analyses of NTR systems, the injection velocity is commonly ignored but its neglect gives rise to error in the effective exhaust velocity that is achieved by a given system. Thus, the effective exhaust velocity may be estimated through adaptation of Equation 2.2 via the summation of the propellant injection velocity and the characteristic velocity, which may be considered to be a velocity increment due to heating within the core. An estimation of the NTR effective exhaust velocity is presented in Equation 2.7.

$$v_{inj} = \frac{\dot{m}}{\rho_{inj} A_{CSF}} \quad (2.5)$$

**Equation 2.5:** The propellant injection velocity ( $v_{inj}$ ) as a function of the mass flow rate ( $\dot{m}$ ), injection density ( $\rho_{inj}$ ) and the total cross sectional area of flow channels ( $A_{CSF}$ ).

$$A_{CSF} = n_{FC} \pi r_{FC}^2 \quad (2.6)$$

**Equation 2.6:** The total cross sectional area of flow channels ( $A_{CSF}$ ) with respect to the total number of flow channels within the core  $n_{FC}$  and the flow channel radius  $r_{FC}$ .

$$v_e^* = (c^* + v_{inj}) C_R \quad (2.7)$$

**Equation 2.7:** The practical effective exhaust velocity ( $v_e^*$ ) with respect to propellant injection velocity ( $v_{inj}$ ), characteristic velocity  $c^*$  and the coefficient of thrust  $C_R$ .

## 2.10 Tungsten core power and propulsion reactors

The overall efficiency of any nuclear fission power and propulsion system is limited most fundamentally by the efficiency of the heat transfer from fuel to propellant within the core and the thermal power density of the fuel elements. Similarly, the successful fabrication, operational performance and safety of reactor fuels for space power and propulsion applications is clearly driven by the fabrication techniques and materials adopted. Under the Rover/NERVA programs, the NTR reactor cores comprised of carbon-based fuel elements in which fuel materials were dispersed within graphite matrices (see Figure 5.2 Bottom). The most efficient propellant for NTR systems is hydrogen when consideration is given to specific impulse (See Table 5.1). Unfortunately, hydrogen is highly erosive to graphite structures at elevated temperatures and under turbulent flow. Efforts were made to reduce the effect of hot hydrogen erosion through the provision of protective claddings during the Rover program, but these efforts did not completely eliminate the problem. Figure 5.10 illustrates the mass loss rate as a function of axial position. It was noted that a region known as the mid-band axial position experienced the greatest mass loss rates

irrespective of fuel composition. This mid-band region corresponded to the position of greatest temperature gradient and thus thermal stresses are believed to have caused fracture points. The brittleness of carbon-based fuel elements is an inherent problem for operational safety and containment during accident scenarios involving impact and the ease of material extraction from the carbon matrix presents several non-proliferation issues.

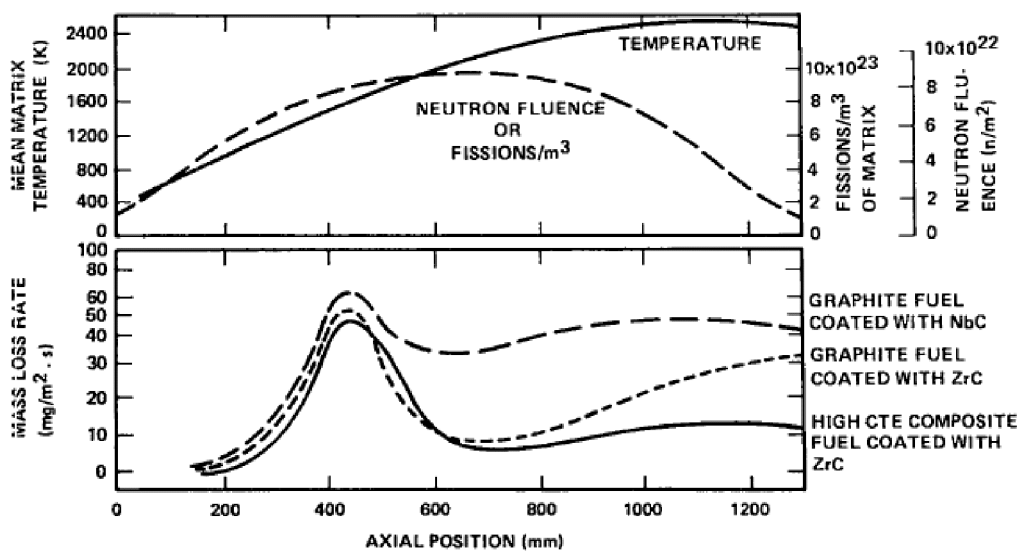


**Figure 5.10:** Mass loss from Pewee and NF-1 NTR reactors tested under the Rover/NERVA programs. Mass loss is presented as a function of axial position and reactor environment. The peak in the mass loss curve is the so-called midband or midrange corrosion. The best performance was obtained from the composite fuels coated with zirconium carbide (ZrC). [31]

Tungsten has a greater thermal conductivity than that of graphite, a high melting point, and is more resistant to creep deformation at elevated temperatures. Tungsten is also more resistant to fuel migration within its matrix and is more resistant to physical changes induced by radiation, such as neutron absorption [32]. It has been shown that fission product gases released within a tungsten-cermet matrix can be effectively contained for temperatures up to 1550°C [33]. Thus, tungsten cermet fuels are likely to be more compatible to the hot hydrogen operating conditions within an NTR core [25].

Unlike the fuels developed for the Rover/NERVA program, tungsten cermet based fuels must be operated within the fast neutron spectrum. When compared to reactors operating in the thermal neutron spectrum, fast spectrum reactors are less susceptible to reactivity degradation with respect to an increase in fission product inventory over time due to the relatively low neutron absorption cross sections of abundant fission products at high energies. Thus, it is anticipated that a fast spectrum NTR will have longer reactivity and materials durability lifetimes than those of thermal spectrum systems with graphite fuel matrices.

Previous space reactor programs such as the Argonne National Laboratory (ANL) rocket program and the General Electric 710 (GE-710) program have investigated the use of uranium dioxide encased in tungsten and tungsten-rhenium matrices (cermet fuels) in order to eliminate the problems associated with graphite based fuels [34]. Both programs proved the viability of encasing  $\text{UO}_2$  in both a tungsten and tungsten-rhenium matrix using hot press sintering techniques with varying levels of success. Both programs also revealed that oxygen atoms dissociated from the uranium at the high sintering and operational temperatures, which formed volatiles such as  $\text{WO}_2$  and  $\text{WO}_3$ . In order to mitigate the formation of tungsten oxides,  $\text{ThO}_2$  and  $\text{GdO}_{1.5}$  were added to the fuel in order to suppress the effective dissociation at temperature by increasing the probability for oxygen recombination. The fuel elements were formed in a volume ratio of 60% $\text{UO}_2$ -34%W-6% $\text{GdO}_{1.5}$  or 6% $\text{ThO}_2$ . The uranium was enriched to 93 wt%  $^{235}\text{U}$  and the GE-710 program mixed the tungsten into a 75 wt% W - 25 wt% Re alloy to increase the ductility [35].

Further enhancements of the tungsten-cermet fuel can be made using various tungsten-compatible additives. Rhenium and molybdenum can be added to the tungsten to reduce the brittleness and improve the toughness of the metal matrix. The ductile-to-brittle transition temperature is also adjusted through the addition of these materials. To reduce migration of fission product and fuel inventory, the grain boundaries of the ceramics can also be modified by the addition of thoria ( $\text{ThO}_2$ ) or gadolinium oxide  $\text{Gd}_2\text{O}_3$  which act as stabilizers.

The mechanical properties of refractory alloy cermet fuel elements may allow for the safe operation at high temperatures resulting in NTR systems with large specific impulses while maintaining integrity and capture of nuclear fuels during exposure to hot hydrogen environments. Likewise, refractory alloy fuel elements provide resistance against the high temperatures experienced during atmospheric re-entry and impacts associated with launch failures and spaceflight accidents, while providing inherent physical security and resistance to extraction by pyrolysis or direct pyrotechnic dispersion of fuel materials. The 710 program demonstrated excellent promise for refractory alloy fuels, but the high temperatures experienced by the fuel materials during cermet fabrication via hot isostatic pressing likely contributed to containment failures in some fuel elements through the reduction of the fuel compounds and allowing for the migration of liquid uranium metal throughout the tungsten matrices prior to the closure of the tungsten pores during sintering. The localized formation of tungsten oxides may also have presented mechanical weaknesses within some of the fuel cermets.

Work undertaken by the National Aeronautics and Space Administration attempted to reduce volatilization and reduction of the fuels during high temperature sintering by pre-coating the fuel particles in the same material as the matrix of choice (tungsten) using a spheridisation process [36]. However, the fundamental problems attributed to hot press sintering of cermets resulted in significant grain growth, and thus a lower than theoretical matrix strength was attained.

The volumetric fraction of the fuel materials to be encapsulated within a cermet as discussed in section 5.4 is an influential factor attributed to the material properties such as strength and fuel migration and the overall amount of material that can be released to the external environment in the event of fracture, which, in the case of the nuclear thermal rocket is the hydrogen propellant stream. The effective critical mass of a tungsten cermet core is also dependant upon the volumetric loading of the fuel elements. To demonstrate this relationship, a model of the Pewee NTR core was created using the MCNP Monte Carlo radiation transport code and its graphite based  $^{235}\text{U}$  composite fuel was substituted with tungsten cermets of varied fuel-tungsten volumetric ratios. The Rover/NERVA Pewee engine was selected for modelling due to the availability of a large inventory of design data to the author and colleagues at the Center for Space Nuclear Research at Idaho National Laboratory. Uranium Nitride ( $^{235}\text{UN}$ ) was selected as the fuel compound due to its stability under neutron irradiation and a matrix of pure tungsten was assumed. Details and cross sectional diagram of the MCNP model adopted for the study are presented in Figure 5.11. Figure 5.12

illustrates the results for the Monte Carlo modelling of the cermet Pewee core effective k value as a function of volumetric ratio of uranium nitride to tungsten.

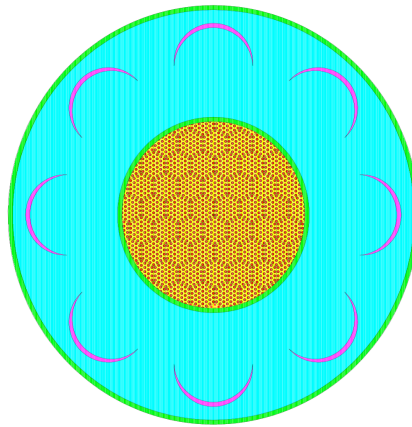


**Figure 5.11:** Cross sectional view of the MCNP model used in the determination of criticality or effective k value for a tungsten cermet fuelled Rover/NERVA Pewee engine. Here a core of 27 cm diameter composed of UN-tungsten cermet fuel elements equal to the Rover/NERVA fuel geometry is surrounded by a beryllium reflector and a total of 8 control drums segmented with a B<sub>4</sub>C neutron absorber.

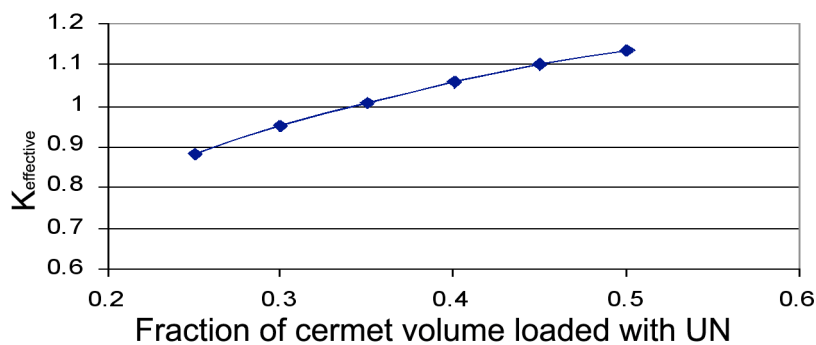


**Figure 5.12:** The criticality / effective k value for a Rover/NERVA Pewee core fuelled by tungsten-uranium nitride cermet elements as a function of volumetric fuel loading between 25% and 50% UN.

Launch Safety is a significant contributing factor that should be considered within the design of any fission reactor that is built for space applications. Reactor cores that are designed to operate in the thermal neutron spectrum are more susceptible to uncontrolled criticality during accidental submersion into fresh or sea water due to reflection and in the case of water infiltration, enhancement of moderation [25, 26]. This was also considered to be a

limiting factor for the use of the Topaz II reactor system purchased from the former Soviet Union by NASA in the 1990's [37] which led to unimplemented design modification efforts prior to the cancellation of the US program. Monte Carlo modelling using MCNP [38] of fast reactor systems undertaken by the author in collaboration with J.D. Bess at the Center for Space Nuclear Research revealed that a tungsten based fast reactor is unlikely to achieve criticality in accidental submersion events with the exception of intact impact into wet silica sands [25]. When considering core lifetime, launch safety and proliferation resistance, it is apparent that fast spectrum tungsten cermet reactors offer a greater solution than equivalent graphite based thermal reactors such as those used in the Rover/NERVA program.

## **2.11 Thermal analysis of Nuclear Thermal Propulsion**

Within the frame of reference for the reactor core of an NTR propulsion system, the propellant acts as a coolant and thus the operating power output of the core must be equal to the rate at which heat can be removed from the system including thermal losses. Figure 2.2 (Top) illustrates fuel element assemblies that were developed during the Rover/NERVA Nuclear Thermal Rocket programs in the US. In the Rover/NERVA designs, several (19) propellant flow channels are integral to the structure of each fuel element. Careful design of the propellant flow channels should facilitate efficient heat transfer between the fuel and the propellant/coolant. Equation 2.8 relates the total power removed by a single-phase propellant heated to a hot temperature by difference  $\Delta T$ . A system which uses a propellant that undergoes a phase change during operation must also

provide sufficient power and hence energy equivalent to the latent heat in addition to the power required to elevate the propellant temperature.

$$P = \dot{m} c_p \Delta T \quad (2.8)$$

**Equation 2.8:** Power that must be extracted from the core of an NTR by a propellant raised in temperature by  $\Delta T$  with a mass flow rate  $\dot{m}$  and specific heat capacity  $c_p$ .

If we consider the axial temperature distribution of a simple core design with a uniform fission power distribution, the region closest to the propellant inlet will be cooler than the region closest to the exit. This can be demonstrated through detailed analysis of heat transfer between the core and the propellant. In practice, this axial temperature gradient across the core can be minimised by manufacturing a core with a suitable axial power distribution by varying the fuel loading concentrations with respect to position.

Maximisation of heat transfer to the propellant within the core of an NTR engine is facilitated by forced convection via turbulent flow through flow channels within individual fuel elements. Estimation of the heat transferred to the propellant from the walls to the propellant may be made through the consideration of the heat transfer coefficient,  $h$  ( $\text{W m}^{-2} \text{K}^{-1}$ ) and the total surface area ( $A_{\text{SFC}}$ ) of flow channels within the NTR core. The rate at which thermal energy may be transferred in bulk from core to propellant is therefore estimated in Equation 2.9. It should be noted that the log mean value of the temperature difference is used since the value of the heat transfer coefficient varies with respect to temperature due to the temperature dependency of the thermo-physical properties of the propellant.

$$P = \left( A_{SFC} \Delta T_{Log-Mean} \right) \frac{dh}{dt} \quad (2.9)$$

**Equation 2.9:** Power that is transferred from the core of an NTR to a propellant raised in temperature by  $\Delta T$ , where  $h$  is the heat transfer coefficient and  $A_{SFC}$  is the total surface area of the propellant flow channels.

In the case of the nuclear rocket engine, the heat transfer coefficient ( $h$ ) is governed by the thermal conductivity of the propellant, which varies in practice as a function of temperature, and is enhanced by the overall dominance of the turbulent flow. The unit-less Nusselt number ( $\eta$ ) may be used to quantify the ratio of convective to conductive heat transfer between the inside wall of the flow channel and the propellant. Since the heat varies across the entire diameter of the flow channel, this must be accounted for by consideration of the hydraulic diameter. The hydraulic diameter  $D_H$  is not equal to the diameter of the flow channel for complex channel geometries since it is related to the wetted region in which fluid flows. In the case of a circular cross section, the  $D_H$  is however equal to the channel diameter ( $2r$ ) as shown in Equation 2.10. The dependency of the heat transfer coefficient to the thermal conductivity, hydraulic diameter and Nusselt number is presented in Equation 2.11 for dimensional analyses of NTR propellant systems.

$$D_H = \frac{4A_{CSF}}{L_{circ}} = \frac{4\pi r^2}{2\pi r} = 2r \quad (2.10)$$

**Equation 2.10:** The hydraulic diameter for a circular flow channel of radius  $r$ , cross sectional area  $A_{CSF}$  and circumference  $L_{circ}$ .

$$h = \frac{k\eta}{D_H} \quad (2.11)$$

**Equation 2.11:** The heat transfer coefficient for a turbulent propellant flowing through a flow channel of hydraulic diameter  $D_H$  with a Nusselt number  $\eta$ .

Estimation of the heat transfer coefficient (h) may be made for forced convection conditions via turbulent flow by implementation of the Dittus-Boelter correlation, which relates the Nusselt Number ( $\eta$ ) to the Prandtl number ( $P_r$ ) and the Reynolds ( $R_e$ ) number. In the case of an NTR propellant where the fluid is acting as a coolant, the value of n in the Dittus-Boelter correlation was found to be 0.3. It is understood that for a fluid that acts to heat a tube through which it flows, the value of n is equal to 0.4. The Dittus-Boelter correlation is presented in Equation 2.12 below.

$$\eta = 0.023R_e^{0.8}P_r^n \quad (2.12)$$

**Equation 2.12:** The Dittus-Boelter correlation for the Nusselt number ( $\eta$ ) with respect to the Reynolds number  $R_e$ , Prandtl number  $Pr$ . In the case of an NTR propellant,  $n = 0.3$ .

The Reynolds Number ( $R_e$ ) is a dimensionless ratio of a fluid's inertial forces ( $\rho v^2/D_H$ ) to viscous forces ( $\mu V/D_H^2$ ) [39]. Through empirical evaluations of the Reynolds Number, it is understood that the onset of turbulent flow within circular flow channels may be observed where  $R_e \geq \sim 2.3 \times 10^3$  [40]. Thus, in preliminary flow channel design, the hydraulic diameter must be engineered such that turbulent flow exists throughout the axial profile.

$$R_e = \frac{\rho V D_H}{\mu} = \frac{V D_H}{\nu} \quad (2.13)$$

**Equation 2.13:** The Reynolds number for a propellant of density  $\rho(T,P)$ , kinematic viscosity  $\nu(T,P)$  and dynamic viscosity  $\mu(T,P)$  travelling through a channel with hydraulic diameter  $D_H$  at a velocity  $V$ .

The Prandtl number provides a numerical ratio of the momentum diffusivity or kinematic viscosity to the thermal diffusivity within a turbulent fluid. This may in turn be related to the thermal conductivity of the fluid. Equation 2.14 presents this relationship to the Prandtl number.

$$Pr = \frac{\nu}{\alpha} = \frac{c_p \mu}{k} \quad (2.14)$$

**Equation 2.14:** The Prandtl Number  $Pr$  with respect to kinematic viscosity  $\nu(T,P)$  and thermal diffusivity ( $\alpha$ ) of the propellant. Also presented is its relationship to specific heat capacity  $c_p(T)$ .

Clearly, a basic estimation of the flow channel design can be determined by implementation of Equations 2.9 to 2.14 from a given set of start conditions. However, such a model may be considered somewhat inaccurate for practical system design purposes due to the temperature and pressure dependency of the thermo-physical properties used to estimate the heat transfer coefficient. In practice, a Finite Element Analysis (FEA) based computational fluid dynamics (CFD) code such as Ansys [41] or Comsol must be used.

To date, the principal of nuclear thermal propulsion has been demonstrated through the extensive ground testing performed in the U.S. and in Russia. The results from these tests highlighted significant operational time dependant failures in the integrity of fuel forms that were historically adopted. Radiological contamination of the propellant as it exited the nozzle of the engine was observed during these tests [27]. Such failure of fuel matrices is not desirable for operational lifetime or for safety. One possible solution to the problems with the traditional graphite fuel forms is proposed and discussed in Chapter 6.

## 2.12 References

- [1] E. Levnor, I. Linkov, J. M. Proth, "*Strategic Management of Marine Ecosystems*". Springer; 2005. ISBN: 1-4020-3158-0.
- [2] Office of Polar Programs Environment Section. "*Environmental Action Memorandum: Installation, Maintenance and Removal of Automatic Weather Stations in Antarctica*". Office of Polar Programs. 18th February 1993.
- [3] V.P. Chechev, N.K. Kuzmenko, "*Table of Radionuclides*". Vol 2. Monographie Bureau International Des Poids et Mesures BIPM-5; 2004.
- [4] W. R. Corliss, Harvey D. G., "*Radioisotopic Power Generation*". Prentice-Hall, New Jersey; 1964.
- [5] G.L Bennett. "Space nuclear power: opening the final frontier". Proceedings of: Fourth International Energy Conversion Engineering Conference and Exhibit (IECEC), 2006; San Diego, California. AIAA.
- [6] J. A. Angelo, D. Burden, "*Space Nuclear Power*". Krieger Publishing, Malabar, FL.; 1985. ISBN: 0-89464-000-3.
- [7] M.S. Khan, W.L. Moguel, I. Dubrawsky. "*Viking Spacecraft*". The University of Texas at Austin, Austin, TX. November 22nd 1991.
- [8] C. E. Kelly. "MHW RTG performance during LES 8/9 and voyager missions". Proceedings of: Fourth symposium on Space Nuclear Power Systems, 1987; New Mexico University.
- [9] M.S. El-Genk, "Deployment history and design considerations for space reactor power systems". *Acta Astronautica*. 64 (2009) 833-849.
- [10] M. Benkö, et al, "*Space Law in the United Nations*". Martinus Nijhoff Publishers; 1985.
- [11] M.S. El-Genk, T.M. Schriener, "Performance and radiological analyses of a space reactor power system deployed into a 1000–3000 km earth orbit". *Progress in Nuclear Energy*. 52 (2010) 236-248.
- [12] M. Wade. "Encyclopedia Astronautica". <http://www.astronautix.com/project/rorsat.htm>.
- [13] V.P. Nikitin, B.G. Ogloblin, E.N. Sokolov, et al., "'YENISEI' SPACE NUCLEAR POWER SYSTEM". *Atomnaya Energiya*. 88 (2000) 95-108.
- [14] A.A. Pustovalov. "Nuclear thermoelectric power units in Russia, USA and European Space Agency research programs". Proceedings of: 16th International Conference on Thermoelectrics; August 26-29, 1997; Dresden, Germany. IEEE 0-7804-4057-419.
- [15] A.A. Pustovalov in private communication to A. Fournier-Sicre, Head of ESA Permanent Mission in Moscow. November 4th 1995
- [16] G.L. Bennett, J.J. Lombardo, R.J. Hemler, et al. "Mission of Daring: The General-Purpose Heat Source Radioisotope Thermoelectric Generator". Proceedings of: Fourth International Energy Conversion Engineering Conference and Exhibit (IECEC), 2006; San Diego, California. AIAA.
- [17] U.S. Department of Energy. "*Draft Environmental Impact statement for the proposed consolidation of Nuclear Operations related to production of Radioisotope Power Systems*". DOE/EIS-0373D. p.19.
- [18] Radioisotope Power Systems Committee of the National Research Council, "*Radioisotope Power Systems: An Imperative for Maintaining U.S. Leadership in Space Exploration*". National Academies Press; 2009. ISBN: 0-309-13858-2.

- [19] C.P. Bankston, K.L. Atkins, E.F. Mastal, D.G. McConnell, "Technology development issues in space nuclear power for planetary exploration". *Acta Astronautica*. 24 (1991) 161-170 DOI: [10.1016/0094-576\(91\)90163-Y](https://doi.org/10.1016/0094-576(91)90163-Y).
- [20] T. Todd, R. Herbst, B. Mincher, S. Frank, J. Law, J. Swansom. "Plutonium-238 Recovery From Irradiated Neptunium Targets Using Solvent Extraction". INL/CON-06-11850. Idaho National Laboratory, Idaho Falls, ID. October 2006.
- [21] K. Clausen, H. Hassan, M. Verdant, "The Huygens probe system design". *Space Science Reviews*. 104 (2002) 155-189.
- [22] J. Lebreton, D. Matson, "The Huygens probe: science, payload and mission overview". *Space Sci. Rev.* 104 (2002) 59-100.
- [23] M.J.L. Turner, "Rocket And Spacecraft Propulsion". 2<sup>nd</sup> ed. Praxis Publishing Ltd, Chichester; 2005. ISBN: 3-540-22190-5.
- [24] G.P. Sutton, O. Biblarz, "Rocket Propulsion Elements". 7<sup>th</sup> ed. John Wiley & Sons Inc., New York; 2001. ISBN: 0-471-32642-9.
- [25] S.D. Howe, R.C. O'Brien, N. Barra, et al. "Returning humans to the moon: comparison of chemical engine and nuclear rocket performance as an earth departure stage". Proceedings of: 2007 Space Nuclear Conference; June 24-28, 2007. American Nuclear Society, ISBN: 0-89448-053-7.
- [26] S.D. Howe, R.C. O'Brien. "Nuclear Thermal Rockets: History, Benefits and Issues Impacting Future Operations". Proceedings of: 57th Joint Army-Navy-NASA-Air Force (JANNAF) Propulsion Meeting, 2010; Colorado Springs, CO.
- [27] D. Koenig. "Experience gained from the Space Nuclear Rocket Program (Rover)". Los Alamos National Laboratory, Los Alamos, NM. May 1986.
- [28] S.V. Gunn, "Development of Nuclear Rocket Technology". *AIAA*. 89-2386 (1989).
- [29] V. Zakirov, V. Pavshook, "Russian Nuclear Rocket Engine Design for Mars Exploration". *Tsinghua Science and Technology*. 12 (2007) 256-260.
- [30] G.V. Konyukhov, A.I. Petrov, S.A. Popov, et al., "Prototype of a Nuclear Rocket Motor - The IGRIT Reactor". *Atomic Energy*. 97 (2004) 604-607.
- [31] "A safety evaluation of SNAP reactor systems". Report of the Committee on the Nuclear Space Program. Atomic Industrial Forum Inc. 1968.
- [32] R.J. Hanrahan Jr, R.L. Smith III, J. Morgan. "Review of the historical capabilities and testing of composite and cermet fuels in Los Alamos". LA-UR-02-7186. Los Alamos National Laboratory, Los Alamos, NM. 2002.
- [33] D.A. Seifert, R.L. Stuart, P.K. Conn, H.W. McLaughlin, G.J. Luersen. "Fission product behavior within two W- $UO_2$  cermet fuel elements irradiated in a temperature gradient". *Nuclear Space Programs Space Systems*. General Electric, Cincinnati, Ohio. 1968.
- [34] D.E. Burkes, D.M. Daniel, J.E. Werner, S.D. Howe. "An Overview of Current and Past W- $UO_2$  CERMET Fuel Fabrication Technology". Proceedings of: 2007 Space Nuclear Conference, 2007; Boston, MA.
- [35] General Electric. "710 high-temperature gas reactor program summary report. Volume III. Fuel Element development". General Electric. 1968. Pages: 146. GEMP-600 (Vol.3);

- [36] P.D. Takkunen. "*Fabrication of cermets of uranium nitride and tungsten or molybdenum from mixed powders and from coated powders*". *NASA Technical Note D-5136*. NASA Lewis Research Center, Cleveland, OH. 1969.
- [37] L.W. Connell, L.C. Trost. "*Reentry Safety for the Topaz II Space Reactor: Issues and Analyses*". *SAND94-0484*. Sandia National Laboratories, Albuquerque, NM. 1994.
- [38] X-5 Monte Carlo Team. "*MCNP - a general Monte Carlo n-particle transport code, version 5*". *LA-UR-03-1987*. Los Alamos National Laboratories, Los Alamos, New Mexico. 2003.
- [39] R.W. Fox, A.T. McDonald, P.J. Pritchard, "*Introduction to Fluid Mechanics*". 6th ed. John Wiley and Sons. ISBN: 0750665386.
- [40] V.C. Patel, W. Rodi, G. Scheuerer, "Turbulence Models for Near-Wall and Low Reynolds Number Flows- A Review". *AIAA*. 23.9 (1985) 1308-1309.
- [41] "*Ansys Finite Element and multi-physics analysis software package*" [computer program]. Version 10. Ansys Inc., Cannonsburg, PA, USA.

# 3

## Current radioisotope heat source encapsulation technology

In this chapter, two unclassified radioisotope heat source assemblies produced in the United States are described: the General Purpose Heat Source (GPHS) Module with a thermal power output of 250 W [1] and the Light Weight Radioisotope Heating Unit (LWRHU), with a thermal output power of 1 W [2]. The 8 W heat source known as Angel [3], which is produced in Russia, is similar in design to the LWRHU [2] is also discussed. The fundamental elements of these heat sources rely on the use of  $^{238}\text{Pu}$  encapsulated in a refractory cladding and surrounded by a composite insulator and ablative liner/impact aeroshell assembly.

In accordance with UN resolution 47/68, all radioisotope heat sources for use in space must be capable of preventing the dispersal of nuclear materials into the Earth's environment during nominal and accidental situations. For this reason, careful engineering of the radioisotope containment must be ensured. In today's climate where global terrorism is a serious threat, the preservation of security for nuclear materials is essential at all stages of production and under all possible conditions. When considering operational temperatures and temperatures achieved under extreme conditions such as launch failure and atmospheric re-entry scenarios which include orbit decay and minimum angle of attack, , it is also important to select a radioisotope encapsulation technique or material that will prevent the dispersal of the enclosed nuclear materials under such conditions.

### 3.1 The General Purpose Heat Source (GPHS)

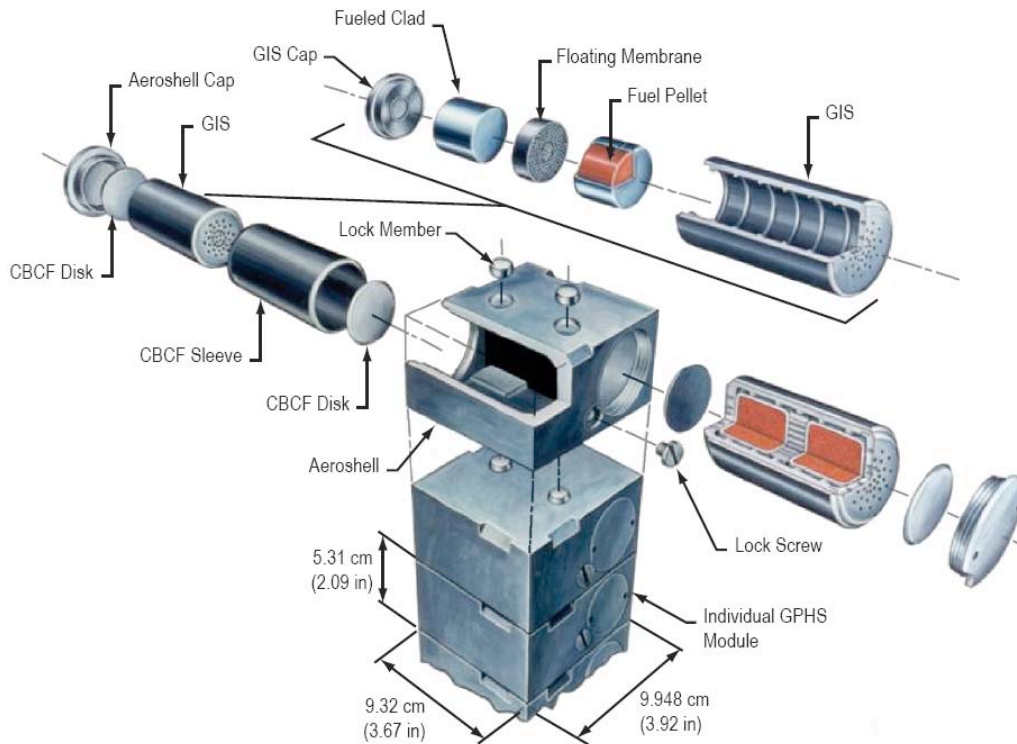


**Figure 3.1:** The General Purpose Heat Source (GPHS) module assembly and module stack. Image Courtesy of the United States Department of Energy.

The General Purpose Heat Source (GPHS) was primarily designed to provide heat in a power generation system and consisted of 18 modules stacked to form the core of these RTGs. The required thermal power level for any system can be achieved by coupling modules in multiples of 250  $W_{th}$ . The fuel used to form the GPHS fuel pellets is  $^{238}\text{PuO}_2$ . The GPHS fuel pellets are produced and clad in iridium alloy DOP-26 at the Los Alamos National Laboratory and shipped, for assembly into the GPHS modules, at the Idaho National Laboratory. The geometry of each fuel pellet is cylindrical ( $2.76 \pm 0.02$  cm diameter by  $2.76 \pm 0.024$  cm long) with a chamfer at each end [4]. The GPHS fuel pellets are produced from a purified powdered feedstock of  $\text{PuO}_2$  with an assay of 82.2 %  $^{238}\text{Pu}$  by weight [4].

The feedstock materials are purified via an aqueous recovery process that can accept an input of impure source materials or existing  $\text{PuO}_2$  that may be in an oxidation state (such as IV+) that does not conform to requirements for use in the GPHS architecture. Before starting pellet production, the feedstock chemical form and grain size must conform to specific requirements. In recent years, the  $^{238}\text{PuO}_2$  purchased by the United States from Russia for use in radioisotope power systems has been of the form of  $^{238}\text{PuO}_2$  (IV+). The final stages of the aqueous processing involves the production of  $\text{Pu}^{3+}$  Oxalate [5] which undergoes calcination in the presence of oxygen that is enriched in  $^{16}\text{O}$  [6]. The resultant feedstock material is  $^{238}\text{PuO}_2$  (III+), the compound that has been qualified for safe operation during accident scenarios. The feedstock must be processed via ball milling to produce particle sizes  $< 250 \mu\text{m}$ , 60% of which is sintered at  $1100 \text{ }^\circ\text{C}$  while 40% is sintered at  $1600 \text{ }^\circ\text{C}$ . The granules of  $\text{PuO}_2$  are sintered at the respective temperatures for 6 hours in a platinum boat in an argon atmosphere saturated with  $\text{H}_2^{16}\text{O}$  or in a mixed reaction gas consisting of argon and  $^{16}\text{O}_2$  [5]. This reaction cover gas is produced by the passing of argon gas through a liquid  $\text{H}_2^{16}\text{O}$  bubbler followed by purification in a tube furnace containing titanium beads held at  $750 \text{ }^\circ\text{C}$  [7]. The granules sintered at  $1600 \text{ }^\circ\text{C}$  have a larger average size than those sintered at  $1100 \text{ }^\circ\text{C}$ . This is due to grain growth enhancement at the higher temperatures. The density of these grains is in excess of 95% of the theoretical density. This sintering process ensures that the correct grain size and morphology of the feedstock is achieved prior to hot pressing of the fuel pellets. This process also facilitates the displacement of  $^{17}\text{O}$  and  $^{18}\text{O}$  based plutonia which produce  $\alpha$ -n neutrons [8]. The two powders (containing different average grain sizes) are blended together in a  $40_{\text{large grain}} : 60_{\text{small grain}}$  ratio for pellet pressing. This morphology and mixture ratio has

been empirically determined to provide the required pellet bulk density (approximately 85 % of the theoretical density). The final pellet is also resistant to shrinkage and cracking during fabrication, a property attributed to the fraction of the dense powder grains that are sintered at the higher temperature.

Pellet production is achieved by hot pressing 151 g of PuO<sub>2</sub> feedstock in a graphite die, with an average force of 12.4 kN, at a temperature of 1500 °C - 1525 °C for 28 minutes [5]. This translates into a pressure of approximately 20.7 MPa. The pellet produced by this hot press process is reduced to a stoichiometry of PuO<sub>1.93</sub> by reactions with the graphite during the sintering process. Before the pellet can be used, an oxidation stage is required to restore its stoichiometry to PuO<sub>2</sub>. This is achieved by pressureless sintering of the hot pressed pellet in a platinum boat filled with powdered Thoria. This process is carried out in an argon <sup>16</sup>O<sub>2</sub> enriched atmosphere. The addition of Thoria to the platinum boat stage is used to support the pellet and prevent the generation of pressure stress points in the pellet that may arise from its own weight and the direct placement of the pellet in the platinum boat. Two stages of the pressureless sintering are performed, firstly at 1000 °C for 6 hours followed by a period of 6 hours at 1527 °C [5, 7]. This final post-press sintering increases the grain sizes of residual submicron plutonium oxide fines to a size of ~20 to ~30 μm [5], which minimises the production of respirable fine particles in the event of impacts associated with launch accidents. The resultant fuel pellets have an average density of 9.89 g.cm<sup>-3</sup> [4] and are capable of capturing radiogenic helium during pre-assembly and storage but expand at operational temperatures (extreme re-entry temperatures) increasing the porosity and enabling the venting of trapped helium.

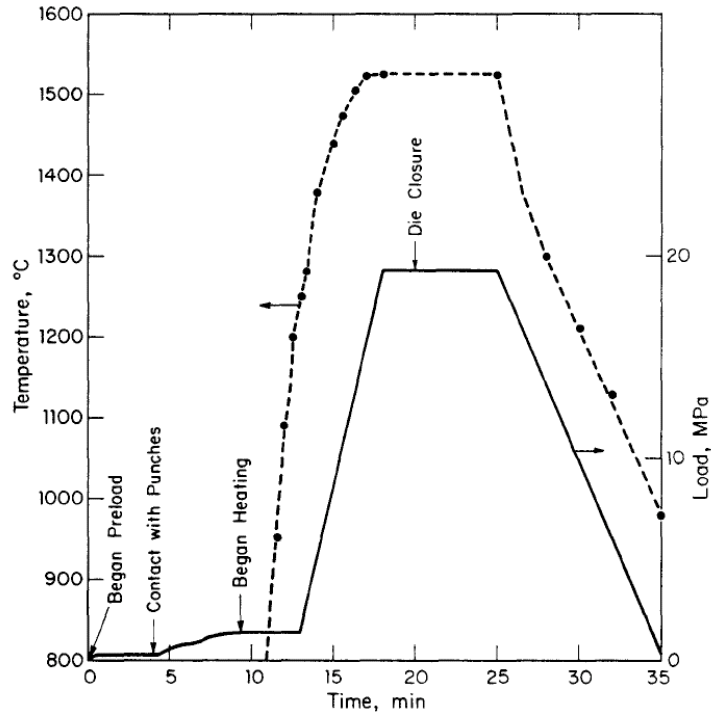


**Figure 3.2:** Typical Hot Press sintering profile for the production of GPHS fuel pellets [9].

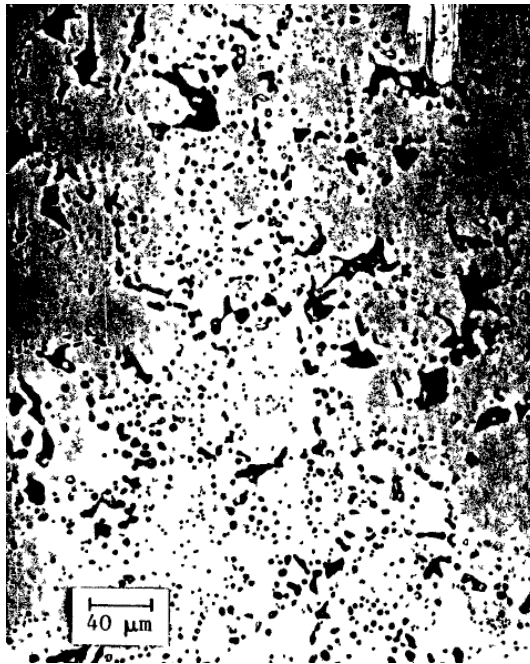


**Figure 3.3:** Micrograph of the longitudinal axis of a typical GPHS fuel pellet. [9]

Following production, each fuel pellet used in the GPHS architecture is individually encapsulated in a vented iridium alloy (DOP-26) clad. The wall thickness on the GPHS fuel clad is 0.73 mm [10]. The cladding is assembled from two pieces (manufactured by Oak Ridge National Laboratory): a vented cup and a shield cup. The

vented cup features a vent hole that is filtered by a sintered iridium frit (porous matrix) that allows radiogenic helium to escape without affecting the containment of fine displaced PuO<sub>2</sub> particles in the event of an accident or impact [10]. The iridium frit is produced by sintering 0.0725 g of iridium powder to 67% theoretical density [10], which allows helium to flow through it at a rate of 4.5 to 7.5 cm<sup>3</sup>/min at a feed pressure of 7 kPa [10]. The vent assembly has a thickness no greater than 0.41 mm and is produced by the diffusion bonding of a cover disc that is vented to the interior of the clad and a backing disc that is vented to the exterior of the clad over the iridium frit [10] (see Figure 3.4). For pre-assembly storage and transport of the fuelled clads, an iridium contamination cover blister is applied to the exterior of the vent during the manufacturing of clads. This is only removed immediately prior to the final assembly of a GPHS module. The purpose of the cover blister is to reduce the probability of contamination by plutonium oxide fines during shipping and storage prior to module assembly. The lower half of the cladding consists of the shield cup that includes a 0.127 mm thick iridium foil between the ceramic PuO<sub>2</sub> pellet and the joint between the two halves of the cladding [11]. This shield isolates the plutonium dioxide fuel pellet and is essential for the prevention of material volatilization during the welding process that seals the two halves of the cladding together [11]. Tungsten inert gas welding with a Hobart welder is used to join the two halves of the iridium cladding [11]. This is an arc welding process that is conducted in an inert argon environment to prevent the contamination of the welds by airborne impurities. This is important since such impurities may lead to long term corrosion and may weaken the overall strength of the weld.

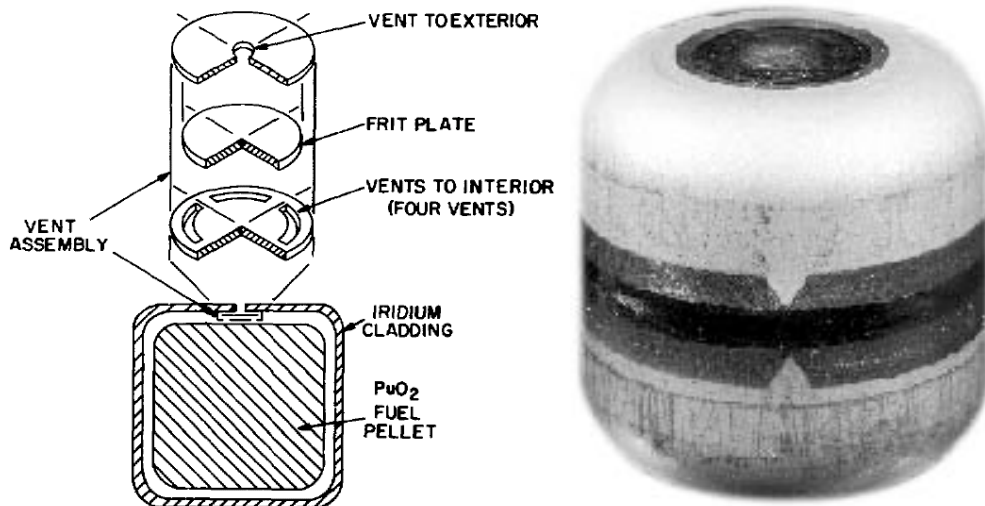


**Figure 3.4:** (Left) Schematic Diagram of the GPHS fuel Clad and vent design [12]. (Right) Photograph of a fuelled GPHS clad with vent cover applied, courtesy of United States Department of Energy.



**Figure 3.5:** Cross sectional micrograph of the GPHS vent assembly [10]

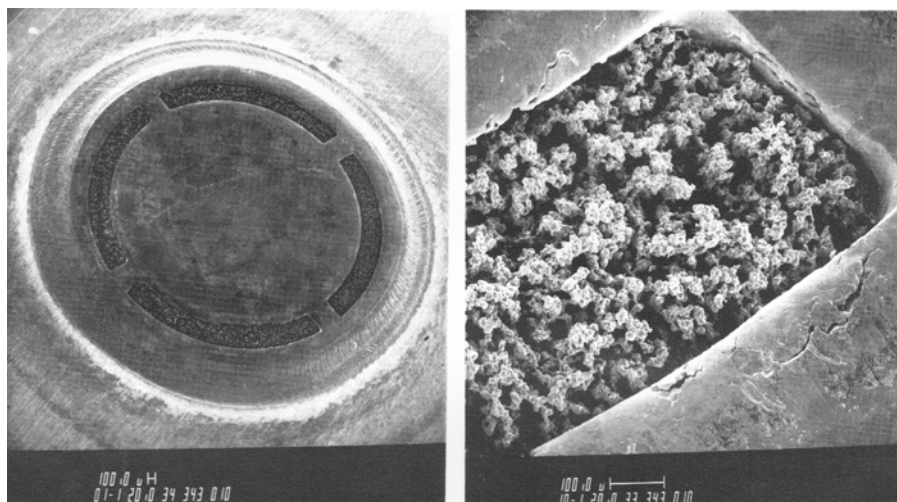


**Figure 3.6:** (Left) Scanning Electron Microscope image of the inside of the vent assembly showing the four openings in the cover disk exposed to the sintered iridium frit. (Right) Enlarged image of the exposed region of the sintered iridium frit [13].

Completed GPHS fuel clads are installed into a Fine Weave Pierced Fabric (FWPF) Graphite Impact Shell (GIS) in pairs. The two sealed heat sources housed in a GIS are separated by a porous FWPF floating membrane that allows the precise

positioning of each heat source for optimum thermal performance while allowing a vent path for radiogenic gases. The Purpose of the GIS is to provide protection from impacts caused by atmospheric re-entry or launch vehicle accidents. Both ends of the GIS are vented by multiple holes to prevent helium retention. One end of the GIS features a threaded opening that is closed by a cap. See Figure 3.1.

A thin walled insulator manufactured by Oak Ridge National Laboratory [14] comprising of a Carbon Bonded Carbon Fibre (CBCF) sleeve and two thin CBCF disks is used to envelop each GIS in order to insulate it and the fuel from severe effects of brief temperature excursions during worst case re-entry conditions [4, 15]. The CBCF insulator ensures that the temperature in the GIS is greater than 800 °C such that the ductility of the fuel cladding is preserved in the event of a post re-entry impact [4]. The CBCF sleeve and disks have a thickness of 1 mm [16] and an average thermal conductivity of 0.059 W m<sup>-1</sup> K<sup>-1</sup> [16]. The CBCF sleeve is not gas-tight so as to allow radiogenic helium to escape under normal operational conditions [4]. The CBCF sleeve is occasionally referred to as the Post Impact Containment Shell (PICS) since it offers some degree of containment of fine isotope powder grains in the event of a ruptured clad [17].

The final stage of a GPHS module assembly involves the insertion of two fuelled GIS/PICS assemblies into a single square block aeroshell. The aeroshell is made from FWPF and provides an ablative barrier from the high temperatures experienced during atmospheric re-entry events and flash fire accidents, while providing good thermal conductivity between the heat source and a power conversion system. The GIS/PICS assemblies are secured inside the two separate cavities in the aeroshell by

means of a threaded aeroshell cap. A locking screw is used to prevent the loosening of the aeroshell cap [4]. With the exception of the CBCF insulator and FWPF billets produced by Textron Products Inc., all of the components for the aeroshell and GIS assembly are manufactured at Idaho National Laboratory.

The GPHS modules are designed and qualified to withstand impacts at a velocity of  $55 \text{ m s}^{-1}$  and a clad temperature of  $970 \text{ }^\circ\text{C}$  [17], which is a predicted post re-entry temperature for a module having reached a peak temperature of  $1740 \text{ }^\circ\text{C}$  [18]. Computational fluid dynamics modelling has been used to determine that sub-orbital accidental re-entries could result in the ablation of between 0.28 mm and 1.37 mm of the outer surface of the module, whereas re-entries due to orbit decay are predicted to result in an ablation of 1.37 mm [4]. The most severe re-entry temperatures are reached by very low angle ( $\gamma$ ) re-entry profiles such as super-orbital near skip-out ( $\gamma = -5.3^\circ$ ) and multiple skip re-entry ( $\gamma < -5.3^\circ$ ) [19], where the final re-entry interface occurs below the skip-out boundary [4]. A re-entry interface is commonly defined as the point at which contact is made between an object with a velocity less than the orbital velocity for its current position makes contact with the atmosphere of a planet. Calculations have shown that typical ablation for these two scenarios is 1.73 mm and 3.30 mm respectively [4].

Module qualification testing included:

- ageing tests [18]
- testing resistance to fire [18]
- ablation [19]
- impact [4, 18, 20].
- vibration testing [18]
- explosion overpressurisation tests [4, 21]
- edge on flyer plate testing [4, 22]

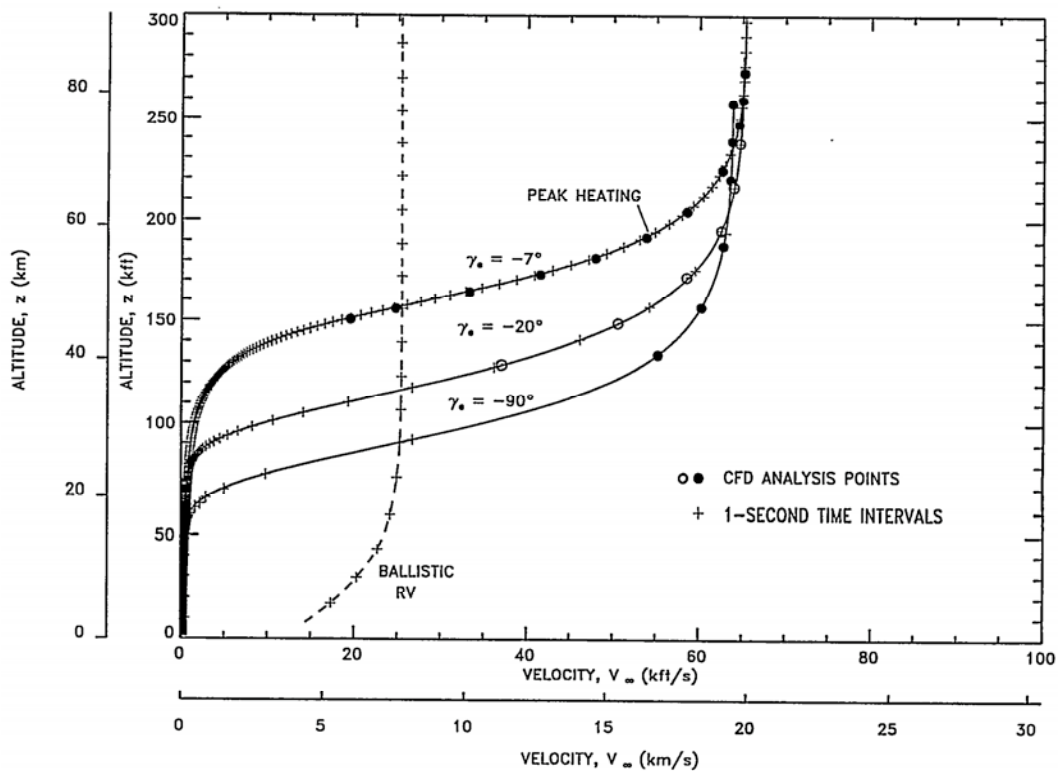


**Figure 3.7:** Comparison of GPHS module re-entry velocity versus altitude profiles for shallow angle ( $\alpha < 7^\circ$ ), intermediate angle ( $20^\circ < \alpha > 7^\circ$ ) and steep ( $90^\circ < \alpha > 20^\circ$ ) re-entry interface angles of attack. Also plotted is a typical ballistic re-entry vehicle velocity profile and the point of maximum heating for the GPHS modules coincident on the minimum interface angle boundary [4].

During the U.S. Defence Nuclear Agency’s “Direct Course” test, in which 554 Metric Tons [23] of Ammonium Nitrate Fuel Oil (ANFO) liquid explosive were used to simulate the effects of a 1 kT tactical nuclear weapon, the General Electric Advanced

Energy Programs Department deployed a parallel experiment in which a simulated GPHS-RTG was subjected to pressures similar to those that would be experienced by the explosion of a launch vehicle carrying such a generator [23, 24]. Pressure transducers measured an incident overpressure of around 10.3 MPa at the GPHS-RTG simulator. Most significantly, the GPHS modules were entirely destroyed and fragments of iridium and graphite were strewn several hundreds to thousands of feet away from the experimental setup [23]. Approximately 70 percent of the fragments from the four iridium fuel clads from the flight model GPHS module that was loaded into the experimental setup were located after the tests by members of the Nuclear Emergency Search Team (NEST). This was made possible by the pre-test irradiation of the Ir fuel clads containing depleted  $\text{UO}_2$  at the Los Alamos Omega West Reactor to produce  $^{192}\text{Ir}$ . The result obtained by the Direct Course experiment highlights the potential susceptibility of the GPHS architecture to explosive destruction and dispersal of radioisotope materials.

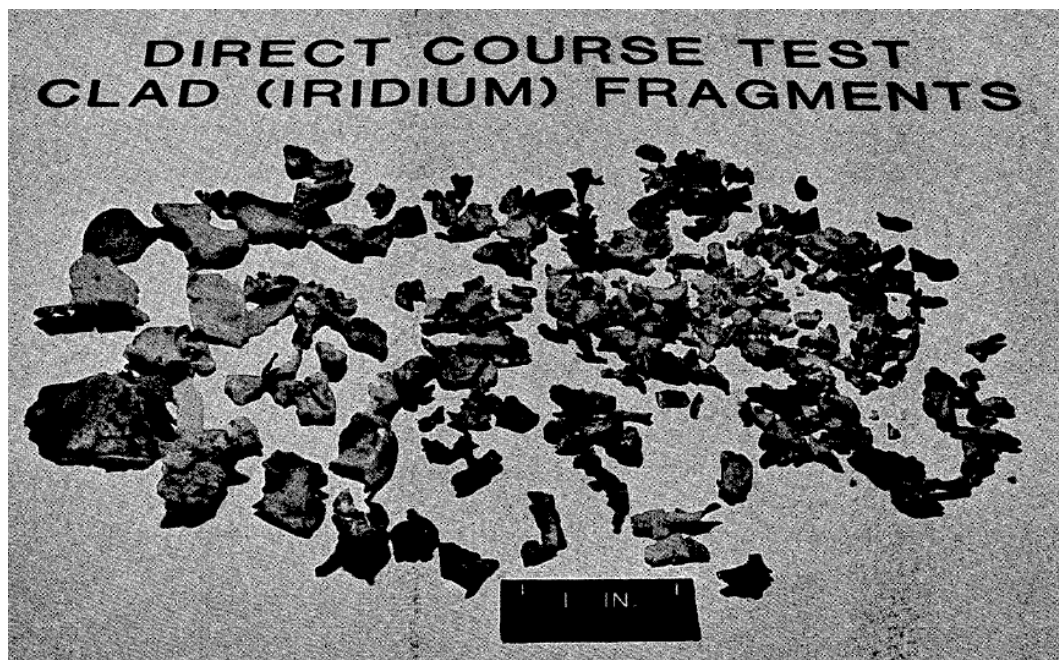


**Figure 3.8:** Activated Iridium clad fragments found by Nuclear Emergency Search Team members after the ‘Direct Course’ explosion test [23].

The Fine Weave Pierced Fabric (FWPF) used for the GIS and ablative aeroshell components is fabricated from a feedstock of Ultra High Modulus carbon fibre strands made commercially by Hexcel as product UHM-1K PAN (polyacrylonitrile) Carbon Fibre [14]. The AVCO division of Textron Products Inc. of Anaheim, California is responsible for the production of FWPF billets beyond feedstock[14]. The UHM-1K fibres are woven into a fine sheet and placed into a support cradle. Depending on the size of the required finished billet of FWPF, multiple layers (typically many thousand) are stacked and compressed. Once under compression a piercing device composed of many hundreds of  $\sim 1$  mm diameter needles (rods) is driven through the compressed stack of weaves. Once pierced, the needles are replaced by carbon-phenolic rods [25]. At this point in the fabrication process, known as perform, the density of the assembly is on average  $0.85 \text{ g/cm}^3$  [25]. In order to make the pierced stack rigid, 15V coal-tar pitch oil [25] is driven into the structure under pressure prior to a bake out cycle under atmospheric pressure at a temperature that is proprietary to Textron. The average density for billets post rigidization is  $1.047 \text{ g/cm}^3$  [25]. On completion of this initial rigidization process, the billets are subjected to a 5-cycle densification process performed by ATK (originally by the General Electric Company). This process uses the same 15V coal-tar pitch oil driven into the billet under hot isostatic conditions [25]. This process is called Hot Isostatic Pressure Impregnation Carbonisation (HIPIC) and each cycle involves the injection of pitch oil at pressures of approximately 1.01 MPa [25] and at temperatures that are, as in the case of the Textron process, proprietary. It is understood that this application of heat during impregnation is to reduce the viscosity of the 15 V coal-tar pitch oil so as to facilitate uniform penetration of the micro-pores of the billet matrix. Graphitization heat treatment is performed by ATK in between each

HIPIC procedure at temperatures in excess of 2000 °C [25]. The final density of a billet after the 5-cycle densification process is on average 1.95 g/cm<sup>3</sup> [25].

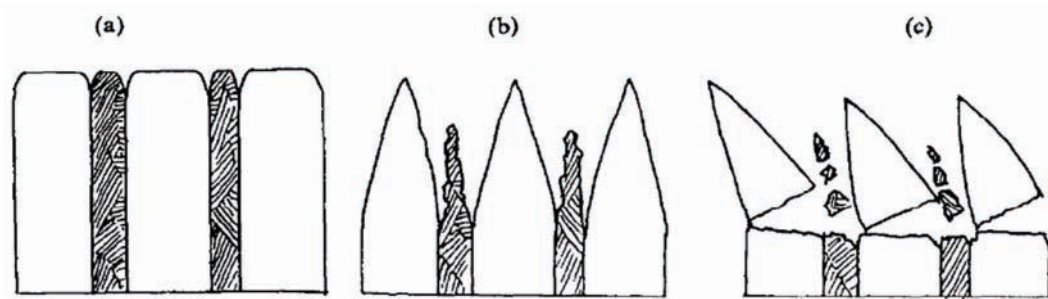


**Figure 3.9:** Structure and ablation process of Fine Weave Pierced Fibre composite structures [26]. **(a)** The initial microstructure of FWPF prior to ablation showing the bulk pierced fabric (white) and the orthogonal carbon-phenolic rods (shaded). **(b)** Vaporisation of the surface and inter-media boundaries. **(c)** Fracture of weakened surfaces via aerodynamic stress and shock.

The original module design as flown on the Galileo, Ulyses and Cassini missions had a mass of 1.433 kg [4] and a geometry of 53.09 mm x 97.18 mm x 93.17 mm [4]. This module design is often referred to as the “Heritage module”. Modification to the GPHS module design came prior to the assembly of the GPHS-RTG built for NASA’s New Horizons mission to Pluto and the Kuiper Belt that was launched in 2006. The modification was made due to concerns regarding the integrity of the module under accident scenarios that could have occurred during high velocity gravity-assist fly-bys of the Earth. This modification resulted in the production of the “Step-1 Enhanced module” with an external geometry of 53.09 mm x 99.6 mm x 93.17 mm and a mass of 1.514 kg [27]. The subtle difference between the Heritage and the Step-1 Enhanced module was in the separation of the GIS assemblies (from 0.53 mm to 2.53 mm) and the filling of the aeroshell void that existed in regions of the heritage module design (between the two GIS assemblies), hence the mass increment.

The most recent modification to the GPHS module design came prior to the assembly of the Multi-Mission RTG built for NASA’s Mars Science Laboratory rover

mission. Five millimetres of FWPF material were added to the height of the GPHS aeroshell following concern over the integrity of the module in modern launcher accidents. This latest modification is known as the Step-2 Enhanced module and has a mass of 1.606 kg and an external geometry of 58.2 x 99.6 x 93.2 mm [27]. The Step-2 module design will also be used by the Advanced Stirling Radioisotope Generator (ASRG). At the time of writing, the Step-2 Enhanced module design is undergoing ablated-impact testing to ensure improved safety of the module.

### **3.2 Light Weight Radioisotope Heater Unit (LWRHU)**

The Light Weight Radioisotope Heater Unit (LWRHU) produces a thermal output power of 1 W. The complete LWRHU has an average total mass of 39.9 grams, a length of 31.9 mm and a diameter of 25.9 mm [2]. The same  $^{238}\text{PuO}_2$  compound that is used to fuel the GPHS is used to fuel the LWRHU. In the case of the LWRHU, the  $\text{PuO}_2$  is encapsulated in a platinum-rhodium alloy. The alloy is 70% Pt and 30% Rh by at. %.. Qualification tests on LWRHUs were similar to those for the GPHS modules and included: hard surface impacts (up to  $50 \text{ ms}^{-1}$ ) [28], thermal shock tests associated with atmospheric re-entry, explosive shock tube testing [28, 29]. Pressure and containment tests were also performed for the system immersed in sea water for 1.75 years at both sea level and at a depth of 6000 m [28]. The complete LWRHU has an average total mass of 39.9 grams, a length of 31.9 mm and a diameter of 25.9 mm [2].

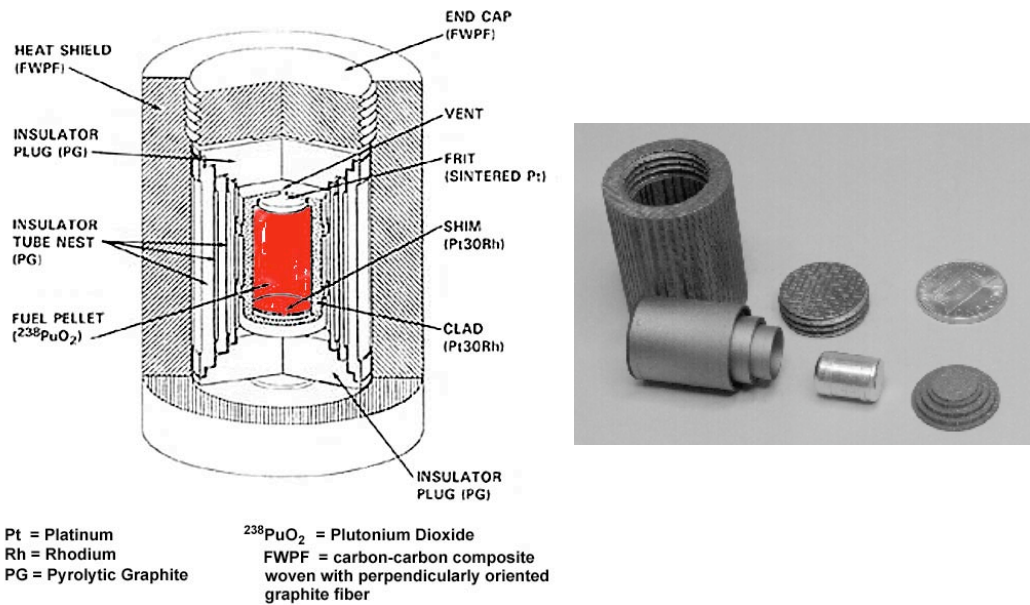


**Figure 3.10:** (Left) Schematic of the 1  $W_{th}$  Light Weight Radioisotope Heater Unit (LWRHU) assembly. (Right) Photograph of the LWRHU components compared to a U.S. 1 cent coin at top right. Images courtesy of the United States Department of Energy.

### 3.3 Angel RHU/RTG heat source

The Russian ANGEL RHU/RTG heat source is very similar in design to the LWRHU developed in the United States. Its thermal loading is approximately 8.5  $W_{th}$  and is fuelled by two  $^{238}\text{PuO}_2$  pellets. Little qualification data or test information is available for the ANGEL systems, but it is assumed that function of the insulation and aeroshell structures is identical to that of the US LWRHU.

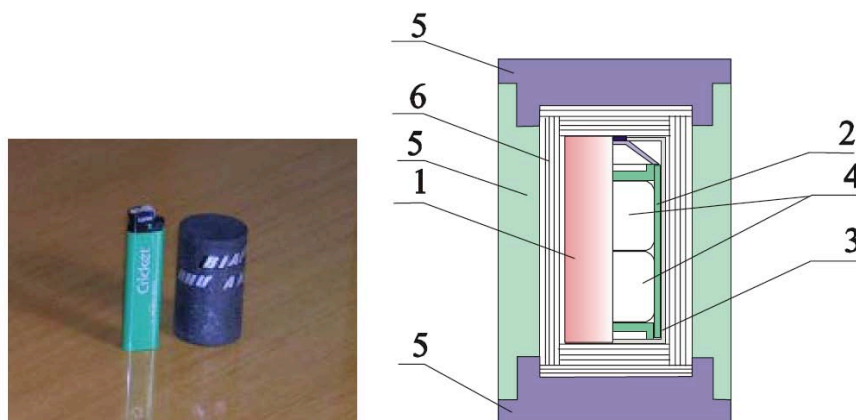


**Figure 3.11:** (Left) Photograph of the 8  $W_{th}$  Angel RHU compared to a cigarette lighter. (Right) Schematic of the 8  $W_{th}$  Light Weight Radioisotope Heater Unit (LWRHU) assembly; 1) heat source, 2) Corrosion resistant cladding, 3) Impact shell, 4)  $\text{PuO}_2$  Pellets, 5) Outer aeroshell and end caps, 6) Thermal Insulation.[30]

### 3.4 Helium production and its effect upon the encapsulation of radioisotopes

Radioisotopes, such as  $^{238}\text{Pu}$  and  $^{241}\text{Am}$ , with an alpha decay mode, will produce an accumulation of helium and without adequate ventilation the helium accumulation will result in a pressure increase. Over a short period of time the effect is negligible, but in the case of alpha emitting isotopes that are useful for RTGs, where activity is high and time periods can span decades, the helium buildup can be significant. The entire decay chain should also be considered since non-alpha emitting heat sources may give rise to alpha-emitting daughter products in addition to gaseous daughter products.

The activity of the radioisotope will determine the rate of helium production. The activity of a radioisotope is related to the decay constant  $\lambda$ .

$$N = N_0 e^{-\lambda t} \tag{3.1}$$

$$A_0 = N_0 \lambda \tag{3.2}$$

Equation 3.1 is the relationship between  $N$ , the number of isotope nuclei present at time  $t$  from the measurement of nuclei present initially ( $N_0$ ). This may also be used to determine the number of decays that have taken place after time  $t$ . It is often useful to relate the initial number of nuclei present in a source in terms of its initial activity at the time of manufacture,  $A_0$  (decays/s). This may be determined by the use of Equation 3.2.

The pressure can be determined by using the ideal gas equation. The ideal gas equation is given by:

$$PV = nRT \quad (3.3)$$

$P$ , is the pressure of a gas in a given volume,  $V$ ,  $R$  is the universal gas constant,  $T$ , the temperature of the system and  $n$ , the number of moles of gas present.

Using these two equations, it is therefore possible to determine the pressure of the gas in an unvented structure at any given time,  $t$ .

$$P(t) = \frac{N_0 RT}{V_{void} N_A} [1 - e^{-\lambda t}] \quad (3.4)$$

Equation 3.4 can be used to evaluate the pressure,  $P$  (Pa), at any time  $t$  (seconds) after sealing a radioisotopic source with decay constant  $\lambda$  ( $s^{-1}$ ) and total matrix void volume  $V_{void}$  ( $m^3$ ) at operational temperature  $T$  (Kelvin). Substituting 3.2 in 3.4:

$$P(t) = \frac{A_0 RT}{V_{void} N_A \lambda} [1 - e^{-\lambda t}] \quad (3.5)$$

The rate of change in pressure with respect to time may be found through the derivative of equation 3.5;

$$\frac{dP}{dt}(t) = \frac{A_0 RT}{V_{void} N_A} e^{-\lambda t} \quad (3.6)$$

From equation 3.6, equation 3.5 may be written in integral form in equation 3.7 below;

$$P(t) = \frac{A_0 RT}{V_{void} N_A} \int_{t_0}^t e^{-\lambda t} .dt \quad (3.7)$$

The volume  $V_{void}$  used in equations 3.1 to 3.7 above refers to the total void volume in a helium-porous radioisotopic fuel matrix. It is assumed that this volume is rigid and does not change during pressurisation. It should be noted that these equations may only be valid for a complete heat source where it is assumed that the helium evolved during the alpha decay process is given free mobility throughout the matrix. Since  $V_{void}$  is a function of the matrix (bulk) density, it is possible to determine  $V_{void}$  of a given source in terms of its mass,  $m$ , theoretical density,  $\rho_{Th}$ , and the ratio of the product bulk density to theoretical density,  $\varepsilon$ ;

$$V_{void} = \frac{m}{\rho_{Th}} \left( \frac{1}{\varepsilon} - 1 \right) \quad (3.8)$$

To illustrate the significance of the helium retention problem over the a 30 year time period, a typical lifetime of a modern heat source, the specifications of a GPHS fuel pellet are considered with the exclusion of helium ventilation. In a GPHS fuel pellet there are 188 g of  $^{238}\text{PuO}_2$  pressed to approximately 80 % ( $\varepsilon=0.8$ ) of its theoretical density ( $\rho_{Th}=11.46 \text{ g/cm}^3$ ). Its initial activity may be assumed to be 2.84 kCi based on a specific activity for  $^{238}\text{PuO}_2$  of 15.1 Ci/g [8].  $^{238}\text{Pu}$  has a half-life of 87.74 years [8] and therefore has a decay constant ( $\lambda$ ) of  $2.505 \times 10^{-10} \text{ s}^{-1}$ . In a total pellet volume of approximately  $20.5 \text{ cm}^3$ , we assume a  $V_{void}$  of  $4.101 \text{ cm}^3$  at operational temperatures of  $600 \text{ }^\circ\text{C}$  ( $873 \text{ }^\circ\text{K}$ ) in which helium can accumulate. This assumption is supported by the measurement of helium released from GPHS fuel pellets  $\text{PuO}_2$  at operational temperatures [12]. Using Equation 3.5 the total pressure in a sealed GPHS fuel pellet after 30 years would be 2.60 MPa.

To understand the physical impact the pressure increase has on the cladding, the hoop stress (circumferential stress) on a thin walled pressure vessel should be considered. For a given diameter to wall thickness ratio that is greater than a factor of 10, the hoop stress of a thin wall cylinder may be determined by Equation 3.9 below.

$$\sigma_{\theta} = \frac{Pr}{w} \quad (3.9)$$

$\sigma_{\theta}$  = hoop stress (Pa)

$P$  = Inner Pressure (Pa)

$r$  = Inner Radius (m)

$w$  = Wall Thickness (m)

Typically, a pressure vessel will fail when the hoop stress is greater than or equal to the ultimate tensile stress. For an Iridium DOP-26 cladding, the ultimate tensile strength  $\sigma_U$  is 590 MPa at 600 °C [31]. The result from applying equation 3.15 substituted into equation 3.19 can be used to estimate the hoop stress in addition to the physical specifications for the cladding. For the purpose of this example we use the clad thickness  $w$  of 0.73 mm [4] and an inner radius  $r$  of 1.421 cm to estimate that when the internal pressure is 2.60 MPa, the hoop stress is 50.59 MPa indicating a significant safety margin of more than a factor of 10 when compared to the tensile strength of the Ir cladding. From this result it is clear that in the case of a clad GPHS fuel module, the source will remain sealed over a period of 30 years, which spans production, storage and operation in flight. Welded joints, present in the design of the GPHS fuel cladding [11], can introduce weaknesses that may not conform to the safety margin requirements on the cladding material. The failure pressure may be much lower than that associated with the limits in tensile strength of the encapsulating walls [11]. This is a primary reason for venting heat sources that operate at high temperatures for space applications. A secondary reason for the provision of ventilation paths in a cladding material is the

risk associated with rupturing on impact, in a mission failure scenario, resulting in the release and potentially the dispersal of radioactive materials in the environment. [28].

### 3.5 References

- [1] G.L. Bennett, J.J. Lombardo, R.J. Hemler, et al. "Mission of Daring: The General-Purpose Heat Source Radioisotope Thermoelectric Generator". Proceedings of: Fourth International Energy Conversion Engineering Conference and Exhibit (IECEC), 2006; San Diego, California. AIAA.
- [2] G.H. Rinehart. "*Lightweight Radioisotope Heater Unit (LWRHU) Production for the Cassini Mission*". LA-13143. Los Alamos National Laboratory, Los Alamos, NM. May 1996.
- [3] A.B. Chmielewski, A. Borshchevsky, R. Lange, B Cook. "*A Survey of Current Russian RTG Capabilities*". 94-0898. NASA Jet Propulsion Laboratory, Monterey, California, USA. 1994.
- [4] Lockheed Martin Astronautics. "*GPHS-RTGs in Support of the Cassini Mission*". Lockheed Martin, Philadelphia, PA. August 1998 Final Technical Report. Document No. RR18; DOE/SF/18852-T97.
- [5] G.H. Rinehart, "Design Characteristics And Fabrication Of Radioisotope Heat Sources For Space Missions". *Progress in Nuclear Energy*. 39 (2001) 305-319.
- [6] D.L. Plymale, "The Exchange of Isotopically Enriched Oxygen with  $^{238}\text{PuO}_2$ ". *J. Inorg. Nucl. Chem.* 30 (1968) 886.
- [7] R.A. Kent. "*LASL Fabrication Flowsheet for GPHS Fuel Pellets*". LA-7972-MS. Los Alamos Scientific Laboratory, Los Alamos, NM. August 1979.
- [8] R.C. O'Brien, R.M. Ambrosi, N.P. Bannister, S.D. Howe, H.V. Atkinson, "Safe radioisotope thermoelectric generators and heat sources for space applications". *Journal of Nuclear Materials*. 377 (2008) 506-521.
- [9] D.T. Rankin, J.W. Congdon, J.T. Livingston, N.D. Duncan. "*Ceramic Fuel Pellets for Isotopic Heat Sources*". DP-MS-80-51. Savannah River Laboratory, Aiken, SC. 1980.
- [10] G.B. Ulrich. "*The Metallurgical Integrity Of The Frit Vent Assembly Diffusion Bond*". Y/DV-1321. Oak Ridge Y-12 Plant, Oak Ridge, TN. 1994.
- [11] C.M. Lynch, P.F. Moniz, M.A.H. Reimus. "*Evaluation And Characterization Of General Purpose Heat Source Girth Welds For The Cassini Mission*". LA-UR-98-2722. Los Alamos National Laboratory, Los Alamos, NM. 22nd June 1998.
- [12] D.E. Peterson, C.E. Frantz. "*Reentry Thermal Testing of a General Purpose Heat Source Fueled Clad*". LA-9227. Los Alamos National Laboratory. March 1982.
- [13] E.W. Johnson. "The Forming Of Metal Components For Radioisotope Heat Sources". Proceedings of: Space Nuclear Power Systems; 11 - 13 January, 1984. Orbit Nook Company Inc, ISBN: 0-89464-004-6.
- [14] J.P. Moore. "*Quarterly Technical Progress Report of Radioisotope Power System Material Production and Technology Program Tasks For July Through September 2000*". ORNL/CF-00/34. Oak Ridge National Laboratory, Oak Ridge, TN. 13<sup>th</sup> November 2000.

- [15] J.F. King. "Annual Technical Progress Report of Radioisotope Power Systems Materials Production and Technology Program Tasks for October 1, 2007 through September 30, 2008". ORNL/TM-2009/099. Oak Ridge National Laboratory, Oak Ridge, TN. 1<sup>st</sup> April 2009.
- [16] J.P. Moore. "SEMI-ANNUAL TECHNICAL PROGRESS REPORT OF RADIOISOTOPE POWER SYSTEM MATERIALS PRODUCTION AND TECHNOLOGY PROGRAM TASKS FOR OCTOBER 1, 2001 THROUGH MARCH 31, 2002". ORNL/CF-02/10. Oak Ridge National Laboratory, Oak Ridge, TN. 1<sup>st</sup> May 2002.
- [17] M.A.H. Reimus, T.G. George. "General-Purpose Heat Source: Research and Development Program High-Silicon Fuel Characterization Study; Half Module Impact Tests 1 and 2". LA-13101-MS. Los Alamos National Laboratory, Los Alamos, NM. March 1996.
- [18] W.J. Maraman. "GENERAL-PURPOSE HEAT SOURCE PROJECT AND SPACE NUCLEAR SAFETY AND FUELS PROGRAM". LA-8279-PR. Los Alamos Scientific Laboratory, Los Alamos, NM. December 1979.
- [19] A. Schock. "Design Evolution and verification of the General-Purpose Heat Source". Fairchild Space and Electronics Company, Germantown, Maryland. 1983.
- [20] T.G. George. "General-Purpose Heat Source Development: Safety Verification Test Program Titanium Bullet / Fragment Test Series". LA-10724-MS. Los Alamos National Laboratory, Los Alamos, NM. June 1986.
- [21] T.A. Cull, T.G. George, D. Pavone. "General-Purpose Heat Source Development: Safety Verification Test Program Explosion Overpressure Test Series". LA-10697-MS. Los Alamos National Laboratory, Los Alamos, NM. September 1986.
- [22] T.G. George. "General-Purpose Heat Source Safety Verification Test Program: Edge-On Flyer Plate Tests". LA-10872-MS. Los Alamos National Laboratory. March 1987.
- [23] GE Advanced Energy Programs Department. "GPHS-RTG System Explosion Test Direct Course Experiment 5000". Report No. GESP-7181. General Electric. 1st March 1986.
- [24] S.E. Bronisz. "Space Nuclear Safety Program". LA-10057-PR. Los Alamos National Laboratory, Los Alamos, NM. March 1984.
- [25] G. Rellick, "Densification Efficiency Of Carbon-Carbon Composites". *Carbon*. 28 (1990) 589-594.
- [26] J.C. Han, X.D. He, S.Y. Du, "OXIDATION AND ABLATION OF 3D CARBON-CARBON COMPOSITE AT UP TO 3000°C". *Carbon*. 33 (1995) 473-478.
- [27] R. Wiley, R. Carpenter. "Small Radioisotope Power Source Concepts". Proceedings of: Space Technology and Applications International Forum (STAIF); 10th February, 2004; Albuquerque, NM.
- [28] R.E. Tate, C.C. Land. "Environmental Safety Analysis Tests on the Light Weight Radioisotope Heater Unit (LWRHU)". LA-10352-MS. Los Alamos National Laboratory, Los Alamos, NM. May 1985.
- [29] M.A.H. Reimus, G.H. Rinehart. "Light-Weight Radioisotope Heater Unit (LWRHU) Sequential Impact Tests". LA-13339-MS. Los Alamos National Laboratory, Los Alamos, NM. August 1997.
- [30] A.A. Pustovalov. "Role and Prospects of Application of RTG on Base of Plutonium-238 for Planetary Exploration". JSC Research- Industrial Enterprise <<BIAPOS>>. 2007.
- [31] J.H. Schneibel, C.A. Carmichael, E.P. George. "High Strain Rate Tensile Testing of DOP-26 Iridium". ORNL/TM-2007-81. Oak Ridge National Laboratory, Oak Ridge, TN. November 2007.

# 4

## **Alternative and reduced radiation isotope power sources**

The primary design parameter that must be delivered during the development of any nuclear power source for use in space or on Earth is safety. Such power sources should be capable of releasing useable energy to the host system while presenting the most minimal risks to that system and to the outside environment under all nominal and emergency conditions of operation. The term as low as reasonably achievable (ALARA) is conventionally used as a criterion in nuclear engineering to ensure that exposure of workers and the general public to radiation is kept as low as to what is practically achievable, up to a maximum of what is considered to be a safe limit. This same criterion can, and should be applied to all development of radioisotope power systems. The maximum safe radiation exposure limit for humans is a legal limit that has been derived from the medical understanding of the effects radiation on the human body. It is important to note that different forms of radiation have different effects upon biological, and indeed non-biological materials, but in the safety design of nuclear power sources, we are only concerned about ionising radiation (Alpha, Beta, Gamma, or X-ray radiation).

The energetics of ionising radiation is characteristic of the isotope or source from which it is emitted. When designing an isotope heat or power source, it is understood that the selection of the isotope is directly related to the overall efficiency of the system. Isotopes that emit only Alpha radiation are ideally suited to the production of heat since this radiation can be easily attenuated and absorbed by the source material matrix, thus the specific heat

produced by such material mainly depends upon the specific activity of the isotope and the kinetic energy of the radiated alpha particle. Isotopes that emit Beta ( $\beta^-$ ) radiation are also useful as heat sources but may require material, external to the source, to capture the radiated Beta particles (electrons) that escape the source matrix and hence recover otherwise lost energy. Beta radiation sources also require external shielding for Bremsstrahlung, the secondary X-Ray radiation that results from the deceleration of the Beta particles by interactions between atoms within the source and, where applicable, the surface layers of electron capture shielding. As can be appreciated, a radioisotope that follows a beta decay scheme should not be selected by considering specific power alone given that where minimising the radiation exposure of the external environment to the source is most important, an effective specific power that accounts for the mass of shielding must be determined. When considering these effective specific powers and shielding, it is quite conceivable that an alpha radiation source isotope may have a greater overall specific source power than that of an appropriately shielded Beta emitting source.

Radioisotope sources whose decay chains involve positron emission ( $\beta^+$ ) either through dominant decay steps or significant secondary decay are not considered to be useful as heat sources for space applications. During the positron-electron annihilation processes that yield heat within the source matrix, two gamma rays are emitted, both with energies equal to the rest mass of the electron and positron (511 keV) respectively. These hard gamma rays require significant shielding in order to safely handle the source, which in turn lowers the effective source power density to a level that is easily exceeded by systems fuelled by alpha and beta emitting isotopes.

In this chapter, several isotopes and their physical forms are considered for application as fuels for space power systems. Specifically the theoretical substitution of  $^{238}\text{Pu}$  fuels with alternative isotopes such as  $^{241}\text{Am}$ ,  $^{208}\text{Po}$ ,  $^{210}\text{Po}$  and  $^{90}\text{Sr}$  within conventional RTG systems is evaluated for both performance and impact upon the local radiation environment via Monte Carlo modelling. Where Gamma radiation is generated by a radioisotope, the minimisation of radiation dose to the local environment may be reduced via heat source encapsulation within a tungsten matrix [1]. Such benefits are again modelled via Monte Carlo techniques. Mixed isotope sources are also considered for enhancement of specific power and effective composite source half-life.

#### **4.1 $^{238}\text{Pu}$ and Alternative Radioisotopes**

The careful selection and design of a radioisotope fuel source will make it possible to derive the most mass efficient shielding configuration for radioisotope heat and power systems. The selection of an isotope for a specific application is dependent on several requirements. These requirements include; mission duration, electrical power levels, whether the device is to be used for heating in addition to the generation of electricity, proximity to sensitive instrumentation and biological systems, and the overall mission mass budget.

The nature of space engineering calls for power systems that can typically be stored while remaining useful upon removal from storage. Since the 1970's,  $^{238}\text{Pu}$  has been accepted and used as the most suitable radioisotope for a variety of space and security missions given

its long useful half-life, availability up to the present time and its manageable neutron and soft gamma-ray emission spectrum.

A range of isotopes were considered as potential candidates to replace  $^{238}\text{Pu}$  in RTGs given its currently limited availability and significant fast spectrum fission cross section. These included  $^{241}\text{Am}$ ,  $^{210}\text{Po}$ ,  $^{208}\text{Po}$  and the already extensively used  $^{90}\text{Sr}$ . These isotopes are primarily alpha particle sources with the exception of  $^{90}\text{Sr}$ , which undergoes beta decay.

Despite its high thermal power density (see Table 2.1), the use of  $^{90}\text{Sr}$  as a direct substitute for  $^{238}\text{Pu}$  in the current U.S. GPHS architecture and use within a low mass heat source is impractical without enhancement of shielding structures due to the emission of secondary X-rays from Bremsstrahlung and gamma rays with energies up to 2 MeV from  $^{90}\text{Y}$  [2], the short-lived daughter nuclei from the beta decay of  $^{90}\text{Sr}$ . The Beta decay chain for  $^{90}\text{Sr}$  is presented in appendix B1.

$^{252}\text{Cf}$  is another alpha emitter that, if produced in significant quantity would lend itself very well to the application of heat generation. Unfortunately its production in the fuels cycle is in relative trace quantities and as such must be purposefully produced via the irradiation of Am/Cm targets in a high flux reactor. Such work has been performed at the Oak Ridge National Laboratory using the HFIR reactor [3]. Its primary mode of decay is via  $\alpha$  emission (96.914 %) while 3% is via spontaneous fission. Since the specific activity of  $^{252}\text{Cf}$  is high, the spontaneous fission, and hence the derived neutrons ( $\nu_{\text{ave}} = 3.7675$  per S.F.) present a significant yield.  $^{248}\text{Cm}$ , the daughter product of  $^{252}\text{Cf}$   $\alpha$  decay may be considered stable for

consideration of decay chain heat generation since its half-life is  $3.48 \times 10^5$  years. To date, the peaceful use of  $^{252}\text{Cf}$  has mostly been in the production of high yield, compact neutron sources. The decay chain for  $^{252}\text{Cf}$  is presented in appendix B4.

$^{144}\text{Ce}$  is produced as a fission product that is produced in significant quantities within commercial power reactors, at a yield estimated by the author of 379g per metric ton of irradiated heavy metal irradiated to 51 GW days per metric ton of uranium. Its half-life is 285 days and specific thermal power is approximately  $25.5 \text{ W}_{\text{th}}/\text{g}$ . In addition to consideration for Bremsstrahlung,  $^{144}\text{Ce}$  is a significant gamma emitter with peak energies of up to 133.5 keV, and as such significant shielding is required. While this does not preclude its use as fuel for terrestrial RPS systems, its use for space systems is somewhat prohibited by its inferred shielding mass. The Beta decay chain for  $^{144}\text{Ce}$  is presented in appendix B2.

$^{137}\text{Cs}$  is another isotope that follows a beta decay chain and yields a significant specific thermal power. Unfortunately, its decay features a significant hard gamma ray delayed radiation emission that proceeds through an isomeric level of  $^{137}\text{Ba}$ . This is a 661.7 keV gamma ray that prevents the use of any significantly large isotope heat source for space fuelled by  $^{137}\text{Cs}$  due to excessive shielding requirements. Its use may be suitable for some static terrestrial applications. The Beta decay chain for  $^{137}\text{Cs}$  is presented in appendix B3.

A similar problem is exhibited by the use of  $^{243}\text{Cm}$ , which has an alpha particle energy spectrum that includes alpha energies of 6.0 MeV, 5.8 MeV and 5.7 MeV with relative emission probabilities of 6%, 81% and 13% respectively [4]. Although the isotope has a high

power density, it also has a total Gamma Ray emission probability of 61.6% per decay with an average energy of 130 keV [5]. Simple shielding with high-density materials would be able to dramatically reduce the flux of low energy Gamma Rays with a mass penalty. The production and extraction of  $^{243}\text{Cm}$  from commercial fission fuel cycle wastes is extremely challenging due to its relatively low abundance (see section 5.4). The long decay chain for  $^{243}\text{Cm}$  is illustrated in appendix B5.

$^{242}\text{Cm}$  is an isotope that follows an alpha decay chain with a half-life of 162.8 days. Its abundance in discharged light water reactor fuels has been estimated by the author to be of the order of 25.9 g per metric ton of irradiated heavy metal irradiated to 51 GW days per metric ton of uranium.  $^{242}\text{Cm}$  is a soft gamma emitter but presents a significant neutron yield due to spontaneous fission. For this reason, the handling of  $^{242}\text{Cm}$  heat sources has the implicit requirement for the use of moderated hot cells. Notably  $^{242}\text{Cm}$  was examined under the SNAP program but no devices are known to have been fuelled due to the handling constraints and unsuitability for use in proximity to sensitive electronics. The  $^{242}\text{Cm}$  decay chain is presented in appendix B6.

$^{244}\text{Cm}$  is an isotope that follows an alpha decay chain with a half-life of 18.1 years. Its abundance in discharged light water reactor fuels has been estimated by the author to be of the order of 85.6 g per metric ton of irradiated heavy metal irradiated to 51 GW days per metric ton of uranium.  $^{244}\text{Cm}$  is a soft gamma emitter (42.8 keV) but presents a significant neutron yield due to spontaneous fission. For this reason, as in the case of  $^{242}\text{Cm}$ , the handling of

$^{244}\text{Cm}$  heat sources has the implicit requirement for the use of moderated hot cells or heavily moderated glove boxes. Similarly to  $^{242}\text{Cm}$ ,  $^{244}\text{Cm}$  was also examined under the SNAP program but no devices are known to have been fuelled due to the handling constraints and unsuitability for use in proximity to sensitive electronics. The  $^{244}\text{Cm}$  decay chain is presented in appendix B7.

$^{210}\text{Po}$  has been considered and demonstrated historically as a useful alpha source for fuelling RTGs [6].  $^{210}\text{Po}$  has a specific activity of  $4.5 \text{ kCi.g}^{-1}$  and a power density of  $137 \text{ W}_{\text{th}}.\text{g}^{-1}$ . The half-life of  $^{210}\text{Po}$  is 138.38 days [19]. When compared to  $^{238}\text{Pu}$  under the SNAP program, the shorter half-life of  $^{210}\text{Po}$  resulted in the favoured use of  $^{238}\text{Pu}$  for space applications. The delay between generator assembly and launch required heat sources fuelled with  $^{210}\text{Po}$  to have much greater beginning of life thermal power outputs in order to deliver the minimum beginning of mission power levels required by the host spacecraft.

Both isotopes of Polonium  $^{208}\text{Po}$  and  $^{210}\text{Po}$  have a single step alpha decay chain respectively resulting in the formation of stable  $^{204}\text{Pb}$  and  $^{206}\text{Pb}$  respectively. Note that a low probability of alpha decay exists for  $^{204}\text{Pb}$  to  $^{200}\text{Hg}$ . Less than  $1 \times 10^{-3} \%$  of the decays of  $^{210}\text{Po}$  and  $^{208}\text{Po}$  result in Gamma-Ray production with respective energies of 803.1 keV and 291.8 keV.  $^{210}\text{Po}$  and  $^{208}\text{Po}$  have a respective specific power density of 400 and 52 times that of  $^{238}\text{Pu}$ . Given the negligible gamma ray emission rate from these sources, very little high density shielding is required for systems fuelled with the Po isotopes. Both isotopes of polonium have a very low melting point ( $252^\circ\text{C}$ ) and a boiling point of  $962^\circ\text{C}$  [7]. For this

reason careful consideration must be made into heat rejection systems for the pure isotope so as to prevent its vaporisation.

$^{208}\text{Po}$  is produced commercially by means of proton irradiation of  $^{207}\text{Bi}$  targets inside a cyclotron. Because of the inefficiency of such production,  $^{208}\text{Po}$  is inherently expensive.  $^{210}\text{Po}$  is the most cost effectively produced isotope of Polonium since it can be produced by neutron irradiation of  $^{209}\text{Bi}$  inside a nuclear reactor. The capture of neutrons by  $^{209}\text{Bi}$  nuclei results in the production of  $^{210}\text{Bi}$  which has a 5 day half-life [2] and decays by Beta emission to  $^{210}\text{Po}$ . Since the natural composition of Bismuth metal is 100%  $^{209}\text{Bi}$ , no pre-irradiation enrichment is required and hence target production is relatively trivial for  $^{210}\text{Po}$  production.

Despite the requirement for large beginning of life power levels, the use of  $^{210}\text{Po}$  and  $^{208}\text{Po}$  as RTG power sources could be considered for deep space missions provided that an adaptive heat exchange system could be used to maintain an appropriate temperature gradient across the power conversion system. Such a system may feature a pumped cooling fluid such as liquid metals. Adjustment of the flow rate of working fluid would allow for tuning of the heat flow from the cold side of a power conversion system to a heat rejection mechanism. Such mechanisms would result in a mass penalty and effectively lower the system power density. This would also add to the complexity of the system and may call for the qualification of the operational lifetime of the system. For these reasons and due to their short half lives (2.898 and 0.38 years for  $^{208}\text{Po}$  and  $^{210}\text{Po}$  respectively [2]), the isotopes of Polonium are better suited to short duration mission applications. Consideration for issues of material stability and

its highly corrosive nature has presented challenges for its historical use in the U.S. SNAP program.

$^{241}\text{Am}$  has a specific thermal power that is approximately one fifth that of  $^{238}\text{Pu}$  and a half-life that is approximately 5 times greater than that of  $^{238}\text{Pu}$ . The spontaneous fission probability for  $^{241}\text{Am}$  is  $4.30 \times 10^{-10}$  % of all decays. This is equivalent to a  $10^3$  reduction in neutron flux when compared to an equivalent amount of  $^{238}\text{Pu}$  in their pure isotopic form. The maximum photon energy produced by  $^{241}\text{Am}$  is 59.5 keV [2]. These photons can easily be shielded using relatively thin layers of high-density materials. Eight centimetres of aluminium shielding would reduce the intensity of the Gamma Ray radiation to approximately 10% of its original. The adaptation of tungsten as a shielding material results in a volumetrically efficient configuration given that a tungsten shield of thickness 0.38 millimetres is capable of shielding 59.5 keV Gamma Ray radiation to 10% of its original intensity.

$^{241}\text{Am}$  is easily extracted in significant abundance from stockpiles of transuranic waste; the bi-product of nuclear fission reactors. The production of  $^{241}\text{Am}$  occurs in two steps. Firstly  $^{241}\text{Pu}$  is formed during double neutron capture reactions within the core of a reactor.  $^{241}\text{Pu}$  has a half-life of 14.4 years and decays via beta emission to form  $^{241}\text{Am}$  [2].  $^{241}\text{Am}$  may also be obtained from decommissioned nuclear weapons. Nuclear weapons are generally fuelled by  $^{239}\text{Pu}$  but contain small quantities of  $^{241}\text{Pu}$  which decays to  $^{241}\text{Am}$  as outlined above.

Figures 5.10 and 5.11 illustrate the spontaneous fission neutron spectra that dominate for pure  $^{241}\text{Am}$  and  $^{238}\text{Pu}$  sources. The data illustrated in Figures 4.1 and 4.2 was produced through the modelling of a  $1\text{ cm}^3$  source consisting of the corresponding isotopes using the Monte Carlo N-Particle transport code MCNPX 6<sup>TM</sup> [8]. Using this code, the source was assigned appropriate spontaneous fission probabilities ( $1.85 \times 10^{-7}$  % of decay events for  $^{238}\text{PuO}_2$  [9] and  $4.30 \times 10^{-10}$  % of decay events for  $^{241}\text{AmO}_2$  [9]) and a neutron energy spectrum was calculated by means of a tally function throughout the volume of the source. The statistics generated by these MCNPX simulations were resultant from the calculation of  $1 \times 10^6$  spontaneous fission events.

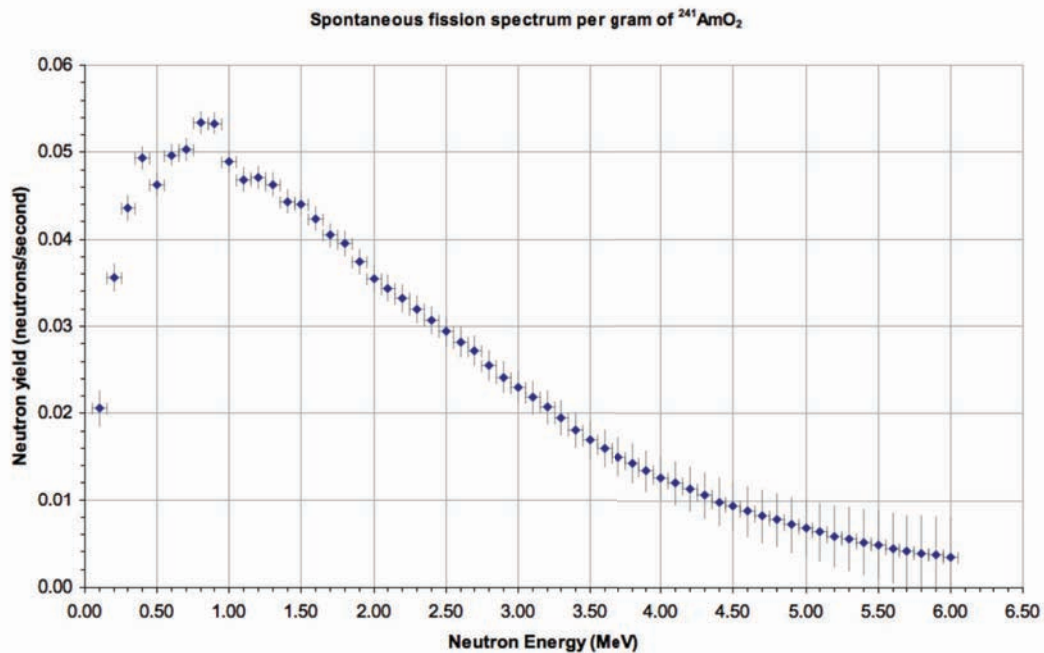


**Figure 4.1:** Spontaneous fission (S.F.) neutron yield per gram of  $^{241}\text{Am}$ . This S.F. spectrum was generated using the Monte Carlo N-Particle transport code MCNPX version 6 [8], the statistics from which were derived from the calculation of  $1 \times 10^6$  spontaneous fission events.

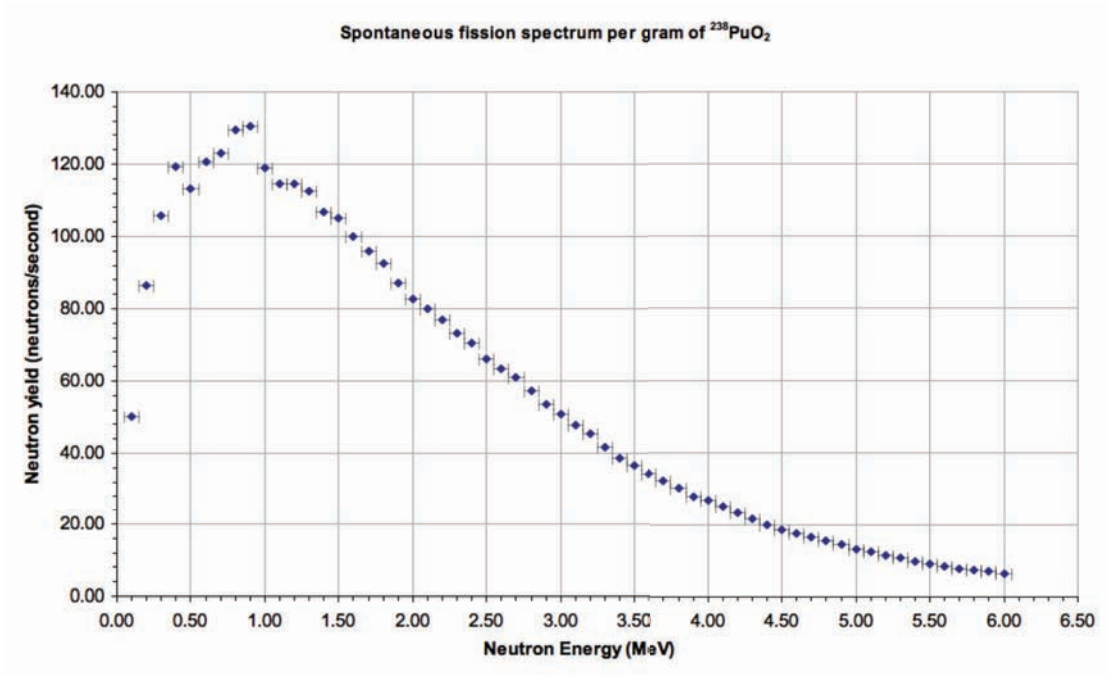


**Figure 4.2:** Spontaneous fission (S.F.) neutron yield per gram of  $^{238}\text{Pu}$ . This S.F. spectrum was generated using the Monte Carlo N-Particle transport code MCNPX version 6 [8], the statistics from which were derived from the calculation of  $1 \times 10^6$  spontaneous fission events.

Both  $^{241}\text{Am}$  and  $^{238}\text{Pu}$  are chemically stable under the nominal operating temperatures and conditions ( $<1000^\circ\text{C}$ ) for heat sources in their oxide forms. These are  $\text{AmO}_2$  and  $\text{PuO}_2$  respectively. These oxide compounds are formed when Americium nitrate or Plutonium nitrate is heated in an oxygenated atmosphere (air) between  $700^\circ\text{C}$  and  $800^\circ\text{C}$ . Natural oxygen is composed of 99.757%  $^{16}\text{O}$ , 0.038%  $^{17}\text{O}$  and 0.205%  $^{18}\text{O}$  [2]. The threshold energy for the  $^{16}\text{O}$  alpha-neutron ( $\alpha, n$ ) reaction is 15.24 MeV [10] and hence this particular reaction does not occur for  $^{238}\text{Pu}$  or  $^{241}\text{Am}$  in their oxide compounds. Although low in concentration, the ( $\alpha, n$ ) reaction cross-sections for  $^{17}\text{O}$  and  $^{18}\text{O}$  are significant for alpha particles with energies in the range from 0 to 6 MeV. Quantitatively, for alpha particles with energies of 5.5 MeV, the cross sections of  $^{17}\text{O}$  and  $^{18}\text{O}$  are 206 milibarns and 440 milibarns respectively [11].

The  $^{17}\text{O}$  ( $\alpha, n$ ) reaction has a Q value of +0.587 MeV and a threshold energy of 0 MeV [12]. The  $^{18}\text{O}$  ( $\alpha, n$ ) reaction has a Q value of -0.697 MeV and a threshold energy of 0.852 MeV [12]. Thus, for pure isotopes with predominantly low spontaneous fission probabilities, and hence relatively low neutron flux, when an oxide or dioxide compound of such isotopes is formed, an entirely different neutron emission spectrum is produced.

In order to facilitate accurate modelling of RTG radiation sources, the calculation of a total neutron energy spectrum was necessary. By treating the radiation source as a homogenous mixture of oxygen and the parent radionuclide with a unified molar mass  $M_0$ , it is possible to estimate the stopping power of the matrix [13]:

$$\frac{dE}{dx} = \left( \frac{e^2}{4\pi\epsilon_0} \right)^2 \left( \frac{N_A \rho}{M_0} \right) \left( \frac{4\pi z^2 Z}{mc^2 \beta^2} \right) \left[ \ln \left( \frac{2mc^2 \beta^2}{10Z} \right) - \ln(1 - \beta^2) - \beta^2 \right] \quad (5.1)$$

**Equation 2.1:** The Bethe Bloch formula for a material with molar mass  $M_0$ , density  $\rho$  and reaction target atomic number  $Z$  for an incident particle with charge  $z$  and velocity  $v$  (where  $\beta$  is the ratio of velocity to speed of light  $c$ ) [13, 14].

Using the stopping power of the compound matrix it is possible to estimate the neutron yield for a thick source. An energy spectrum can easily be obtained from equation 5.2:

$$Y = I \left( \frac{N_A \rho}{M_0} \right) \int_{E_0}^E \sigma(E) \frac{dx}{dE} dE \quad (5.2)$$

**Equation 2.2:** Neutron yield for a thick target of compound with molar mass  $M_0$  and density  $\rho$  where  $\sigma$  is the reaction cross section as a function of energy [14, 15].

Total neutron spectra were produced for both  $^{241}\text{AmO}_2$  and  $^{238}\text{PuO}_2$  by the combination of their spontaneous fission neutron spectra and the neutron yields as a result of

( $\alpha$ ,n)-reactions with  $^{17}\text{O}$  and  $^{18}\text{O}$  obtained through the application of equations 5.1 and 5.2. These spectra were generated via the use of a computational code developed by the author and are illustrated in Figures 5.12 and 5.13 below.

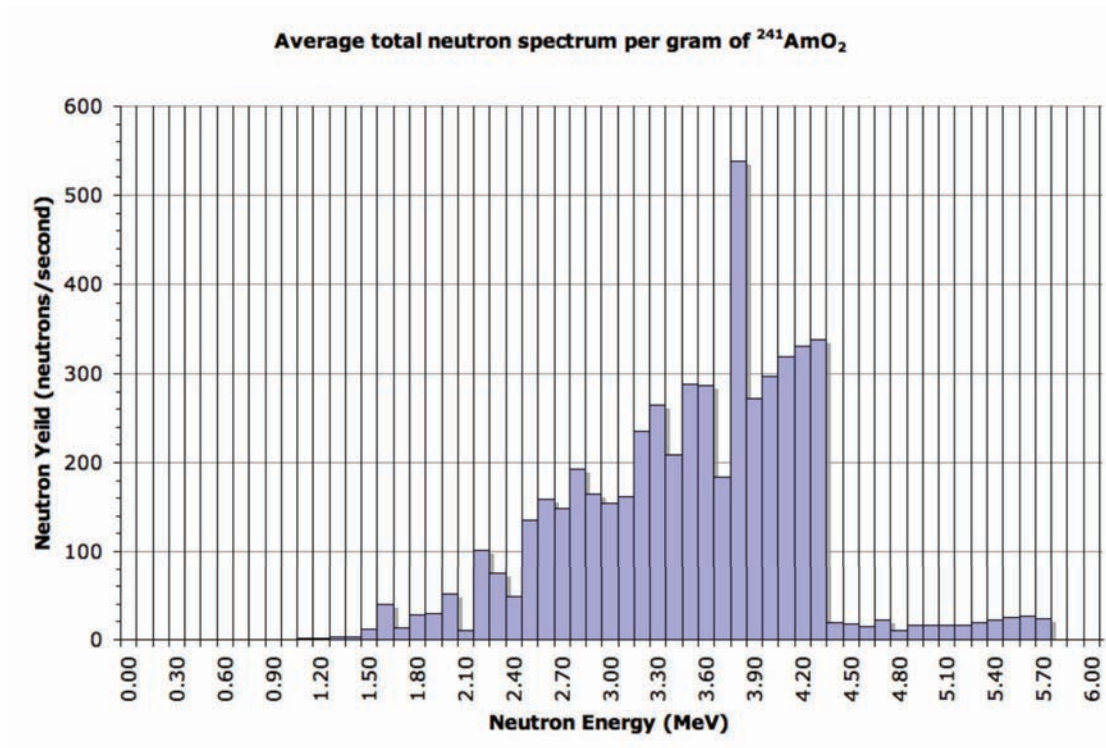


Figure 4.3: Total neutron yield per gram of  $^{241}\text{AmO}_2$  compound matrix based on an average  $\alpha$  energy of 5.46 MeV.

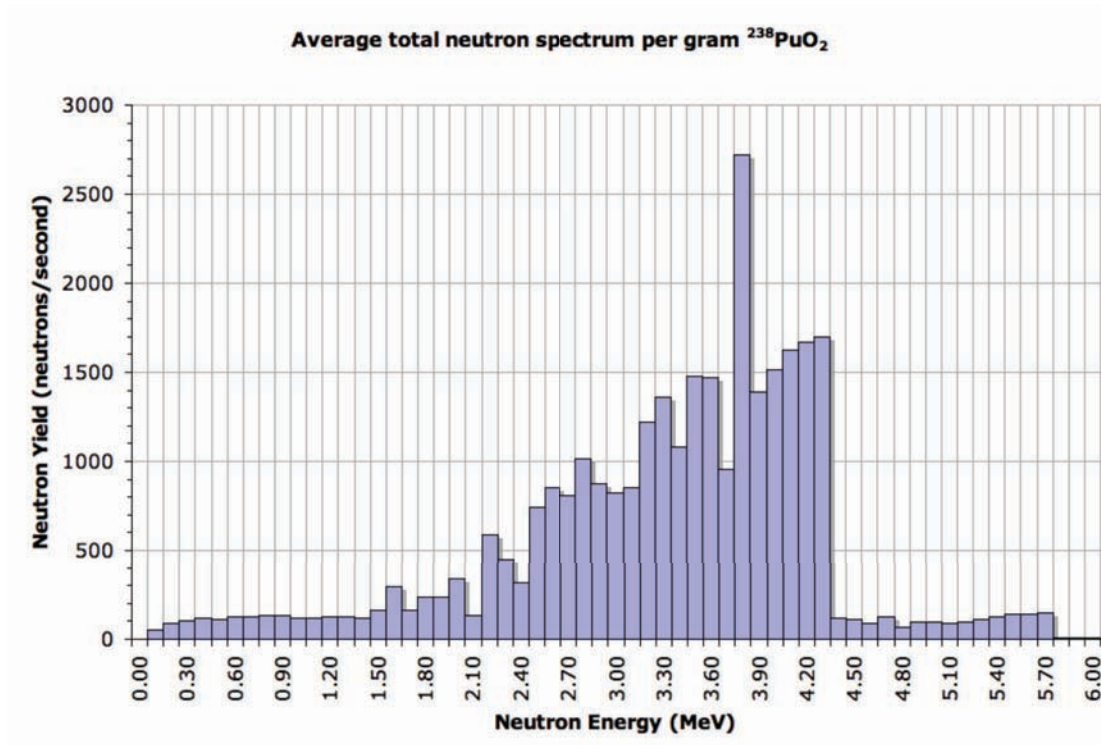


Figure 4.4: Total neutron yield per gram of  $^{238}\text{PuO}_2$  compound matrix based on an average  $\alpha$  energy of 5.49 MeV.

It can be deduced from Figures 4.3 and 4.4 that the neutron yield from the  $(\alpha, n)$  reaction with  $^{17}\text{O}$  and  $^{18}\text{O}$  is the dominant feature in the total neutron spectra for both  $^{238}\text{PuO}_2$  and  $^{241}\text{AmO}_2$ . Upon examination of the total neutron yield per gram of  $^{241}\text{Am}$  and  $^{241}\text{AmO}_2$ , there is a stark contrast. The neutron yield for  $^{241}\text{Am}$  in a pure metallic form is around  $1.353 \text{ n}\cdot\text{s}^{-1}\cdot\text{g}^{-1}$  (derived from spontaneous fission), whereas that of  $\text{AmO}_2$  is around  $5.321 \times 10^3 \text{ n}\cdot\text{s}^{-1}\cdot\text{g}^{-1}$ . For metallic  $^{238}\text{Pu}$  the neutron yield is around  $2.932 \times 10^3 \text{ n}\cdot\text{s}^{-1}\cdot\text{g}^{-1}$  and for  $\text{PuO}_2$  the neutron yield is of the order of  $3.030 \times 10^4 \text{ n}\cdot\text{s}^{-1}\cdot\text{g}^{-1}$ . These results and the spectra illustrated in Figures 4.5 and 4.6 above were verified using the SOURCES 4C code [16].

If a reduction in the total neutron yields for both  $^{241}\text{AmO}_2$  and  $^{238}\text{PuO}_2$  is required for safety, chemical processing of the materials may be performed which includes oxygen enrichment. The principal of oxygen enrichment is to alter the composition of the oxide from the natural oxygen isotopic ratios to one that is mostly composed of  $^{16}\text{O}$ . A process has been established for the oxygen enrichment of  $^{238}\text{PuO}_2$  [17]. This process involves the heating of  $\text{PuO}_2$  formed in a natural oxygen environment up to around 1000 °C while simultaneously subjecting the materials under positive pressure to a flow of  $^{16}\text{O}$  enriched oxygen carried in Argon gas [18] with approximately 4:1 flow ratio of  $^{16}\text{O}$  to argon [17]. This main procedure is undertaken for approximately 30 minutes and allows the  $^{16}\text{O}$  atoms to exchange from the gas flow into the  $\text{PuO}_2$  ceramic while the exhaust flow from the process carries away approximately 98% of the original  $^{17}\text{O}$  and  $^{18}\text{O}$  content. The processing time is the main driving variable for the final level of enrichment for any given  $^{16}\text{O}$  flow rate and processing temperature. The resultant reduction in the neutron flux for oxygen enriched  $\text{PuO}_2$  is approximately 91.1% [17] down to around  $2.697 \times 10^3 \text{ n.s}^{-1}.\text{g}^{-1}$ . In terms of the yield due to  $\alpha$ -n reactions, oxygen enrichment reduces the  $\alpha$ -n neutron yield from 92% of the total flux to a contribution of only 13.4% of the total yield (approx.  $359 \text{ n.s}^{-1}.\text{g}^{-1}$  of  $^{238}\text{PuO}_2$ ). Thus, approximately 86.6% of the total neutron yield for oxygen-enriched  $^{238}\text{PuO}_2$  is derived from spontaneous fission.

Given the level of success of the oxygen enrichment processing of  $\text{PuO}_2$ , it is equally conceivable that an almost identical process can be applied to the enrichment of  $\text{AmO}_2$  materials. Under such processing, the maximum permissible exchange temperature should not exceed 1100 °C, the dissociation temperature of  $\text{AmO}_2$ . Assuming that the oxygen exchange

process can achieve the same degree of  $^{16}\text{O}$  purity and given that  $^{241}\text{Am}$  produces  $10^3$  times fewer spontaneous fission neutrons than  $^{238}\text{Pu}$ , it is estimated a 97.97% reduction in the total neutron yield for  $^{241}\text{AmO}_2$  can be achieved. This would result in a total neutron yield of approximately  $1.08 \times 10^2 \text{ n.s}^{-1} \cdot \text{g}^{-1}$  of  $^{241}\text{AmO}_2$ .

The radioactivity properties for the isotopes determined above is summarised in Table 4.1 below. Table 4.1 also includes basic material properties for each isotope along with common physical forms.

Isotope & Form	Decay	Half Life $T_{1/2}$ (Years)	Theoretical Specific Activity (Ci.g <sup>-1</sup> )	Theoretical Specific Thermal Power (W.g <sup>-1</sup> )	Density (g.cm <sup>-3</sup> )	Neutron Flux (n.s <sup>-1</sup> .g <sup>-1</sup> )	Average charged particle energy (MeV)	Principle Gamma Ray Energy (keV)	Mass required per 100W <sub>th</sub> (g)	Production source
<sup>238</sup> Pu (Metallic)	α γ Spont. Fission	87.74	17.13	0.557	19.84	2.932×10 <sup>3</sup>	*** 5.49	43 99 152	180	Neutron irradiation of <sup>237</sup> Np or <sup>241</sup> Am
<sup>238</sup> Pu (PuO <sub>2</sub> )	α γ Spont. Fission	87.74	15.10	0.491 [0.345 *] Aged 30 yrs	11.46	3.030×10 <sup>4</sup> ----- (Natural oxide) ----- 2.697×10 <sup>3</sup> ----- (Enriched oxide) -----	*** 5.49	43 99 152	200	
<sup>241</sup> Am (Metallic)	α γ Spont. Fission	432.70	3.43	0.111	13.67	1.364	*** 5.46	26 33 59	900	α Decay of <sup>241</sup> Pu in nuclear fission products or from weapons maintenance
<sup>241</sup> Am (AmO <sub>2</sub> )	α γ Spont. Fission	432.70	3.03 (100% purity) 2.73 (90% purity) 2.97 (Measured)	0.098 (100% purity) 0.089 (90% purity) 0.094 (Measured)	11.68	5.906×10 <sup>3</sup> (100% Purity) 5.321×10 <sup>3</sup> (90% Purity) ----- (Natural Oxide) ----- 1.199×10 <sup>2</sup> (100% Purity) 1.080×10 <sup>2</sup> (90% Purity) ----- (Enriched Oxide) -----	*** 5.46	26 33 59	1124	
<sup>241</sup> Am (Am <sub>2</sub> O <sub>3</sub> )	α γ Spont. Fission	432.70	3.12	0.101	11.77	4.854×10 <sup>3</sup> (Natural Oxide) 9.853×10 <sup>1</sup> (Enriched Oxide)	*** 5.46	26 33 59	935	
<sup>208</sup> Po (Metallic)	α γ	2.90	590	17.81	9.30	-	5.12	** None	6	
<sup>210</sup> Po (Metallic)	α γ	0.38	4.5×10 <sup>3</sup>	137	9.30	-	5.30	** Few	0.7	Neutron irradiation of <sup>209</sup> Bi
<sup>210</sup> Po (PoBiO <sub>3</sub> )	α γ	0.38	2.0×10 <sup>3</sup>	61.31	8.99	2.052×10 <sup>5</sup>	5.30	** Few	1.63	
<sup>210</sup> Po (PoGd)	α γ	0.38	2.6×10 <sup>3</sup>	78.39	10.00	-	5.30	** Few	1.28	

**Table 4.1:** Summary of the key properties of the isotopes considered.

\* Calculated from data presented by G. Bennett et al [5] for current materials (approx. 25-30 years old).

\*\* Very low probability of emission. \*\*\* Alpha decay dominates energy spectrum

Isotope & Form	Decay	Half Life $T_{1/2}$ (Years)	Theoretical Specific Activity (Ci.g <sup>-1</sup> )	Theoretical Specific Thermal Power (W.g <sup>-1</sup> )	Density (g.cm <sup>-3</sup> )	Neutron Flux (n.s <sup>-1</sup> .g <sup>-1</sup> )	Average charged particle energy (MeV)	Principle Gamma Ray Energy (keV)	Mass required per 100W <sub>th</sub> (g)	Production source
<sup>242</sup> Cm Metallic	α γ Spont. Fission	0.447	3.3×10 <sup>3</sup>	121	13.50	3.92×10 <sup>6</sup>	*** 6.04	44	0.83	Neutron irradiation of <sup>241</sup> Am
<sup>242</sup> Cm (Cm <sub>2</sub> O <sub>3</sub> )	α γ Spont. Fission	0.447	3.0×10 <sup>3</sup>	109	11.7	4.2×10 <sup>6</sup>	*** 6.04	44	0.08	
<sup>243</sup> Cm Metallic	α γ Spont. Fission	29.1	4.2	1.78	13.50	2.71×10 <sup>2</sup>	*** 5.83	277.6 228.2	56.2	
<sup>243</sup> Cm (Cm <sub>2</sub> O <sub>3</sub> )	α γ Spont. Fission	29.1	3.8	1.62	11.7	7.81×10 <sup>3</sup>	*** 5.83	277.6 228.2	61.7	Neutron irradiation of <sup>243</sup> Am
<sup>244</sup> Cm Metallic	α γ Spont. Fission	18.1	8.2	2.80	13.50	2.2×10 <sup>6</sup>	*** 5.80	43	35.7	
<sup>244</sup> Cm (Cm <sub>2</sub> O <sub>3</sub> )	α γ Spont. Fission	18.1	6.9	2.53	11.7	2.0×10 <sup>6</sup>	*** 5.80	43	39.5	
<sup>252</sup> Cf (Metallic)	α γ Spont. Fission	2.65	536	28.39	15.1	2.3×10 <sup>12</sup>	<u>8.95</u> 5.93 α 103.77 SF	43 100	3.52	Neutron irradiation of <sup>244</sup> Cm/ <sup>241</sup> Am
<sup>252</sup> Cf (Cf <sub>2</sub> O <sub>3</sub> )	α γ Spont. Fission	2.65	489	25.90	12.8	4.2×10 <sup>11</sup>	<u>8.95</u> 5.93 α 103.77 SF	43 100	3.86	

Table 4.1 continued: Summary of the key properties of the isotopes considered.

\*\* Very low probability of emission.

\*\*\* Alpha decay dominates energy spectrum

Isotope & Form	Decay	Half Life T <sub>1/2</sub> (Years)	Theoretical Specific Activity (Ci.g <sup>-1</sup> )	Theoretical Specific Thermal Power (W.g <sup>-1</sup> )	Density (g.cm <sup>-3</sup> )	Neutron Flux (n.s <sup>-1</sup> .g <sup>-1</sup> )	Average charged particle energy (MeV)	Principle Gamma Ray Energy (keV)	Mass required per 100W <sub>th</sub> (g)	Production source
<sup>90</sup> Sr (metallic)	β	28.78	140	0.935	2.64	-	0.546	Brem.	107	<sup>235</sup> U Fission Product
<sup>90</sup> Sr (SrO)	β	28.78	118.87	0.789	5.10	-	0.546	Brem.	127	<sup>235</sup> U Fission Product
<sup>90</sup> Sr (SrTiO <sub>3</sub> )	β	28.78	67.79	0.452	5.11	-	0.546	Brem.	222	Fission Product
<sup>137</sup> Cs Metallic	β γ	30.07	98	0.270	1.87	-	0.55	Brem. 283 662	370	Fission Product
<sup>137</sup> Cs CsCl	β γ	30.07	78	0.220	3.97	-	0.55	Brem. 283 662	455	Fission Product
<sup>144</sup> Ce	β γ	0.780	3.2×10 <sup>3</sup>	25.5	6.77	-	0.29	Brem. 133 80.1	3.85	Fission Product
<sup>144</sup> Ce (CeO <sub>2</sub> )	β γ	0.780	2.62×10 <sup>3</sup>	21.0	7.13	-	0.29	Brem. 133 80.1	4.76	Fission Product
<sup>144</sup> Ce (Ce <sub>2</sub> O <sub>3</sub> )	β γ	0.780	2.74×10 <sup>3</sup>	22.0	6.80	-	0.29	Brem. 133 80.1	4.54	Fission Product

**Table 4.1 continued:** Summary of the key properties of the isotopes considered.

Brem. = Bremsstrahlung. Percentage purity refers to radiological purity.  
\*\* Very low probability of emission.

In order to assist in the selection of the most appropriate isotopes for use under a space or planetary mission architecture, a plot of electrical power output versus mission time was generated for a typical beginning of mission power level for a modern surface experiment. See Figure 4.5. The beginning of mission power level chosen for this study was 5 W<sub>e</sub> since this is also typical of the order of what would be required to provide power for a small, compact planetary science payload. From the above study, only the isotopes that could be housed in proximity to sensitive electronics were selected. As can be seen in Figure 4.5, after 30 years of operation, <sup>241</sup>Am fuelled sources are capable of delivering approximately 95.3% of the beginning of mission power. After the same period, <sup>238</sup>Pu fuelled devices can deliver a maximum of 78.9% of the beginning of mission electrical power.

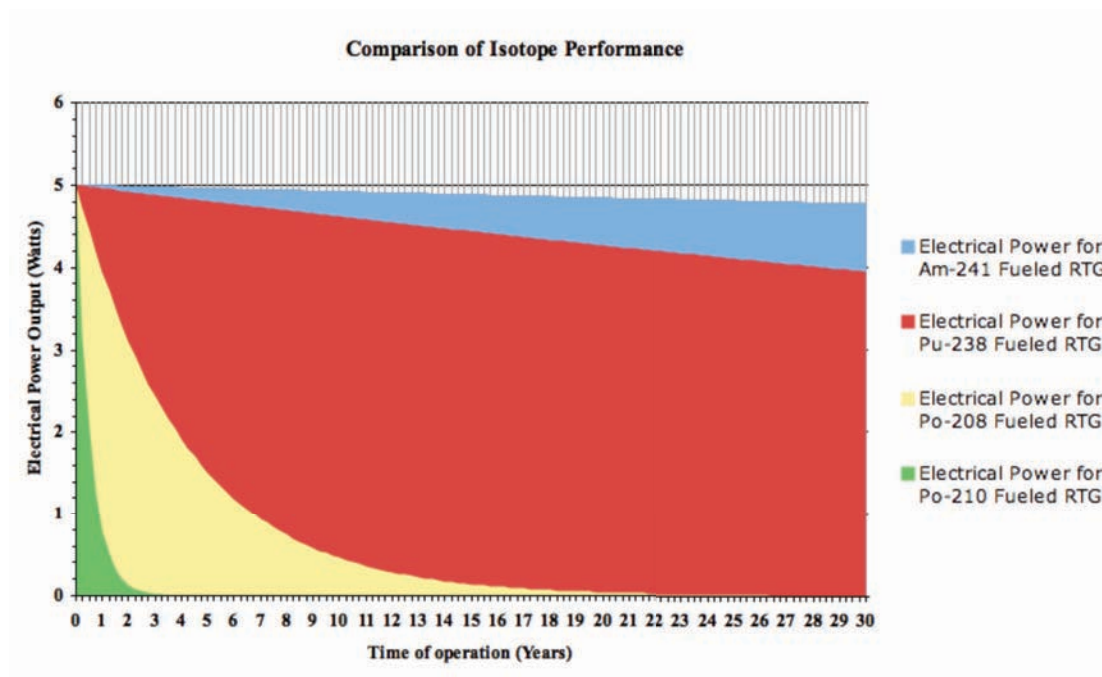


**Figure 4.5:** A plot of calculated system performances for example theoretical RTGs with a beginning of mission power output of 5W<sub>e</sub> fuelled by candidate alternative reduced radiation isotopes. These performances are compared to that of a similar device fuelled by Pu-238.

As expected, the results in Figure 4.5 show that  $^{210}\text{Po}$  and  $^{208}\text{Po}$  sources are ideal for missions where the thermal power and radioactivity are required to drop to a minimum after a relatively short operating period. Both isotopes decay into stable lead. An example of such requirements may be for use by probes that are required to penetrate through ice sheets on icy moons or for terrestrial glaciology studies. Once the required depth has been achieved, the thermal output of the system would decay to a negligible level after a relatively short period and would have little impact on the environment or potential biosphere.

#### **4.2 Monte Carlo radiation environment modelling and shielding criteria.**

An initial study performed by the author investigated the theoretical substitution of the GPHS  $^{238}\text{Pu}$  fuel pellets with several of the candidate isotopes listed in Section 5 above. The study explored the effect of isotope selection on the system mass, thermal power output and radiation dose. The fundamental aim of the study was to identify an isotopic substitution that would yield a reduced impact upon the local radiation environment well providing sufficient thermal energy for the GPHS architecture to remain useful. The candidate isotopes studied were  $^{241}\text{Am}$  in a  $^{241}\text{AmO}_2$  ceramic pellet form,  $^{241}\text{AmO}_2$  in tungsten matrices with varying tungsten volume fractions, encapsulated  $^{208}\text{Po}$  and  $^{210}\text{Po}$ , and  $^{90}\text{Sr}$  in a  $^{90}\text{SrO}$  ceramic form. The study also investigated the effects upon radiation dose by the use of fuels in both natural oxide composition, and in  $^{16}\text{O}$  enriched oxide form. The isotopes of curium were not identified as substitutive materials for  $^{238}\text{Pu}$  due to their

very large specific neutron yields that would require drastic re-design of the GPHS module assembly process, such as the provision of hot cells.

The substitution of  $^{238}\text{Pu}$  by polonium isotopes was examined for both  $^{208}\text{Po}$  and  $^{210}\text{Po}$  encapsulated in a tungsten matrix by means of spark plasma sintering (SPS), see chapter 6. For the purposes of this study, a 10% pellet volume fraction of Polonium was assumed. This encapsulation architecture could maintain capture of all 15.25 grams of the Polonium loading in each pellet. The hazards associated with this particular substitution are most certainly not attributed to normal operation. Given that Polonium has a vaporisation temperature that is lower than the predicted SPS sintering temperature of Tungsten ( $\sim 1500^\circ\text{C}$ ), production of a consolidated Polonium-Tungsten matrix may be challenging and the long-term corrosive behaviour of polonium within tungsten matrices [19] may require additional lining and envelopment of the pellet in order to maintain long-term capture. Alternatively a Polonium-Aluminium substitute matrix could be produced. Since aluminium has been consolidated using a Spark Plasma Sintering furnace at around  $500^\circ\text{C}$  -  $550^\circ\text{C}$  by M. Zadra et al [20] and given that this is less than the vaporisation temperature of Polonium, it is likely that such encapsulation could be engineered. Such a consolidation would depend heavily upon the existing GPHS module internal aeroshell to ensure safe re-entry of the cermet into the atmosphere but is likely to be able to maintain capture of the Polonium loading.

A Monte Carlo model of the GPHS module was created by the author in order to evaluate the effect of isotope selection on radiation dose. The Monte Carlo code MCNPX<sup>TM</sup> [8, 21] was used to carry out the simulations. MCNPX is a general-purpose Monte Carlo N-Particle transport code developed by Los Alamos national laboratory as an extension to the MCNP radiation transport code [8], which is capable of coupled neutron, photon and charged particle transport, via the inclusion LAHET intranuclear cascade code [22]. The accuracy of the code has been experimentally validated and has been widely used for applications such as fusion [23] and fission reactor [24] design, Shielding calculations [25] and radiography simulation [26].

Monte Carlo analysis of a specific problem is performed by the simulation of the behaviour of individual particles and/or photons of interest and recording specific aspects of their average behaviour. In the process, the individual probabilistic events that comprise a reaction or interaction with local materials are simulated sequentially. Probability distributions that may describe these events are statistically sampled to represent the complete problem and series of events. Such analyses may be determined with respect to energy and time. The statistical sampling process used by Monte Carlo simulation is based on the generation of random numbers. Here, source particles/photons are tracked throughout their life to their termination through absorption, annihilation or escape from a region of interest. Thus, probability distributions are randomly sampled using known transport data to determine the results at each conceptual step through three-dimensional space.

Execution of the MCNPX code requires the user to define an input file consisting of materials present, problem geometry, type of problem to be assessed, radiation / particle generation source, and a series of data storage arrays referred to as tallies. The MCNPX code treats user defined three-dimensional configurations of materials as geometric cells that are bound by first and second degree surfaces, and exist in fourth degree elliptical tori [8]. Through the definition of material properties, specifically density and isotope, the materials bound within any given geometric cell are referenced to an integrated database of nuclear properties and reactions. The nuclear reactions database that is integrated within MCNPX is the International Atomic Energy Agency's Evaluated Nuclear Database File (ENDF/B-VI) [27] which provides reaction cross sections, and hence allows the code to determine the probability of a reaction between an incident particle or photon and a specific material in addition to secondary particle or photon production with respect to energy and spatial position. Tallying of radiation interactions within regions of interest allows for dose equivalencies to be calculated for a given problem.

Upon execution of the code, source particles and/or photons are generated at randomised points within a geometric cell volume that has been defined by the user as a particle or radiation source. The diffusion and transport of the source particles is tracked through three dimensional geometries that have been defined in the users input file while accounting for angular deflection through Coulomb scattering, collisional energy loss and the production of secondary particles, Bremsstrahlung and annihilation Gamma Rays where applicable. For photon transport, the code accounts for incoherent and coherent scattering, in addition to the possibility of fluorescent emission after photoelectric

absorption. Unfortunately, at the time of writing,  $\alpha$ -n reactions are not calculable by the MCNPX code. For this reason, neutron source distributions must be pre-defined by a user allowing for the source generation of neutrons for transport simulation.

MCNPX tally results are natively normalized to be per source particle (referred to as source histories) and are recorded in a data table in an output file that is generated upon complete code execution. These normalized tallies are accompanied by an estimated relative error,  $R$ , that is defined by the estimated standard deviation of the mean divided by the mean value. The MCNPX code may be executed for a user-defined number of source particle generations/histories that may be realised as iterations. Since the relative error is typically proportional to  $1/\sqrt{N}$ , where  $N$  is the number of source histories or data points, the estimated accuracy of the tally results may be enhanced via the increase in the number of source histories created. The number of source histories ( $N$ ) also determines the computational time required for simulation, which in turn may be reduced via the implementation of parallel processing. The accuracy of the nuclear reaction databases used by the MCPX code is key to the success and accuracy of the overall results. Since reaction cross sections / probabilities for the ENDF/B-VI databases are measured experimentally, it is anticipated that their accuracy is fundamental to the accuracy of the simulated results generated by the code.

The initial MCNPX model was set up to represent the current GPHS architecture (see chapter 3) which includes a graphite module casing and two graphite internal aeroshell structures, each containing two iridium clad  $^{238}\text{PuO}_2$  fuel pellets separated by a graphite

floating membrane. In this model, the fuel pellets have an equal length and diameter of 27.6 mm [28] and the iridium cladding has a thickness of 0.5 mm. The activity of each pellet was calculated to be approximately 2.8 kCi based on a specific activity of  $15.1 \text{ Ci.g}^{-1}$  for the  $^{238}\text{PuO}_2$  ceramic. The output power of each  $^{238}\text{PuO}_2$  pellet was also found to be  $62.5 \text{ W}_{\text{th}}$ . Graphite was used as a substitute for the carbon-bonded-carbon sleeve that covers the internal aeroshell of the GPHS module. The GPHS geometry model used under the MCNPX software package is illustrated in Figure 4.6 below. The dose rates recorded were calculated for a spherical shell of water with a thickness of 10 mm and an internal radius of 1m from the centre of the GPHS module.

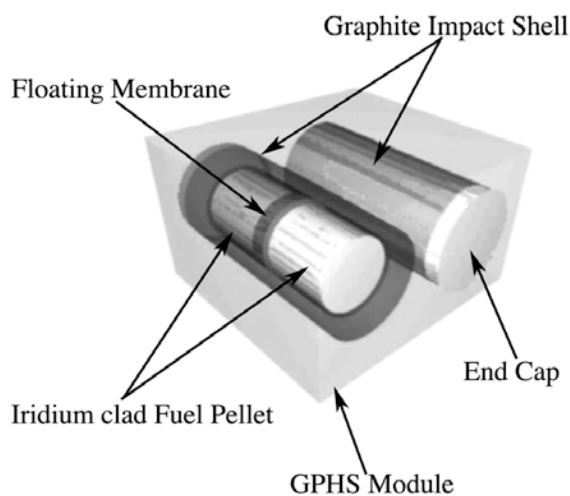


**Figure 4.6:** 3-dimensional drawing of the GPHS module MCNPX [8] geometry model.

The results from this study are shown in Table 4.2. The fuel mass and thermal power output for a single module is represented graphically in Figures 4.7 and 4.8 below. As can be seen in these results, there is a very small mass increase associated with the direct substitution of the original  $^{238}\text{Pu}$  plutonium dioxide fuel pellets with  $^{241}\text{Am}$

americium dioxide. In addition, there is approximately an 80% reduction in the thermal power output of a single GPHS module.

One advantage of using  $^{241}\text{AmO}_2$  as a replacement fuel is in the 90% gamma ray dose reduction. For the GPHS architecture, it is clear from table 4.2 that encapsulation in a tungsten cermet has an overall detrimental effect on the module mass and thermal power density. Given that the graphite impact shells of the GPHS modules provide protection during critical mission failures such as launch abort scenarios, and that the iridium cladding around the fuel pellets provides some degree of soft X-Ray and Gamma-Ray shielding, there is little advantage in using tungsten based matrices for the encapsulation of the  $\text{AmO}_2$  fuel as a direct replacement for the current GPHS  $^{238}\text{PuO}_2$  fuel pellets. However, for non-proliferation safety measures, encapsulation within a tungsten or tungsten carbide matrix may prove to be advantageous. Such advantages are considered later in this chapter.

The application of  $^{208}\text{Po}$  and  $^{210}\text{Po}$  encapsulated in aluminium matrices to the GPHS architecture is extremely attractive for small systems that demand a high initial power density over relatively short durations. As discussed in section 2 above, the mission duration and minimum power requirements would ultimately define the suitability of such isotope selection. It is appreciable that for future lunar missions, small dynamic converter based isotope power systems that take advantage of the GPHS architecture by using 1 or 2 GPHS modules, such as the NASA Advanced Stirling Radioisotope Generator (ASRG), could be a potential application for the  $^{208}\text{Po}$  or  $^{210}\text{Po}$  isotopes. Under such an application, it is quite conceivable that a system similar to the ASRG could provide up to  $580 \text{ W}_e$  for a

minimum of 2-3 years through the employment of adaptive radiator designs in addition to providing thermal management for electrical and/or mechanical systems during extended periods of darkness such as lunar night.

The fuelling of a GPHS module with  $^{90}\text{SrO}$  results in a 55.5% decrease in the module fuel mass and an increase in thermal output power by 4.4%. However, the dramatic increase in gamma radiation dose produced by such substitution implies that increased shielding would be required which in turn could make the use of  $^{90}\text{Sr}$  in the form of  $^{90}\text{SrO}$  incompatible with the GPHS architecture. These findings are consistent with those presented in the study by S. Oandso et al [29].

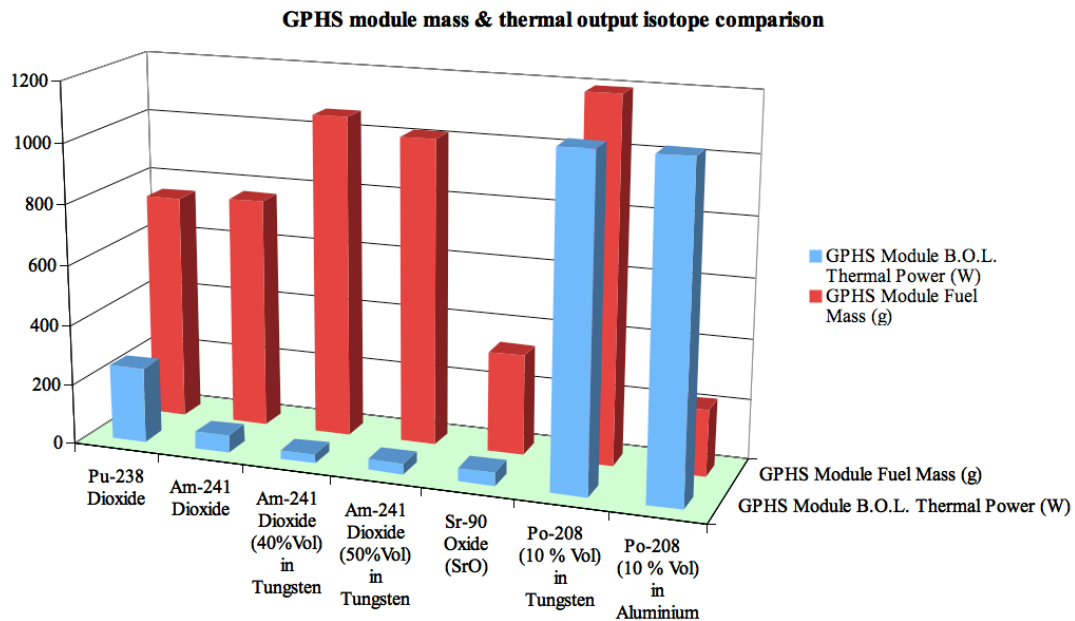


**Figure 4.7:** A beginning of life thermal performance and fuel mass comparison of substitute isotope candidates (excluding  $^{210}\text{Po}$ ) when used to fuel a GPHS module in contrast to the current performances of the GPHS modules fuelled by  $^{238}\text{PuO}_2$ .

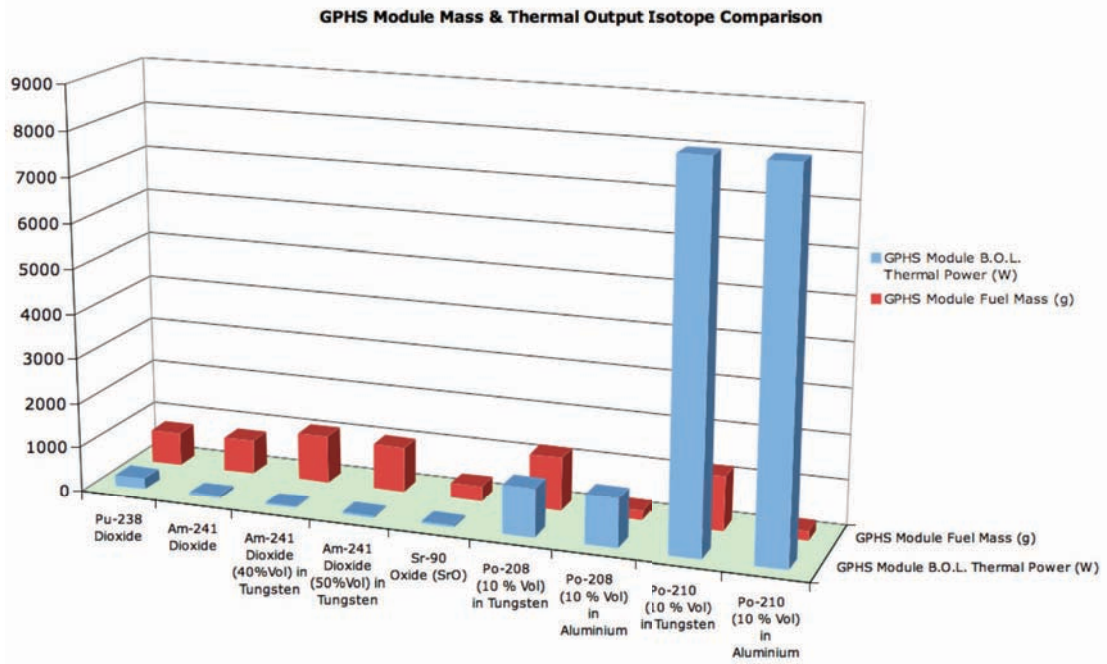


**Figure 4.8:** A beginning of life thermal performance and fuel mass comparison of all substitute isotope candidates when used to fuel a GPHS module in contrast to the performances of the GPHS modules fuelled  $^{238}\text{PuO}_2$ .

GPHS Module Fuel Form:	Pu-238 <sup>238</sup> PuO <sub>2</sub> Ceramic Pellet	Am-241 <sup>241</sup> AmO <sub>2</sub> (40%vol.) and W (60% vol.) Cermet	Am-241 <sup>241</sup> AmO <sub>2</sub> (50%vol.) and W (50%vol.) Cermet	Am-241 <sup>241</sup> AmO <sub>2</sub> Ceramic Pellet	Sr-90 <sup>90</sup> SrO Ceramic Pellet	Po-208 <sup>208</sup> Po (10%vol.) and W (90%vol.) Cermet	Po-208 <sup>208</sup> Po (10%vol.) and Al (90%vol.) Cermet	Po-210 <sup>210</sup> Po (10%vol.) and W (90%vol.) Cermet	Po-210 <sup>210</sup> Po (10%vol.) and Al (90%vol.) Cermet
Pellet Mass (g):	1.88×10 <sup>2</sup>	2.66×10 <sup>2</sup>	2.54×10 <sup>2</sup>	1.91×10 <sup>2</sup>	8.3×10 <sup>1</sup>	2.99×10 <sup>2</sup>	5.50×10 <sup>1</sup>	2.99×10 <sup>2</sup>	5.50×10 <sup>2</sup>
Total Fuel Mass (g):	7.51×10 <sup>2</sup>	1.07×10 <sup>3</sup>	1.02×10 <sup>3</sup>	7.66×10 <sup>2</sup>	3.34×10 <sup>2</sup>	1.20×10 <sup>3</sup>	2.20×10 <sup>2</sup>	1.20×10 <sup>3</sup>	2.20×10 <sup>2</sup>
Change in Module Mass (g):	0	+314	+264	+14	-417	+445	-531	+446	-531
Pellet Activity (Ci):	2.84×10 <sup>3</sup>	2.89×10 <sup>2</sup>	3.47×10 <sup>2</sup>	5.21×10 <sup>2</sup>	9.87×10 <sup>3</sup>	9.00×10 <sup>3</sup>	9.00×10 <sup>3</sup>	6.85×10 <sup>4</sup>	6.85×10 <sup>4</sup>
Change in Pellet Activity (Ci):	0	-2.55×10 <sup>3</sup>	-2.49×10 <sup>3</sup>	-2.32×10 <sup>3</sup>	+7.03×10 <sup>3</sup>	+6.16×10 <sup>3</sup>	+6.16×10 <sup>3</sup>	+6.80×10 <sup>4</sup>	+6.80×10 <sup>4</sup>
Module Activity (Ci):	1.13×10 <sup>4</sup>	1.16×10 <sup>3</sup>	1.39×10 <sup>3</sup>	2.08×10 <sup>3</sup>	3.95×10 <sup>4</sup>	3.60×10 <sup>4</sup>	3.60×10 <sup>4</sup>	+2.74×10 <sup>5</sup>	+2.74×10 <sup>5</sup>
Change in Module Activity (Ci):	0	-1.01×10 <sup>4</sup>	-9.91×10 <sup>3</sup>	-9.22×10 <sup>3</sup>	+2.82×10 <sup>4</sup>	+2.46×10 <sup>4</sup>	+2.46×10 <sup>4</sup>	2.72×10 <sup>5</sup>	2.72×10 <sup>5</sup>
Module Thermal Power (W):	2.50×10 <sup>2</sup>	3.63×10 <sup>1</sup>	4.30×10 <sup>1</sup>	6.80×10 <sup>1</sup>	2.61×10 <sup>2</sup>	1.09×10 <sup>3</sup>	1.09×10 <sup>3</sup>	8.36×10 <sup>3</sup>	8.36×10 <sup>3</sup>
Change in Module Thermal Power (W):	0	-2.14×10 <sup>2</sup>	-2.07×10 <sup>2</sup>	-1.93×10 <sup>2</sup>	+1.10×10 <sup>1</sup>	+8.36×10 <sup>3</sup>	+8.36×10 <sup>2</sup>	+8.33×10 <sup>3</sup>	+8.33×10 <sup>3</sup>
Neutron Dose rate at 1m radius from GPHS (Sv/hr):	6.534×10 <sup>-4</sup> ± 9.00×10 <sup>-6</sup>	3.036×10 <sup>-5</sup> ± 7.94×10 <sup>-7</sup>	3.788×10 <sup>-5</sup> ± 2.68×10 <sup>-7</sup>	8.238×10 <sup>-5</sup> ± 1.86×10 <sup>-7</sup>	-	-	-	-	-
Neutron dose rate as a percentage of <sup>238</sup> PuO <sub>2</sub> fuelled GPHS dose rate (%):	100	4.6	5.8	12.6	-	-	-	-	-
Gamma dose rate at 1m radius from GPHS (Sv/hr):	1.880×10 <sup>-6</sup> ± 1.09×10 <sup>-8</sup>	6.882×10 <sup>-8</sup> ± 3.17×10 <sup>-10</sup>	8.273×10 <sup>-8</sup> ± 2.79×10 <sup>-10</sup>	1.740×10 <sup>-7</sup> ± 1.44×10 <sup>-9</sup>	6.448×10 <sup>-2</sup> ± 1.90×10 <sup>-5</sup>	-	-	-	-
Gamma dose rate as a percentage of <sup>238</sup> PuO <sub>2</sub> fuelled GPHS dose rate (%):	100	3.7	4.4	9.3	3.43×10 <sup>4</sup>	-	-	-	-
Worker maximum recommended exposure time (hours per year):	31	657	527	242	0.31	>	>	>	>
Neutron Dose rate at 1m radius from GPHS fuelled with oxygen enriched materials (Sv/hr):	5.816×10 <sup>-5</sup> ± 1.14×10 <sup>-6</sup>	6.162×10 <sup>-7</sup> ± 1.61×10 <sup>-8</sup>	7.691×10 <sup>-7</sup> ± 5.44×10 <sup>-9</sup>	1.672×10 <sup>-6</sup> ± 3.77×10 <sup>-9</sup>	-	-	-	-	-
Neutron dose rates for modules fuelled by oxygen enriched materials as a percentage of the <sup>238</sup> PuO <sub>2</sub> fuelled GPHS module dose rate (%):	100	1	1.3	3	-	-	-	-	-
Gamma Dose rate at 1m radius from GPHS module fuelled with oxygen enriched materials (Sv/hr):	1.673×10 <sup>-7</sup> ± 1.38×10 <sup>-9</sup>	1.397×10 <sup>-9</sup> ± 6.44×10 <sup>-12</sup>	1.679×10 <sup>-9</sup> ± 5.66×10 <sup>-12</sup>	3.532×10 <sup>-9</sup> ± 2.91×10 <sup>-11</sup>	6.448×10 <sup>-2</sup> ± 1.90×10 <sup>-5</sup>	-	-	-	-
Gamma dose rates for modules fuelled by oxygen enriched materials as a percentage of the oxygen enriched <sup>238</sup> PuO <sub>2</sub> fuelled GPHS module dose rate (%):	100	0.8	1	2	3.85×10 <sup>5</sup>	-	-	-	-
Worker maximum recommended exposure time to modules fuelled by oxygen enriched materials (hours per year):	343	>>	>>	>>	0.31	>	>	>	>

**Table 4.2:** Alternative isotope study results for the replacement of the current PuO<sub>2</sub> fuel in the GPHS module. Data for oxygen enriched oxides and oxides of natural oxygen composition is given for <sup>238</sup>PuO<sub>2</sub> and <sup>241</sup>AmO<sub>2</sub> fuelled modules. “>>” Signifies that a practically unlimited annual exposure time is permissible.

On completion of the initial GPHS study, it became apparent that several shielding criteria for reduced radiation power sources could be met by appropriate isotope selection. As indicated by the results in Table 4.2, the received neutron dose rate at a distance of 1 metre from the centre of the current unenriched  $^{238}\text{PuO}_2$  fuelled GPHS module is of the order of 0.6553 mSv/hr (65.53 mRem/hr). It is clearly possible to make alternative isotope power sources that have a dose rate that is at least an order of magnitude lower than current systems. This would have a dramatic impact on the applicability of RTGs over a greater range of space and terrestrial missions and applications. The radiation dose to sensitive detectors would be reduced, increasing the operational lifetime of instruments [30]. The health and safety hazards for radiation workers and assembly technicians would also be reduced and/or may allow workers to work under occupational safety guidelines for longer periods of time with a given system. Planetary science missions with an astrobiology component and terrestrial studies designed to study ecosystems in extreme environments could benefit from reduced radiation power sources and isotopes that decay into stable daughters after a short period of time. By careful isotope selection, the effective sterilisation factor, and heat generated by the source can be minimised in order to ensure a reduced impact on the environment.

The current legal dose limit for radiation workers in the United Kingdom is 20 mSv per year, or under special cases this is set to a 100 mSv over a 5 year period where no more than a 50 mSv dose can be accumulated in a single year [31]. Based on these current guidelines and the above results from the MCNPX modelling, a radiation worker can work with oxygen-enriched  $^{238}\text{PuO}_2$  fuelled GPHS modules for approximately 343 hours per

year. By making the substitution from oxygen-enriched  $^{238}\text{PuO}_2$  fuel to oxygen-enriched  $^{241}\text{AmO}_2$ , it is possible for workers to spend a practically unlimited period each year working with GPHS modules. For the same electrical output power as current GPHS-RTGs, we would require around 90 modules fuelled with  $^{241}\text{AmO}_2$  instead of 18 modules fuelled with  $^{238}\text{PuO}_2$ . This essentially means that workers must complete approximately 5 times the typical manual workload, but since there is little limitation to exposure time, the only penalty to the entire operation is in the form of the 5 times mass penalty for system heat sources. As can be deduced from Table 4.2, the decrease in dose rates and increase in recommended exposure times with the alternative isotope fuels, with the exception of  $^{90}\text{Sr}$ , greatly outweighs any increase in manual workload for such substitution.

### **4.3 Reduced radiation isotope sources**

So as to establish further comparison between  $^{238}\text{PuO}_2$  sources and those fuelled by  $^{241}\text{AmO}_2$ , the proposed alternative isotope compound with the lowest specific thermal power, a set of Monte Carlo models were developed by the author. This modelling focussed upon the determination of the relationship between a given neutron shield thickness and source size to the neutron doses received at a 1 m radius and the associated source-shield system masses. This investigation was performed by modelling a given source with a layer of neutron shielding in a spherical geometry and executing such models under the MCNPX code. Three thicknesses of boron loaded polyethylene shielding were investigated (5cm, 10cm and 15cm) and the photon and neutron dose rates tallied in a 1 cm thick shell of water at a radius of 1m from the source. The composition of the  $^{241}\text{Am}$  source

was also set as a variable so as to investigate its effect on the overall mass of the assembly. The source was presented in ceramic oxide form ( $^{241}\text{AmO}_2$ ) or encapsulated in tungsten as a cermet, the volumetric composition of which was either 40 % or 50 %  $^{241}\text{AmO}_2$ . In order to provide the desired comparison,  $^{238}\text{PuO}_2$  was also modelled within identical configurations. The oxygen composition within the oxide compounds of both  $\text{PuO}_2$  and  $\text{AmO}_2$  was set as another variable in order to determine the effect of oxygen-enrichment upon the shielding requirements. Thermal power output levels of between 10 and 200 Watts were also set as the third variable for the investigation. The source emission spectra were defined as above. Each specific configuration was simulated in MCNPX version 6c [8], each simulation terminating after a total of  $1 \times 10^6$  source particles had been tracked through the geometry.

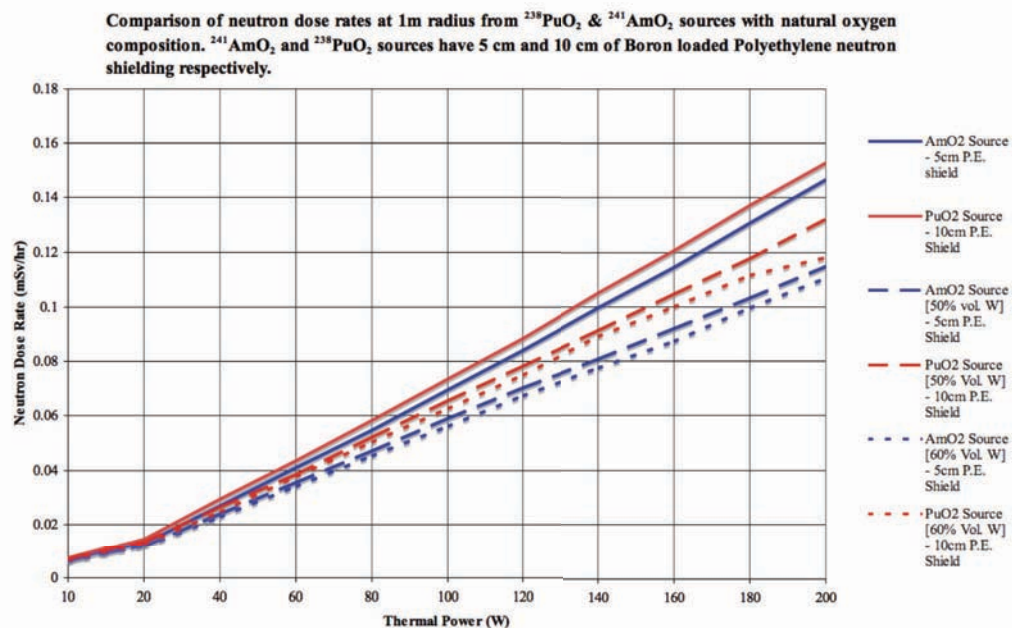


**Figure 4.9:** Comparison of MCNPX [8] derived results for the dose rates of modelled systems fuelled by  $^{241}\text{AmO}_2$  (natural oxygen composition) in oxide form and in tungsten based cermets relative to those of devices with similar dose rates fuelled by  $^{238}\text{PuO}_2$  (natural oxygen composition) in oxide form and tungsten cermets. These system masses are illustrated as a function of source thermal output power and dose rate equivalence. The tungsten volume fraction for cermet-based sources are listed in the key.

Mass comparison for sources with natural oxygen composition. For approximately equal dose rates, the  $^{241}\text{AmO}_2$  and  $^{238}\text{PuO}_2$  sources have 5 cm and 10 cm of Boron loaded Polyethylene neutron shielding respectively.

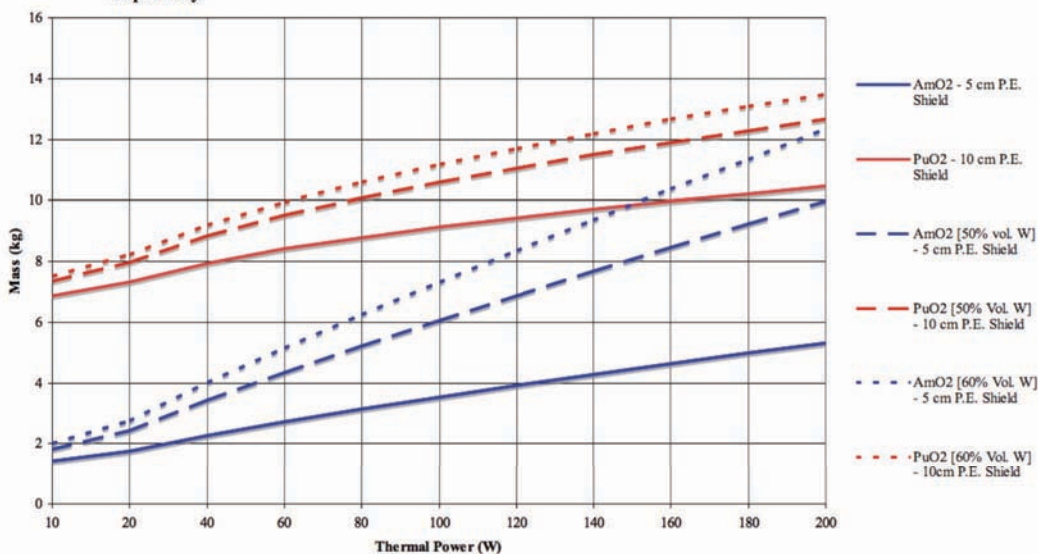


**Figure 4.10:** Comparison of MCNPX [8] derived results for the masses of modelled systems fuelled by  $^{241}\text{AmO}_2$  (natural oxygen composition) in oxide form and in tungsten based cermet relative to those of devices with similar dose rates fuelled by  $^{238}\text{PuO}_2$  (natural oxygen composition) in oxide form and tungsten cermet. These system masses are illustrated as a function of source thermal output power and dose rate equivalence. The tungsten volume fraction for cermet based sources are listed in the key.

For oxide sources with natural oxygen composition, it was determined that  $^{241}\text{AmO}_2$  sources surrounded by a 5 cm thick boron loaded polyethylene (B.L.P.E.) shield resulted in approximately the same neutron dose rates as for  $^{238}\text{PuO}_2$  surrounded by a 10 cm thick B.L.P.E. shield for the thermal power range between 0 and 200 Watts. This is illustrated in Figure 4.9. Figure 4.10 illustrates the associated masses that are observed with this shielding configuration. Over the identical thermal power range for oxygen-enriched sources, the dose rates that were observed for an unshielded  $^{241}\text{AmO}_2$  source were approximately equal to those of  $^{238}\text{PuO}_2$  sources surrounded by a 15 cm thick B.L.P.E. shield (Figure 4.11). This marked difference in shielding requirements is due to the domination of spontaneous fission derived neutron yields for the oxygen-enriched materials and the difference between the spontaneous fission probabilities of  $^{241}\text{Am}$  and  $^{238}\text{Pu}$ . Figure 4.12 illustrates the masses of these configurations for the oxygen-enriched sources.

Comparison of neutron dose rates at 1m radius from oxygen-enriched  $^{238}\text{PuO}_2$  &  $^{241}\text{AmO}_2$  sources. For approximately equal dose rates,  $^{241}\text{AmO}_2$  sources have no shielding and  $^{238}\text{PuO}_2$  sources have 10 cm of Boron loaded Polyethylene neutron shielding.

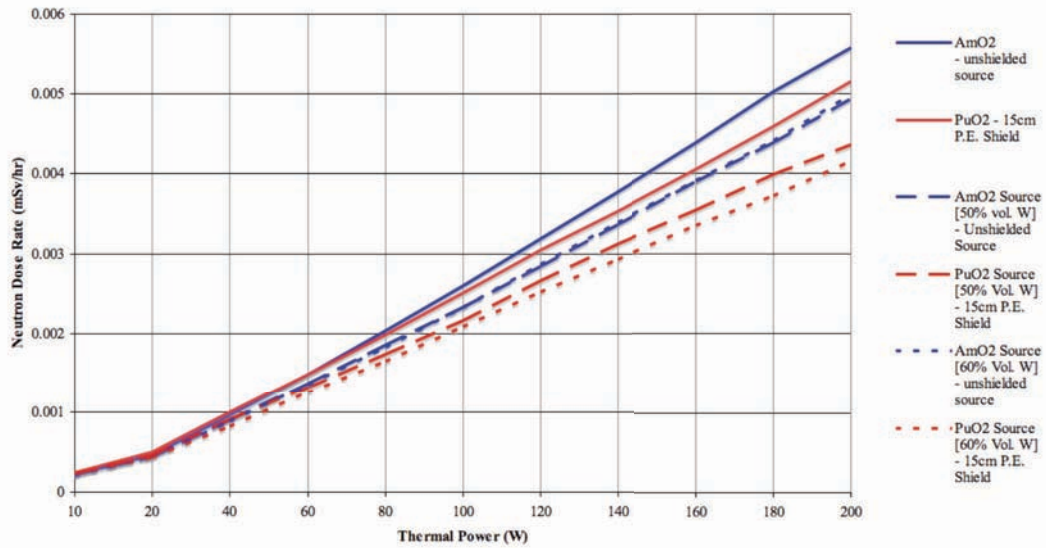


**Figure 4.11:** Comparison of MCNPX [8] derived results for the dose rates of modelled systems fuelled by oxygen-enriched  $^{241}\text{AmO}_2$  in oxide form and in tungsten based cermet relative to those of devices with similar dose rates fuelled by oxygen-enriched  $^{238}\text{PuO}_2$  in oxide form and tungsten cermet. These system masses are illustrated as a function of source thermal output power and dose rate equivalence. The tungsten volume fraction for cermet based sources are listed in the key.

Mass comparison for oxygen-enriched sources. For approximately equal dose rates, the  $^{241}\text{AmO}_2$  sources have no shielding and the  $^{238}\text{PuO}_2$  sources have 15 cm of Boron loaded Polyethylene neutron shielding.

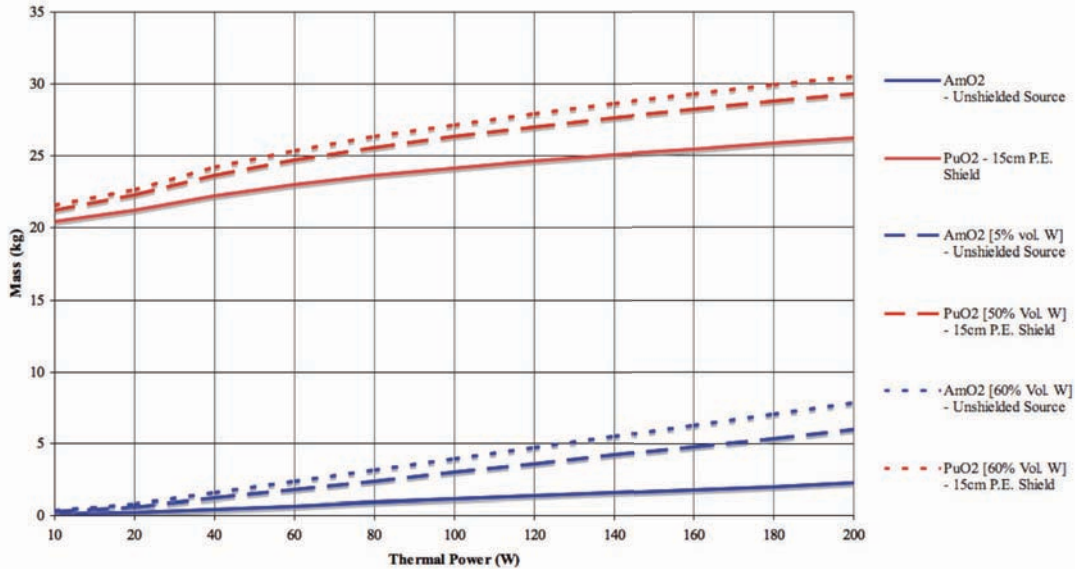


**Figure 4.12:** Comparison of MCNPX [8] derived results for the masses of modelled systems fuelled by oxygen-enriched  $^{241}\text{AmO}_2$  in oxide form and in tungsten based cermet relative to those of devices with similar dose rates fuelled by oxygen-enriched  $^{238}\text{PuO}_2$  in oxide form and tungsten cermet. These system masses are illustrated as a function of source thermal output power and dose rate equivalence. The tungsten volume fraction for cermet based sources are listed in the key.

What is particularly evident within these results is that for any given power level within the range considered, for an equal neutron dose rate to be exhibited by both oxygen-enriched Americium and Plutonium systems, the total masses of the  $^{238}\text{PuO}_2$  configurations is up to 10 times greater than those for  $^{241}\text{AmO}_2$ . This is an extremely important factor that must be considered during isotope selection for power sources where potential radiation exposure to workers or during launch failure scenarios is to be minimised.

As has been demonstrated within this chapter, selection of isotopes for a specific application is extremely important so as to ensure mass and volume efficiency while attaining the desired level of safety. The selection of a given isotope should not be based on isotope compound specific thermal power alone. Full consideration must be given to the amount of shielding that is necessary in order to achieve dose rates to the surrounding environment that are deemed acceptable by the system's designers. It is essentially this resultant system specific power density that must be used in assisting such isotope selection. The half-life, which is intimately associated with specific thermal power output, must also be considered on an application specific basis.

Through the evaluation and comparison of the isotopes discussed in sections 4.1 to present, the author has identified three isotopes, alternative to  $^{238}\text{Pu}$  that can deliver suitable power densities for space or terrestrial missions while minimising the radiation doses delivered by such sources. The  $^{208}\text{Po}$  and  $^{210}\text{Po}$  radioisotopes are best suited to missions requiring short durations of thermal and/or electrical power before decaying into stable isotopes of lead. Such missions include melt-penetration of icy planetary surfaces while

minimising the overall impact upon the environment. The use of the polonium isotopes implies a high initial thermal loading in order to account for the isotopes' short half-life, which in turn demands adaptive radiator or heat pipe design for steady state electrical power output.

$^{241}\text{Am}$  has a half-life that is approximately 5 times greater than that of  $^{238}\text{Pu}$ . We have determined that a  $^{241}\text{AmO}_2$  source neutron yield is approximately an order of magnitude lower than a  $^{238}\text{PuO}_2$  source of equal mass and degree of  $^{16}\text{O}$  oxide enrichment. We have also demonstrated that shielded heat sources fuelled by oxygen-enriched  $^{238}\text{PuO}_2$  have masses that are up to 10 times greater than those fuelled by oxygen-enriched  $^{241}\text{AmO}_2$  with equivalent thermal power outputs and neutron dose rates at 1 m radii. For these reasons,  $^{241}\text{Am}$  is well suited to missions that demand long duration power output from a power supply, such as deep spaceflight missions and similar missions that use instrumentation and electronics systems that are sensitive to or are susceptible to neutron radiation damage.

#### **4.4 Mixed Am-Cm isotope heat sources**

As has been determined above, isotopes such as  $^{241}\text{Am}$  could offer improved safety by reducing the radiation dose field to the surrounding environments without the need for significant amounts of external shielding beyond the source encapsulation. It is suggested that the use of a blend of americium and curium isotopes in the stoichiometry that can be extracted from the typical nuclear fuel cycle to form compounds suitable for the fuelling of RPS and RHU systems. These radioisotope sources differ from those described above and

in previous studies [1] given that in this case a high neutron yield is anticipated, whereas previously the focus was to reduce the neutron dose for reduced risk to radiation workers. The basic approach to heat source design is however the same with the exception that certain scientific missions may tolerate or exploit the neutron yield.

Fuel assemblies composed of  $^{235}\text{U}$  enriched to approximately 3% with the more isotopically abundant  $^{238}\text{U}$  are used within commercial nuclear reactors [32]. While in the reactor,  $^{235}\text{U}$  undergoes fission and results in a spectrum of both radioactive and stable isotopes. Neutrons released by the fission process and the spontaneous fission of daughter radioisotopes can be captured by other nuclei resulting in the formation of heavier elements. Upon discharge from the reactor at the end of its useable lifetime, a fuel assembly contains a myriad of isotopes with a large range of mass numbers. Fuel assemblies are typically committed to a period of interim storage upon discharge, during which the capture of spontaneous fission neutrons continues. Thus, the isotopic composition of the used fuel assemblies varies as a function of time.

Chemical and metallurgical processing methods have been developed to separate certain elements from the myriad of isotopes present in spent nuclear fuel [33]. While nuclear fuel reprocessing was first performed to recover uranium and plutonium [34], other processes have been developed to extract other elements of interest. Some recent initiatives have investigated the extraction of Americium and Curium from spent fuel [33, 35-40], and more specifically, from trivalent lanthanides [33, 41-46]. These developments are outlined below.

*UREX+ Process:*

Much of the work in actinide separations chemistry stems from motivations to reduce the heat output of nuclear waste planned for long-term storage [33, 41-43]. The U.S. Department of Energy's Advanced Fuel Cycle Initiatives are to "1) Reduce high-level waste volume, 2) Greatly reduce long-lived and highly radiotoxic elements, and 3) Reclaim valuable energy content of spent nuclear fuel" [47]. Efforts to develop the UREX+ (Uranium Recovery and Extraction) Process at Argonne National Laboratory (ANL) have yielded data regarding the feasibility of Am/Cm extraction from spent fuel using a Cyanex-301 extractant [41]. The ANL experiment found that, although the estimated Curium recovery rates were high, the cyanex extractant was too unstable and unsuitable for large scale reprocessing [41]. Since that time, however, more stable variants of an extractant called Cyanex have been developed and tested with some success [48]. The TALSPEAK process has also been explored as a possible replacement for the Cyanex treatment.

*TALSPEAK:*

The TALSPEAK (Trivalent Actinide Lanthanide Separation by Phosphorus Extractants and Aqueous Komplexes) process can be used to separate Pu, Np, Am, and Cm from the waste stream. However, the TALSPEAK process could be performed after Uranium, Plutonium, and Neptunium extraction to obtain an Americium/Curium mixture. While the TALSPEAK process has been proven to separate minor actinides from lanthanides, there remain impurities such as lanthanum, cerium, and europium [43].

*SETFICS:*

Developed for the reduction of thermal loading of spent fuels, Japanese research has been pursuing a process known as SETFICS in which light lanthanides are separated from minor actinides [35]. While significant amounts of the lanthanides are removed into the discharged raffinate, significant quantities of Cerium, Neodymium, Europium, Lanthanum, and Samarium remain present in the product due to their high initial abundance.

*SANEX:*

Recent developments in the SANEX (Selective Actinide Extraction) process using a genuine feed solution have resulted in decontamination factors, or ratio of the original quantity to the amount remaining after extraction, for Americium and Curium of 7000 and 1000, respectively [42]. This corresponds to >99.9% recovery of Americium and Curium and >99.9% rejection of lanthanides to the discharged raffinate [42]. Studies have also been performed analyzing the radiolysis of the SANEX extractant that have indicated that the extractant can be maintained during long term plant operation without interfering with the process [49].

After assessing the above Am/Cm recovery processes, a trend was observed within historical separation results. Europium and Samarium are common impurities in minor actinide products and radiolysis of the extractant is potentially problematic for large-scale actinide separations. Since an accurate model of the heat output as a function of time of an Americium and Curium mixture recovered by nuclear reprocessing is of interest, the

product resulting from a SANEX process is assumed. In the analysis presented, an estimation for the specific power of a separated mixture of americium and curium isotopes in its unaltered stoichiometry is determined from their respective masses present in spent nuclear fuel discharged from a light water reactor.

It was assumed that the fuel composition at manufacture was 4.3 weight percent  $^{235}\text{U}$  and 95.7 weight percent  $^{238}\text{U}$ . It was also assumed that the fuel had a burnup of 51 gigawatt-days/metric ton uranium (GWd/MTU) [50]. Based on the recent results of a SANEX demonstration by Magnusson et al [42], the final assumption that Am and Cm can be completely recovered from the waste and that any impurities present are negligible was made. This would not have been a valid assumption for other separation processes, such as SETFICS, as illustrated in Table 4.3. Even a small percentage recovery of the lanthanides and slight loss of actinides is significant due to the larger relative abundance of lanthanides over actinides. Furthermore,  $^{154}\text{Eu}$ ,  $^{155}\text{Eu}$ , and  $^{144}\text{Ce}$  are intense beta and gamma ray emitters. Contamination by these isotopes would increase the hard gamma activity and Bremsstrahlung yield of the product Am/Cm mixture. Thus, contamination by the lanthanides must be minimised in order to minimise shielding requirements. Based on these assumptions, Table 4.4 below gives the calculated masses of the americium and curium isotopes present in discharged fuel after it has been cooled in interim storage for a period of five years. Upon examination of the results in Table 4.4, another simplifying assumption can be made prior to the estimation of the specific thermal power of a processed mixture via the disregard of  $^{242}\text{Am}$ ,  $^{245}\text{Am}$ ,  $^{246}\text{Am}$ ,  $^{241}\text{Cm}$ ,  $^{250}\text{Cm}$ , and their daughter products due to their low concentrations in the recovered product. Lastly, while defining the decay

products, an isotope with a half-life  $\geq 24000$  years was considered to be stable and the isotopes of  $^{239}\text{Np}$  and  $^{242}\text{Am}$  were considered to decay in equilibrium with their parent nuclide due to their short half-life.

Element:	Initial Quantity: (g/MTIHM)	% Recovery SANEX [42]	% Recovery SETFICS [35]
La	1870	<0.01	1.2
Ce	3670	<0.01	0.89
Pr	1710	<0.01	2.3
Nd	6190	<0.01	1.4
Sm	1270	0.01	27
Eu	254	0.08	45
Gd	203	0.32	---
Am	638	103	64
Cm	78	107	61

**Table 4.3:** Americium and curium isotope masses present within light water reactor fuel per metric ton of irradiated heavy metal (MTIHM) after 5 years of interim storage following the discharge from a commercial reactor at a burn up of 51 GWd/MTU.

Isotope:	Mass: (g/MTIHM)
Am-241	$4.38 \times 10^2$
Am-242	$9.98 \times 10^{-6}$
Am-242m	$8.34 \times 10^{-1}$
Am-243	$1.99 \times 10^2$
Am-245	$6.75 \times 10^{-16}$
Am-246	$2.97 \times 10^{-21}$
Cm-241	$7.98 \times 10^{-21}$
Cm-242	$1.32 \times 10^{-2}$
Cm-243	$6.83 \times 10^{-1}$
Cm-244	$7.09 \times 10^1$
Cm-245	$5.72 \times 10^0$
Cm-246	$7.29 \times 10^{-1}$
Cm-247	$9.97 \times 10^{-3}$
Cm-248	$7.70 \times 10^{-4}$
Cm-250	$4.41 \times 10^{-12}$

**Table 4.4:** Americium and curium isotope masses present within light water reactor fuel per metric ton of irradiated heavy metal (MTIHM) after 5 years of interim storage following the discharge from a commercial reactor at a burn up of 51 GWd/MTU.

Having determined the concentrations of the separated isotopes of interest, their decay products were found. Each decay chain was projected until either a stable isotope was reached or until the isotope decayed to a radioactive isotope with a half-life of greater than or equal to  $2.4 \times 10^4$  years. Table 4.5 summarises the assumed decay chains. The mass of each isotope present in the initial separated product mixture or as a decay product was calculated as a function of time via decay chain projection. For each isotope, the residual post decay mass was summed with the mass inbred as a decay product from other isotopes at any given time of interest. A check-sum was performed for each time interval to ensure all mass was accounted for. Finally, the specific power and thermal contribution for each radioisotope was calculated for any given time after separation. A sample set of data is displayed in Table 4.5 for the decayed mixture at an age of 10 years after separation.

Isotope	Half Life (yr)	Decay Ratio	Isotope	Half Life (yr)	Decay Ratio	Isotope	Half Life (yr)	Decay Ratio	Isotope	Half Life (yr)	Decay Ratio	Isotope	Half Life (yr)
<sup>241</sup> Am	4.32×10 <sup>2</sup>	100%	<sup>237</sup> Np	2.14×10 <sup>6</sup>	---	---	---	---	---	---	---	---	---
<sup>242m</sup> Am	1.52×10 <sup>2</sup>	100%	<sup>242</sup> Am	1.83×10 <sup>-3</sup>	17%	<sup>242</sup> Pu	3.76×10 <sup>5</sup>	---	---	---	---	---	---
					83%	<sup>242</sup> Cm	4.46×10 <sup>-1</sup>	100%	<sup>238</sup> Pu	8.77×10 <sup>1</sup>	100%	<sup>234</sup> U	2.46×10 <sup>5</sup>
<sup>243</sup> Am	7.38×10 <sup>3</sup>	100%	<sup>239</sup> Np	6.44×10 <sup>-3</sup>	100%	<sup>239</sup> Pu	2.41×10 <sup>4</sup>	---	---	---	---	---	---
<sup>242</sup> Cm	4.46×10 <sup>-1</sup>	100%	<sup>238</sup> Pu	8.77×10 <sup>1</sup>	100%	<sup>234</sup> U	2.44×10 <sup>5</sup>	---	---	---	---	---	---
<sup>243</sup> Cm	2.85×10 <sup>1</sup>	0.1%	<sup>243</sup> Am	7.38×10 <sup>3</sup>	100%	<sup>239</sup> Np	6.44×10 <sup>-3</sup>	100%	<sup>239</sup> Pu	2.41×10 <sup>4</sup>	---	---	---
		99.9%	<sup>239</sup> Pu	2.41×10 <sup>4</sup>	---	---	---	---	---	---	---	---	---
<sup>244</sup> Cm	1.81×10 <sup>1</sup>	100%	<sup>240</sup> Pu	6.54×10 <sup>3</sup>	100%	<sup>236</sup> U	2.34×10 <sup>7</sup>	---	---	---	---	---	---
<sup>245</sup> Cm	8.50×10 <sup>3</sup>	100%	<sup>241</sup> Pu	1.41×10 <sup>1</sup>	100%	<sup>241</sup> Am	4.32×10 <sup>2</sup>	100%	<sup>237</sup> Np	2.14×10 <sup>6</sup>	---	---	---
<sup>246</sup> Cm	4.73×10 <sup>3</sup>	100%	<sup>242</sup> Pu	3.76×10 <sup>5</sup>	---	---	---	---	---	---	---	---	---
<sup>247</sup> Cm	1.56×10 <sup>7</sup>	---	---	---	---	---	---	---	---	---	---	---	---
<sup>248</sup> Cm	3.39×10 <sup>5</sup>	---	---	---	---	---	---	---	---	---	---	---	---

**Table 4.5:** The decay chains assumed for the constituent isotopes of the separated americium and curium product.

Isotope	Specific Power at 0.01 years after separation (W/g)	Mass in Mixture at 10 years after separation (g/MTIHM)	Heat Contribution at 10 years after separation (W/MTIHM)	Heat Contribution at 10 years (%)
<sup>234</sup> U	0*	7.19×10 <sup>-3</sup>	0*	0*
<sup>236</sup> U	0*	2.39×10 <sup>-2</sup>	0*	0*
<sup>238</sup> Pu	0.5577	5.97×10 <sup>-3</sup>	3.33×10 <sup>-3</sup>	1.76×10 <sup>-3</sup>
<sup>239</sup> Pu	0*	3.34×10 <sup>-1</sup>	0*	0*
<sup>240</sup> Pu	0.0070	2.25×10 <sup>1</sup>	1.58×10 <sup>-1</sup>	8.35×10 <sup>-2</sup>
<sup>241</sup> Pu	0.0032	2.88×10 <sup>-3</sup>	9.22×10 <sup>-6</sup>	0*
<sup>242</sup> Pu	0*	7.39×10 <sup>-3</sup>	0*	0*
<sup>237</sup> Np	0*	6.97×10 <sup>0</sup>	0*	0*
<sup>239</sup> Np	0 <sup>a</sup>	0.00×10 <sup>0</sup>	--- <sup>a</sup>	--- <sup>a</sup>
<sup>241</sup> Am	0.111	4.31×10 <sup>2</sup>	4.83×10 <sup>1</sup>	2.56×10 <sup>1</sup>
<sup>242m</sup> Am	0.0146	7.97×10 <sup>-1</sup>	1.16×10 <sup>-2</sup>	6.17×10 <sup>-3</sup>
<sup>243</sup> Am	0.0067	1.98×10 <sup>2</sup>	1.33×10 <sup>0</sup>	7.04×10 <sup>-1</sup>
<sup>242</sup> Cm	119.1	3.09×10 <sup>-2</sup>	3.64×10 <sup>0</sup>	1.93×10 <sup>0</sup>
<sup>243</sup> Cm	1.775	5.35×10 <sup>-1</sup>	9.50×10 <sup>-1</sup>	5.04×10 <sup>-1</sup>
<sup>244</sup> Cm	2.779	4.83×10 <sup>1</sup>	1.34×10 <sup>2</sup>	7.11×10 <sup>1</sup>
<sup>245</sup> Cm	0.0054	5.72×10 <sup>0</sup>	3.09×10 <sup>-2</sup>	1.64×10 <sup>-2</sup>
<sup>246</sup> Cm	0.0098	7.28×10 <sup>-1</sup>	7.13×10 <sup>-3</sup>	3.78×10 <sup>-3</sup>
<sup>247</sup> Cm	0*	9.97×10 <sup>-3</sup>	0*	0*
<sup>248</sup> Cm	0*	7.70×10 <sup>-4</sup>	0*	0*
<b>Total</b>			<b>1.88×10<sup>2</sup></b>	

**Table 4.6:** Specific powers of product isotopes and sample data for product mixture thermal properties at an age of 10 years after chemical separation.

\* Specific power assumed zero due to long half-life

<sup>a</sup> Assumed to decay in equilibrium with Am-241

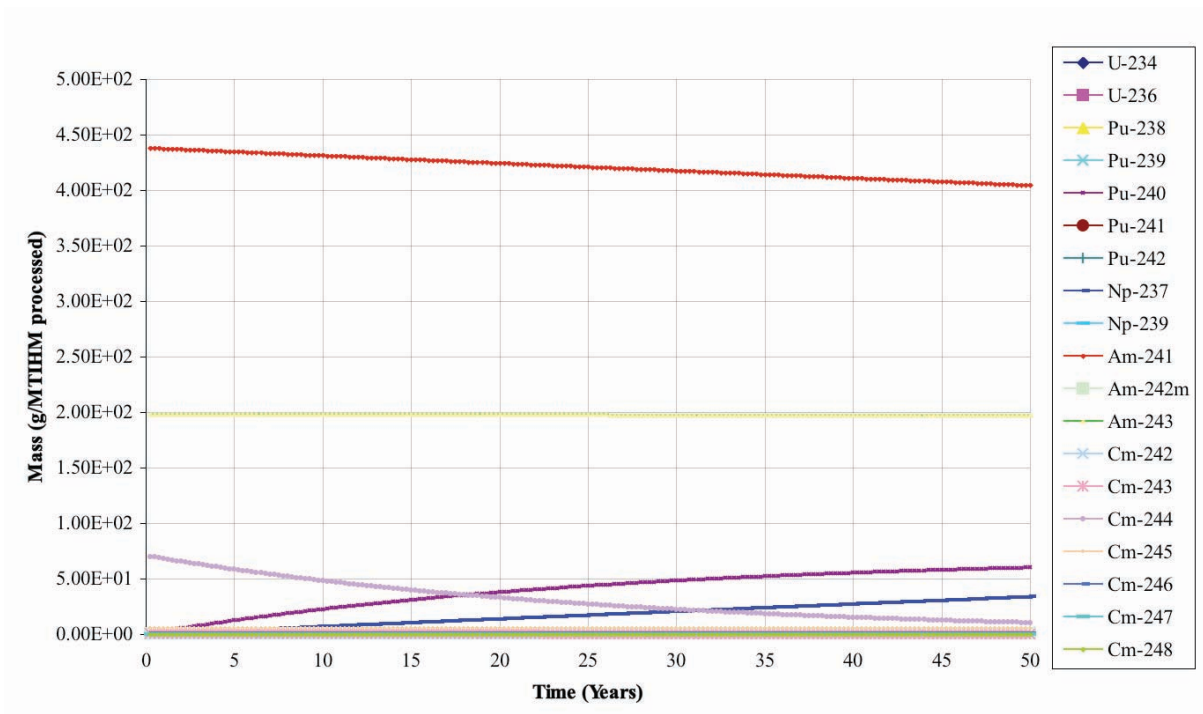


**Figure 4.13:** Mass of blend constituent isotopes per metric ton of irradiated heavy metal as a function of time after separation from irradiated fuel.

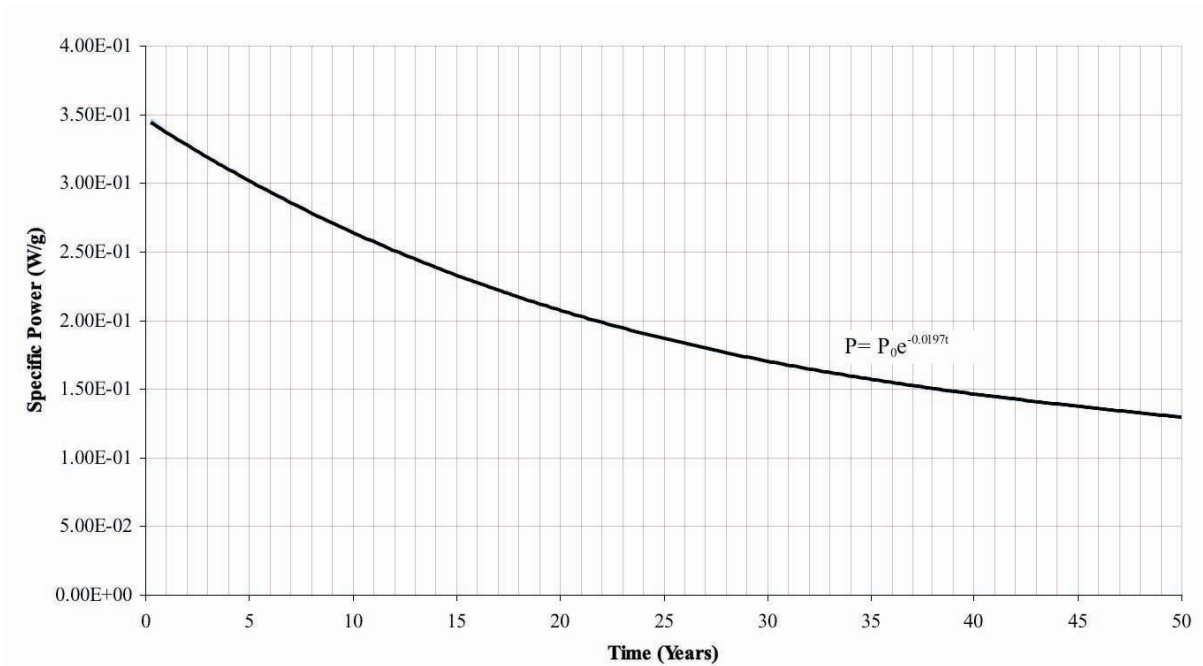


**Figure 4.14:** Specific thermal power in  $W_{th}/g$  as a function of time after separation from irradiated fuel. Data used to estimate the effective half-life for the blend as 35.23 years.

The results from this study indicate that a typical Am-Cm blend that can be derived from commercial power reactor fuel has a theoretical specific power of around  $0.35 \text{ W}_{\text{th}}/\text{g}$ . As illustrated in Figure 4.14, an estimate for the effective half-life of the blend can be made through the evaluation of the decay's specific thermal power. This effective half-life is approximately 35.23 years. Clearly, there are advantages of a blended source over a mono-isotopic heat source. In this case, the specific thermal power is enhanced over that over a pure  $^{241}\text{Am}$  source by the Cm isotope content in the blend. Here, the longevity of the Am isotopes and their decay products extends the effective lifetime of the blend. Also, a pure Cm source exhibits a neutron yield that is around one to two orders of magnitude greater than the commercial fuel derived blend. The neutron yield for the sesquioxide form of the blend was determined through the modelling of the system using the Sources 4C code [16] as a function of isotopic composition, as presented in Figure 4.13, with respect to time after production. The results from this modelling are illustrated in Figure 4.15.

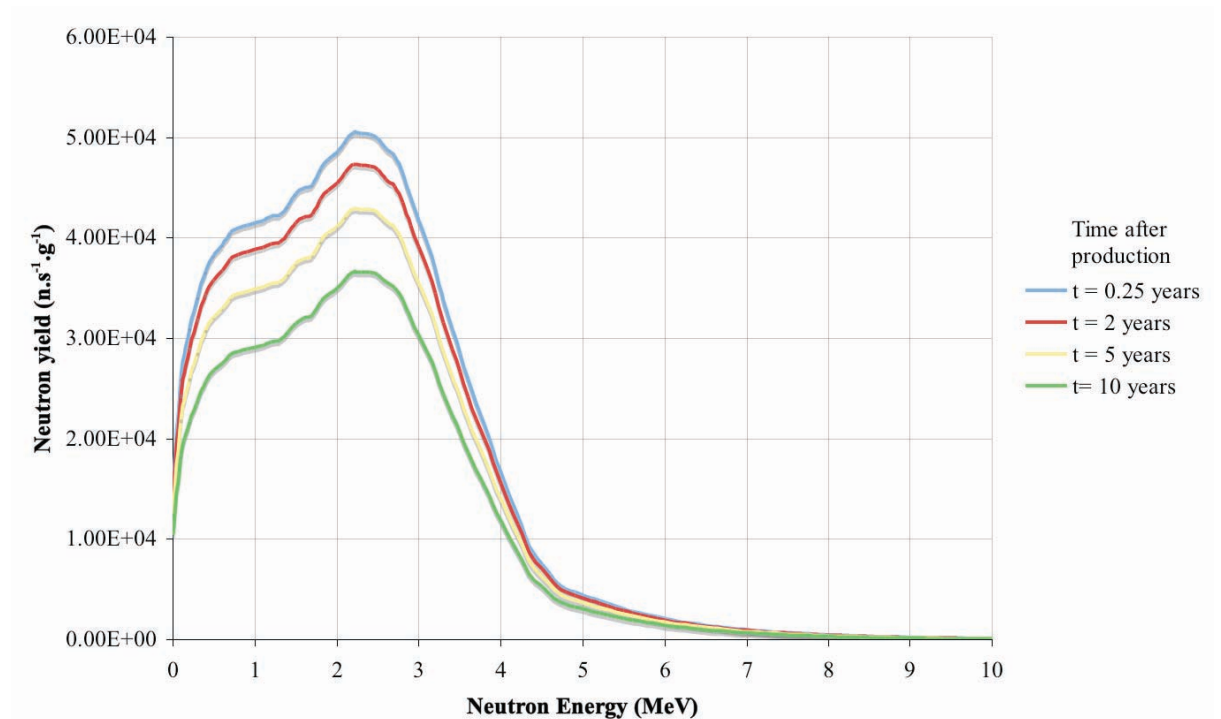


**Figure 4.15:** Neutron yield for the sesquioxide of the americium-curium blend as a function of neutron energy and time after separation from irradiated fuel and oxide production.

## 5.5 Summary of radioisotope heat source solutions

Although historical infrastructure dictated the use of  $^{238}\text{Pu}$  to be most economical for heat source production in the U.S and in Russia, the reduction of such infrastructure in recent years presents us with an opportunity to make careful consideration as to the most appropriate isotope of choice for space and terrestrial applications. For systems that are less susceptible to neutron radiation damage, it is undisputed that from mass and volumetric analyses, an unshielded  $^{238}\text{Pu}$  fuelled power source presents a reliable and well characterised solution. It has been demonstrated within this chapter however that alternative isotopes are suitable for use as heat source fuels, and the selection of some of these isotopes can provide a reduced mass solution when considering heat source total mass including appropriate shielding. It has also been determined that significant quantities of heat source materials can be obtained and used directly from reprocessed fuels discharged by the commercial power reactor fuel cycle as a blend of isotopes. Undoubtedly, the question of supply and quantitative availability of alternative isotopes must be answered before any practical decision can be made for their use under a specific program. From an economical point of view, the U.S. approach to a general-purpose heat source is highly advantageous. Such infrastructure and the capability of the respective program is however highly dependant upon the abundance of supply for a single isotope or specific blend of isotopes. If isotope production infrastructure is uneconomical or beyond the means of interested parties, isotopes such as  $^{241}\text{Am}$  and suitable blends of  $^{241}\text{Am}$  with  $^{242}\text{Cm}$  and  $^{244}\text{Cm}$  heat may be extracted from the commercial fuel cycles. In the form of a sesquioxide with a natural oxygen isotope composition, such blended isotopic compounds are expected to

have a specific thermal power of 0.318 W<sub>th</sub>/g which is closely comparable to that of the current limited stocks of <sup>238</sup>PuO<sub>2</sub> (0.345 W<sub>th</sub>/g [1]).

## 5.6 References

- [1] R.C. O'Brien, R.M. Ambrosi, N.P. Bannister, S.D. Howe, H.V. Atkinson, "Safe radioisotope thermoelectric generators and heat sources for space applications". *Journal of Nuclear Materials*. 377 (2008) 506-521.
- [2] Knolls Atomic Power Laboratory Inc., "*Chart of the Nuclides, 16th Edition*". Lockheed Martin; 2002.
- [3] R.C. Martin, J.B. Knauer, P.A. Balo. "Production, Distribution and Applications of Californium-252 Neutron Sources". *4th Topical Meeting on Industrial Radiation and Radioisotope Measurement Applications (IRRMA '99)*. Raleigh, NC; 1999.
- [4] F. Asaro, S.G. Thompson, I. Perlman, "The Alpha Spectra of Cm<sup>242</sup>, Cm<sup>243</sup>, and Cm<sup>244</sup>". *Phys. Rev.* 92 (3) (1953) 694-702.
- [5] Argonne National Laboratory Environmental Science Division (EVS). "*Curium Human Health Fact Sheet*". August 2005.
- [6] U.S. Department of Energy. "*Processes and characteristics of major isotopes handled at mound*". 1993.
- [7] P.E. Figgins. "*The Radiochemistry of Polonium*". *National Academy of Sciences National Research Council Nuclear Science Series*. 1961.
- [8] X-5 Monte Carlo Team. "*MCNP - a general Monte Carlo n-particle transport code, version 5*". *LA-UR-03-1987*. Los Alamos National Laboratories, Los Alamos, New Mexico. 2003.
- [9] V.P. Chechev, N.K. Kuzmenko, "*Table of Radionuclides*". Vol 2. Monographie Bureau International Des Poids et Mesures BIPM-5; 2004.
- [10] W. Gruhle, T.H. Bauer, T.H. Seligmann, H.H. Heckenbroich, "Evidence for boson-mode excitations in the <sup>16</sup>O(α,n) and <sup>20</sup>Ne(α,n) excitation functions ". *Z. Phys. A*. 262 (1973) 271-278.
- [11] V.A. Vukolov, F.E. Chukreev, "(A,N) reaction data on most important nuclei entered in composition of chemical reagents which used in nuclear fuel work process". *J,VAT/O,4,31,1983*. (1983).
- [12] T. Murata, K. Shibata. "*JENDL (alpha,n) Reaction Data File 2003*". *JENDL-AN*-. Japanese

Evaluated Nuclear Data Library, Japan Atomic Energy Agency. 2003.

[13] M. Stanley-Livingston, H.A. Bethe, *Rev. Mod. Phys.* 9 (1937) 245. DOI: [10.1103/RevModPhys.9.245](https://doi.org/10.1103/RevModPhys.9.245).

[14] R.M. Ambrosi, J.I.W. Watterson, B.R.K. Kala, "A Monte Carlo study of the effect of neutron scattering in a fast neutron radiography facility". *Nucl. Instrum. and Meth. B.* 139 (1998) 286.

[15] H. Matsunobu, T. Oku, S. Iijima, Y. Naito, F. Masukawa, R. Nakasima, "Data Book for Calculating Neutron Yields from (a, n) Reaction and Spontaneous Fission". *Japan Atomic Energy Research Institute JAERI*. 1324 (1992).

[16] W.B. Wilson, R.T. Perry, W.S. Charlton, T.A. Parish, E.F. Shores, "SOURCES-4C, Calculating Alpha, N, Fission, Delayed Neutron Sources and Spectra". *Radiat. Prot. Dosim.* 115 (14) (2005) 117.

[17] O.L. Kruger. "Process of making oxygen enriched plutonium dioxide (PuO<sub>2</sub>)". US patent 4,042,670.1977. August 16, 1977.

[18] D.L. Plymale, "The Exchange of Isotopically Enriched Oxygen with <sup>238</sup>PuO<sub>2</sub>". *J. Inorg. Nucl. Chem.* 30 (1968) 886.

[19] G.R. Grove, J.A. Powers, C.J. Kershner, T.A. Furtsch, R.H. Steinmeyer. "*Poodle Heat Source Development And Demonstration Test*". MLM-1261. Mound Laboratory, Maimisburg, OH. 1965.

[20] M. Zadra, F. Casari, A. Molinari, "Microstructure and Mechanical Properties of Nanostructured Aluminium Consolidated by SPS". *Mater. Sci. Forum.* 534-536 (2007) p.1401.

[21] Los Alamos National Laboratory. <http://mcnpx.lanl.gov>.

[22] H.G. Hughes, M.B. Chadwick, K.J. Adams. "MCNPX - The LAHET/MCNP code merger". Proceedings of: SARE-3 (Simulation of Accelerator Radiation Environments); 7th - 9th May, 1997; Tsukuba, Japan.

[23] E. Mainardi, F. Premuda, E. Lee, "Comparison and physical interpretation of MCNP and TART neutron and  $\gamma$  Monte Carlo shielding calculations for a heavy-ion ICF system". *Nuclear Instruments and Methods in Physics Research B.* 213 (2004) 182.

[24] R. Plukiene, D. Ridikas, "Modelling of HTRs with Monte Carlo: From a homogeneous to an exact heterogeneous core with microparticles". *Annals of Nuclear Energy.* 30 (2003) 1573.

[25] Yabuta, Naohiro. "Shielding analysis of high level waste water storage facilities using MCNP code". Proceedings of: 1st Symposium on Monte Carlo simulation; 10th - 11th September, 1998.

- [26] J. Damilakis, A. Tzedakis, L. Sideri, K. Perisinakis, I.E. Stamatelatos, N. Gourtsoyiannis, "Normalized conceptus doses for abdominal radiographic examinations calculated using a Monte Carlo technique". *Medical Physics*. 29 (2002) 2641.
- [27] International Atomic Energy Agency. "Evaluated Nuclear Data File (ENDF)". <http://www-nds.iaea.org/exfor/endl.htm>.
- [28] G.L. Bennett, J.J. Lombardo, R.J. Hemler, et al. "Mission of Daring: The General-Purpose Heat Source Radioisotope Thermoelectric Generator". Proceedings of: Fourth International Energy Conversion Engineering Conference and Exhibit (IECEC), 2006; San Diego, California. AIAA.
- [29] California Institute of Technology Jet Propulsion Lab (JPL). "*Cassini Program environmental impact study Volume 2: Alternate Mission and Power Supply*". JPL Publication No. D-11777. Cassini document No. 699-070-2. 1994.
- [30] J.E. Brau, O. Igonkina, C.T. Potter, N.B. Sinev, "Investigation of radiation damage effects in neutron irradiated CCD ". *Nucl. Instrum. and Meth. B Phys. Res. A*. 549 (2005).
- [31] United Kingdom Health and Safety Executive. "*Ionising Radiation Regulations 1999*". -(IRR99).
- [32] J.K. Shultis, R.E. Faw, "*Fundamentals of Nuclear Science and Engineering*". 2nd ed. CRC Press, Boca Raton, FL; 2008.
- [33] K.L. Nash, C. Madic, J.N. Mathur, J. Lacquerment. "Chapter 24 - Actinide Separation Science and Technology". *Chemistry of the Actinides and Transactinide Elements*. Springer: 2007: pp.2622 - 2798. ISBN: 1-4020-3598-5.
- [34] L.W. Gray. "From Separations to reconstitution - A short history of Plutonium in the US and Russia". Proceedings of: 217th National Meeting for the American Chemical Society Division of Industrial & Engineering Chemistry, Separations in Nuclear Chemistry Symposium; March, 1995; Anaheim, Ca.
- [35] Y. Koma, M. Watanabe, S. Nemoto, Y. Tanaka, "A Counter Current Experiment for the Separation of Trivalent Actinides and Lanthanides by the SETFICS Process". *Solvent Extraction and Ion Exchange*. 16 (1998) 1357-1367.
- [36] M. Nakahara, Y. Sano, Y. Koma, et al., "Separation of Actinide Elements By Solvent Extraction Using Centrifugal Contactors In The NEXT Process". *Journal of Nuclear Science and Technology*. 44 (2007) 373-381.
- [37] C. Madic, et al, "Recent Developments in the Development of Partitioning Processes of Minor Actinides from Nuclear Wastes obtained in the Frame of the Newpart European Programme (1996-1999)". *Progress in Nuclear Energy*. 40 (2002) 523-526.
- [38] D. Magnusson, et al. "Partitioning of Minor Actinides from PUREX Raffinate by the TODGA Process". Proceedings of: Global 2007, 2007; Boise, ID.

- [39] J.D. Law, et al. "*Flowsheet Testing of the Universal Solvent Extraction Process for the Simultaneous Separation of Cesium, Strontium, and the Actinides from Dissolved INEEL Calcine*". Idaho National Laboratory, Idaho Falls, ID. 2001.
- [40] B. Gannaz, et al, "Extraction of Lanthanides(III) and Am(III) by Mixtures of Malonamide and Dialkylphosphoric Acid". *Solvent Extraction and Ion Exchange*. 25 (2007) 313-337.
- [41] G.F. Vandegrift, M.C. Regalbuto, S. Aase, et al. "Designing and Demonstration of the UREX+ Process Using Spent Nuclear Fuel". *ATATLANTE 2004: Advances for Future Nuclear Fuel Cycles International Conference*. Nimes, France; 2004.
- [42] D. Magnusson, B. Christiansen, M.R.S. Foreman, et al., "Demonstration of a SANEX Process in Centrifugal Contractors using the CyMe4- BTBP molecule on a Genuine Feed Solution". *Solvent Extraction and Ion Exchange*. 27 (2009) 97-106.
- [43] M. Nilsson, K.L. Nash, "A Review of the Development and Operational Characteristics of the TALSPEAK Process". *Solvent Extraction and Ion Exchange*. 25 (2007) 665-701.
- [44] M. Ozawa, et al, "CMPO-TRUEX Process and its Applications in the Separation of Actinides from High-Level Liquid Wastes". *Mineral Processing and Extractive Metallurgical Review*. 21 (2000) 249-275.
- [45] D.R. Petermann, et al. "*Separation of Minor Actinides from Lanthanides by Dithiophosphinic Acid Extractants*". Idaho National Laboratory, Idaho Falls, ID. September 2008.
- [46] A. Geist, et al, "6,6'-Bis(5,5,8,8-tetramethyl-5,6,7,8-tetrahydrobenzo[1,2,4]triazin-3-yl) [2,2']bipyridine, an Effective Extracting Agent for the Separation of Americium(III) and Curium(III) from the Lanthanides". *Solvent Extraction and Ion Exchange*. 24 (2006) 463-483.
- [47] Science and Technology Office of Nuclear Energy. "*Advanced Fuel Cycle Initiative*". Sandia National Laboratory, NM. April 17th 2008.
- [48] M.S. Murali, J.N. Mathur, "Use of a Mixture of TRPO and TBO for the Partitioning of Actinides from High-Level Waste Solutions of PUREX Origin and its Comparison with CMPO and Other Phosphorous-Based Extractants". *Solvent Extraction and Ion Exchange*. 19 (2001) 61-77.
- [49] B. Bisel, et al. "DIAMEX-SANEX Solvent Behavior Under Continuous Degradation and Regeneration Operations". Proceedings of: Global 2007; September, 2007; Boise, ID.
- [50] S.J. Piet, Idaho National Laboratory, in private communication to author, 2008

# 5

## The encapsulation of radioisotopes and nuclear fuels within a tungsten matrix

### 5.1 Tungsten encapsulation of radioisotopic material

The encapsulation of radioisotope materials such as  $^{238}\text{PuO}_2$  and  $^{241}\text{AmO}_2$  in tungsten cermets offers many advantages for the production of radioisotope heat sources from both a radiological and thermo-mechanical standpoint [1]. The production of nuclear fuels for fission reactor systems based on W-UO<sub>2</sub> or W-UN cermets is also of particular interest for increased operational safety and security[2]. It has been estimated that a significant reduction in the  $\alpha$ -n neutron yield from  $\alpha$  emitting radionuclide compounds can be achieved through the production intimate mixing of such compounds with heavy inert materials such as tungsten. For  $^{241}\text{AmO}_2$  it has been estimated that a 65.9% reduction in the  $\alpha$ -n derived neutron yield for a source of given activity can be achieved by mixing its compound with tungsten (60% by volume) [1]. The advantages include the X-ray and gamma ray self-shielding properties of tungsten encapsulated sources [1]. An example is the significant the reduction (to 1% of the initial intensity) in the 59 keV gamma ray emissions from a  $^{241}\text{Am}$  source by a ~1 cm thick tungsten jacket. Such a source would require a ~15.5 cm thick aluminium jacket to achieve the same degree of attenuation. Monte Carlo modelling was used to determine the effect of source encapsulation in tungsten [1] (see chapter 4).

The thermal conductivity of the source material is highly important and can affect the efficiency of the thermoelectric generator. For tungsten this is  $174 \text{ W}\cdot\text{m}^{-1}\cdot\text{K}^{-1}$  at standard temperatures and conditions. Tungsten offers strength and ductility at typical post re-entry impact temperatures in excess of  $800 \text{ }^\circ\text{C}$  [3] due its ductile to brittle transition temperature of around  $350 \text{ }^\circ\text{C} - 480 \text{ }^\circ\text{C}$  [4], and its melting point at  $3422 \text{ }^\circ\text{C}$  could be sufficient to prevent the release of encapsulated materials at elevated temperatures such as those experienced during atmospheric re-entry. It may also be possible to remove the requirement of an external aeroshell for sources encapsulated in tungsten, thereby reducing the overall system volume, and potentially, the heat source mass. For example, a  $100 \text{ W}_{\text{th}}$  spherical  $\text{PuO}_2$  source encapsulated in 2 cm thick pyrolytic graphite aeroshell with a density of around  $3.5 \text{ g/cm}^3$  has a total mass of approximately 837 grams and a volume of around  $199 \text{ cm}^3$ . If the same  $100 \text{ W}_{\text{th}}$   $\text{PuO}_2$  source material is dispersed in a tungsten cermet encapsulate ( $50 \text{ \%}_{\text{vol}}$ ) as described by O'Brien et al [1, 5, 6] the total mass and volume of the encapsulated heat source would be 547 grams and  $35.6 \text{ cm}^3$  respectively. Tungsten is resistant to cutting and ensures that the radioisotope materials cannot be successfully extracted by unauthorized parties via pyrolytic processes.

## **5.2 Traditional sintering technologies**

Traditional powder metallurgical sintering techniques for the fabrication of encapsulating media can be divided into two categories; with applied pressure (hot pressing) and without pressure (pressureless sintering). Pressureless sintering is achieved at temperatures close to the melting temperature ( $T_m$ ) of the processed powdered metals and results in a product that has minimized density variations

throughout its structure. The resultant density of products sintered via pressureless sintering is determined by a combination of sintering temperature and processing time, which is typically of the order of several hours [7]. Hot pressing, otherwise known as sinter-forging, is a technique in which the powdered media is loaded into a die, which in turn is loaded into a heating chamber and pressure is applied to the die with a unidirectional ram [8]. Sinter-forging typically results in products with a higher density than those produced via pressureless sintering [7] but this densification is typically non-uniform throughout the sintered matrix and results from the friction between the walls of the die and the processed materials [8]. Forge sintering typically reduces the processing temperature depending on the material being processed, although this is still close to  $T_m$ . In addition the processing time is reduced by a factor of 10 over pressureless sintering [7].

Hot Isostatic pressing (HIP'ping) is a sintering technique that eliminates the need for rams, dies and external frictional forces. Here, the powdered materials to be processed are loaded into thin walled cans/envelopes that are shaped to the desired finished product and are made from materials that deform plastically at the processing conditions (temperature and pressure) [8]. During densification of the powdered materials, the volume occupied contracts. Since the envelopes/cans are under isostatic pressure during the sintering process, its volume contracts synchronously with the contained material (see Figure 5.1). Given that a photographic reduction in volume and shape can be achieved through HIP'ping, uniform densification and void removal can easily be achieved while producing net complex sintered product geometries. The typical processing temperatures for HIP'ping are material specific and are usually in excess of  $0.7 T_m$  [8].

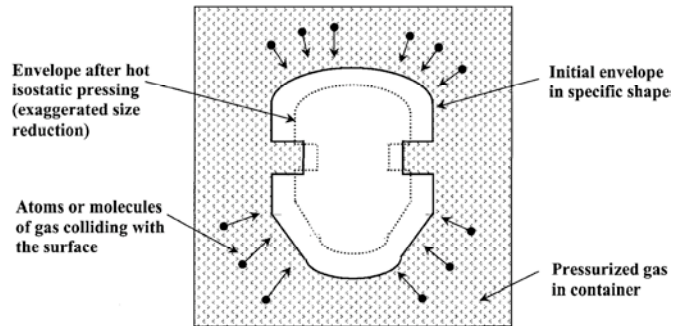


**Figure 5.1:** Illustration of the photographic reduction in shape of an encapsulating envelope and the processed powdered materials during Hot Isostatic Pressing (HIP'ping) [8].

### 5.3 Introduction and overview of the Spark Plasma Sintering process

The focus of this section is the encapsulation of radioisotopic materials such as plutonium dioxide or americium dioxide within a tungsten-based cermet using the spark plasma sintering (SPS) technique [1]. The fundamental rationale for examination and trial of the SPS process was that traditional sintering techniques (such as hot isostatic pressing or 'HIPping') required the materials to be processed at temperatures that were high enough to exceed the dissociation temperatures of the radioisotope oxides. The result would then be the modification of the fuel ceramic composition with the formation of partial bi-metallic regions within the product cermets such as those described in the fuel element development summary in the General Electric report on the development of the 710 High-Temperature Gas Reactor [9]. SPS is capable of processing materials at greatly reduced temperatures and processing times [10], while minimising the grain growth typically attributed to traditional techniques [8]. Grain growth is highly detrimental to the process of densification during sintering. It has been demonstrated in partially densified samples of urania produced by hot pressing that a larger number of pores occur on the faces of grains that have undergone grain growth and hence have a reduction in grain boundary contact area, whereas smaller grains

which have not undergone grain growth have pores concentrated at the grain corners [11]. The pores located in between the faces of grain boundaries have a greater degree of mobility than those pinned at the corners of grain boundaries [12] and hence in extreme cases the grain boundaries break away from the pores resulting in the encompassing of the interstitial pores between the grains [13]. In such instances, the densification process is effectively halted [13], thus it is most ideal to minimise grain growth during sintering in order to maximise the effectiveness of the densification process. In addition, large grains give rise to a reduction in overall material strength and hence grain growth should be avoided. For these reasons, SPS is highly suited to the production of high density cermets with temperature sensitive ceramics such as  $\text{UO}_2$ ,  $\text{PuO}_2$  and  $\text{AmO}_2$ .

In the SPS process, a powder mixture is heated by Joule heating which results from passing an electric current through the powder matrix requiring consolidation. This is effectively the same as conventional resistive heating with the exception that the temperature is varied during the process by the current pulse modulation. There are therefore two distinct operating temperatures for an SPS furnace; the average temperature, and a much higher temperature that is only reached during the flow of the current pulses. The average temperature is tuned to be lower than the melting point of the materials in the matrix. This therefore reduces or prevents the dissociation of the ceramic materials that are to be encapsulated within the cermet.

During each current discharge, metallic material is transported as a plasma by the propagation of sparks across the pores of the matrix (see Figure 5.2 – Left). When the current is switched off, the matrix undergoes rapid cooling resulting in the condensation of the metallic vapours in the regions where there is mechanical contact between powder grains [14]. This condensation produces necks that consolidate these joints (See Figure 5.2 – Right). The material transport in subsequent spark pulses increases due to the greater electric current density in the necks and contacts, when compared with the current density inside the body of each powder grain [15]. The rate of material transport is enhanced by the application of an external compressive force [16] resulting in the plastic deformation of the powder grains at each interface [8] and in a flatter joint with lower electrical resistance. This process propagates throughout the matrix and is enhanced by the external pressure which induces the plastic flow of material to form a sintered cermet with a density that is very close the full theoretical density. This process of propagation is similar to that exhibited in the consolidation of matrices by hot isostatic pressing [8].

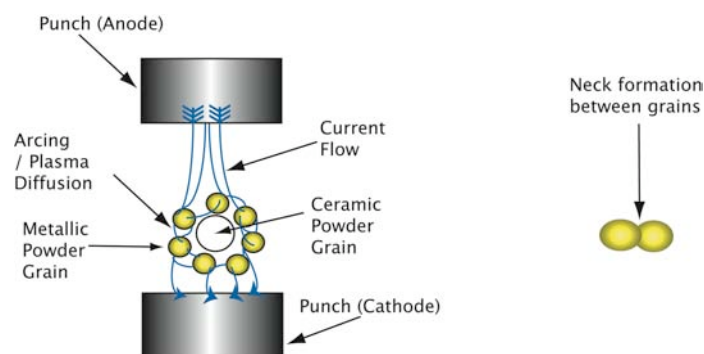


**Figure 5.2:** The principal of Spark Plasma Sintering (SPS). **(Left)** Illustration of the effect of the application of a current pulse to the powdered materials between the two electrode punches. Current discharge causes arcing between conductive grains resulting in rapid localised heating which in turn results in the formation and diffusion of plasma between the conductive grains. **(Right)** As the current pulse is terminated, the diffused plasma cools resulting in the formation of necks between the material grains.

The overall SPS setup consists of a conductive (graphite) die into which the powder mixture is formed, a press and a high power pulsed DC circuit (see Figure 5.3 *Top*). The filled cavity in the die is capped on the top and bottom with graphite punches that are free to move in the axial direction, facilitated by the use of a suitable high temperature lubricant, such as Grafoil® [17], to lubricate the side walls of the die (see Figure 5.4a). The die, punches and, ultimately, the powder mixture, form the completing components for the DC circuit (see Figure 5.3 – *Bottom*). The geometry of the die determines the radial geometry of the pressed and sintered cermet. The ceramic powder (isotopic compound) and tungsten metal powders are mixed to the specified volumetric ratio prior to loading into the graphite die. The die is then put under compression in between two electrodes in a hydraulic press [18] in order to compact the mixture. At this point a several kA current is passed through the material. The current pulse duration is of the order of several microseconds [14].

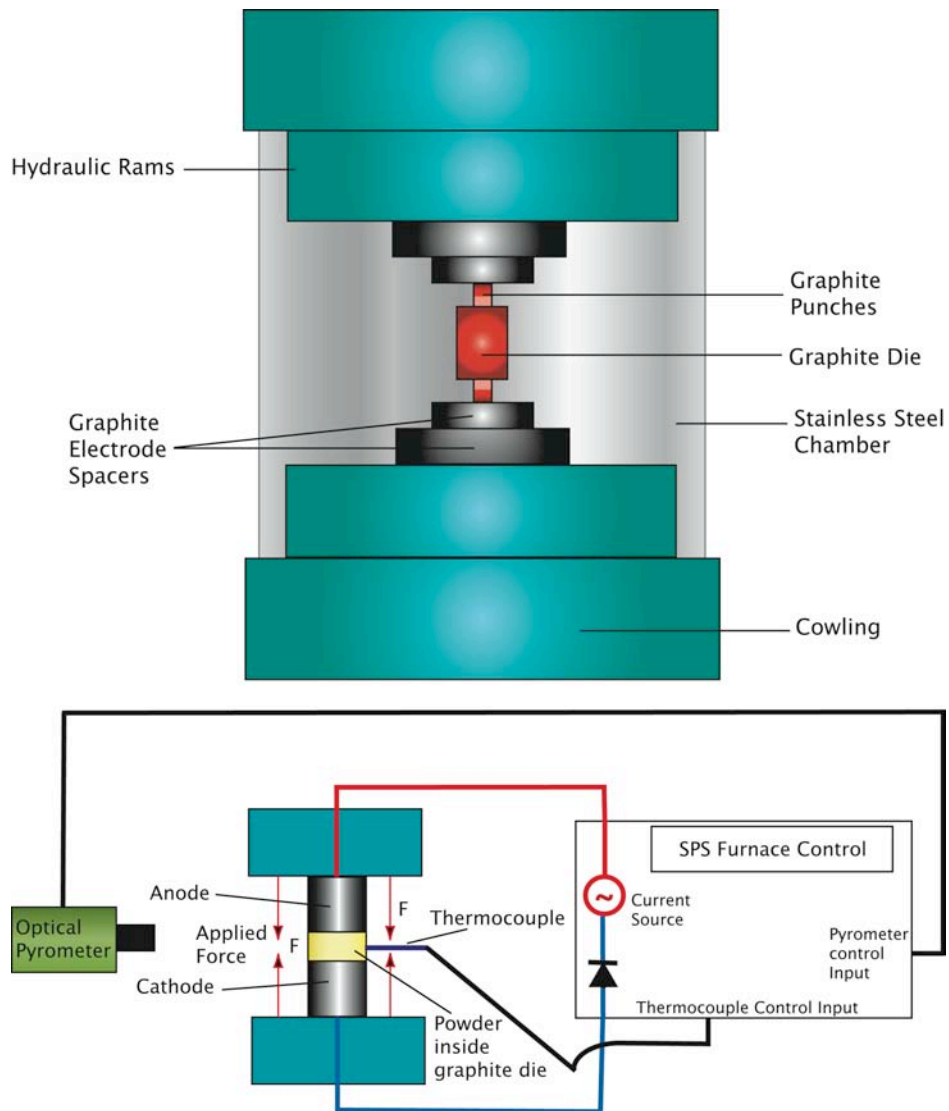


**Figure 5.3:** (TOP) Schematic of the spark plasma sintering furnace chamber containing an assembled graphite die and punches (manufactured by the user). (BOTTOM) Electrical schematic of the SPS furnace with associated temperature control electronics.

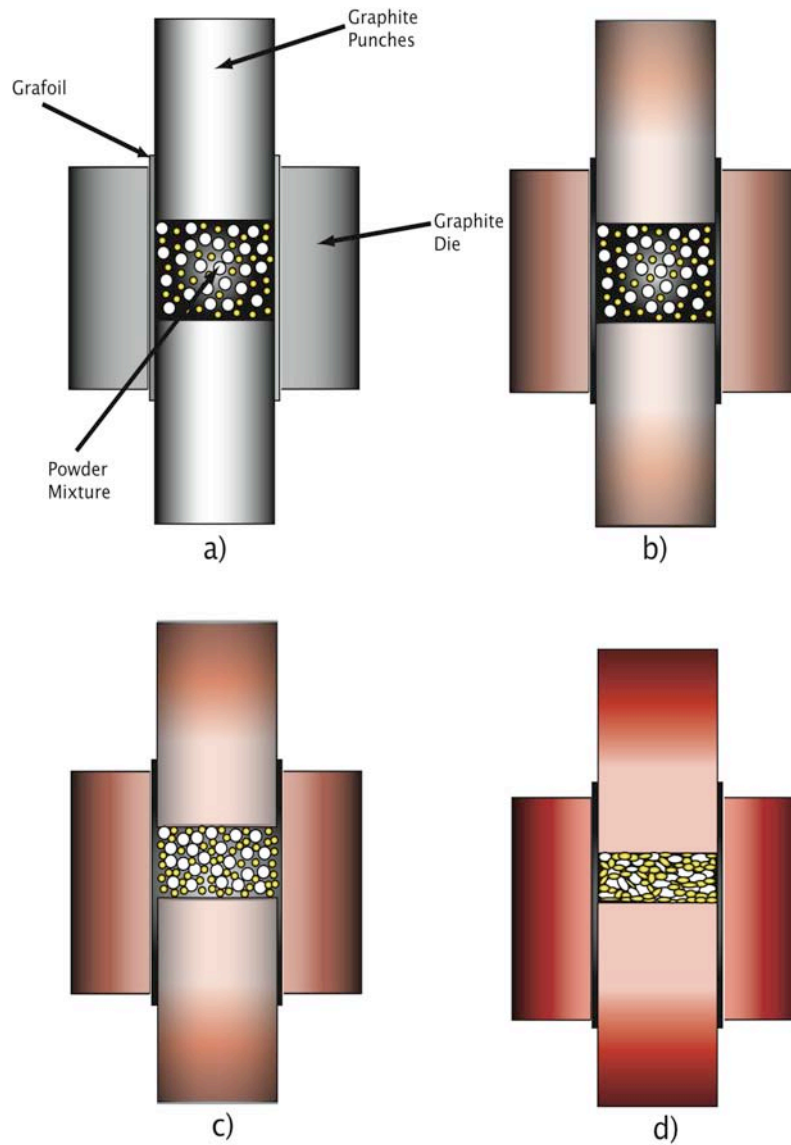


**Figure 5.4** **a)** Punches and die assembly lined with grafoil containing mixed  $\text{CeO}_2$  and Tungsten powder. **b)** The assembled die on loading into SPS furnace (see figure 2.1). Application of minimal pressure and initiation of heating results in small expansion of the materials. **c)** Application of pressure to the punches via the hydraulic rams of the SPS furnace facilitates initial densification by closing of voids. **d)** Neck formation and continued application of pressure achieves final densification of the bulk materials resulting in cermet production.

## 5.4 Experimental demonstration of SPS cermet fabrication

The production of tungsten-based cermets loaded with radioisotope simulants was performed by the author through the fabrication of CeO<sub>2</sub>-W cermets [6]. CeO<sub>2</sub> was selected as a simulant for radioisotope materials such as PuO<sub>2</sub>, AmO<sub>2</sub> and UO<sub>2</sub> since ceria has very similar kinetic properties to these three compounds, in particular the respective Gibbs free energies and approximate melting points. See Table 5.1 below. As such, the kinetic behaviour of the compounds exhibit similar reactivity with other materials. Most significantly, the materials are theoretically unreactive with a tungsten encapsulation matrix. The thermal diffusivities of CeO<sub>2</sub>, UO<sub>2</sub>, PuO<sub>2</sub>, and AmO<sub>2</sub> are also similar. The approximate thermal diffusivities of these compounds are of the order of  $2 \times 10^{-5} \text{cm}^2 \cdot \text{S}^{-1} \cdot \text{K}^{-1}$  [19]. As such, the migration of the surrogate material (CeO<sub>2</sub>) during the sintering process may be assumed to be approximately equal. Finally, it was assumed that the sintering mechanism for the radioisotope compounds and ceria is based upon a solid-state diffusion process at temperatures below their respective melting points. Although some densification of a surrogate cermet matrix may be attributed to the solid state sintering of the oxide compounds at temperature, the consolidation of the tungsten carrier matrix via the SPS mechanism was assumed to dominate.

Compound	Specific Heat Capacity at 298 °K (J/kmol)	$\Delta G_f$ at 298 °K (kJ/mol)	$\Delta H_f$ at 298 °K (kJ/mol)	Melting Point (°K)
CeO <sub>2</sub>	61.634	-1025.379	-1088.677	2600
PuO <sub>2</sub>	66.242	-999.040	-1055.832	2715
UO <sub>2</sub>	63.607	-1031.707	-1084.899	3115

**Table 5.1:** Thermo physical properties of CeO<sub>2</sub> in comparison to those of PuO<sub>2</sub> and UO<sub>2</sub>. For details and derivation of AmO<sub>2</sub> kinetic data, see chapter 6.

Preliminary measurements were made of the densities of tungsten-only SPS sinters produced with two different tungsten powder grain sizes. It was found that the maximum density of sinters made from tungsten powder with an average grain size of 10  $\mu\text{m}$  was 82.7% of the theoretical density of tungsten. For screened tungsten powder with a grain size of 3 – 6  $\mu\text{m}$ , the maximum sinter density measured was 93.6% of the theoretical density of tungsten. The preliminary experimental tests also revealed that these densities could be achieved from a hold time of 20 minutes at a maximum temperature of 1500  $^{\circ}\text{C}$ . It should therefore be noted that the sintering process can be achieved at 44% of the melting temperature of tungsten (tungsten m.p. is approximately 3400  $^{\circ}\text{C}$ ).

The  $\text{CeO}_2$  feedstock used in the tungsten-ceria cermet fabrication had an average grain size of 75  $\mu\text{m}$ . The 3 – 6  $\mu\text{m}$  tungsten particle size was selected in order to ensure that a high cermet theoretical density could be achieved. Since the tungsten used in these cermets was designed to encapsulate the ceria, the larger  $\text{CeO}_2$  powder size allowed the smaller grains of tungsten to fill the voids between the grains of  $\text{CeO}_2$ . Two mixture ratios of tungsten to ceria were used in these experiments for comparison. These ratios were 50 % W to 50 %  $\text{CeO}_2$  and 60% W to 40%  $\text{CeO}_2$  by volume. The dies for these experiments were designed to produce hexagonal sintered cermets with a side length of 11.7 mm and a cross sectional area of  $3.543 \times 10^{-4} \text{ m}^2$ . Each die was loaded with 14 grams of mixture, although gram quantities of material was frequently lost via leakage through the gaps in between the die and punches during the application of pressure after the assembled die was loaded into the SPS furnace. Minimisation of leakage into the furnace chamber was achieved by pre-pressing the filled die in a small hydraulic press.

Temperature control of the furnace is performed by an automatic programmable system that uses a signal input from either a thermocouple or an optical pyrometer. The calibrated range of operation for the furnace thermocouple is between 0 °C and 1200 °C. For this reason, temperature measurement during the production of tungsten-based cermets was performed using the optical pyrometer. The optical pyrometer had a calibration range between 570 °C and 2500 °C. In order to achieve repeatability in the production of the cermets, the automatic furnace controller was programmed to drive the temperature up to 600 °C by limiting the output current of the furnace driver such that 600 °C could not be exceeded during the ramp period. The values assigned to the output limits were derived through preliminary testing of the die and material compositions prior to the production trials presented in this chapter. Once a temperature of 600 °C was achieved, the output limits were removed and control was then governed by the signal from the optical pyrometer. The result of this method of temperature control was in the form of a stepped sintering profile as illustrated in Figure 5.5.

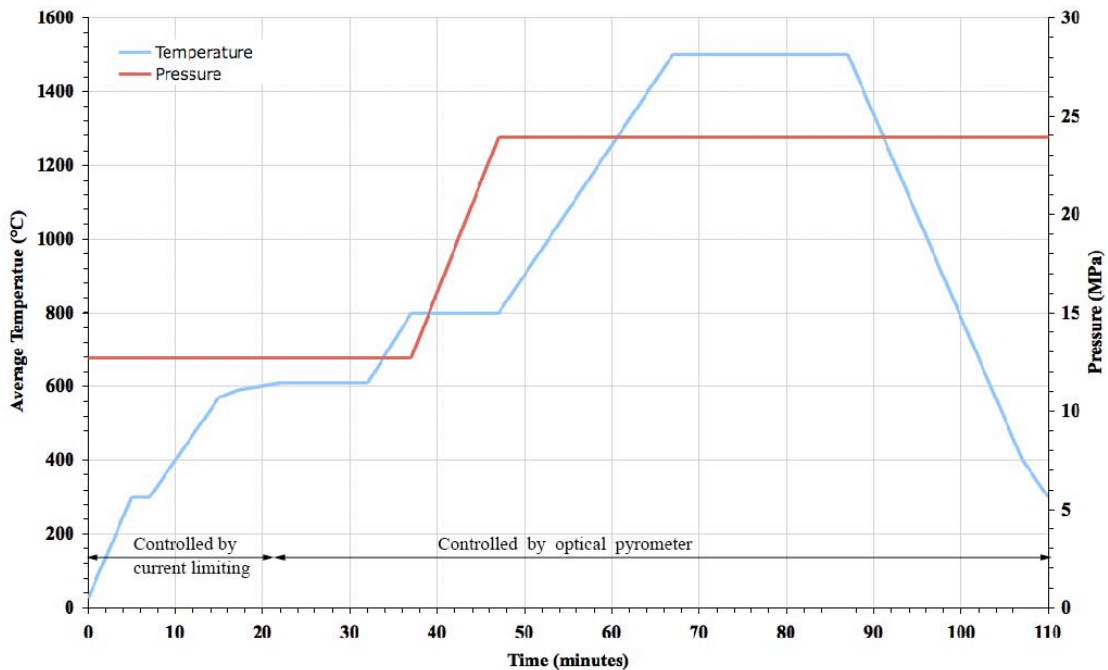


**Figure 5.5:** Sintering temperature-pressure profile for W-CeO<sub>2</sub> cermets produced by SPS.

A hold time of 10 minutes is shown at 800 °C in the sintering profile. At the beginning of the 10 minute hold, the pressure applied to the sample was increased from 12.7 MPa (the minimum installation pressure) to 23.9 MPa at a rate of + 1.12 MPa/minute. The pressure increment was performed during this period of equilibrated temperature in order to minimise the stresses on the cermet and die that could otherwise be caused by thermal expansion. This pressure increase facilitated further mechanical densification of the cermet and full pressure was applied until the end of the sintering profile.

The SPS current pulses used throughout this experimentation had a length of 12  $\mu$ s separated by a 2  $\mu$ s intermission. Peak values for the drive potential and current were typically around 4 V and 1.3 kA respectively.

A total of six tungsten-ceria cermets were manufactured during a controlled investigation. On removal of the cermets from the die, their mass and density was measured and recorded. These results were recorded in table 5.2 below.

Volume Tungsten (%)	Cermet Serial Number	Post Sinter Mass (g)	Measured Density (g/cm <sup>2</sup> )	Theoretical Density (g/cm <sup>2</sup> )	Average Percent Theoretical Density
50	ULCEW001	10.6	12.08	13.45	89.8%
	ULCEW002	9.6	12.19		
	ULCEW003	11.5	11.96		
60	ULCEW004	9.3	13.81	14.61	94.2%
	ULCEW005	10.7	13.78		
	ULCEW006	10.2	13.70		

**Table 5.2:** Cermet density and mass results.

In order to verify the elemental composition and hence mixture ratio of the cermets after sintering, the samples were cut and polished in preparation for examination by Scanning Electron Microscopy (SEM). The polishing process was achieved using a Struers TegraPol-21 polishing machine fitted with successfully fine grades of diamond polishing wheels. The early and intermediate stages of polishing were performed using 9  $\mu\text{m}$  and 3  $\mu\text{m}$  diamond suspensions respectively within a water based coolant/lubricant. The final stage of polishing was performed with a fine polishing cloth (Struers MD-CHEM) lubricated by a 0.04  $\mu\text{m}$  colloidal silica suspension with a pH of 9.8 (Struers OP-S). The SEM system used was the Siron model (XLFEF/SFEG) SEM with Energy Dispersive X-Ray (EDX) capability and was manufactured by the FEI Company. Figure 5.6 is an SEM image of cermet ULCEW004 indicating regions of  $\text{CeO}_2$  and tungsten. Figure 5.6 clearly shows the polycrystalline nature of the  $\text{CeO}_2$  particles. It would appear that some cracking of the individual  $\text{CeO}_2$  particles occurred during the application of high pressure to the mixture within the die. The voids created by this action were mostly filled by the 3-6  $\mu\text{m}$  tungsten particles. A small volumetric fraction remained unfilled, accounting for some of the deficit in full densification of the cermets.

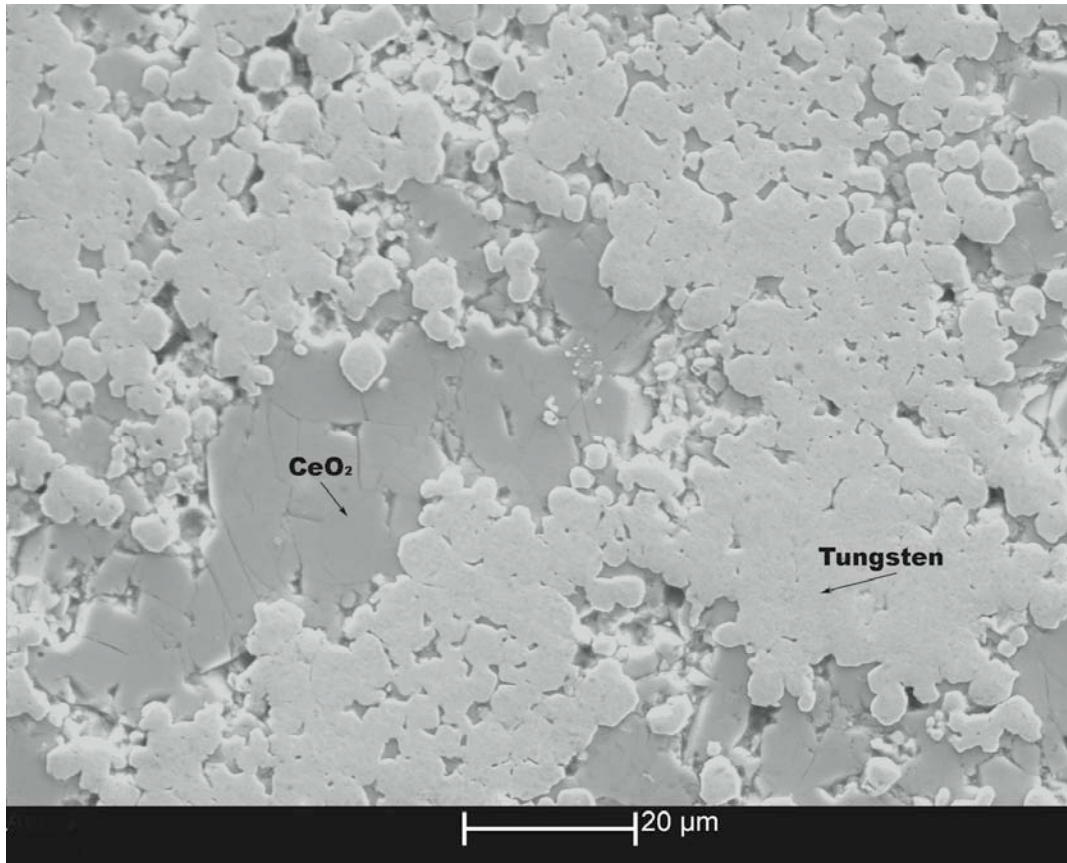


**Figure 5.6:** Scanning Electron Microscope (SEM) image of a tungsten-ceria cermet cross section (serial ULCEW004). The cermet in this image was composed of 40% CeO<sub>2</sub> and 60% W by volume. This volumetric ratio is evident proportion of the cross sectional area covered by each material.

The density measurements were plotted against percentage of tungsten by volume so as to estimate a relationship between these two parameters (see Figure 5.7). The results of P.A. Mataga [20] presented by R.M. German [13] indicate that for a heterogeneous mixture of ‘active’ and ‘inert’ sintering materials (where ‘active’ sintering materials are materials that sinter via neck formation such as the tungsten particles in the context of our research, and the ‘inert’ sintering materials are the ceramics that are to be encapsulated such as AmO<sub>2</sub>), the relationship between the fractional density of sintered cermets and the percentage volumetric composition of ‘active’ sintering materials increases exponentially towards a maximum (~ theoretical density) [13]. However, the data presented in this Chapter is only for the range 50 %<sub>Vol.</sub> – 60 %<sub>Vol.</sub> and lies in a portion of the Mataga curve [13, 20] where the data can

effectively be presented as linear even though the data points may overall be part of an exponential curve. If the assumption is made that the data is part of an exponential relationship, it can be estimated that the density of a cermet expressed as a percentage of its theoretical density can be represented by the function 5.1:

$$\rho(\%) \approx 70.6e^{0.0048[\%_{vol. W}]} \quad (5.1)$$

where  $[\%_{vol. W}]$  is the percentage of tungsten by volume that is mixed with the ceria for this specific combination of relative grain sizes over the range  $50 \% \leq [\%_{vol. W}] \leq 60 \%$ . Based on the results of P.A. Mataga [20] and in conjunction with the data presented, it is predicted that it may be possible to achieve very high densities, close to theoretical density, with a greater volumetric ratio of W to  $CeO_2$  when using the same feedstock morphology, although further experimental investigation is required to support this prediction and to verify the exponential relationship in greater resolution.

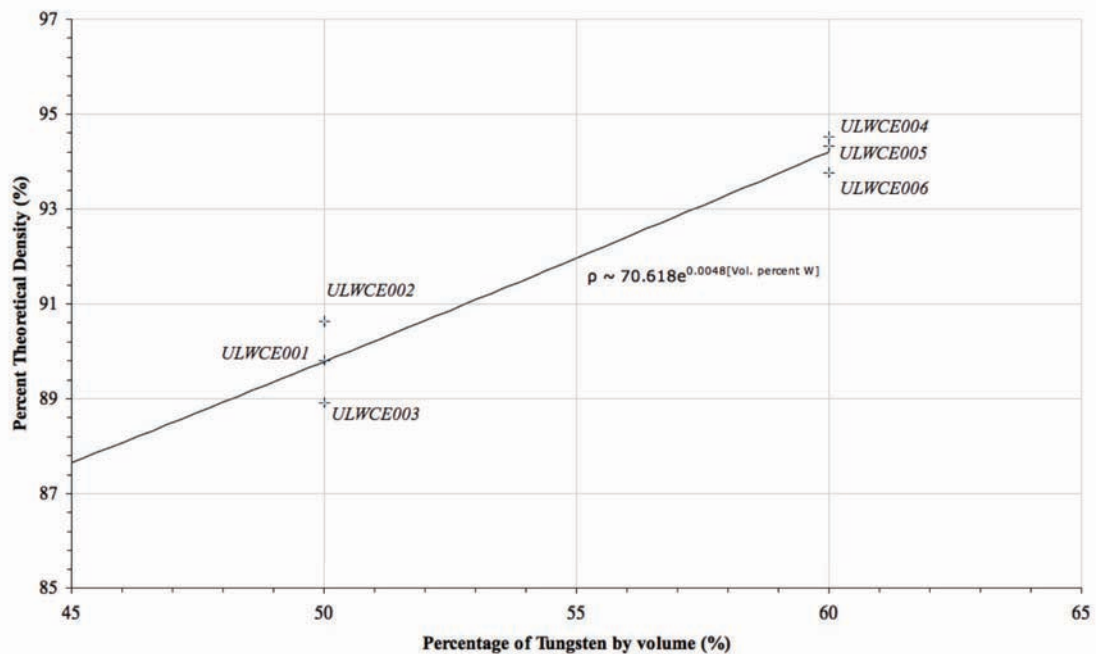


**Figure 5.7:** Preliminary estimation of the relationship between the densities of product cermets expressed as a percentage of their theoretical density plotted as a function of the volumetric concentration of tungsten in the mixture over the range:  $50 \% \leq [\%_{vol. W}] \leq 60 \%$ .

The differences in cermet mass measurements (Table 1) are primarily due to die leakage. Despite attempts to reduce the loss of material, the overall differences in the mass of each test product resulted in differing degrees of densification. Further analysis reveals that the die assemblies that lost the most mass of powdered material through leakage resulted in the highest recorded cermet densities. The variation in the densities of cermets produced from the same mixture ratios may be explained by assuming that the rate of densification per unit mass is a constant for any given die/furnace configuration. Thus, for a fixed sintering time period and die/furnace configuration, the average density of each sample is most fundamentally as a function of its initial mass or initial volume.

## **5.5 Encapsulation of oxide pellets and cermets within a metallic cladding via spark plasma sintering**

As outlined in chapter 3.4, traditional vented heat sources are required to prevent cladding weld failure at high temperatures. The elimination of the requirement for welding would increase the cladding yield pressure to its hoop strength, and could thus remove the requirement to vent a sealed heat source depending on the nature of its matrix.

Part of the work presented in this thesis focuses on the use of SPS as a method of cladding heat sources and ceramic (or metal oxide) pellets with tungsten or aluminium [5]. As a consequence of the positive results obtained with W and Al it is

assumed that the process could be applied to iridium alloys or high performance refractory alloys such as W-Re, W-Ta or ternaries of W-Re-Ta. The fabrication of these cladding materials via SPS in addition to their qualification for space applications will be the subject of future work. The variation in parameters including: sintering time, pressure and temperature, were found to affect the performance of the sintering process. The porosity of an encapsulation cladding could be tailored to control thermal conductivity and act as a homogenous venting frit to reduce internal pressures, the evaluation of this requires further work. The SPS process produces a high-density structure conforming to the shape of the die without the need for further machining. This minimises the number of production stages and increases the safety case for adopting encapsulation methods that potentially reduce risks to radiation workers.

The first stage of SPS encapsulation involves the production of the heat source oxide pellet or cermet. In order to demonstrate this by SPS, powdered ceria with an average grain size of 150-200  $\mu\text{m}$  was sintered to 94% of its theoretical density using the SPS process alone. This demonstrates that grain size reduction (by ball milling or other milling methods) is not required to achieve high densities with SPS. Ball milling, used in the production of  $^{238}\text{Pu}$  heat sources, has been identified as a source of sub micron fine particles that have posed health risks to radiation workers and contamination problems at the Los Alamos facility (See Section 3.1).

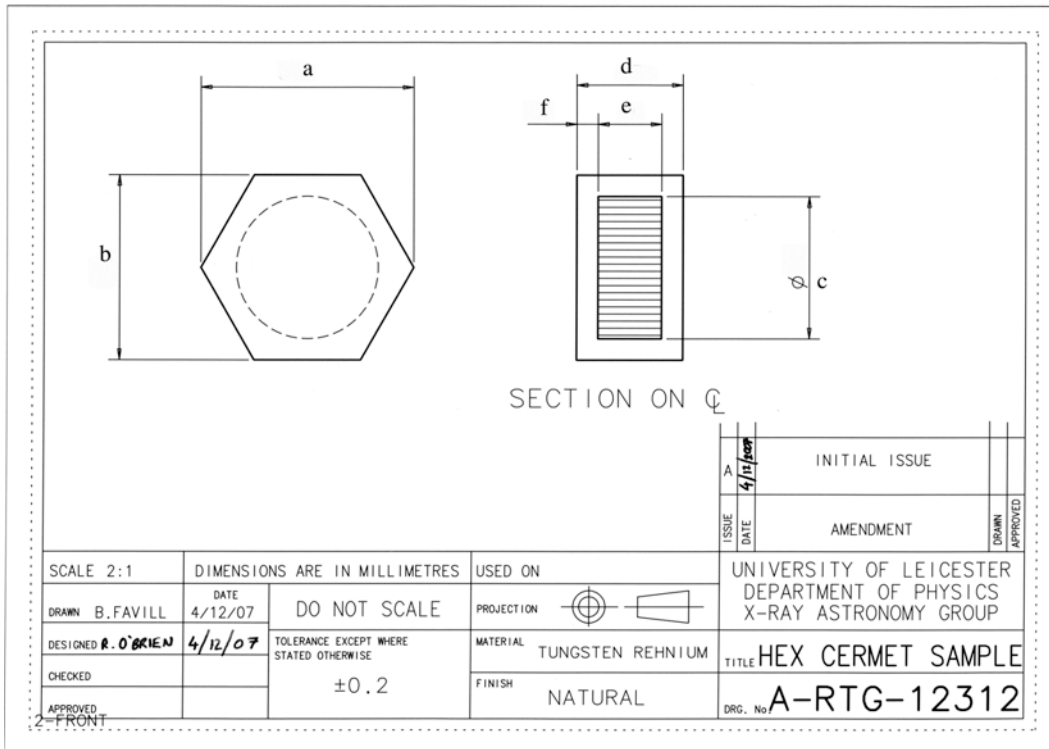


**Figure 5.8:** Schematic design of a tungsten-rhenium clad radioisotope cermet heat source.

Once the heat source pellet or cermet has been produced, the second stage involves placing powdered cladding material around the pellet in a larger die. The resultant product is of net shape equal to that of the larger die. A schematic of the arrangement is presented in Figure 5.8. The cladding material and pellet are sintered at a temperature, pressure and over a time period which will minimise any negative impact upon the integrity of the isotopic fuel pellet and result in the desired material properties for the cladding. Figure 5.9 below illustrates the capability of porosity design and process repeatability.

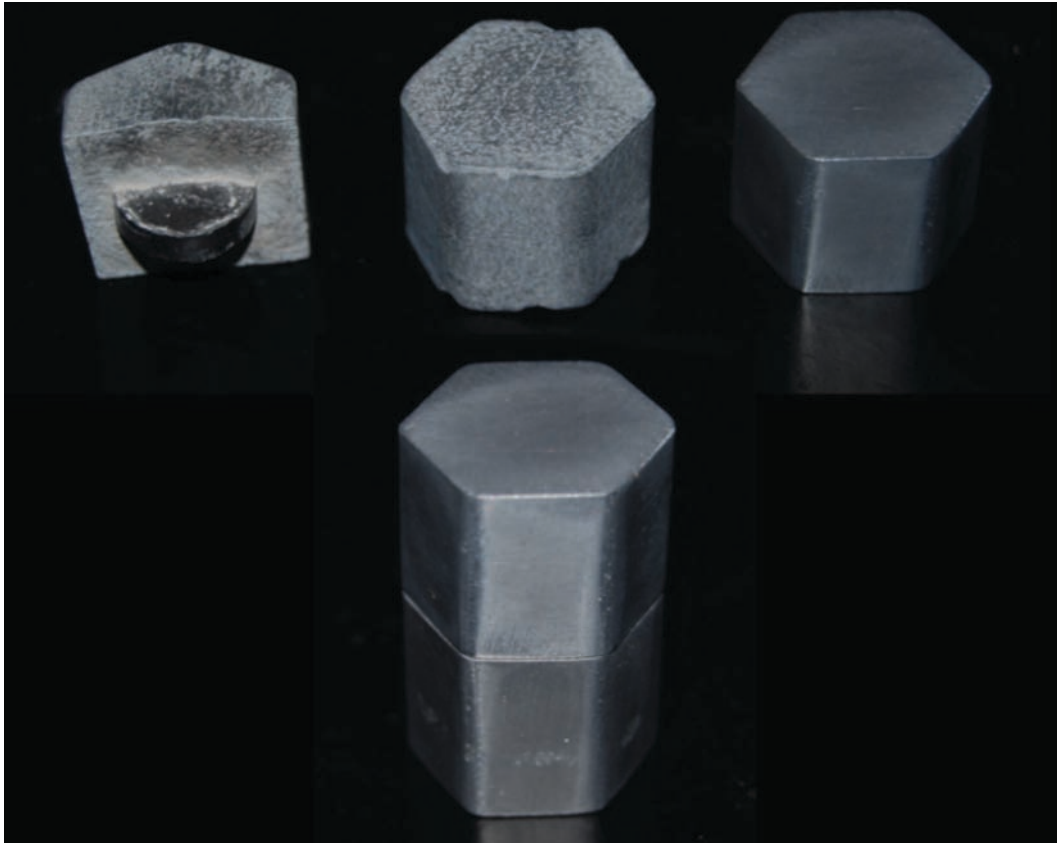


**Figure 5.9:** Encapsulated ceria pellets. Successive degrees of densification are shown from back left to right while the repeatability of the process is demonstrated by the stacked encapsulates at the front.

## 5.6 Tungsten alloy clad GPHS architecture

Under the assumption that a tungsten alloy cladding matrix may eliminate the need for an external aeroshell for atmospheric re-entry protection [5, 6], the benefits of tungsten matrix heat source production featuring the same external geometry as the Step-2 GPHS module design was investigated. The volume and mass of the production module based on FWPF was estimated to be 1.6 kg and 540.25 cm<sup>3</sup> respectively which yields a specific power of 156.25 W/kg and a volumetric power density of 0.463 W/cm<sup>3</sup>. A module is considered that has a 5mm to 1 cm thick tungsten alloy cladding around a <sup>238</sup>PuO<sub>2</sub>-W cermet (50% volume plutonium oxide). Based on the results of the cermet production experiments described above, the module properties including

specific thermal power and volumetric power density were estimated and presented in table 4.3.2 below. A figure of merit was determined from the product of the ratios of clad module to FWPF module volumetric power density and clad module to FWPF module specific thermal power.

Tungsten clad thickness (cm)	0.5	1
External Geometry (cm)	9.96 x 9.32 x 5.82	9.96 x 9.32 x 5.82
Cermet Mass at 94 % theoretical density (kg)	5.186	3.213
Total module mass (kg)	8.460	8.960
Module thermal Power	950.27	588.64
Module Specific Power (W/kg)	112.32	65.69
Module Volumetric Power Density (W/cm <sup>3</sup> )	1.759	1.090
Figure of Merit	2.73	0.99

**Table 5.3:** Tungsten Alloy GPHS Module performance for modules with 5mm and 1 cm thick tungsten alloy claddings.

The results in Table 5.3 indicate that where volumetric constraints are of concern, the move towards a tungsten alloy architecture over fine weave pierced fabric would certainly be advantageous. A module with a 5 mm thick cladding would yield a volumetric power density of 3.8 times that of the FWPF Step-2 module. If the required wall thickness were closer to 1 cm, the volumetric power density would be 2.4 times that of the FWPF module.

Clearly, the use of a dense cladding over the low density FWPF matrix presents a decrement in the specific power of a module. However, by considering a figure of merit that accounts for the overall performance of the system in terms of increments in volumetric power density and the specific power of the module, the adaptation overall shows a positive increase in performance for claddings that are less than 1 cm thick.

## **5.7 Fabrication of high temperature NTP fuels by spark plasma sintering.**

It has previously been proposed by the author that radioisotopic materials could be encapsulated within a tungsten-based cermet using the Spark Plasma Sintering (SPS) technique [1, 25]. The fundamental rationale for the trial of SPS processing for these materials was that traditional sintering techniques such as Hot Pressing requires refractory materials to be processed at high temperatures that would exceed the dissociation temperatures for the radioisotope oxides. The result would then be the formation of complete or partial non-cermet (metallic) regions such as those indicated within the fuel element development summary in the General Electric report on the development of the 710 High-Temperature Gas Reactor [9]. Given that Spark Plasma Sintering is capable of processing materials at greatly reduced temperatures[10] while minimizing the grain growth typically attributed to traditional sintering techniques [8], SPS is highly suited to the production of cermets that contain temperature sensitive ceramics such as  $\text{PuO}_2$  and  $\text{UO}_2$ . This therefore reduces or prevents the dissociation of the ceramic materials that are to be encapsulated within the cermet.

Experimental research conducted by the author at the Center for Space Nuclear Research (CSNR) at Idaho National Laboratory (INL) has demonstrated the capability of SPS to encapsulate simulated nuclear fuels within tungsten cermets. The cermets produced within this research were initially encapsulated in a tungsten jacket via a two-step SPS process. The encapsulated cermets formed segments of the product fuel elements. The segments were joined by diffusion bonding, achieved again via SPS, in order to produce the finished fuel elements. The die used for diffusion bonding of the element segments is shown in Figure 5.13.



**Figure 5.13:** SPS bonding die designed and used by the author to join encapsulates and fuel cermets via diffusion bonding enhanced by SPS.

The external geometries of the demonstration fuel elements were scaled to those of the NERVA NTR fuel elements (see Figure 5.14, left for comparison). The length of the fuel element that can be fabricated is driven most fundamentally by the length of the SPS furnace and the maximum electrical power output of the SPS power supply. Successful bonding is achieved very rapidly over a period of 20 minutes at 1500 °C.

Later development of the fuel element die design facilitated the provision of propellant flow channels within the product cermet fuel elements during sintering by the addition of “mandrel pins” in the desired geometric pattern and corresponding recesses into the bottom and top punches of the SPS die. A procedure was therefore established in which the entire cermet and cladding could be sintered in a single step process. This process also included the provision of a cladding on the inside surfaces of the flow channel by pouring the respective cladding and cermet mixtures into selected regions of the die prior to the removal of paper dividers. Thus, the final product was sintered under identical conditions as outlined previously while delivering a fuel element with integral flow channels in a single step.

Verification of the encapsulation was performed by x-ray diffraction and SEM imaging with electron induced x-ray fluorescence capabilities for tungsten-encapsulated cermets loaded with CeO<sub>2</sub> as an analogue for UO<sub>2</sub>. CeO<sub>2</sub> was again selected as the analogue for these compounds due to their similar kinetic properties, melting temperatures and Gibbs free energies.

The resultant product cermet densities were found to be in excess of 94 % theoretical density for processing temperatures of 0.44 T<sub>m</sub> for tungsten, and the porosity of the cermet matrix was tunable by adjustment of processing time in conjunction with the tungsten volumetric ratio and particle size used, allowing for the compensation for radiogenic gas production to be built into cermet design. Figure 5 clearly shows the polycrystalline nature of the CeO<sub>2</sub> particles. It would appear that some cracking of the individual CeO<sub>2</sub> particles occurred during the application of high pressure to the mixture within the die. The voids created by this action were mostly filled by the tungsten particles, although a small volumetric fraction remained unfilled, accounting for some of the deficit in full densification of the cermets. Further enhancement of densification could be achieved by the minimization of shearing and cracking of the ceramic materials during the application of pressure. Future investigations will examine the production of, and the advantages of using spherical ceramic particles over granular ceramics. It is anticipated that spherical particles will be capable of resisting shear from the surrounding tungsten particles.

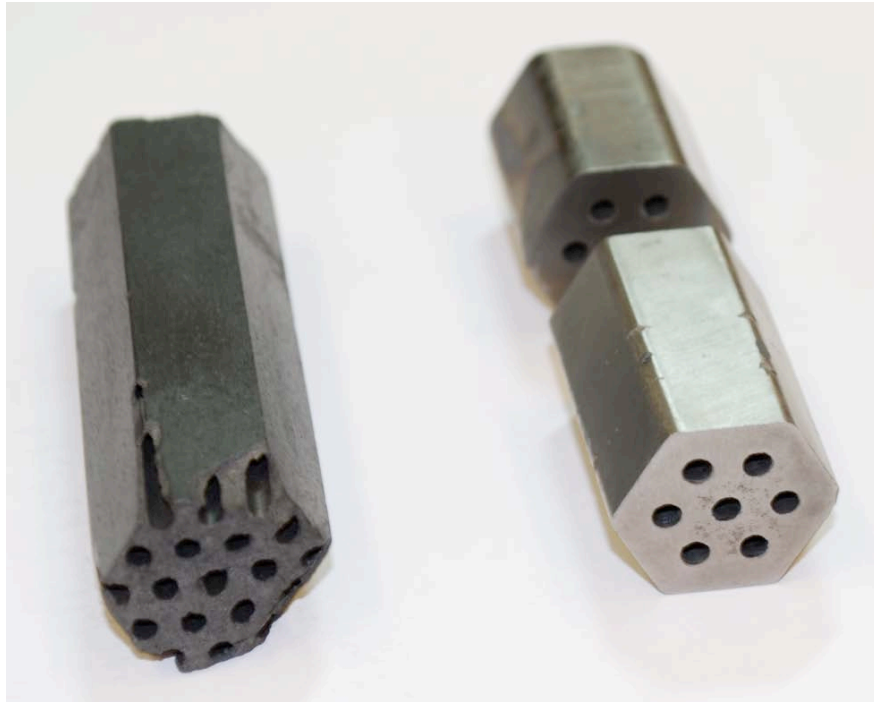


**Figure 5.14:** *(Left)* section of a NERVA graphite matrix Nuclear Thermal Propulsion reactor fuel element, Note susceptibility to cracking. Present for element comparison purposes. *(Right)* An example SRC/CSNR Tungsten alloy encapsulated cermet reactor fuel element.

It should be noted that since the SPS process results in net shape sintered elements, no post sinter machining is required. Thus, Figure 5.14 (Right) illustrates the product elements that can be achieved via single step encapsulation and single step bonding using the SPS process. This capability is most advantageous for batch production of fuel elements since work exposure can be minimised and process losses are greatly reduced when compared to traditional machine cutting and extrusion of geometries.

## 5.8 Conclusions and future work

The Spark Plasma Sintering process has been demonstrated to be compatible with the production of cermets consisting of simulated ceramic radioisotope materials and tungsten. This work has shown that for applications where it may be necessary to control the porosity of cermets, the volumetric ratio of tungsten used in the cermets can be used to tune this porosity. Further investigation into the combined effect of volumetric ratios and grain size could reveal an accurate method for tuning the porosity of cermets and will be the focus of future work. Sub micrometer tungsten powder is of interest for use in cermet fabrication since it is believed that the smaller powder size will significantly enhance void filling between the ceramic grains and hence increase the density of the cermet for any given mixture [30].

Attention to radiogenic gas production must be given to both radioisotope heat source and nuclear fuels encapsulation. As outlined in chapter 3.4, significantly high pressures of helium gas may be attained by large volume sealed radioisotope sources. It is believed that the microencapsulation of isotope compounds within a tungsten matrix may allow sources to be completely sealed, thus retention of radiogenic gases may be achieved in micron sized interstitials of the cermet. Further evaluation of gas retention within cermet systems will be performed in future studies.

Given that the leakage of gram quantities of powdered material from the dies was observed during pressing, consideration must be given to the minimization or elimination of furnace contamination if radioisotope materials are used. For this reason, operation of an SPS furnace for sintering radioisotope materials should be performed in

an isolated environment such as in a glove box or hot cell. Although pre-pressing of the die assemblies throughout the tests performed minimised material leakage in the furnace, further investigation of the advantages of using binders and alternative die designs to facilitate the SPS process is necessary. Such die designs may eliminate the requirement of pre-pressing prior to the insertion of an assembled die into the furnace.

Further enhancement of densification could be achieved by minimising the shearing and cracking of the ceramic materials during the application of pressure. Future investigations will examine the production of, and the advantages of using spherical ceramic particles over granular ceramics. It is anticipated that spherical particles will be capable of resisting shear caused by the surrounding tungsten particles.

The design of fuel elements for Nuclear Thermal Rocket reactor systems involves an optimisation and trade between effective reactivity of the fuels (effective cross section) and heat transfer from the fuel particles to the propellant via a given matrix. Each prismatic fuel element produced for the Rover and NERVA NTR engines featured 19 flow channels that were driven to higher length to diameter ratios (approximately 500:1) so as to maximise heat transfer to the propellant through a trade between contact time (propellant core residence time) and the system critical diameter.

Work performed by the author has identified processing techniques that will allow for the fabrication of tungsten matrix fuel elements that feature helical flow channels that run at varying pitch angles. Further discussion of these techniques and practical demonstration of element fabrication will be the topic of future publications. Figure 5.15 below represents the design that may be achieved via the process.

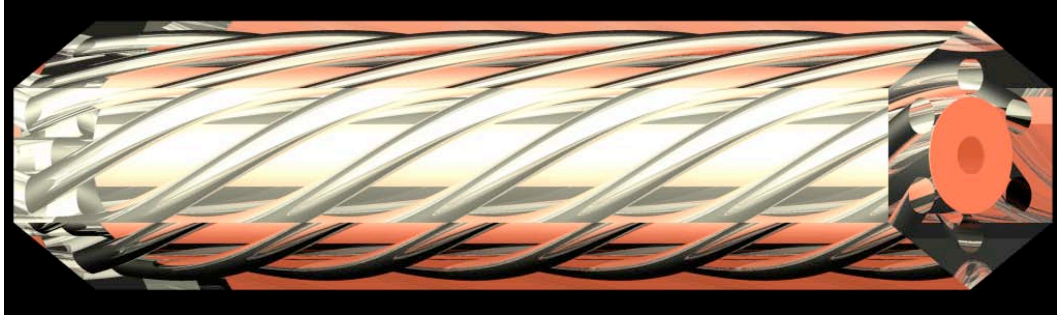


**Figure 5.15:** Example of a fuel element design containing twisted coolant or propellant flow channels

Where the circumference of a helix is equal to the product of its radius of curvature and  $2\pi$ , the path length of a helix, is given by Equation 5.2. Given this, it is possible to estimate the increase in path length for any given helical design relative to a straight flow channel as presented in Equation 5.16.

$$L_H = N\sqrt{(2\pi r)^2 + p^2} \quad (5.2)$$

**Equation 5.2:** The path length of a helical channel where N is the total number of revolutions in a given axial distance, r is the radius of curvature and p is the helical pitch. Pitch is defined as the axial separation between one complete revolution in the helical path.

$$L_\delta = \frac{N\sqrt{(2\pi r)^2 + p^2}}{pN} \quad (5.3)$$

**Equation 5.3:** The length gain factor for a helical path relative to a straight section flow channel.

As an example, a helical channel with a radius of 5 mm and pitch of 20 mm has a path length of 37.2 mm/revolution, which is a factor ( $L_\delta$ ) of 1.862 times the length of the equivalent straight section channel (20 mm). Clearly, such increases in path length results in a greater residence time for a propellant within the reactor core. Equally, it is anticipated that the length to diameter ratio of an NTR core can be reduced by a factor of  $L_\delta$  while transferring the same energy per unit time as for the longer straight flow path. Such modification to the standard core design may result in a

radially reflected core that is more neutronically efficient. The efficiency increment may be predicted since the core must increase in radius for the helical design core with a given critical mass since a greater void fraction exists within the bulk of any given fuel element, and hence an increase in mean free paths is experienced by fission neutrons throughout the core, resulting in a greater fission probability per neutron generation, or greater potential  $k_{\text{eff}}$ . Further coupled multi-physics modelling of the helical system is anticipated by the author and will be the subject of future publications.

Overall, the work presented in this chapter demonstrates the capability and suitability of the SPS process for the production of radioisotope encapsulates for nuclear fuels and other applications where the mechanical capture of radioisotope materials is required. A testing program that is beyond the scope of this work has been proposed to determine the resistance to high temperature plasma such as experienced by atmospheric re-entry conditions and exposure to explosive overpressures as may be experienced by launch vehicle malfunction. In addition to mechanical testing, the thermo-physical properties of encapsulation matrices, such as thermal conductivity and ductile to brittle transition temperatures (DBTT) shall be evaluated for encapsulate claddings of controlled porosity. Most fundamentally, the composition of an encapsulating alloy will be controlled to yield a DBTT below the typical impact temperature for a given heat source design. The encapsulate performance shall be benchmarked against existing thermal and impact protection materials such as Fine Weave Pierced Fabric. The results from the proposed studies will be the subject of future publications.

At the time of writing, the author, in collaboration with colleagues at the Center for Space Nuclear Research, Idaho National Laboratory and NASA Marshall Space Flight Center, is preparing for an experimental evaluation of the characteristics and estimated lifetime of NTR fuels that are fabricated via SPS when operated within a hot hydrogen environment. Both pure tungsten and tungsten-rhenium alloy matrices will be fabricated and tested. The findings of these experiments will be the subject of a series of future papers.

## 5.10 References

- [1] R.C. O'Brien, R.M. Ambrosi, N.P. Bannister, S.D. Howe, H.V. Atkinson, "Safe radioisotope thermoelectric generators and heat sources for space applications". *Journal of Nuclear Materials*. 377 (2008) 506-521.
- [2] R.C. O'Brien, R.M. Ambrosi, S.D. Howe, N.P. Bannister, H.V. Atkinson. "Fabrication of prismatic fuel elements for space power and nuclear thermal propulsion reactors by spark plasma sintering". Proceedings of: Nuclear and Emerging Technologies for Space (NETS-2009), Paper Number 206153; June 14-19, 2009; Atlanta, GA.
- [3] A. Schock. "*Design Evolution and verification of the General-Purpose Heat Source*". Fairchild Space and Electronics Company, Germantown, Maryland. 1983.
- [4] Y. Zhang, A.V. Ganeev, J.T. Wang, J.Q. Liu, I.V. Alexandrov, "Observations on the ductile-to-brittle transition in ultrafine-grained tungsten of commercial purity". *Materials Science and Engineering A*. 503 (2009) 37-40.
- [5] R.C. O'Brien, R.M. Ambrosi, S.D. Howe, N.P. Bannister, H.V. Atkinson. "Production of safe radioisotope heat sources by Spark Plasma Sintering". Proceedings of: Nuclear and Emerging Technologies for Space (NETS-2009), Paper Number 206155; June 14-19, 2009; Atlanta, GA.
- [6] R.C. O'Brien, R.M. Ambrosi, N.P. Bannister, S.D. Howe, H.V. Atkinson, "Spark Plasma Sintering of simulated radioisotope materials in tungsten cermets". *Journal of Nuclear Materials*. 393 (2009) 108-113. DOI: [10.1016/j.jnucmat.2009.05.012](https://doi.org/10.1016/j.jnucmat.2009.05.012).
- [7] A.J.A. Winnubst, Y.J. He, P.M.V. Bakker, R.J.M. Olde Scholtenhuis, A.J. Burggraaf. "Sinter Forging as a Tool for Improving the Microstructure and Mechanical Properties of Zirconia Toughened Alumina". In: Badwal S.P.S., M.J. Bannister, R.H.J. Hannink, eds. *Science and Technology of Zirconia V*. Technomic Publishing Company, Inc.; Lancaster, PA.: 1993: pp.284-291. ISBN: 1-56676-073-9.

- [8] H. V. Atkinson, S. Davies, "Fundamental aspects of Hot Isostatic Pressing: An Overview". *Metallurgical and Materials Transactions A*. 31 (2000) 2981-3000.
- [9] General Electric. "710 high-temperature gas reactor program summary report. Volume III. Fuel Element development". General Electric. 1968. Pages: 146. GEMP-600 (Vol.3);.
- [10] X. Wang, Y. Xie, H. Guo, O. Van der Biest, J. Vleugels, "Sintering of WC-Co powder with nanocrystalline WC by spark plasma sintering". *Rare Metals*. 25 (2006) 246-252.
- [11] A. Xu, A.A. Solomon. "The Effects of Grain Growth on the Intergranular Porosity Distribution in Hot Pressed and Swelled UO<sub>2</sub>". Proceedings of: Ceramic Microstructures '86; July 28-31, 1986; University of California, Berkely, CA. Plenum Press, ISBN: 0306426811.
- [12] F.M.A. Carpay. "The Effect of Pore Drag on Ceramic Microstructures". Proceedings of: Ceramic Microstructures '76. Westview Press, Boulder CO, 1977, pp. 171-178, ISBN: 0891583076.
- [13] R.M. German, "*Sintering Theory And Practice*". John Wiley & Sons Inc., New York; 1996. ISBN: 0-471-05786-X.
- [14] M. Rosinski, E. Fortuna, A. Michalski, Z. Pakiela, K. J. Kurzydowski, "W/Cu composites produced by pulse plasma sintering technique (PPS)". *Fusion Engineering and Design*. 82 (2007) 2621-2626.
- [15] N.I. Kuskova, S.I. Tkachenko, "Radial Distributions of Rapidly Varying Currents and Fields in a Cylindrical Conductor". *Technical Physics Letters*. 28 (2002) 604-605.
- [16] J. Zhang, L. Wang, W. Jiang, L. Chen, "Effect of TiC content on the microstructure and properties of Ti<sub>3</sub>SiC<sub>2</sub>-TiC composites in situ fabricated by spark plasma sintering". *Materials Science and Engineering: A*. 487 (2008) 137-143.
- [17] "*Grafoil Flexible graphite*". GrafTech International, Cleveland, OH.
- [18] C-C. Jia, H. Tang, X-Z. Mei, F-Z. Yin, X-H. Qu, "Spark plasma sintering on nanometer scale WC-Co powder". *Materials Letters*. 59 (2005) 2566-2569.
- [19] Center for Information and Numerical Data Analysis and Synthesis (CINDAS), "Thermo Physical Materials Database (TPMD)". (2010).
- [20] P.A. Mataga. "Retardation of Sintering in Heterogeneous Powder Compacts". In: Handwerker C.A., J.E. Blendell, W.A. Kaysser, eds. *Sintering of Advanced Ceramics*. American Ceramic Society; Westerville, OH: 1990: pp.689-709. ISBN: 0944904203.
- [21] "*A safety evaluation of SNAP reactor systems*". Report of the Committee on the Nuclear Space Program. Atomic Industrial Forum Inc. 1968.

- [22] R.J. Hanrahan Jr, R.L. Smith III, J. Morgan. "Review of the historical capabilities and testing of composite and cermet fuels in Los Alamos". LA-UR-02-7186. Los Alamos National Laboratory, Los Alamos, NM. 2002.
- [23] D.A. Seifert, R.L. Stuart, P.K. Conn, H.W. McLaughlin, G.J. Luersen. "Fission product behavior within two W-UO<sub>2</sub> cermet fuel elements irradiated in a temperature gradient". Nuclear Space Programs Space Systems. General Electric, Cincinnati, Ohio. 1968.
- [24] S.D. Howe, R.C. O'Brien, N. Barra, et al. "Returning humans to the moon: comparison of chemical engine and nuclear rocket performance as an earth departure stage". Proceedings of: 2007 Space Nuclear Conference; June 24-28, 2007. American Nuclear Society, ISBN: 0-89448-053-7.
- [25] D.E. Burkes, D.M. Daniel, J.E. Werner, S.D. Howe. "An Overview of Current and Past W-UO<sub>2</sub> CERMET Fuel Fabrication Technology". Proceedings of: 2007 Space Nuclear Conference, 2007; Boston, MA.
- [26] P.D. Takkunen. "Fabrication of cermets of uranium nitride and tungsten or molybdenum from mixed powders and from coated powders". NASA Technical Note D-5136. NASA Lewis Research Center, Cleveland, OH. 1969.
- [27] S.D. Howe, R.C. O'Brien. "Nuclear Thermal Rockets: History, Benefits and Issues Impacting Future Operations". Proceedings of: 57th Joint Army-Navy-NASA-Air Force (JANNAF) Propulsion Meeting, 2010; Colorado Springs, CO.
- [28] L.W. Connell, L.C. Trost. "Reentry Safety for the Topaz II Space Reactor: Issues and Analyses". SAND94-0484. Sandia National Laboratories, Albuquerque, NM. 1994.
- [29] X-5 Monte Carlo Team. "MCNP - a general Monte Carlo n-particle transport code, version 5". LA-UR-03-1987. Los Alamos National Laboratories, Los Alamos, New Mexico. 2003.
- [30] T. Nishimura, M. Mitomo, H. Hirotsuru, M. Kawahara, "Fabrication of silicon nitride nano-ceramics by spark plasma sintering". *Journal of Materials Science Letters*. 14 (1995) 1046-1047.

# 6

## Experimental encapsulation of americium oxides in tungsten

The experimental work described in this chapter focussed on the demonstration of the encapsulation of americium oxides in a tungsten carrier matrix at temperatures applicable to SPS processing. AmO<sub>2</sub> powder was examined with scanning electron microscopy (SEM) and X-ray diffraction (XRD) analysis to verify its composition and characterize its morphology. Finally pressed pellets of AmO<sub>2</sub> and two compositions of W-AmO<sub>2</sub> blends were simultaneously sintered and analysed via differential scanning calorimetry (DSC) and XRD.

The encapsulation of radioisotope materials, specifically <sup>241</sup>Americium oxides, in tungsten cermets is of particular interest for the production of radioisotope heat sources for thermal management and radioisotope power systems [1]. The desire to encapsulate americium oxides in a tungsten-based cermet and encapsulate is clearly beneficial in addressing the issues of security and launch safety. Chapter 4 describes the potential that americium oxide could be encapsulated in a tungsten-based cermet using the spark plasma sintering (SPS) technique [1]. Chapter 5 describes how the SPS process could be applied to the production of tungsten encapsulated nuclear fuels for space and terrestrial reactors [2, 3].

## 6.1 Calculation of the AmO<sub>2</sub> Gibbs free energies and the W/Am oxide Ellingham diagram.

The Gibbs free energy  $G$  is a thermodynamic property attributed to any chemical element or compound at a specific temperature  $T$  or pressure  $P$  [4].  $\Delta G$  may be described as the maximum work that may be obtained from a chemical system [4]. Such work may be associated with the reduction of other compounds. Compounds whose Gibbs free energies are less than those of other species, i.e. more negative, may be described as energetically preferential over the other species within a potential reaction [4]. The magnitudes of the Gibbs free energies for elements and compounds may be represented diagrammatically as a function of temperature on a diagram termed the Ellingham diagram. Where two compounds are initially present within a mixture, the compositions of the two reagents may change with the addition of sufficient energy into the system if  $\Delta G$  is initially negative, resulting in the formation of alternative products. The intersections of Gibbs free energy values for the reagents and products at a given temperature indicate the onset of such reactions. This may again be illustrated on an Ellingham diagram. Thus, the Ellingham diagram may be used to determine if, and at what temperature a given mixture will react to form alternative products.

The Gibbs free energy for AmO<sub>2</sub> was calculated from the thermodynamic data in Table 6.1 by substitution of the appropriate values into Equation 6.1 below for temperatures between 298 K and 2000 K. The derived values for  $\Delta G(T)$  were plotted on the Ellingham diagram illustrated in Figure 6.1. The  $\Delta G(T)$  values for Am<sub>2</sub>O<sub>3</sub>, a potential product of AmO<sub>2</sub> reduction are plotted in addition to the temperature dependant energies of common tungsten oxide compounds as derived from data published by Barin [5].

$$\Delta G_r(T) = \Delta_r H_m^\circ(T_0) + \left( \int_{T_0}^T \Delta_r C_{p,m}^\circ dT \right) - T \left( \Delta_r S_m^\circ(T_0) + \left\{ \int_{T_0}^T \frac{\Delta_r C_{p,m}^\circ}{T} dT \right\} \right) \quad (6.1)$$

**Equation 6.1:** Determination of the Gibbs free energy of a compound.

$\Delta_r G_m^\circ(298K)$	Molar Gibbs free energy	=	-874.492 kJ.mol <sup>-1</sup>
$\Delta_r S_m^\circ(298K)$	Molar Entropy	=	-193.552 J.K <sup>-1</sup> .mol <sup>-1</sup>
$\Delta_r H_m^\circ(298K)$	Molar Enthalpy	=	-932.2 kJ.mol <sup>-1</sup>
$\Delta_r C_{p,m}^\circ$	Molar Specific Heat Capacity	=	18.758 J.K <sup>-1</sup> .mol <sup>-1</sup>

**Table 6.1:** Thermodynamic data for AmO<sub>2</sub> [6]

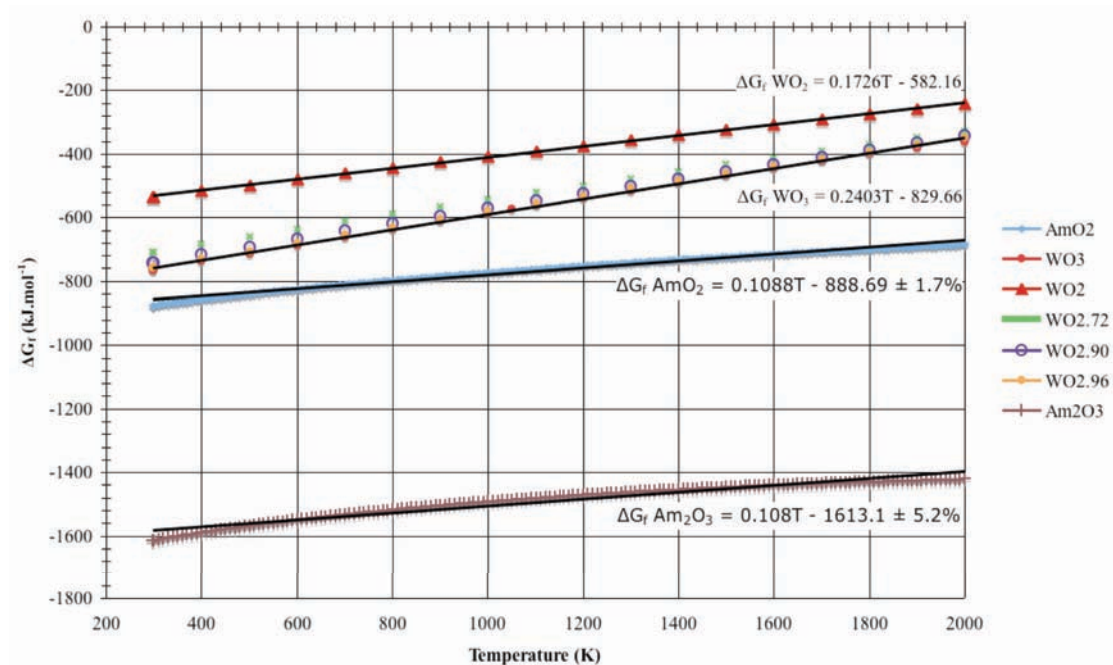


**Figure 6.1:** Ellingham diagram for AmO<sub>2</sub> thermodynamic data (calculated from the data displayed in Table 1 using Equation 1), Am<sub>2</sub>O<sub>3</sub>, and thermodynamic data for species of tungsten oxides published by Barin [5].

It can be deduced from Figure 6.1 that the reduction of the oxides of <sup>241</sup>Am by tungsten should not occur while in its solid state. Thus under atmospheric pressure (101.1 kPa), AmO<sub>2</sub> is energetically preferential over the oxides of tungsten. The high vapour pressures of the americium oxides [7] should be considered in order to derive the temperature and pressure requirements for a sintering process such as spark plasma sintering.

## 6.2 Sample preparation for DSC, XRD and SEM analysis of W-AmO<sub>2</sub> systems

A total of 6 sample pellets were prepared from 3 blends (2 samples per mixture) of americium dioxide with tungsten (See Table 6.2) for a combined analysis of the effects of pressureless sintering via Differential Scanning Calorimetry (DSC), followed by X-Ray Diffraction (XRD) analysis for elemental composition determination in conjunction with Scanning Electron Microscopy (SEM) of the sintered samples. 3 wt% Polyethylene Oxide (Polyox) was selected and added to the batch mixtures after mixing W:AmO<sub>2</sub> ratios, for use as a binder in order to maintain physical integrity of the sample pellets during transfer of the samples between appropriate facilities due to its characterised performance, degradation by radiolysis, and its heritage use in mixed oxide fuel fabrication. 3 wt% Polyox was determined experimentally to be the minimum binder content to ensure mechanical integrity would be preserved.

<b>Batch Number:</b>	<b>L1</b>	<b>L2</b>	<b>L3</b>
<b>Vol% AmO<sub>2</sub> :</b>	50	40	100
<b>Vol % W :</b>	50	60	0
<b>Number of Pellets / ID:</b>	2 (L1-1 & L1-2)	2 (L2-1 & L2-2)	2 (L3-1 & L3-2)
<b>Pellet Diameter (mm)</b>	5	5	5
<b>Pellet Post Press Mass (g)</b>	L1-1 = 0.180 L1-2 = 0.172	L2-1 = 0.169 L2-2 = 0.168	L3-1 = 0.134 L3-2 = 0.126

**Table 6.2:** Composition of pellets and their batches

The mixing of each batch was performed via the use of a Spex brand Ball Mill using two tungsten balls within a controlled argon inert atmosphere Glovebox maintained at 1 atmosphere pressure. The ball mill was operated for a total of 5 minutes per batch. See Figure 6.2 (*left*) for an image of the sample material after homogenization via the ball mill. Once mixed, the batch was divided between two samples and poured into the die (Figure 6.2 (*right*)).



**Figure 6.2:** (*Left*) Post ball mill mixing of sample batch L1. (*Right*) Pouring W-AmO<sub>2</sub> mixture into die.

On the filling of the die, the top punch and support plate were installed into the open end of the die. Once assembled, the die was installed into a Carva press with a maximum applicable force of 44.5 kN (Figure 6.3 (*Left*)). The Carva press resides in a glovebox, which again as an atmosphere of 100 % Argon held at 101 kPa. A force of 8.9 kN was applied to the assembled dies and a dwell time of 5 seconds was allocated for the green compaction of the pellets. These pressing parameters were determined empirically through examination of inert tungsten – ceria mixtures in which the ceria (CeO<sub>2</sub>) was used as a surrogate for <sup>241</sup>AmO<sub>2</sub>. When the fabrication was complete, the green pellets were pressed out of the die and prepared for transfer for DSC and XRD process and analyses.

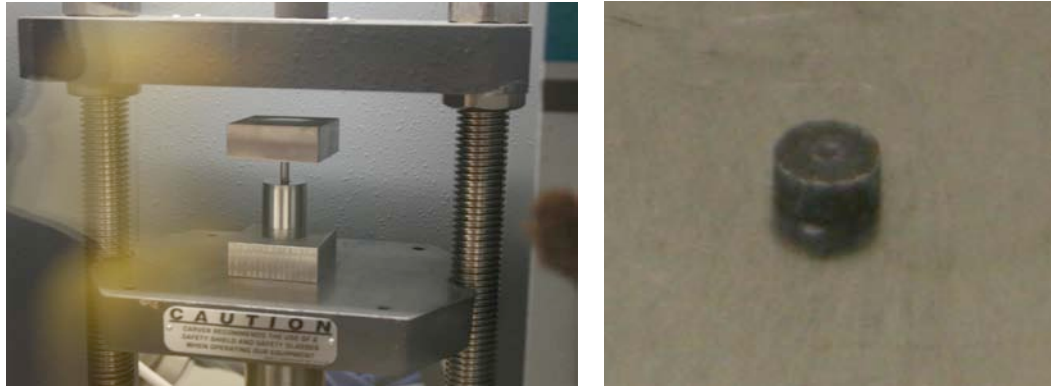


**Figure 6.3:** (Left) Loaded Die configuration in the Carva press. (Right) GreenW-AmO<sub>2</sub> pressed pellet.

### **6.3 Evaluation and SEM analysis of AmO<sub>2</sub> experimental feedstock material**

AmO<sub>2</sub> is a black powder in its +3 oxidation state, potentially due to crystal defects, and its crystal lattice geometry is face centred cubic. The morphology of the Am<sup>III+</sup>O<sub>2</sub> feedstock used during this study was investigated via the use of Scanning Electron Microscopy (SEM). Two samples of the powder feedstock were prepared and mounted onto SEM stages which were in turn coated with palladium via vapour deposition to prevent contamination of the microscope and surrounding equipment. Images of the feedstock are presented in Figure 6.4.

The Image J software package [8] was used to analyse the particle distribution of the sampled americium oxide fines and agglomerate sites seen in the SEM images. An average constituent particle size of approximately 4.8 µm was determined for the particular feedstock used throughout this investigation. Calibration of the software technique was based upon the scale bars embedded within the SEM imagery. It should be noted that sub micrometer fines were also present while the bulk agglomerate sites occupied a large distribution of sizes between 4 µm and 400 µm. It is likely that

agglomeration of the  $\text{AmO}_2$  particles occurred initially during the calcination process for oxide powder production, but continues to occur during mechanical activities and due to electrostatic charge.

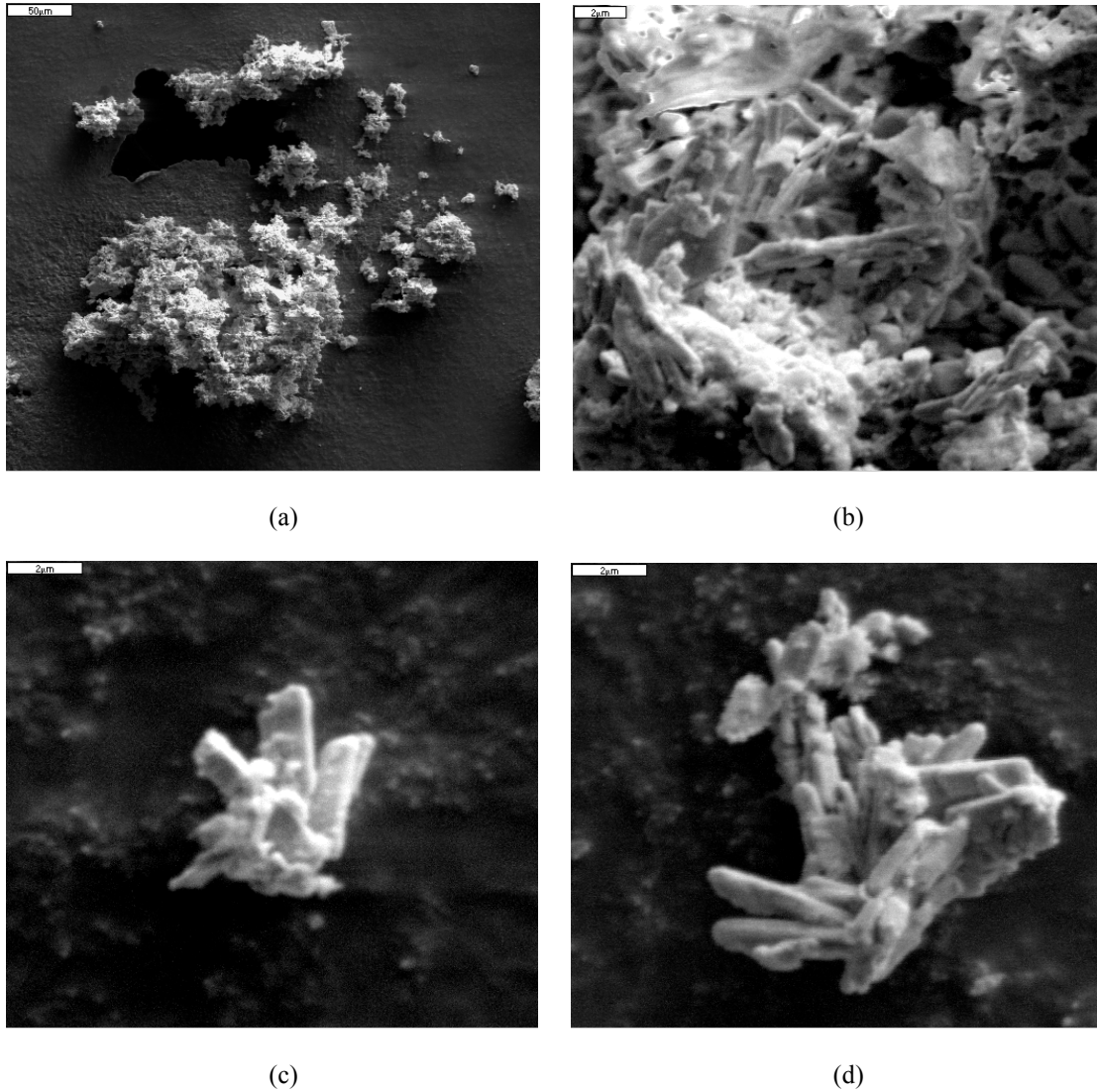


**Figure 6.4:** (a) Typical distribution of americium oxide agglomerates. (b) Structure of large agglomerate sites. (c) Typical features of a fine agglomerate site. (d) Features of a medium size agglomerate site.

Energy dispersive X-ray spectroscopy (EDX) analysis of  $\text{AmO}_2$  particles was performed to ensure insignificant contamination of the feedstock by inactive processing chemicals. Predicted potential contaminants were Cr, Al, Ca, Si, Ce, Fe, Ni, Zn, Mn, Ti, Na. These contaminants were estimated to be less than 1% of the total chemical composition of the feedstock as a result of the calcination process. The results from this

analysis are in agreement with data provided by the material supplier for the specific batch used.

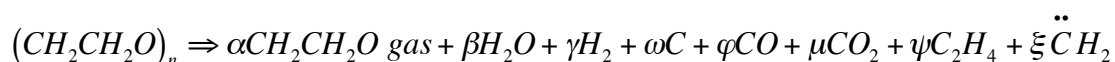
#### **6.4 DSC analysis of W-Am<sub>x</sub>O<sub>y</sub> systems**

Differential scanning calorimetry (DSC) is a technique used to determine the energy required to raise a sample in temperature relative to a known and calibrated reference sample. Exothermic activity may also be evaluated. The mass of the sample subjected to DSC may also be monitored via an integral balance. DSC was used to observe thermal activity in the pellets while simultaneously sintering them at temperatures proportional to those achieved for tungsten cermet fabrication in a Spark Plasma Sintering furnace. Although it was anticipated that the americium oxides were energetically preferential over the oxides of tungsten (see above), the addition of the Polyox binder to the chemical system introduced a reducing agent, carbon, upon its thermal decomposition.

The sample pellets were loaded into a platinum crucible lined with a homogenous yttria liner (Y<sub>2</sub>O<sub>3</sub>) and closed to the outside environment via a platinum lid. Yttria was selected as a liner due to its inert nature at elevated temperatures in the presence of tungsten. The liner was necessary to eliminate the potential reduction of the americium compounds or any products of reaction by the platinum metal crucible. The pressureless sintering/annealing of the individual sample pellets during DSC measurement was performed between room temperature and 1300 °C ramped from ambient at a rate of 10 °C/minute to validate the theory of AmO<sub>2</sub> stability within a tungsten matrix. An isotherm was maintained for a period of 15 minutes upon achieving

the maximum temperature to allow for the instrument to equilibrate prior to cooling. Following the isotherm, the samples were restored to room temperature at a rate of 10 °C/minute.

During heating, Polyox which is a non-ionic homopolymer of the form  $(CH_2CH_2O)_n$  decomposes in two distinct stages [9]. Firstly into its non-polymeric gas from the molten solid followed by the decomposition of its vapour into its constituent elements and molecules which include (but are not quantified here - see Choukourov et al [9]):



Carbon and Carbenes, the latter of these potential products of the Polyox decomposition, are highly reactive. In significant quantities and distributed throughout the matrix, these materials are likely to alter the stoichiometry of the americium oxide and indeed interact with the metallic tungsten.

In order to observe the thermographic effect of the Polyox decomposition, a small sample of Polyox with a mass of  $0.2358 \pm 0.008$  g was prepared and subjected to the same DSC profile that would be adopted for the AmO<sub>2</sub> and AmO<sub>2</sub>-W samples, i.e. a ramp rate of 10 °C per minute up to a temperature of 1300 °C. The DSC data for this analysis is plotted in Figure 6.5. This experimental data verifies the findings of Choukourov et al [9] given that two distinct stages of Polyox decomposition. It is evident that peak melting of the Polyox occurred a temperature of 72.4 °C. Again, through analysis of Figure 6.5, the peak vaporization and decomposition of the molten

Polyox occurred at a temperature of 402.8 °C. The final stage in volatilization is observed at 1200 °C. It should be noted that the post decomposition mass of the Polyox sample was  $0.0037 \pm 0.0008$  g and that a significant quantity of carbon residue was visible upon removal of the crucible from the DSC. Thus, approximately 1.6 % of the initial Polyox mass remained as a carbon residue.

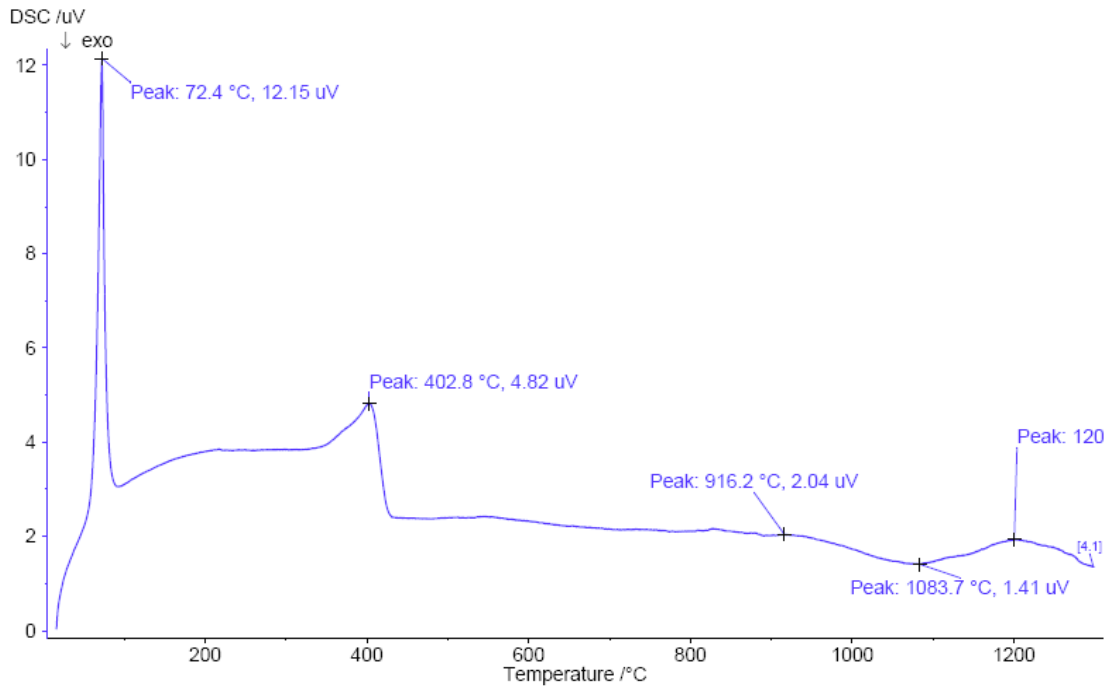


**Figure 6.5:** DSC profile for the decomposition of Polyox with respect to increase in temperature at a rate of 10 °C/min and at 101 kPa Ghettered Argon refreshed at 20 ml/min. 15 min isothermal hold at 1300 °C followed by controlled cooling to 1300 °C not shown.

Each of the six sample pellets loaded with americium dioxide were sintered and annealed via the same DSC profile described above. The results are presented in Figures 6.6 to 6.17 below. The endothermic features from the Polyox thermal decomposition process are present in the heating profile for each sample, but the features are spread over a broader temperature range. One potential reason for this could be due to the extended and restricted inter-granular path length through the cermet matrix that must be taken by gaseous products of polyox decomposition.

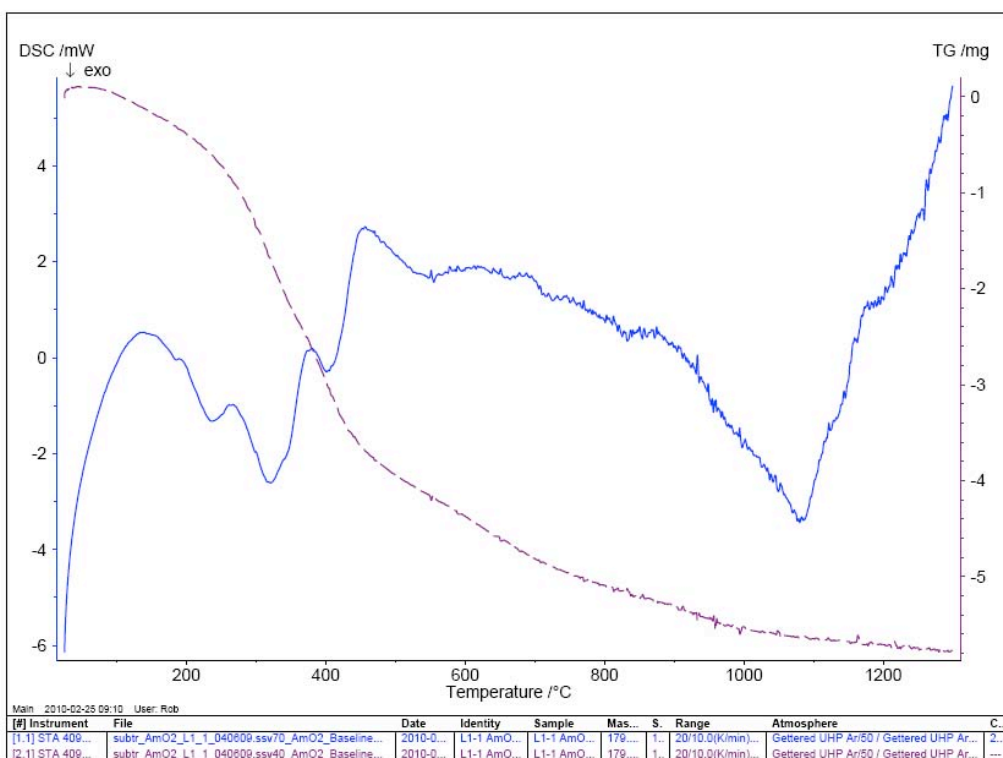


Figure 6.6: DSC heating profile for sample L1-1

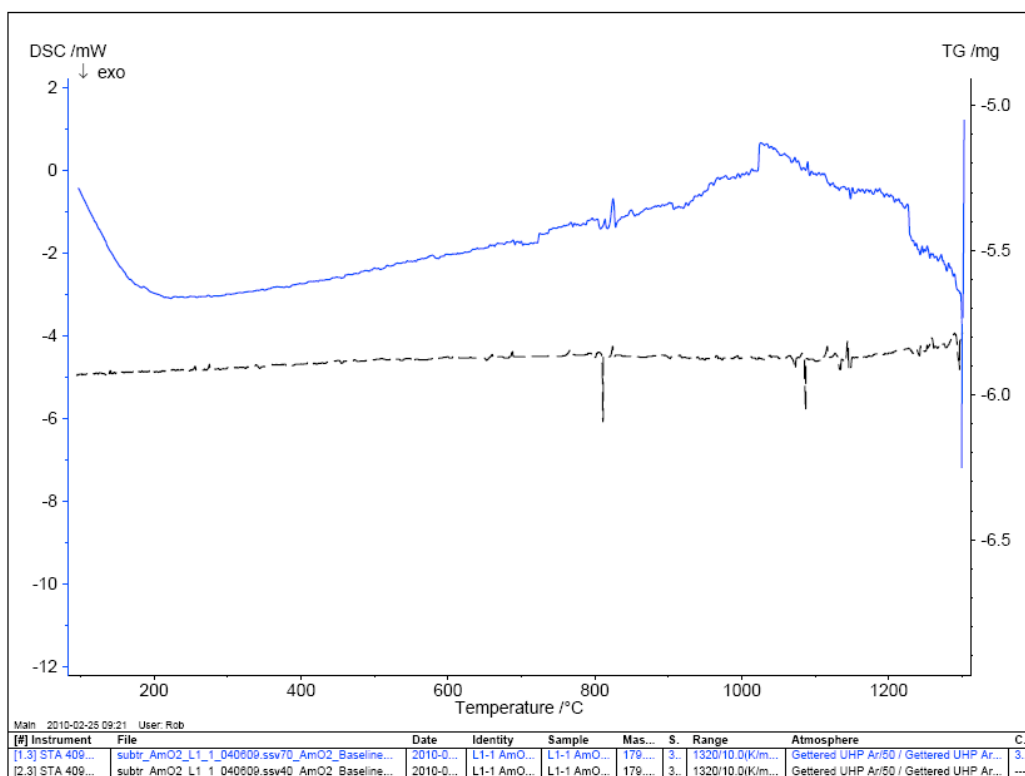


Figure 6.7: DSC cooling profile for sample L1-1

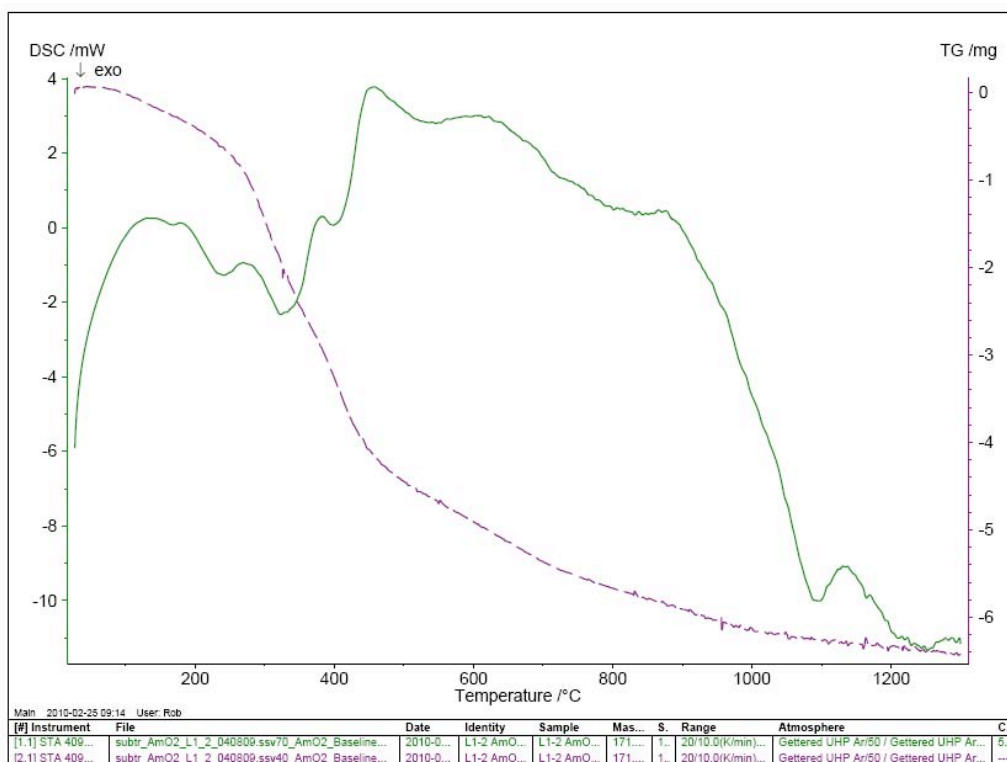


Figure 6.8: DSC heating profile for sample L1-2

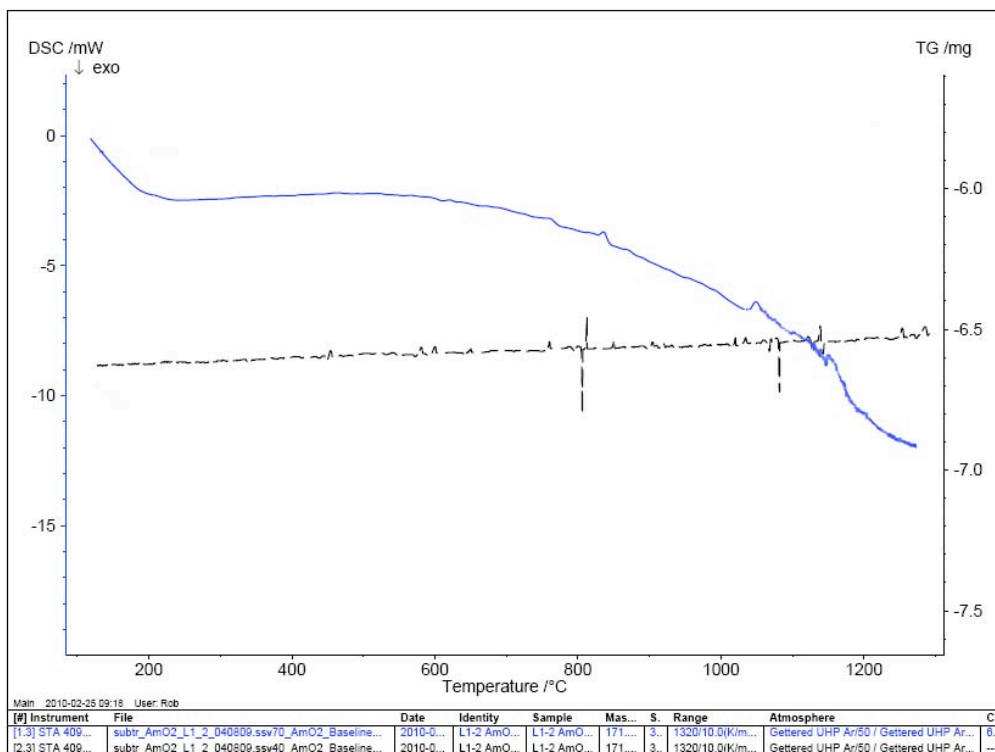


Figure 6.9: DSC cooling profile for sample L1-2.

Fi

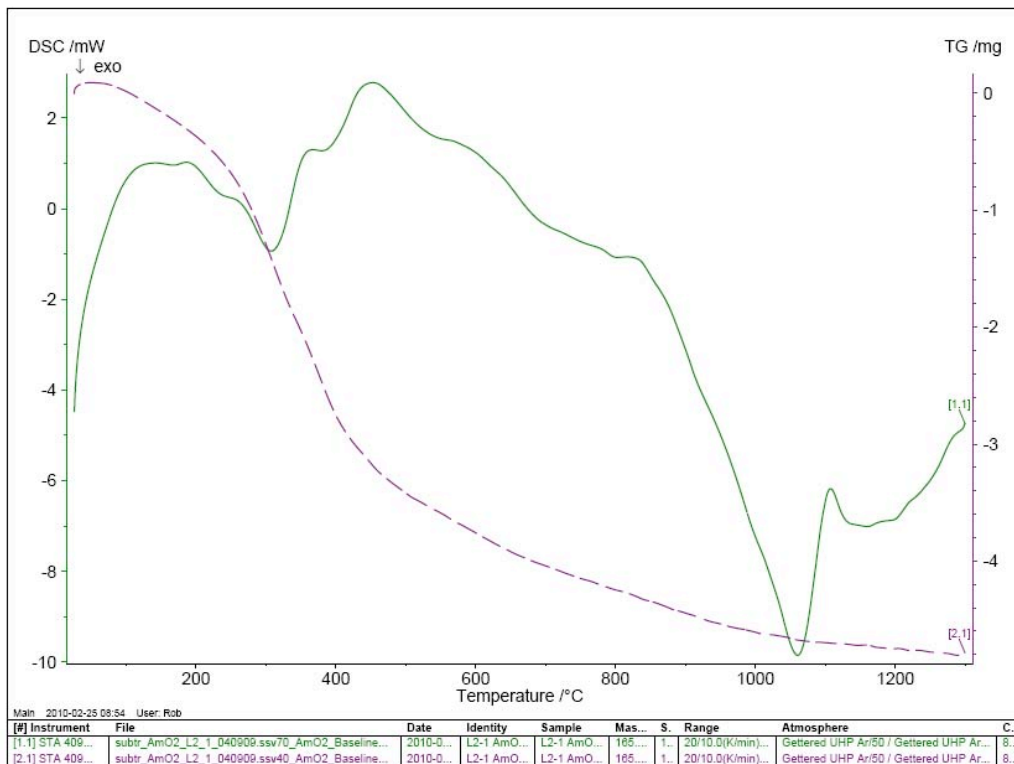


Figure 6.10: DSC heating profile for sample L2-1

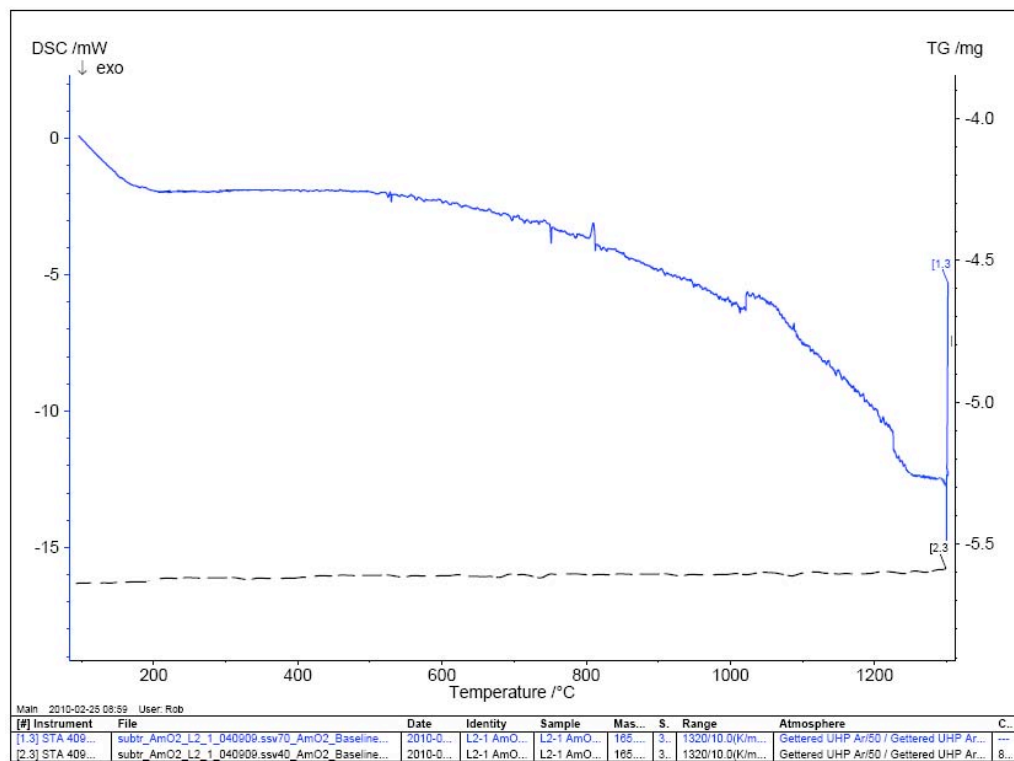


Figure 6.11: DSC cooling profile for sample L2-1

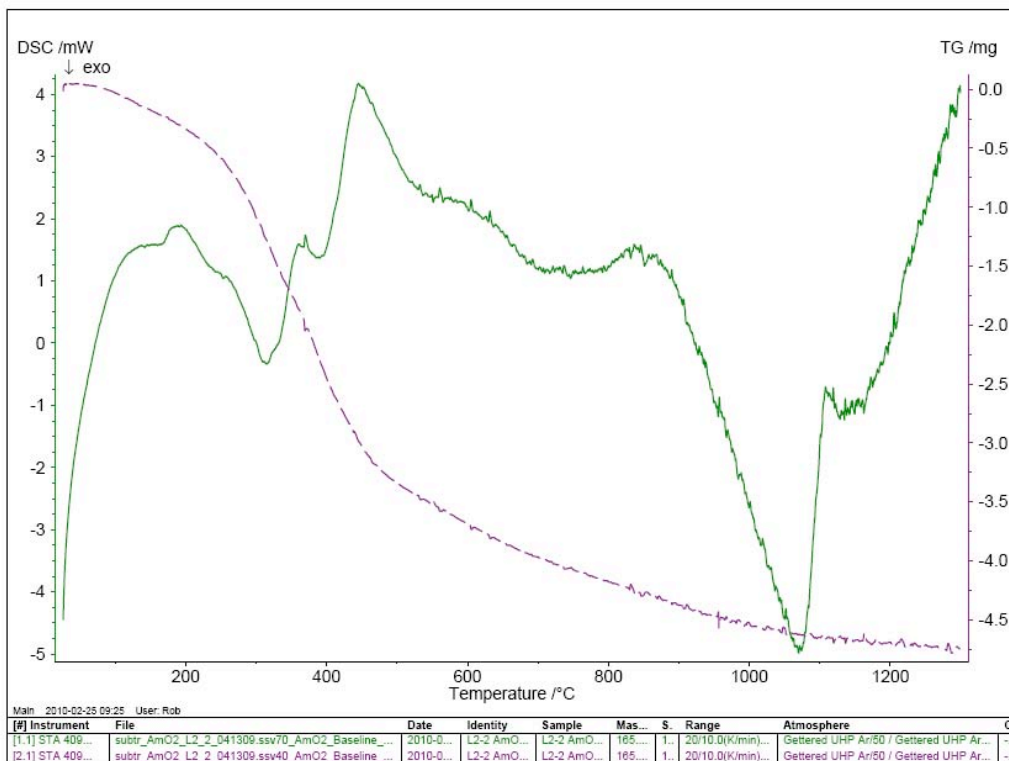


Figure 6.12: DSC heating profile for sample L2-2

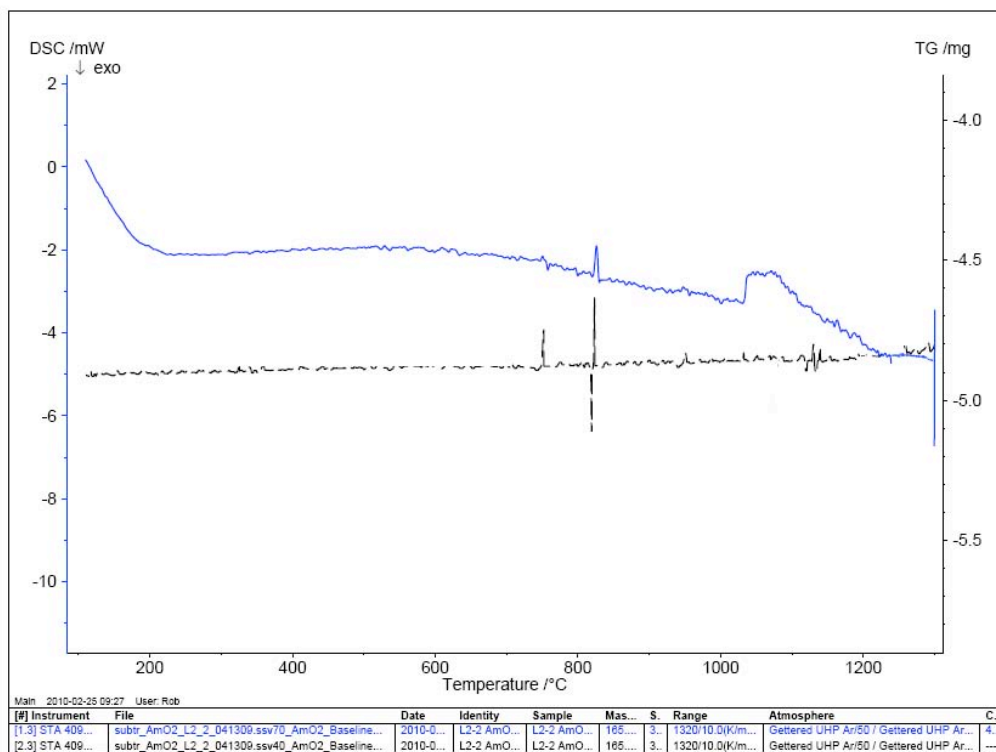


Figure 6.13: DSC cooling profile for sample L2-2

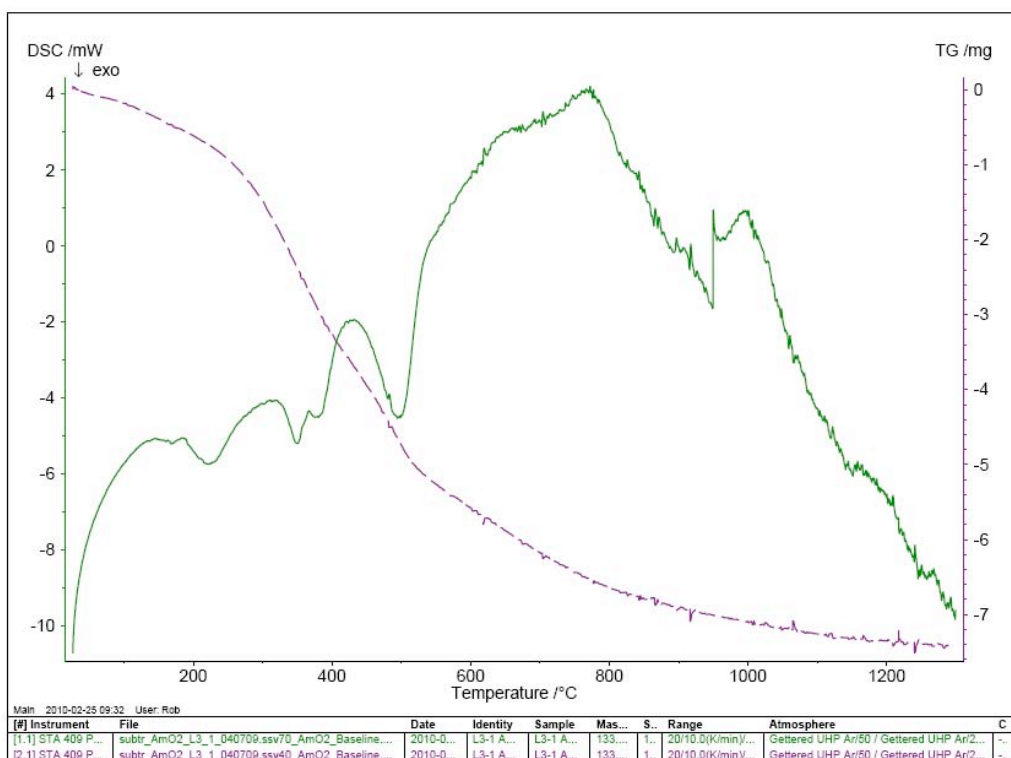


Figure 6.14: DSC Heating profile for sample L3-1

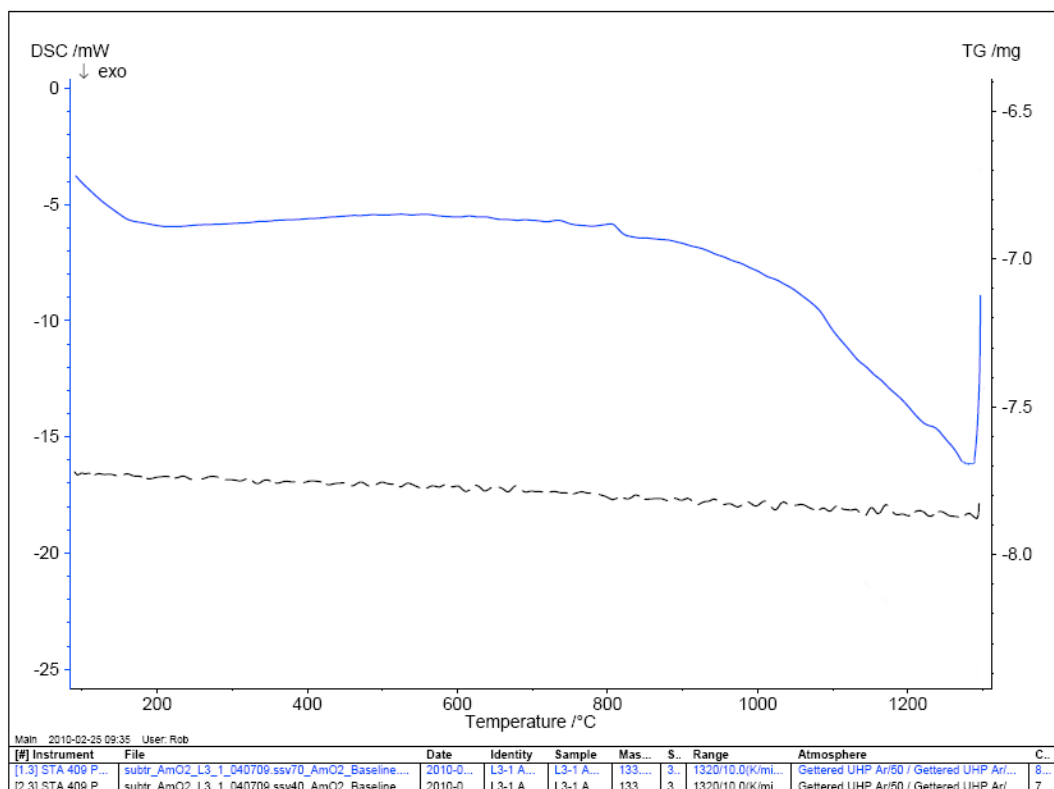


Figure 6.15: DSC cooling profile for sample L3-1

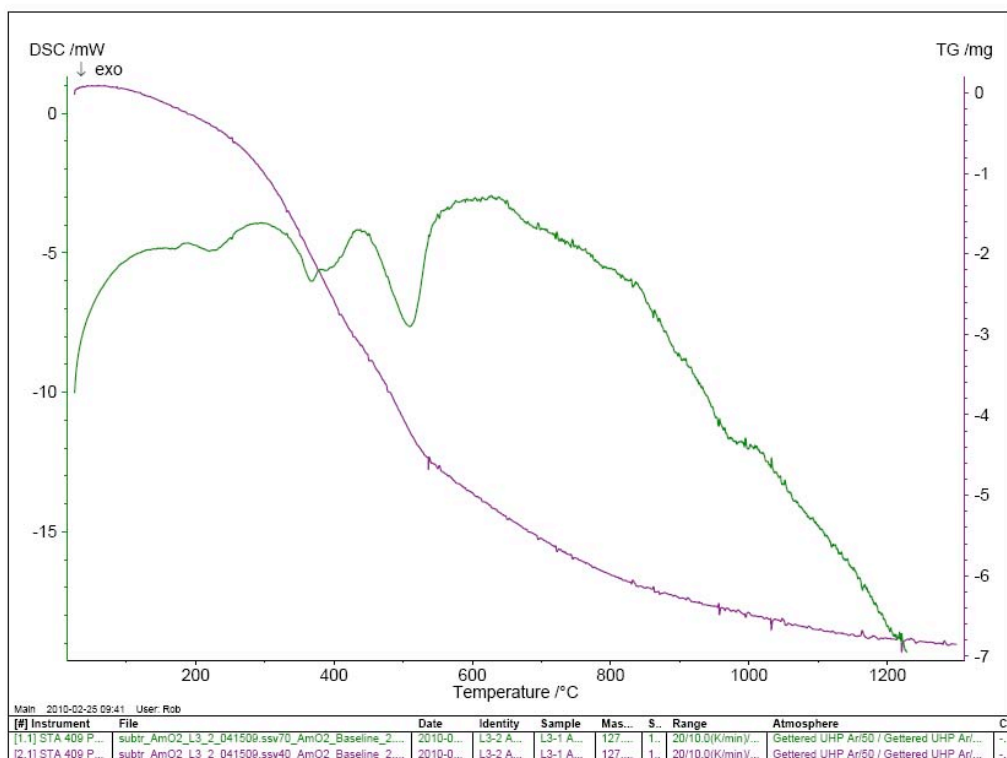


Figure 6.16: DSC heating profile for sample L3-2

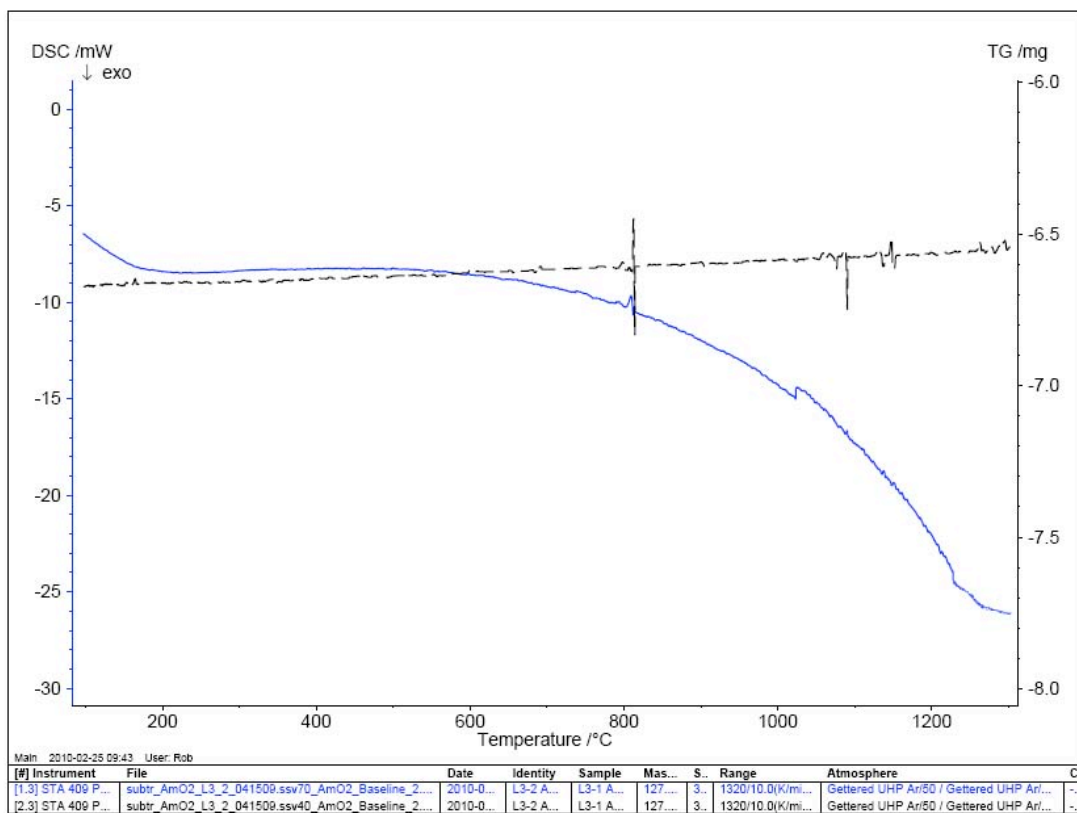


Figure 6.17: DSC cooling profile for sample L3-2

Evidence of significant noise can be observed in the DSC data. Some endothermic noise may be accounted for by flash releases of gaseous products of the polyox thermal decomposition process caused by the accumulation of sufficient pressure to break the seal between the lid and walls of the crucibles. Other significant noise originated in mechanical noise in the local environment. Most notably, the intensity of the mechanical noise produced the most severe impact on the results for the L3 batch samples. Such noise could not be eliminated via damping due to the current setup of the DSC and its fixed configuration within an active Glovebox. Despite inaccuracy of the exo/endermic values, the overall trend and net magnitude of the thermograph is comparable to the profiles of the L1 and L2 batch samples indicating that the exothermic energy release is most significantly driven by AmO<sub>2</sub> reduction. The exothermic profile noted within the L3 batch results may also be accounted for by the significant <sup>241</sup>Am decay heat which was estimated to be of the order of 6 mW for the L3 samples.

Overall, it may be deduced from the data presented in Figures 6.14 to 6.16 that the that the exotherms exhibited in Figures 6.6 to 6.13 are not enhanced by the presence of tungsten within the cermet system. The presence of carbon residues (derived from the decomposition of the binder) in a high temperature AmO<sub>2</sub> system may influence the rate of AmO<sub>2</sub> dissociation at atmospheric pressure, the onset of which is significant at around 700 °C. It is likely that such energy release may also facilitate the sintering of matrix materials, thus reaction sintering. In addition, the enthalpy of formation for tungsten carbide and ditungsten carbide at 1300 °C is -38.185 kJ.mol<sup>-1</sup> and +3.103 kJ.mol<sup>-1</sup> respectively [5]. Given the availability of energy within the cermet system, a

reaction between the tungsten matrix and carbon residues may be possible resulting in carbide formation.

## **6.5 XRD analysis of sintered AmO<sub>2</sub> and W-AmO<sub>2</sub> systems**

The analysis of samples composed of heavy element crystals via X-Ray Diffraction (XRD) is limited to surface and near-surface analysis due to significant attenuation of incident and diffracted signals. The samples analysed throughout this study were not planed through the centre prior to mounting in the XRD instrument focal plane and hence the results are indicative of surface composition only. Further subsurface analysis would be required to determine the internal composition of the samples, but significant considerations and mitigation of contamination of the active facility would be required when cutting such samples. Such sample preparation was not available in the glovebox used. The results for the XRD scans of each pellet composition were obtained and are presented in Figures 6.18 to Figure 6.20 below.

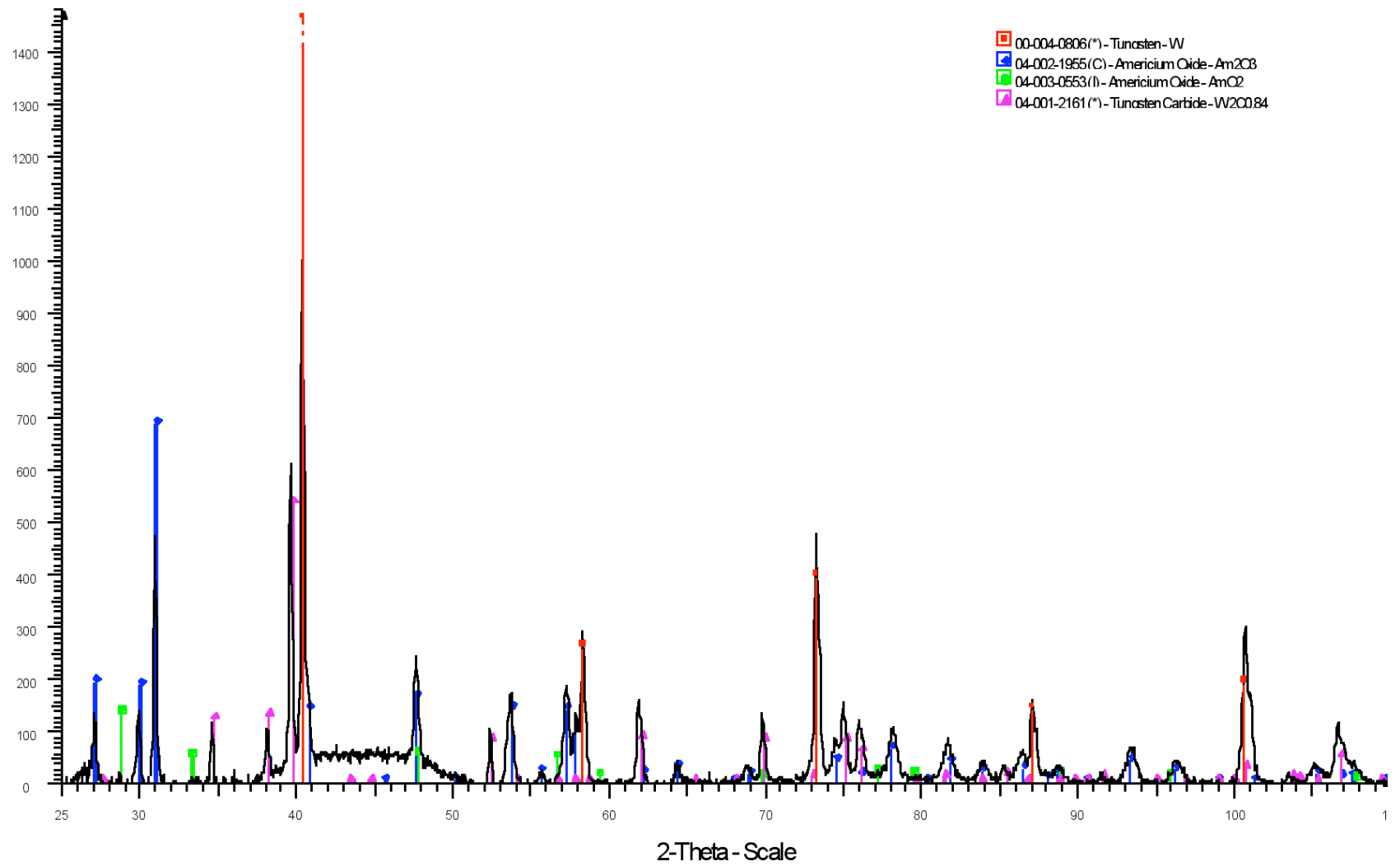


**Figure 6.18:** XRD results for Sample L1-2. The number of counts is plotted on the Y-axis as a function of 2-Theta angle.

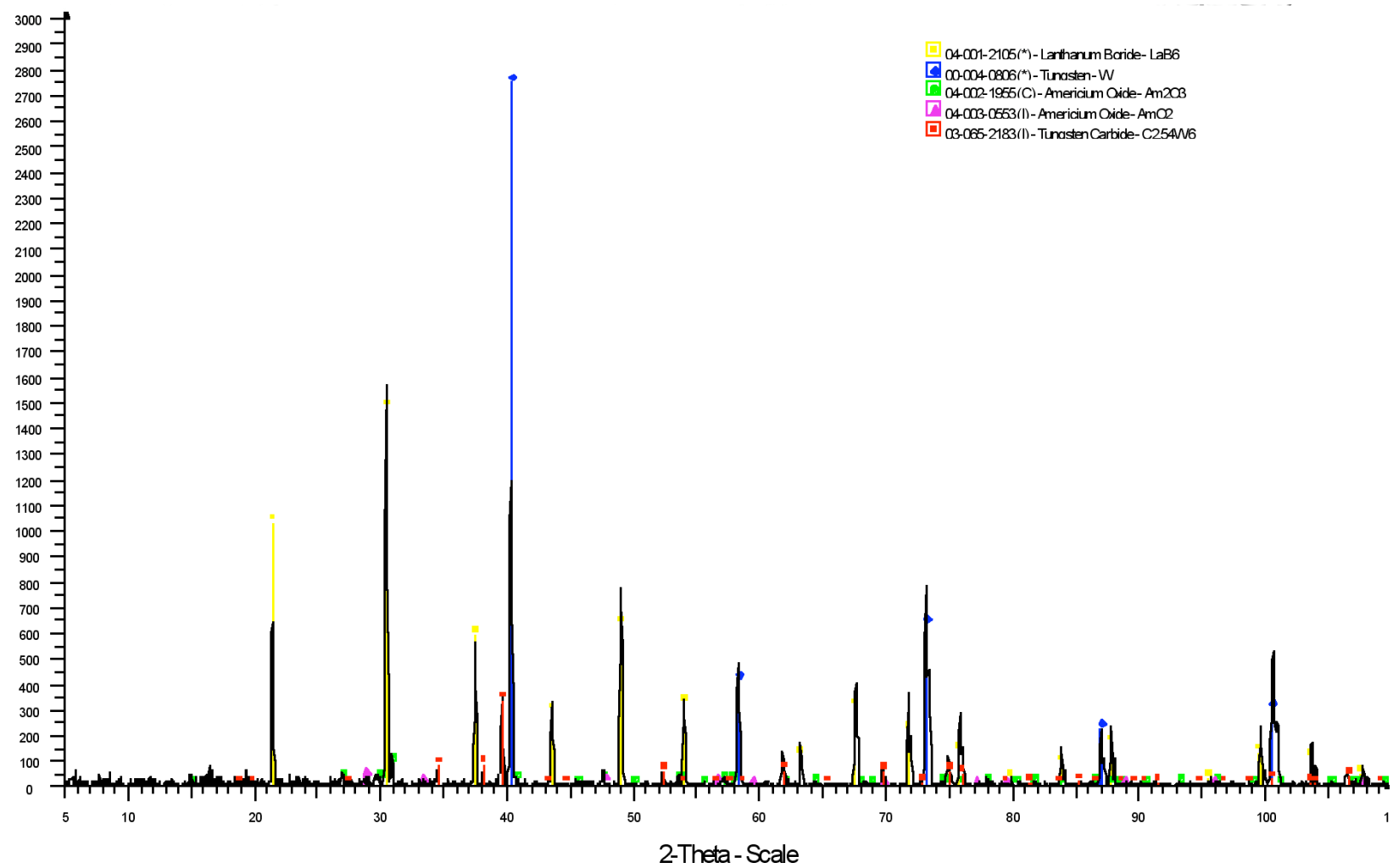


**Figure 6.19:** XRD results for sample L2-2. The number of counts is plotted on the Y-axis as a function of 2-Theta angle.

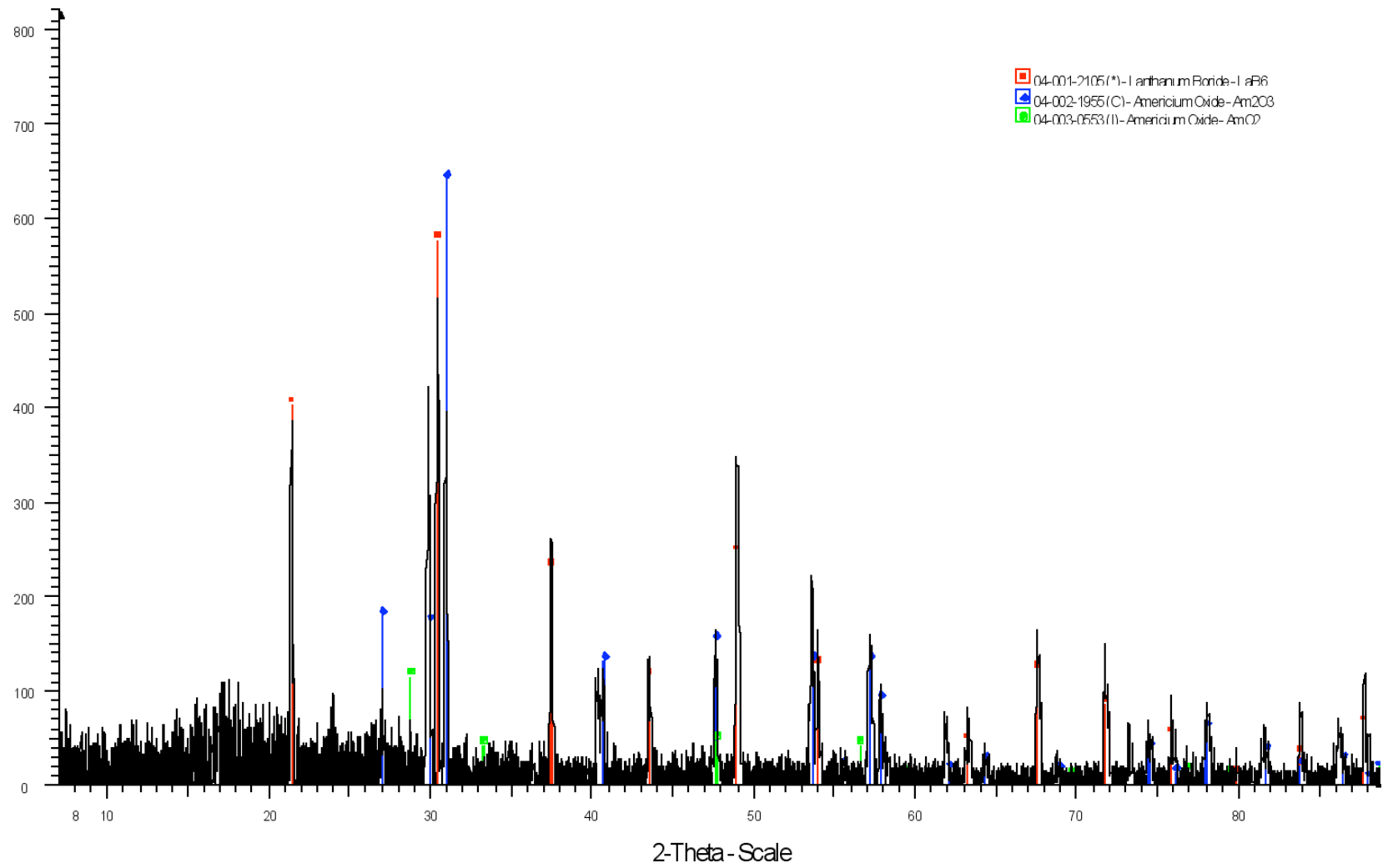


**Figure 6.20:** XRD results for sample L3-2. The number of counts is plotted on the Y-axis as a function of 2-Theta angle.

Due to the sintering/annealing of the samples at 1 atmosphere of Gettered (purified) Argon in the DSC chamber, it is anticipated that the composition of the americium oxides within the samples varies in stoichiometry between americium dioxide ( $\text{AmO}_2$ ) and americium sesquioxide ( $\text{Am}_2\text{O}_3$ ) with respect to processing time. This is due to the high vapour pressure of americium dioxide resulting in vapour dissociation in addition to vapour reduction by carbon to form carbon monoxide or carbon dioxide [7]. If a film barrier of  $\text{Am}_2\text{O}_3$  was produced on the surface of the americium dioxide particles, the reduction and dissociation may be delayed. Figure 6.21 is a simulated XRD pattern for a complex of  $\text{AmO}_2$  and  $\text{Am}_2\text{O}_3$  produced using data from the UK Crystal Database System (CDS) [10] using a combination of the Crystalmaker and CrystalDiffract software packages [11]. If partial redox had occurred in the physical samples, the XRD patterns would have been similar in composition, although the relative intensity or number of counts at each 2-theta value would vary with practical stoichiometry. As can be seen in the experimental data for the samples, peaks for  $\text{AmO}_2$  may not be distinguished from noise, indicating that the  $\text{AmO}_2$  was reduced in excess of 95% to  $\text{Am}_2\text{O}_3$ .

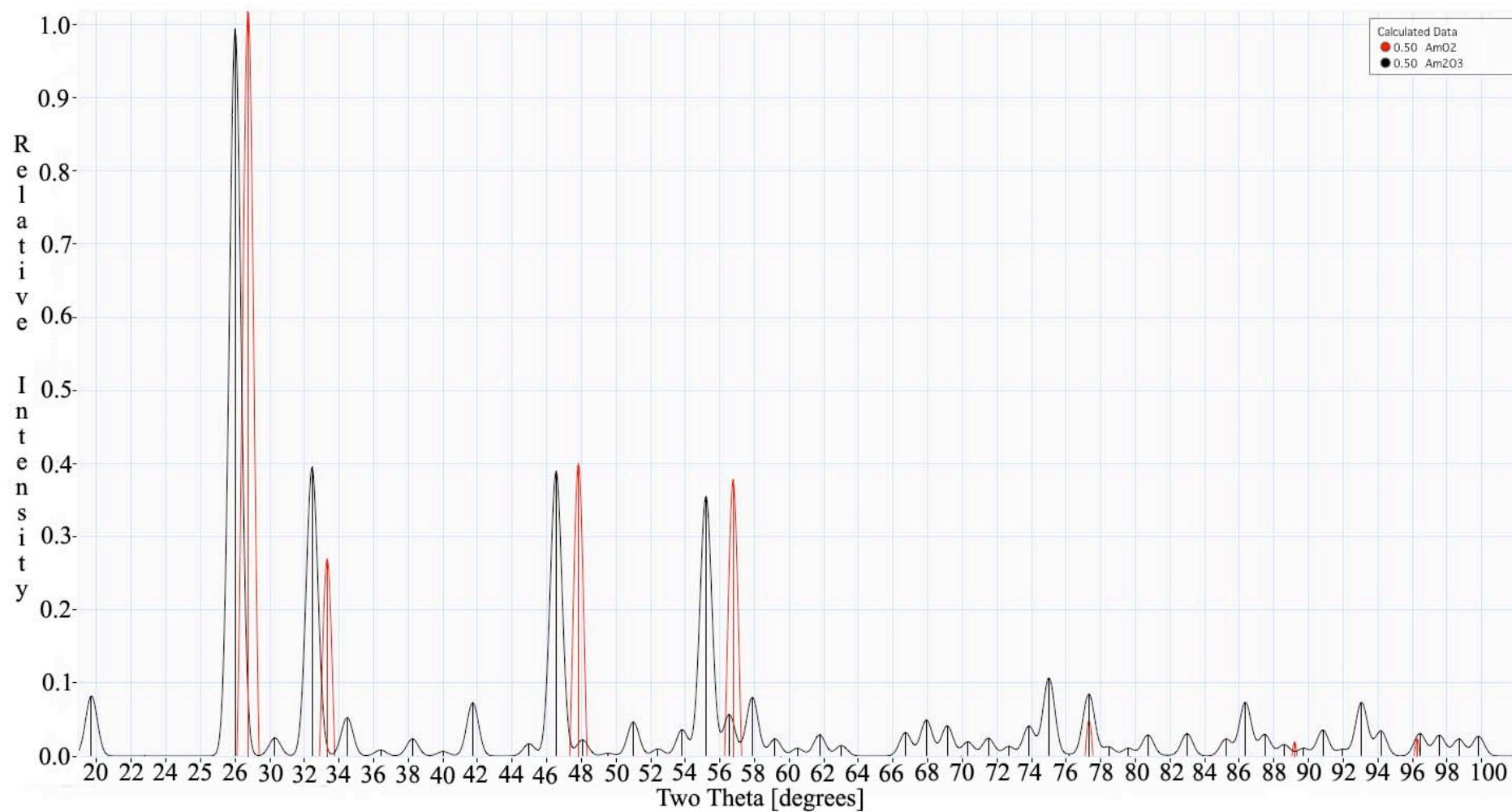


**Figure 6.21:** Simulated XRD pattern for a 1:1 mixture of  $\text{AmO}_2$  with  $\text{Am}_2\text{O}_3$ . Produced via data from the UK Crystal Database System (CDS) using a combination of the Crystalmaker and CrystalDiffract software packages.

In addition to the reduction of the  $\text{AmO}_2$ , the presence of carbon residues and volatiles in the pellet resulted in the formation of tungsten carbide compounds of varying stoichiometry and concentration. The diffraction pattern for the  $\text{LaB}_6$  instrument standard could not be removed from the instrument and is present in the sample scans, but can be subtracted from the results to estimate the surface concentration of materials present. The hexagonal carbide structure  $\text{W}_2\text{C}_{0.84}$  was observed in significant concentrations. Based on the abundance of the carbon residue products of Polyox decomposition, it is estimated that the total tungsten carbide in the system accounts for  $\sim 1\%_{\text{at}}$  of the total W- $\text{W}_2\text{C}$  matrix distribution. Given the high temperature CO and  $\text{CO}_2$  environment that surrounded the pellet during the sintering and annealing process in the closed crucible (from Polyox decomposition & reduction of  $\text{AmO}_2$  by carbon residues), it is not surprising that a significant proportion of carbide compounds exist at the surface. Thus the XRD-derived relative intensity of tungsten carbide is unlikely to reflect the average bulk composition. For Sample L1-2 where 50  $\%_{\text{vol}}$  of tungsten was present, the  $\text{W}_2\text{C}_{0.84}$  compound represented approximately 17.5  $\%_{\text{at}}$  of the top surface matrix. For Sample L2-2 where 60  $\%_{\text{vol}}$  of tungsten was present, the  $\text{W}_2\text{C}_{0.84}$  compound represented 10.3  $\%_{\text{at}}$  of the top surface matrix. Further analysis of inert systems is required for determination of the bulk  $\text{W}_2\text{C}$  formation and will be the subject of a future publication.

## 6.6 SEM analysis of sintered AmO<sub>2</sub> and W-AmO<sub>2</sub> systems

Once sintered and annealed during the DSC heating/analysis, samples L1-1, L2-1 and L3-1 were examined using SEM. A Zeiss DSM 960A SEM with EDX capability was used for the examination. Prior to transfer to the SEM, the samples were coated in palladium metal via vapour deposition using an RF sputtering source held in vacuum. The function of the palladium coating was to minimise radiological contamination of the SEM and transfer equipment that may arise from the dislocation of loose particulate matter.

*L1-1 – 50 %<sub>vol</sub> Americium oxide : 50 %<sub>vol</sub> Tungsten:*

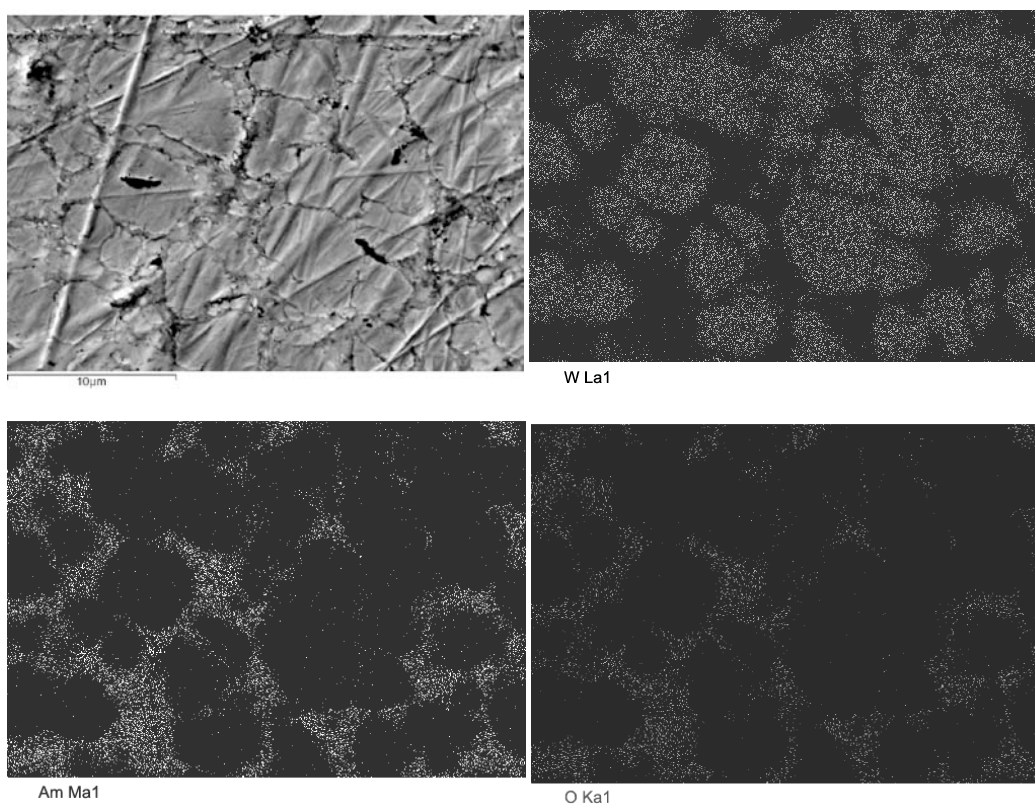


**Figure 6.22:** SEM image and EDX elemental maps for the tungsten, americium and oxygen content of Sample L1-1.

The SEM image and elemental maps illustrated in Figure 6.22 indicate that the americium and oxygen content of the sample is well constrained to the interstitial regions between tungsten agglomerates. The polycrystalline structures in the americium oxide regions of the sample indicates evidence for reaction sintering as demonstrated in polycrystalline SiN by Chakraborty [12], was most likely facilitated by the exothermic energy release during reduction of  $\text{AmO}_2$  to  $\text{Am}_2\text{O}_3$ . Overall, images of the sample reveal the desired fifty percent volumetric mixture ratio was achieved during sample  $\pm 6\%$  across a distribution of regions of interest as calculated using the ImageJ [8] technique described earlier in this chapter.

*L2-1 – 40 %<sub>vol</sub> Americium oxide : 60 %<sub>vol</sub> Tungsten:*

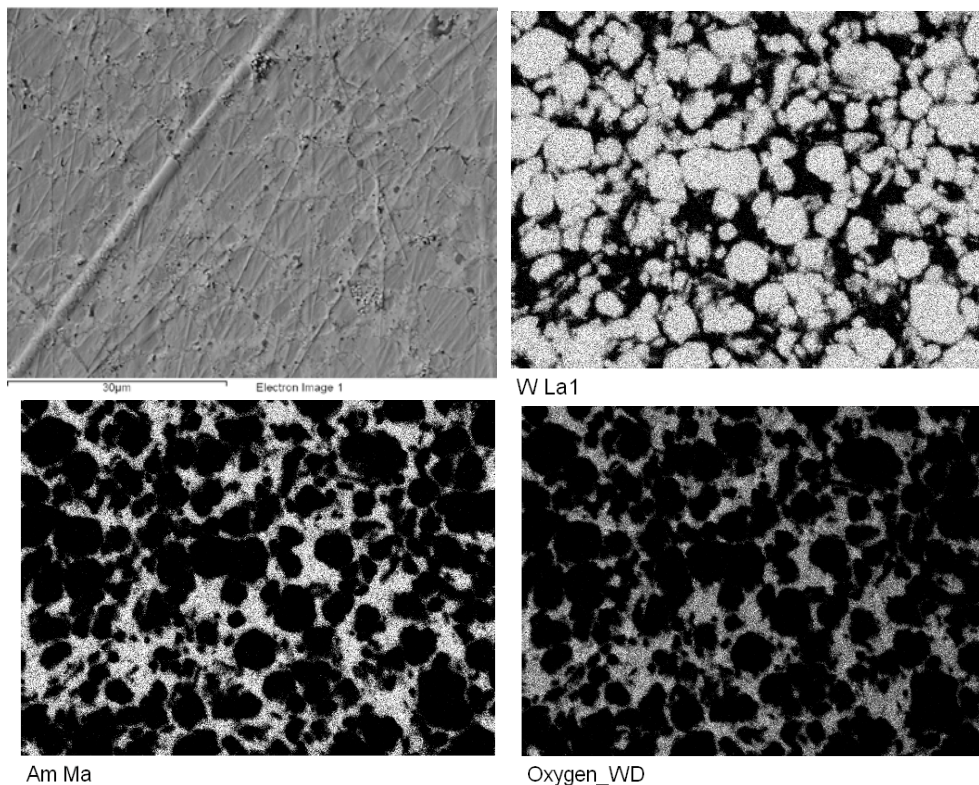


**Figure 6.23:** SEM images and EDX elemental maps for the tungsten, americium and oxygen content of Sample L2-1 (40%<sub>vol</sub> americium oxide: 50 %<sub>vol</sub> tungsten).

The SEM and EDX results for sample L2-1 (Figure 6.23) indicate that the desired volumetric ratio of 40 % americium oxide was achieved to within 2% over the distribution of image regions of interest that were sampled. As was exhibited in sample L1-1, the americium and oxygen concentrations are confined to the interstitial regions of the tungsten cermet matrix. Polycrystalline structured americium oxide was also predominant, supporting the theory of reaction sintering.

*L3-1 – 50 %<sub>vol</sub> Americium oxide : 50 %<sub>vol</sub> Tungsten:*

The surface of sample L3-1 illustrates the brittleness of the Am<sub>2</sub>O<sub>3</sub> ceramic matrix. Pullouts are visible as craters in Figure 6.24 caused by mechanical polishing. Surface contamination by silica, seen as several bright particles within the image, is also noted which is most likely attributed to the polishing media used. The fine polycrystalline structure of the americium oxide is once again noted. This is clearly illustrated in Figure 6.25. Further evidence for reaction sintering is presented and carbon residues are visible in the sintered matrix.

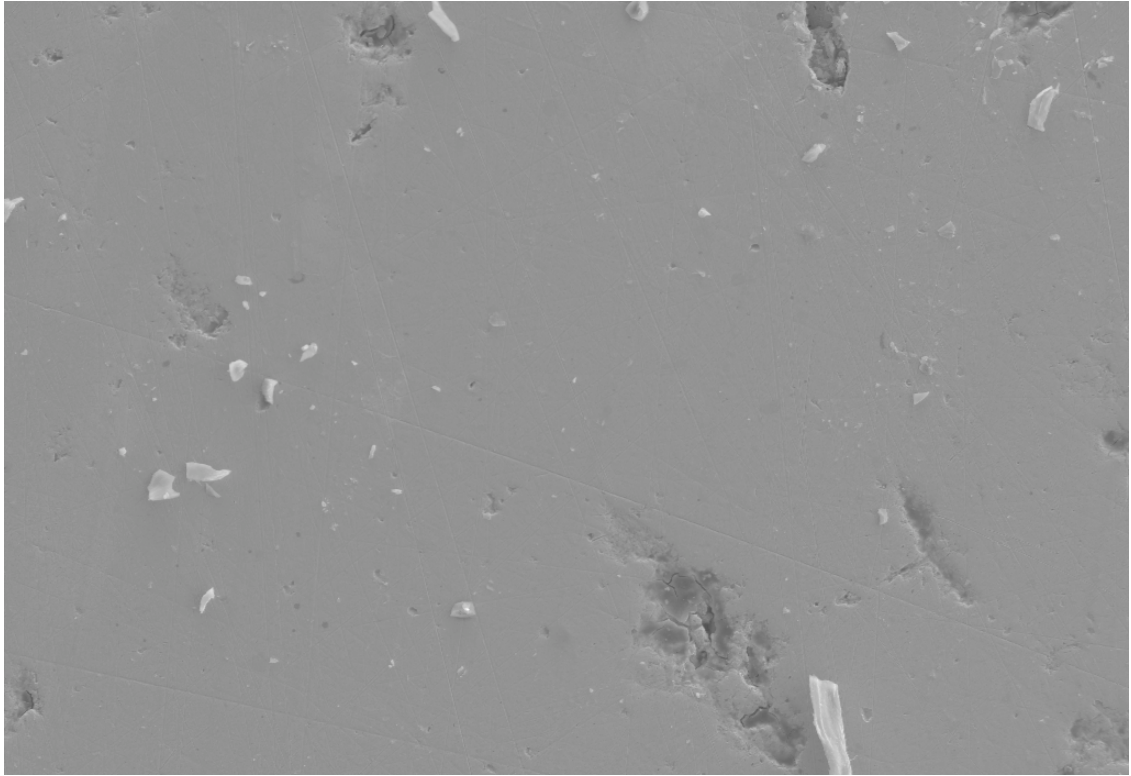


**Figure 6.24:** SEM image of Sample L3-1. Surface pullouts of material due to abrasive polishing technique are visible as cratering. Silica contamination from polishing process is also visible as bright spots.

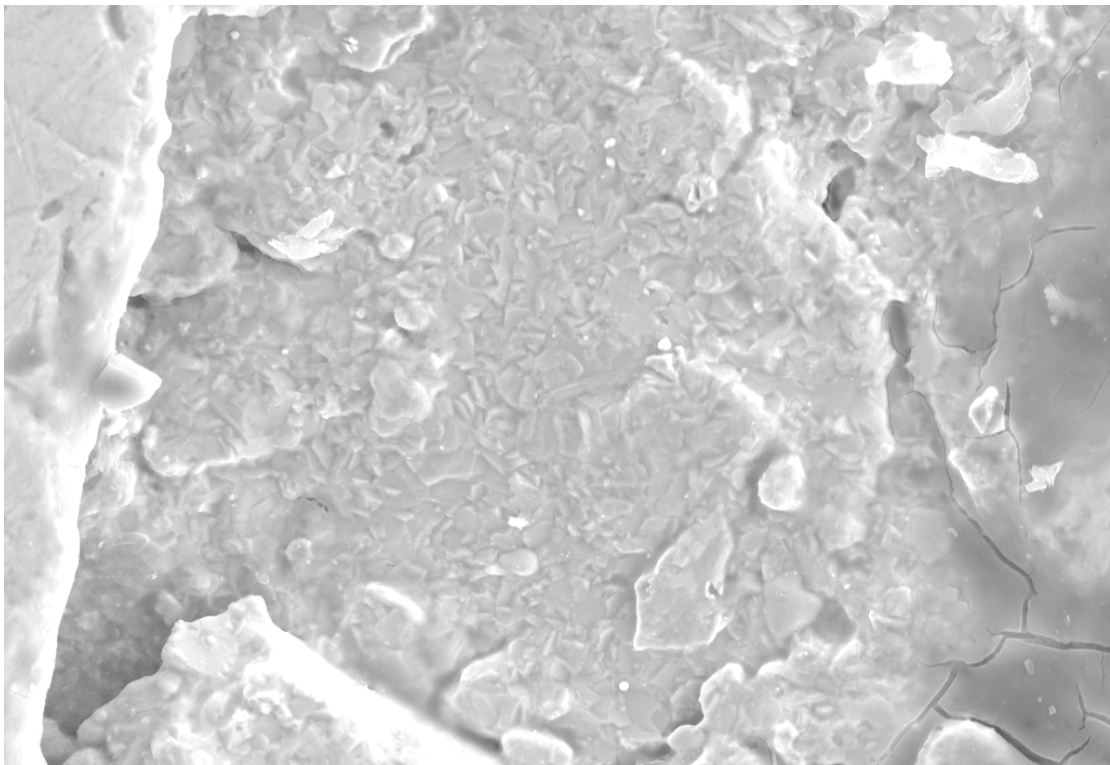


**Figure 6.25:** SEM image of a pullout region of Sample L3-1. Here the polycrystalline structure of the  $\text{Am}_2\text{O}_3$  matrix is visible with evidence of reaction sintering as a result of dissociation-redox for the  $\text{AmO}_2$ . Darker contrast regions at peripheral left is carbon residue from Polyox thermal decomposition and volatilisation process.

## 6.7 Estimation of feedstock Specific Thermal Power

By subjecting a sample of AmO<sub>2</sub> to an isothermal hold at 30 °C in a DSC, the thermal output of the source was measured to be 11.798mW ± 0.002 mW. Dividing by the mass of the source, the specific thermal power was estimated to be 0.094 ± 0.002 W/g. This value is consistent with the DSC plots of Figures 6.16 and 6.17 due to the significant thermal loading of the L3 samples. This is clearly visible as start and end points in the thermographic data.. A thermal image was taken of the source after it had been isolated in a thermosetting plastic and cut in half in preparation for imaging via SEM. The thermosetting plastic acted as an insulator. After allowing the sample to equilibrate with the environmental temperature in a fume hood, a thermal image was taken using a Fluke Ti32 thermal camera. The composite optical and thermal image is illustrated in Figure 6.26 below.

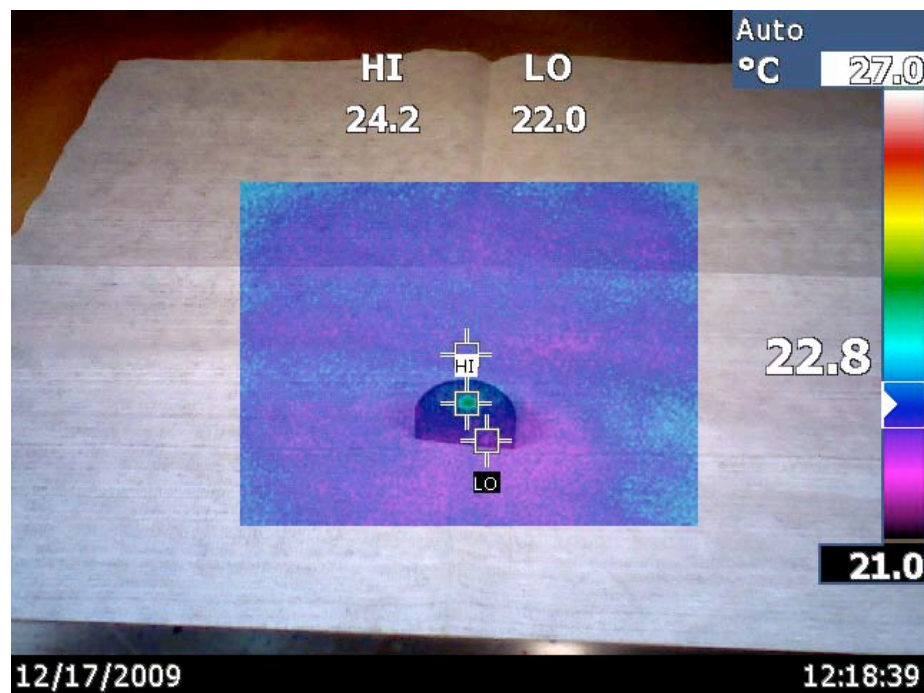


**Figure 6.26:** Composite optical and thermal image of americium oxide heat source indicating heat production at a rate of 5.9 mW.

Sample L3-1 had a mass of 0.1260 g, of which approximately 0.064g was prepared for SEM analysis. Figure 6.26 shows that the ambient temperature during imagery was approximately 22 °C. The peak temperature of the sample was observed to be 24.2 °C. Assuming that limitation of the peak temperature is mostly dominated by radiation losses to the surroundings it is possible to estimate the specific power that would give rise to the sample temperature observed via the use of the Stefan-Boltzmann equation (see Equation 2.26). An estimated radiating surface area of  $1.5 \times 10^{-5} \text{ m}^2$ , and an emissivity of 0.9 was used to estimate a radiated power of 5.97 mW and a specific power of 0.093 W/g. Thus examination of Figure 6.26 reveals an estimated specific power that is approximately equal to the value of 0.094 W/g as determined by DSC analysis.

## 6.8 Discussion and Conclusions

The results from the study of the AmO<sub>2</sub> feedstock indicate that a high purity feedstock is available in sufficient quantities for heat source fabrication. The specific thermal power was estimated to be  $0.094 \pm 0.002 \text{ W/g}$ .

Due to the processes of autoradiolysis, the crystal structure of AmO<sub>2</sub> becomes damaged resulting in the expansion of its unit cell volume [13]. For the encapsulation process to yield a source that is capable of long-term operation without compromise due to swelling, it is important to utilize the most volumetrically stable compound. Am<sub>2</sub>O<sub>3</sub> is a hexagonal close packed crystal and its resistance to swelling has been observed in the context of autoradiolysis [13]. Data presented by Konings et al. and shown in Figure

6.27 [14] indicate that the melting temperature of americium sesquioxide is marginally higher than that of americium dioxide. Confirmation of the sesquioxide resistance to swelling must be confirmed in a future time dependant study of encapsulation matrices. However, the results of the current work suggest that the choice of americium sesquioxide is advantageous due to the physical stability of the overall encapsulate. It has been demonstrated that the process of americium dioxide to sesquioxide conversion via redox and forced dissociation is possible in short cycles under the conditions of spark plasma sintering.

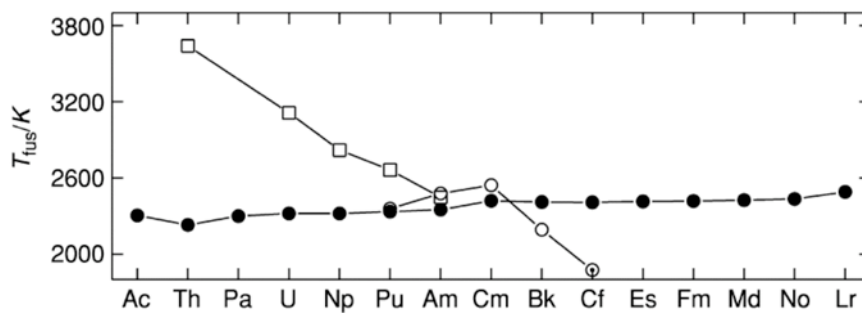


**Figure 6.27:** The melting points of the lanthanide sesquioxides ●, the actinide sesquioxides ○, and the actinide dioxides □ [14].

The sample pellets were pressed to simulate the effect of the applied pressure conditions of Spark Plasma Sintering. It is anticipated that any dissociation and reduction of americium oxide within cermets produced via SPS may be enhanced at the surface and may vary as a function of depth and radius. Such spatial response is due to the relaxation of the green pellets upon removal from the die and the effective vapour pressures exhibited by the  $\text{AmO}_2$ . Any completely reduced americium oxide or sesquioxide would result in the production of free metallic americium. This is most likely to occur at the surface. It would be possible for Am metal to leave the  $\text{W-Am}_x\text{O}_y$  matrix at elevated temperatures due to its melting temperature of  $1149 \pm 5$  K. Thus for the deliberate reduction of  $\text{AmO}_2$  to  $\text{Am}_2\text{O}_3$  via the SPS encapsulation process, it is

important that minimum force be applied during the early stages of sintering to yield a uniform (but incomplete) reduction to Am metal in the region of the surface.

The processing conditions represented by the DSC sintering profile used in this study indicate that the reduction of the  $\text{Am}^{\text{III}+}\text{O}_2$  feedstock to  $\text{Am}^{\text{III}+}_2\text{O}_3$  is possible for short processing times, for the feedstock morphology used. Due to the absence of thermochemical data for  $\text{AmO}_2$  vapour, an estimate of the rate of reaction cannot be determined at this time, but is of concern. No americium metal was detected at the surface of samples via XRD. It can be seen throughout the DSC results that the onset of significant reduction of the americium feedstock occurs at approximately 700 °C. This can be seen in the form of a Gaussian exotherm that continues until the sample is restored to a temperature less than 700 °C via cooling. This exothermic event is also enhanced by the formation of tungsten carbides, whose activation is likely assisted via the release of energy during  $\text{AmO}_2$  reduction.

Overall, good uniformity of tungsten-americium oxide dispersions within the cermet matrix has been produced, thus demonstrating that micro-encapsulation of the americium oxide is possible using feedstock blends arising from the ball mill mixing process. Further examination of alternative mixing techniques will be investigated by the author in future studies to eliminate the need for ball milling, thus reducing the production of fine particles of isotopic compounds during mixing. Evidence for reaction sintering of the resultant oxides during the reduction of  $\text{AmO}_2$  to  $\text{Am}_2\text{O}_3$  suggests that heat evolution during bulk processing must be considered and appropriate furnace controls should be implemented in order to prevent overheating. Future DSC assessment must be performed on new cermet samples in order to characterise

reduction rates of reaction for specific mixture ratios of feedstock and morphology should this be required.

## 6.9 References

- [1] R.C. O'Brien, R.M. Ambrosi, N.P. Bannister, S.D. Howe, H.V. Atkinson, "Safe radioisotope thermoelectric generators and heat sources for space applications". *Journal of Nuclear Materials*. 377 (2008) 506-521.
- [2] R.C. O'Brien, R.M. Ambrosi, S.D. Howe, N.P. Bannister, H.V. Atkinson. "Fabrication of prismatic fuel elements for space power and nuclear thermal propulsion reactors by spark plasma sintering". Proceedings of: Nuclear and Emerging Technologies for Space (NETS-2009), Paper Number 206153; June 14-19, 2009; Atlanta, GA.
- [3] D.E. Burkes, D.M. Daniel, J.E. Werner, S.D. Howe. "An Overview of Current and Past W-UO<sub>2</sub> CERMET Fuel Fabrication Technology". Proceedings of: 2007 Space Nuclear Conference, 2007; Boston, MA.
- [4] B.E. Smith, "*Basic Chemical Thermodynamics*". Imperial College Press, London; 2004. ISBN: 1-86094-445-0.
- [5] Ihsan Barin, "*Thermochemical data of pure substances*". Vol I & II; 1989. ISBN: 0-89573-866-x.
- [6] R.J. Silva, G. Bidoglio, M.H. Rand, P.B. Robouch, H. Wannwer, I. Puigdomenech, "*Chemical Thermodynamics of Americium*". Elsevier Science; 1995. ISBN: 044482281x.
- [7] C. Thiriet, R.J.M. Konings, "Chemical thermodynamic representation of AmO<sub>2-x</sub>". *Journal of Nuclear Materials*. 320 (2003) 293-298.
- [8] "*ImageJ*" [computer program]. Version 1.43; 2009.
- [9] A. Choukourov, A. Grinevich, O. Polonskyi, et al., "Vacuum Thermal Degradation of Poly(ethylene oxide)". *J.Phys. Chem. B*. 113 (2009) 2984-2989.
- [10] Daresbury Laboratory. "ICSD Inorganic Crystal Structure Database". Daresbury Laboratory, Daresbury WA4 4AD, United Kingdom.
- [11] "*CrystalMaker for Mac OS X*" [computer program]. Version 7.2.4. CrystalMaker Software Ltd., Yarnton, Oxfordshire, United Kingdom; 2007.
- [12] D. Chakraborty, J. Mukerji, "Characterization of silicon nitride single crystals and polycrystalline reaction sintered silicon nitride by microhardness measurements". *Journal of Materials Science*. 15 (1980) 3051-3056.
- [13] W.H. Runde, W.W. Schulz. "Chapter 8 - Americium". *Chemistry of the Actinides and Transactinide Elements*. Springer; Dordrecht, The Netherlands: 2007; pp.1265 - 1395. ISBN: 1-4020-3598-5.
- [14] R.J.M. Konings, L.R. Morss, J. Fuger. "Chapter 19 - Thermodynamic properties of actinides and actinide compounds". *Chemistry of the actinide elements*. Vol 4. Springer; Dordrecht, The Netherlands: 2007. ISBN: 1-4020-3598-5.

# 7

## **Potential applications and mission architectures enabled by nuclear power and propulsion systems**

The Nuclear Thermal Rocket (NTR) is considered by the author to be an essential near term technology development for the improvement of efficiency of space exploration to Mars and beyond. Mass and economic savings have also been determined through the use of NTRs for near Earth missions such as the placement of payloads on the surface of the moon from a low Earth orbit [1]. In Chapter 6 it has been suggested that historical difficulties with fuel form production may be overcome by modern sintering techniques and that the adoption of tungsten alloy cermet-based fuels may solve the problems of fragility and susceptibility to erosion and fission product release from the fuel matrix. The limitation to nuclear energy in space will always be driven by a combination of economics and socio-political support. Provided that these materials challenges can be overcome and that sufficient public understanding and support can be generated, it is perceived that the already demonstrated principle of NTR propulsion will become a practical option for NASA by the mid-twenty-first century.

Many exciting applications to nuclear energy in the context of space exploration are conceivable, limited only by imagination. The author presents three examples of such applications below.

## 7.1 Melt Penetration Missions

The subsurface environments of planets and icy moons are of great interest to planetary scientists since ice crusts or caps form an effective hermetical seal that preserve microbial colonies and biological life markers [2] and protect volatile chemicals from intense radiation such as in the Jovian system, or severely cold temperatures and low pressures such as on Mars. Without conclusive analysis through in-situ or sample return methods, the precise composition of ice crust is largely inferred from spectral analyses from surfaces or cryovolcanic ejecta in the case of Europa and Ganymede, two of Jupiter's largest moons. Cryovolcanic activity was observed on Saturn's moon Enceladus by NASA's Cassini spacecraft (see Figure 7.1). It is believed that the cryovolcanic plumes originate from fractured regions on the surface of Enceladus that are often referred to as 'tiger stripes'.

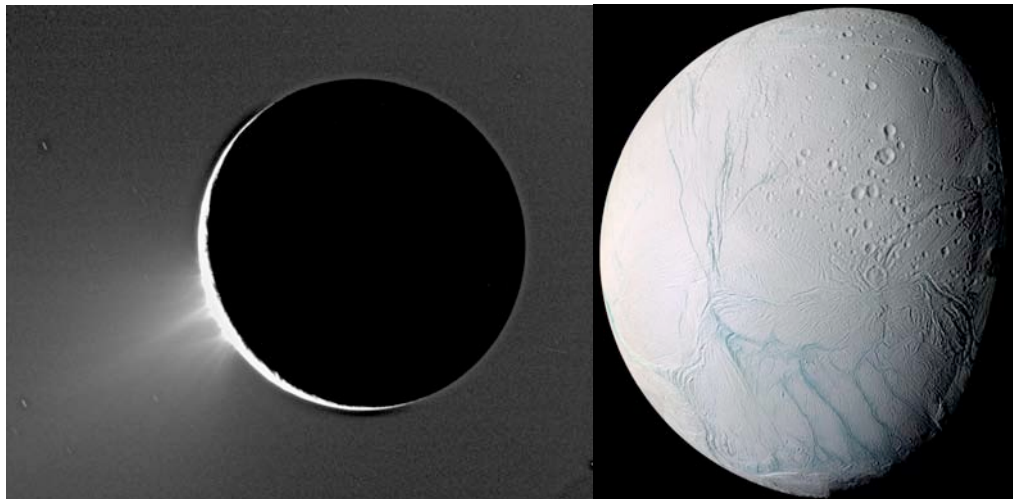


**Figure 7.1** Evidence for cryovolcanism on Enceladus as observed by NASA's Cassini spacecraft in 2005. Images courtesy of NASA, Cassini Imaging Team.

Water is the most abundant and refractory ice in the Solar System [3], whereas nitrogen and carbon bearing ices are likely to condense at extremely cold temperatures that exist at large orbital radii from the sun [3]. More specifically, ancient ices at

temperatures less than 220 K, pressures less than 0.2 GPa and under the effects of bombardment by protons, UV, and ionising radiation exposure such as the case for Jovian and Saturnian moons, water ice most commonly exists in one of three phases of amorphous ice and hexagonally crystalline ice  $I_h$  [4]. These are Restrained Amorphous ice ( $I_{ar}$ ), Low Density Amorphous ice ( $I_{al}$ ) and High Density Amorphous ice ( $I_{ah}$ ) [4]. Table 7.1 details the basic properties of water ice at low pressure and after bombardment by electrons and annealing over time.

Name	Structure	Density, $\rho$ g/cm <sup>3</sup>	Form after electron bombardment	Form after annealing
$I_h$	Hexagonal	$0.93 \pm 0.02$	$I_h$	$I_h$
$I_c$	Cubic	$0.93 \pm 0.02$	$I_c$	$I_h$
$I_{ar}$	Restrained Amorphous	$0.93 \pm 0.02$	$I_{ar} + I_c$	$I_h$
$I_{al}$	Low Density Amorphous	$0.94 \pm 0.02$	$I_{ar} + I_c$	$I_{ar} + I_c / I_{al}$
$I_{ah}$	High Density Amorphous	$1.10 \pm 0.10$	$I_{ah}$	$I_{al} / I_{ah}$

**Table 7.1** – Forms of water ice at low pressure [4].

The self-diffusion or diffusivity coefficient ( $D$ ) of  $H_2O$  molecules within ice lattices is useful in determination of the rate of annealing for ices and is weakly dependant upon the thermal diffusivity within the lattice. Little data exists for the molecular diffusivity of high-density amorphous ices but is estimated by Kouchi et al. to exist within the shaded regions of Figure 7.2 below.

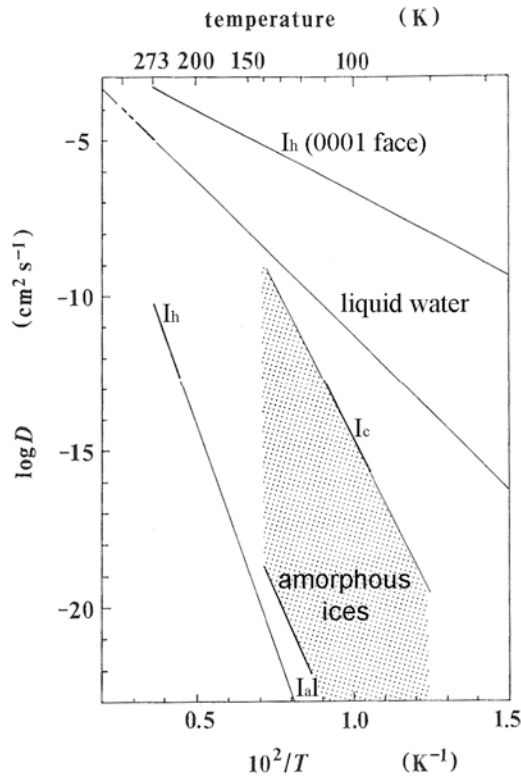


**Figure 7.2** Coefficient of diffusivity of different ice phases compared to that of water as a function of temperature [5].

The thermal diffusivity of ice has been estimated to be around  $1.04 \times 10^{-7} \text{m}^2 \text{s}^{-1}$  at 100 K and varies linearly with respect to temperature by the function  $\alpha_L = [1.35 + 0.002(T - 273)] \times 10^{-7} \text{m}^2 \text{s}^{-1}$  [6]. This is somewhat comparable to the molecular diffusivity of the amorphous ices at 100 K as illustrated in Figure 7.2.

Since the drilling of rocks using traditional rotary drill technology typically results in the blunting of the cutting surfaces of the drill while penetrating hard surfaces such as rock and ice, a practical limit is imposed on the depth to which a single drill head can reach. An alternative to mechanical cutting is melt drilling, in which sufficient energy is deposited into a localised region of the material to be penetrated up to and beyond the point that the melting temperature of the material is exceeded. Laser drilling and hot water drilling are methods of melt drilling, but are typically power intensive. Hot water drilling has been successfully applied to the production of bore holes into

glacial structures and ice sheets [7] for geological research. Here, surface snow or ice water stored within a tank is melted via a heat source, typically fuelled by diesel or kerosene. In order to initiate drilling, the heated water is pressurised and ejected through a nozzle onto the ice surface that is to be penetrated. The process continues and the depth increases as the surface is melted and melt water is removed and recycled into the hot water system. Most glacial ice sheets and indeed oceanic ice sheets are extremely dynamic [8], often resulting in the production of extreme shear forces [9] upon articles and structures that are frozen into the ice structure. For this reason, during hot water drilling, thermal energy must be continuously deposited into the walls of the ice in order to maintain the desired aperture of the borehole while simultaneously advancing the depth. Depending on the depth and diameter of the required borehole, a vast quantity of energy must be transferred to the ice while hot water drilling. The combustion of kerosene yields around 39 MJ per litre. Typical hot water ice drilling operations to depths of around 2.5 km at 254 mm diameter requires the combustion of around 49,000 litres of kerosene [10]. Clearly such melt drilling via chemical combustion is unsuitable for space missions.

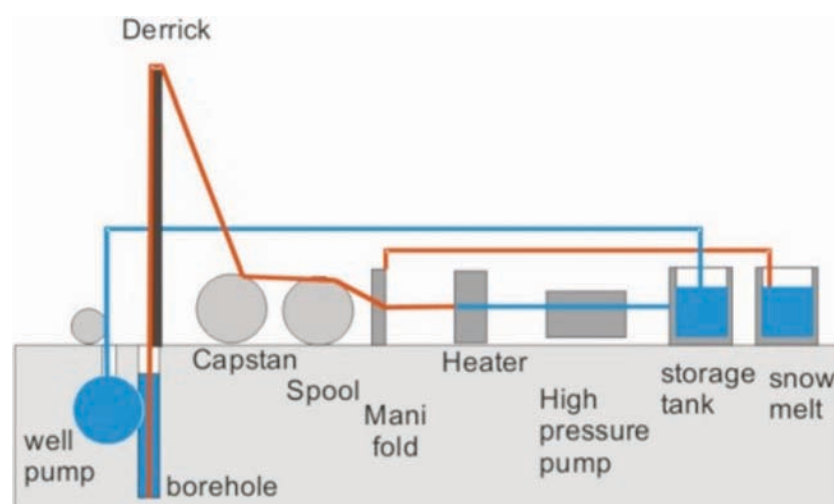


**Figure 7.3:** Schematic of a hot water drill system [7].

Instead of utilising energy released during chemical combustion, nuclear power lends itself well to an alternative technique in melt drilling due to the vast energy capacity of a compact radioisotope or nuclear power source. Work undertaken by Los Alamos National Laboratory resulted in a series of concepts for melt penetrators that were powered and heated via a small nuclear reactor [11]. The Los Alamos designs were focussed upon the penetration of rock for tunnel excavation purposes, however the principal of rock penetration is essentially identical to that of ice penetration. Practical demonstration of subscale, electrically heated prototypes of the design proved extremely successful [12]. Here, heat generated via the nuclear fission process is delivered to the rock surface to be penetrated via refractory heat pipes [11]. In doing so, the temperature of the rock interface is raised above its melting temperature and due to the application of an axial propulsive force in the direction of desired travel, the penetrator is advanced to a greater depth [11]. As the penetrator is advanced, molten material is transported across the extremity of the device where it is cooled via natural conduction and radiation or assisted by water spray cooling [11], thus forming an amorphous glassy wall.

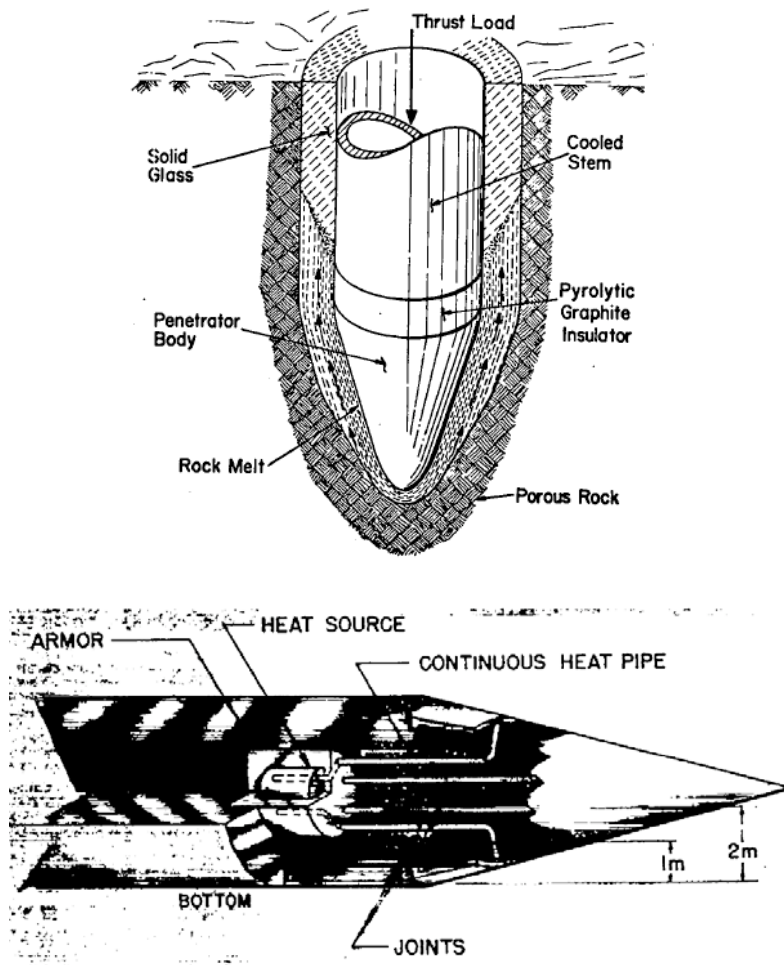


Figure 7.4: Concept penetration of rock via nuclear subterrene [12].

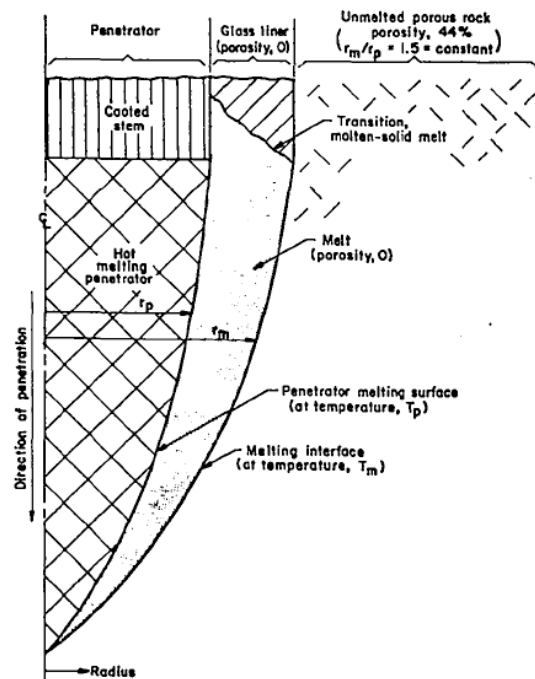


Figure 7.5: Cross sectional characteristics of rock penetration via a nuclear subterrene [13].

The Los Alamos Subterrene concept presents an exciting solution to the penetration of both icy and rocky planetary surfaces. The high power density and the ability to produce small, compact fast spectrum fission reactors is highly suitable to flagship missions. Questions are often raised over the reliability and safety of space reactor designs in terms of operational lifetime and accident security. Such concerns may be addressed through careful reactor design and fuel form selection so as to ensure safety under all nominal and accident conditions [1].

*Pulsed Penetration by Radioisotope Power:*

As an alternative to the adaptation of reactor technologies, a smaller, less complicated platform could be developed to offer similar long-range ice penetration capabilities while fuelled by a radioisotope heat source. Preliminary work on this concept has been conducted at the Jet Propulsion Laboratory (JPL) at the California Institute of Technology into a Cryo-Hydro Robot (CHIRPS) that is powered by 4 or 5 General Purpose Heat Source (GPHS) modules [14], generating a thermal output in excess of 1 kW [15].

In the current work, a different approach is suggested for the method of heat delivery to the ice. As an alternative to the continuous coupling of a radioisotope heat source to the surface of the ice, an intermediate thermal energy storage mechanism can be employed that can be thermally isolated from the penetrated material at the end of periodic thermal discharge / penetration cycles. In doing so, energy is accumulated in between thermal discharges and the temperature of the heat source is recovered. The

use of a thermally capacitive heat source allows for a smaller radioisotope inventory to be used while achieving higher initial heat source temperatures. Due to the nature of the thermal cycling process, a period of time is required for the temperature of the heat source to recover, thus the rate of penetration is significantly dependant upon the recovery time and hence thermal design.

Initially, the capacitive heat source is thermally isolated from the outside environment via an insulated linear actuator so that the decay heat produced by the radioisotope raises the temperature of the heat source. Once the desired operational temperature has been achieved, the linear actuator is used to thermally connect the heat source to the inside of a thin walled region in the penetrator's shell, where efficient coupling to the ice can be made. Heat is supplied to the surface of the ice so that the melting temperature is exceeded. Simultaneously, forward thrust is applied via internal momentum transfer actuators, such as those used by the Beagle 2 Mole [16], and a piston at the rear exterior. The mechanical thrust may be enhanced via steam production and the sublimation of volatiles trapped within the ice. When the stored heat has been transferred to the ice, the heater cools to a pre-determined temperature, thus pausing the depth advancement. In order to continue with penetration, the heat source must be decoupled once again from the ice and allowed to re-attain its initial temperature. The penetration process continues through multiple cycles until the desired depth has been achieved.

Radiated heat that would otherwise be lost to the environment may be harnessed through Thermophotovoltaic, infra-red antenna arrays [17] or through thermoelectric converters coupled to a black body thermal absorber (graphite). Similarly, heat pipes

may be used to transfer energy from a graphite absorber to a pair or multiple pairs of Free Piston Stirling engines.

The heat source design requires the use of a material that has a high specific heat capacity over the temperature range of interest, with a radioisotope loading nested inside the heat capacitor matrix. The use of tungsten-radioisotope cermets [18, 19] installed in a beryllium matrix is an appropriate solution to this requirement from a thermo-mechanical and safety standpoint. Beryllium is capable of providing significant shielding of neutron fluxes generated by the radioisotope source while offering excellent thermal conductivity and large heat capacity. Work performed by Karditsas et al. [20] at the United Kingdom Atomic Energy Agency Fusion Division has evaluated the specific heat capacity of Be as a function of temperature over the range of 300 K to 1500 K. The data presented by Karditsas et al. [20] are plotted in Figure 7.6 below. The specific heat capacity of Beryllium was found to vary by the function  $C_p = 974.77 \ln(T) - 3668.70$ .

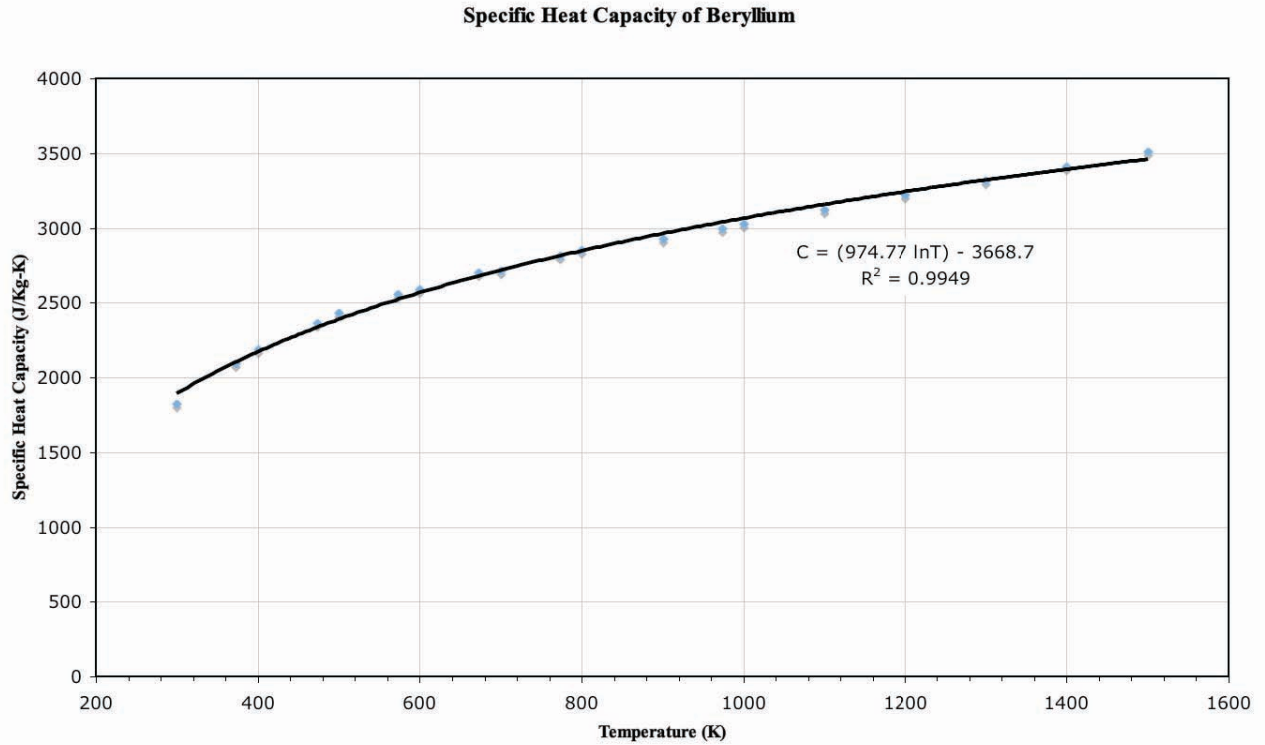


**Figure 7.6:** Plot of data produced by Karditsas et al. [20] for the specific heat capacity of Beryllium as a function of temperature.

*Thermal Requirements:*

In order for a heated penetrator to melt through a solid surface, the temperature of the surface material must be elevated to a temperature that is greater than or equal to its melting temperature. In order to determine the minimum energy requirements for the penetrator, it can be assumed that the maximum temperature achieved in the surface is equal to the melting temperature. Equation 7.1 relates the energy required to raise the temperature of a mass of material  $m$  and specific heat capacity  $C_p$  to its melting point  $T_m$  from an initial steady state temperature  $T_0$ .

$$Q_{\Delta T} = mC_p(T_m - T_0) \tag{7.1}$$

**Equation 7.1:** Energy  $Q$  required to raise material of mass  $m$  and specific heat capacity  $C_p$  to its melting point  $T_m$  from its initial temperature  $T_0$ .

In order for a mass of material held at its melting temperature to undergo the solid-to-liquid phase change, energy must be supplied to the material equal to the total latent heat of fusion  $\Delta H_L$  for the solid. Equation 7.2 relates this energy requirement to a sample of mass  $m$ .

$$Q_M = m\Delta H_L \quad (7.2)$$

**Equation 7.1:** Energy  $Q$  required to melt material of mass  $m$  and latent heat of fusion  $\Delta H_L$ .

In context of a descending melt penetrator at steady state temperature, the mass of material that is melted is constant at any given time, but the position at which the energy is deposited is continuously moving at a velocity  $v$  equal to that of the penetrator descent rate. Therefore, an estimate of the minimum energy and hence power requirements for a moving penetrator can be made via the substitution of the mass  $m$  with the product of penetrator cross sectional area, density and velocity, and thus finding the sum of the solutions for Equations 7.1 and 7.2. This is presented as Equation 7.3.

$$\dot{Q}_{\Delta T M} = \rho v \pi r_p^2 ( \{ T_m - T_0 \} C_p + \Delta H_L ) \quad (7.3)$$

**Equation 7.3:** Energy  $Q$  per unit time or power required to heat and melt a vertical shaft with a radius that is greater than or equal to the radius of the melt penetrator  $r_p$  at a penetration rate of  $v \text{ ms}^{-1}$  and where  $\rho$  is the density of the ice or material to be penetrated.

The energy requirements are higher in practice due to conduction losses across the interface between penetrator and bulk material. As such, a temperature gradient will be established from the penetrator head temperature down to the ambient temperature. Determination of these losses will vary with respect to ambient temperature  $T_0$ , heater head/ penetrator length  $l$ , penetrator radius  $r_p$  and material properties such as thermal conductivity at each time step in the descent profile.

Since the heat losses forward and radial from the penetrator are determined at each time step, consideration may be required into thermal diffusion from these points under certain situations. Work undertaken by Ling et al. [21, 22] into moving heat sources in the context of mechanical bearings suggests that where the velocity of the heat source is much greater than the ratio of thermal diffusivity  $\alpha$  to penetrator length  $l$ , the heat may be treated as quasi-stationary. This is interpreted physically as a conditional requirement for the penetrator to move at a penetration rate  $v$  that is much faster than rate at which heat can diffuse along  $l$ . It is found empirically that the relationship in Equation 7.4 must be valid with a value of two orders of magnitude or higher [21, 22]. Thus, penetration will only occur where Equation 7.4 holds true.

$$v \gg \frac{\alpha}{l} \quad \therefore \frac{v}{\alpha/l} \geq \sim 1 \times 10^2 \quad (7.4)$$

**Equation X.4:** *Velocity condition for neglect of thermal diffusion.*

In the case of a pulsed radioisotope system, the rate at which energy is transferred to the ice surface is directly proportional to the temperature of the core and hence penetrator head. Since the temperature is exponentially proportional to contact time with the surface, so too is the penetration rate. Penetration will therefore advance at an initial rate  $v_0$  and will decrease exponentially until the penetrator is stationary where thermal diffusion rates within the bulk ice are greater than or equal to the rate at which energy may be supplied from the hot head of the penetrator.

As an example, for low density amorphous ice held at 100 K, the thermal conductivity  $\lambda$  of the ice has been estimated to be between  $0.6 \text{ Wm}^{-1}\text{K}^{-1}$  for  $70 \text{ K} < T < 135 \text{ K}$  by James [6] and  $3.948 \text{ Wm}^{-1}\text{K}^{-1}$  for ice at 100 K by Fukusako [23].

For the purpose of this example, the value determined by Fukusako shall be used. The specific heat capacity  $C_p$  is approximately  $1392 \text{ J.kg}^{-1}.\text{K}^{-1}$  and the density of the amorphous ice is assumed to be  $0.94 \text{ g/cm}^3$  [4]. The thermal diffusivity of the amorphous ice  $\alpha$  is  $3.017 \times 10^{-6} \text{ m}^2.\text{s}^{-1}$  as calculated from Equation 7.5, which is of order of magnitude to the results produced by James [6].

$$\alpha = \frac{\lambda}{\rho C_p} \quad (7.5)$$

**Equation 7.5:** Thermal diffusivity  $\alpha$  of a material with density  $\rho$ , thermal conductivity  $\lambda$  and specific heat capacity  $C_p$ .

Thus for a penetrator of length  $l = 50 \text{ cm}$ , the minimum penetration rate for the energy uptake from the heat source to dominate in melting over thermal diffusion according to Equation 7.4 is approximately  $0.6 \text{ mm/s}$ . Understanding the velocity and thermal energy requirements for melt penetration and providing that Equation 7.4 is valid, penetration will occur and thus an estimation of the minimum energies required to penetrate the surface may be made via implementation of Equation 7.3.

Using the same example with a velocity of  $0.6 \text{ mm/s}$ , which we have shown to be the minimum velocity for model validity, we can estimate that the minimum penetration thermal power requirement is approximately  $8.38 \text{ kW}$ . The parameters used for this calculation are outlined in Table 7.2 below.

Parameter	Value
Penetrator radius, $r_m$	10 cm
Penetrator length, $l$	50 cm
Ice Melting temperature, $T_m$	273 K
Ice Ambient temperature, $T_0$	100 K
Ice Specific Heat Capacity, $C_p$	1392 J.kg <sup>-1</sup> .K <sup>-1</sup> [23]
Ice Density, $\rho$	940 kg.m <sup>-3</sup> [4]
Latent heat of fusion $\Delta H_L$ at 273 K	333.9 kJ.kg <sup>-1</sup> [23]
Penetration rate, $v_{ave}$	0.6 mm.s <sup>-1</sup>
Useable heat source capacity	4 MJ
Radioisotope / form	<sup>238</sup> PuO <sub>2</sub> in W cermet
Radioisotope thermal loading	200 W <sub>th</sub>
Heat source geometry	Conical
Heat source height & radius	16.8 cm x 8.4 cm
Minimum core to ice conducted power	8.38 kW
Pulse operational period	480 seconds

**Table 7.2:** Parameters used for example calculation for a melt penetrator.

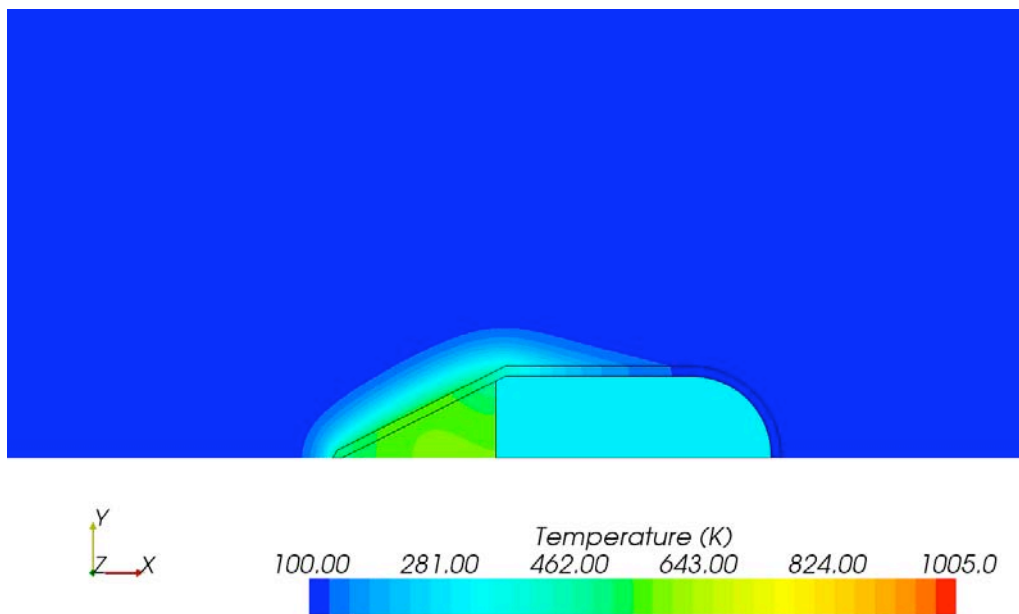


**Figure 7.7:** CFD temperature plot exceeding ice sublimation conditions for a stationary penetrator at 30.8 seconds after initial thermal contact of core to ice. In this plot, the x-axis represents the axis along which penetration would proceed.

In order to examine the melt capability of this system, an axially symmetric computational fluid dynamic (CFD) model was generated in order to determine its time dependant behaviour. A snapshot of a stationary penetrator at a frozen position is shown in Figure 7.7 at a time of 30.8 seconds after initial contact of the core with a

conductive wall. This demonstrates the capability of the system to induce surface vaporisation of localised regions of ice, showing that sufficient melt can be achieved with a radioisotope powered heat capacitor. Further analysis of melt penetration missions using radioisotopes will be the subject of future papers. Detailed analyses and comparison of pulsed and continuous penetration schemes will be the subject of a future paper.

## **7.2 A Mars Hopper**

The desire for surface exploration platforms with long-range mobility on Mars, or indeed on the surface of any planetary body or moon, is of extreme interest to planetary scientists. To date, exploration has been successfully performed by landers targeted at a specific site of interest, such as the Viking 1 and Viking 2 [24], and the Phoenix Polar lander [25] missions, or wheeled rovers such as Mars Pathfinder [26] and the Mars Exploration Rovers (MERs) Spirit and Opportunity [27]. The issues of power and wheeled traction limit from the maximum achievable range of such platforms. Although remarkable in their performance, the MERs have only covered distance of 8.7 km (Spirit) and 18.6 km in a period of 5 years [27]. Although there is some benefit in strategic spot sampling based on targeted site selection from high resolution mapping instruments, spot sampling at a few locations, with a selection bias towards locations that are safe landing sites, will not provide an accurate geophysical map of Mars.

To address these limitations, several airborne Mars exploration programs have been proposed and considered. Balloon, rotor and winged aircraft such as the NASA Aerial Regional-scale Environmental Survey of Mars (ARES) platform [28] have been evaluated, each offering specific advantages and limitations. All three approaches are significantly affected by local atmospheric conditions such as pressure, temperature and density. Rocket propelled platforms have also been evaluated, based on chemical or solar-electric propulsion [29]. Rocket platforms are less affected by atmospheric conditions but introduce different levels of risk due to the complexity of vertical landing and take off control systems. In addition, resistojets [29] and chemical propulsion systems are limited by electrical power and propellant storage.

As described in Chapter 2, rocket propulsion can be achieved through the passing of a propellant through a nuclear heat source such as a fission reactor core. Fission based power sources offer high specific thermal power, but are complex with regard to operation and the required control equipment, and can easily have a mass in excess of several hundred kilograms. For small systems, radioisotope heat sources present a simple and effective solution to the generation of heat. Historically, radioisotope thrusters have been significantly researched and developed. The U.S. POODLE program resulted in the production of a series of radioisotope-powered thrusters that were developed for attitude control of the United States Air Force Manned Orbital Laboratory (MOL). Although MOL was never flown, the POODLE Reaction Control System was tested to Technology Readiness Level six (TRL-6) [30, 31]. Each POODLE engine was fuelled by 3 capsules of  $^{210}\text{Po}$  clad within a tungsten-25% rhenium capsule [30] providing a total thermal inventory of 5 kW [32] and a maximum operating temperature of 1500 °C [30]. Clearly the thermal input power to the

propellant is limited to the thermal inventory of radioisotope present within the thruster and thus the performance of the engine is limited to low levels of thrust [32].



**Figure 7.7:** Author's Illustration of a Mars Hopper powered by a heat capacitive Radioisotope Thermal Rocket (RTR) operating between regions of interest that are inaccessible to wheeled rover platforms.

Based on the beryllium heat capacitor principal described in Section 7.1, work undertaken by the author and colleagues at the Center for Space Nuclear Research at Idaho National Laboratory has identified a novel mission concept that will facilitate long range mobility across the entire surface of Mars, limited only by the half-life of the radioisotope used to supply energy to the heat capacitor. In this design, CO<sub>2</sub> is liquefied from the Martian atmosphere via a miniaturised compressor / refrigeration system and is stored within a tank while a thermally isolated heat-capacitive core is elevated in temperature by radioisotope decay heat. Once the core has achieved its target temperature, CO<sub>2</sub> is fed through a series of flow channels within the core, elevating the temperature of the gas prior to its exit through a rocket nozzle for generation of

propulsive thrust. Unlike Radioisotope Thermal Rocket (RTR) engine designs such as the POODLE Reaction Control System thruster [32], the thrust of a heat capacitive RTR is not limited to the thermal power of the isotope inventory. Instead, the propellant power extraction limit (and hence thrust) is a function of the maximum thermal conductivity of the core-propellant thermal path resistance or thermal conductivity. Figure 7.8 illustrates the proposed CO<sub>2</sub> refrigeration and storage system that, at the time of writing, is under experimental development by the author in collaboration with Utah State University.

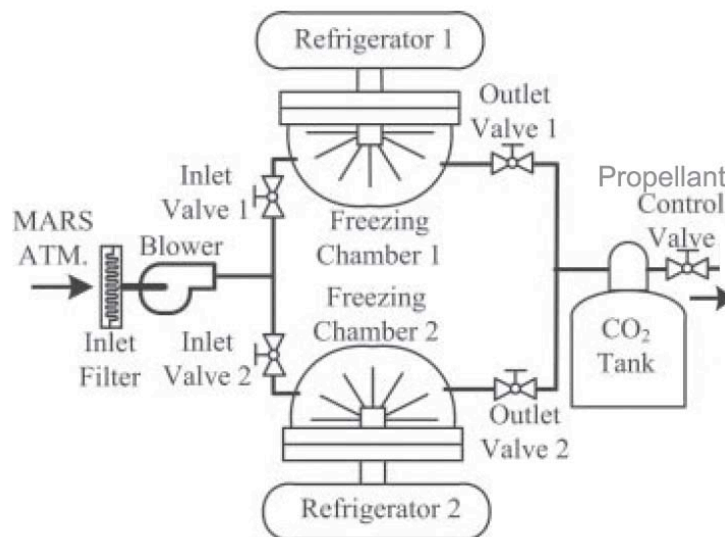


**Figure 7.8:** CO<sub>2</sub> compression and storage system schematic under development by the author in collaboration with Utah State University.

Production and storage of liquefied CO<sub>2</sub> is achieved through the intake of the CO<sub>2</sub> rich Mars atmosphere into a refrigeration chamber. This is facilitated via the use of a simple low power blower pump. Prior to refrigeration, the chamber is sealed via the closing of the inlet valves. Once activated, the refrigeration system chills the gas and results in the freezing of the CO<sub>2</sub> content to form dry ice. Upon freezing, the dry ice is transferred to a smaller chamber where it is melted at 227 K to form self-pressurised

liquid CO<sub>2</sub>. The resultant product may then be transferred and stored in a tank at 227 K under a pressure of 1.93 MPa.

In order to achieve the desired maximum core temperature, the beryllium core will be supported by a zirconium oxide (zirconia) seal and plenum assembly internal to an evacuated chamber. For a specified mass of beryllium and hence a known energy storage capacity, in addition to a specific radioisotope inventory, the thermal losses from the system in the form of conduction through the zirconia and radiation to the interior walls of the vessel will determine the maximum temperature achievable by the design. Thus, a target temperature can be specified and the system geometries evaluated for design performance verification. Provided that the efficient thermal design is achieved, thermal losses to the surroundings will be dominated by radiation. This may be reduced via the application of thin film coatings of reflective materials or by an insulating sleeve such that the surface temperature is maintained at a lower temperature than the bulk core.

Thermal losses via radiation may be harnessed for power generation applications using single or hybrid power conversion mechanisms. This may be possible through the use of a black body absorber on the inner surface of the evacuated vessel that provides a thermal interface between the heat radiated and the hot side of a converter such as thermoelectrics or Stirling engines. Alternatively, the black body absorber may replace the traditional heat exchangers used within a Brayton or Rankine cycle (see chapter 3) by allowing for the flow of a working fluid through its interstitial structure. Such methods of power generation are limited to the steady state and heating modes for the hopper core. Thus, it is implied that an alternative power source be used,

such as a chemical battery where the core is below a threshold temperature, i.e. at the end of a propulsive operation. Figure 7.9 illustrates a potential configuration in which a working fluid is cycled through a black body absorber on the inside vessel wall. A similar approach may be used to preheat propellant prior to injection into the upper plenum of the RTR core.

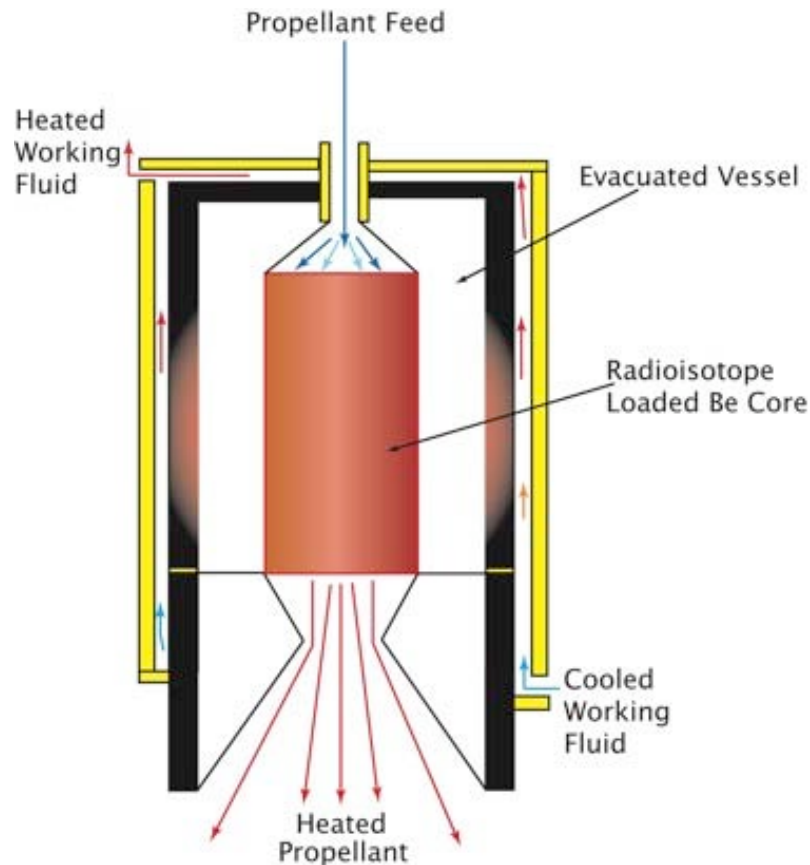


**Figure 7.9:** Schematic of a heat capacitive Radioisotope Thermal Rocket (RTR) engine. Also illustrated is a potential heat exchanger schematic within the walls of the evacuated chamber that may be used directly within a dynamic power conversion system or for the preheating of propellants prior to injection into the upper plenum of the RTR core.

Clearly, the most challenging operation during a Mars Hopper mission would be the repeated landings in unknown or poorly characterised regions of interest. Repeated take-off and landing on a schedule dictated by the thermodynamics of the RTR system will require a degree of autonomy for the Hopper. An orbiting spacecraft can provide high-resolution imagery of potential landing sites, coordinates, an idea of weather

conditions and act as a relay station for transmitting data and communicating with terrestrial stations. Although the level of autonomy is an open issue, as a minimum requirement the “hopping” sequence should be controlled by the craft. As such, highly sophisticated onboard flight control systems are required. Through collaboration with colleagues at the Idaho National Laboratory Robotics and Unmanned Aerial Vehicle (UAV) division, several instruments for the landing system have been identified in addition to their attributed mass and power requirements. These include High altitude and Point Return radar altimeters, 3D optical surface computer vision for low altitude obstacle identification and avoidance control, and low power solid state laser altimeters for medium altitude and point return. Preliminary assessment of the systems required for autonomous operation suggests that a total mass of ~12.6 kg and a power budget of 132 W are required.



**Figure 7.10:** Author’s Illustration of a Mars Hopper at the apogee of its “hop”. Attitude control and ground-looking instrumentation assess and select potential landing sites prior to activation of a descent control firing of the heat capacitive RTR.

A FORTRAN 90 code was developed in order to determine the thermal and kinetic performance of a vehicle propelled by an open cycle CO<sub>2</sub> radioisotope thruster, and to model the ascent and descent flight characteristics. A target range of between 5 and 30 km per flight / hop was used, based on an assessment of existing and planned wheeled rover platform lifetime performance and the desire to sample multiple sites of interest during a two-year Mars circumnavigation mission.

In order to determine the performance of a heat capacitive RTR, the temperature dependency of the specific heat capacity of the core is considered in addition to its thermal conductivity and the reciprocal thermo physical properties of the propellant that will be used. In the case of the Mars hopper simulation code, thermo physical data for CO<sub>2</sub> determined by the National Institute of standards (NIST) [33] was incorporated in addition to the beryllium properties determined by Karditsas et al. [20]. By partitioning the thermal energy content of the core into discrete time intervals after engine start up and through the incorporation of Equations 2.1 to 2.14 (see chapter 2) within the FORTRAN code, the specific impulse and hence thrust is assessed as a function of temperature and time.

$C_p(T) = A + BT - CT^2 + Dt^3 - E/T^2$	
A (298 – 1200 K)	24.99735
B (298 – 1200 K)	55.18696
C (298 – 1200 K)	33.69137
D (298 – 1200 K)	7.948387
E (298 – 1200 K)	6.447293

**Table 7.3:** Specific heat capacity of carbon dioxide as a function of temperature between 298 K and 1200 K [33].

Projection of the hopper platform trajectory is handled by the code accounting for aerodynamic drag, using a specified drag coefficient (C<sub>D</sub>) and platform cross

sectional area, and the time/temperature dependent thrust for a specified CO<sub>2</sub> mass flow rate, constant thrust angle, isotope thermal inventory, propellant mass and payload mass. Since a Mars Hopper must make a soft landing, determination of the optimum timing for the descent and landing burn of the engine is essential. This is performed within the code via an iterative process such that at burnout, the platform has zero horizontal and vertical velocity at the surface of Mars. A safety margin of 5 % for residual propellant at landing is also used in descent burn timing optimisation.

Three cases were studied based on a specified payload mass and energy storage capacity. A case for a 200 kg payload was proposed as a comparison to the payload aboard a flagship class mission such as the Mars Science Laboratory. Similar modelling for a small platform with a payload of 10kg was also considered. Once these parameters were established, the required isotope inventory, propellant and structure mass could be determined. Two heat capacitive beryllium cores were provided for ascent and descent thrust respectively, and the projected range per hop was estimated. For each of the three cases, a summary of the results are presented in Table 7.4. Graphical results for each of the 3 cases are presented in Figures 7.11- 7.13.

Parameter	Case 1	Case 2	Case 3
Mass payload (kg)	200	10	10
Total Energy stored (MJ)	100	100	6
Isotope power (kW)	1	1000	500
Mass <sup>238</sup> Pu (kg)	2.0	2.0	1.0
Number of heat capacitive cores	2	2	2
Mass Beryllium (kg/core)	55.0	55.0	2.16
Mass flow(kg/s)	4.3	3.0	0.6
Mass initial (kg)	850	680	121
Mass propellant (kg)	310	344.	63
Mass final/mass initial	0.66	0.51	.48
Ascent burn time (s)	40	72.	70
Initial Thrust (N)	5421	3812	688
Thrust at Burnout (N)	3840	2487	397
Burn Out Velocity (ms <sup>-1</sup> )	153	241	208
Range (km)	7.37	15.82	11.13

**Table 7.4:** Simulation results for three example Mars Hopper case profiles.

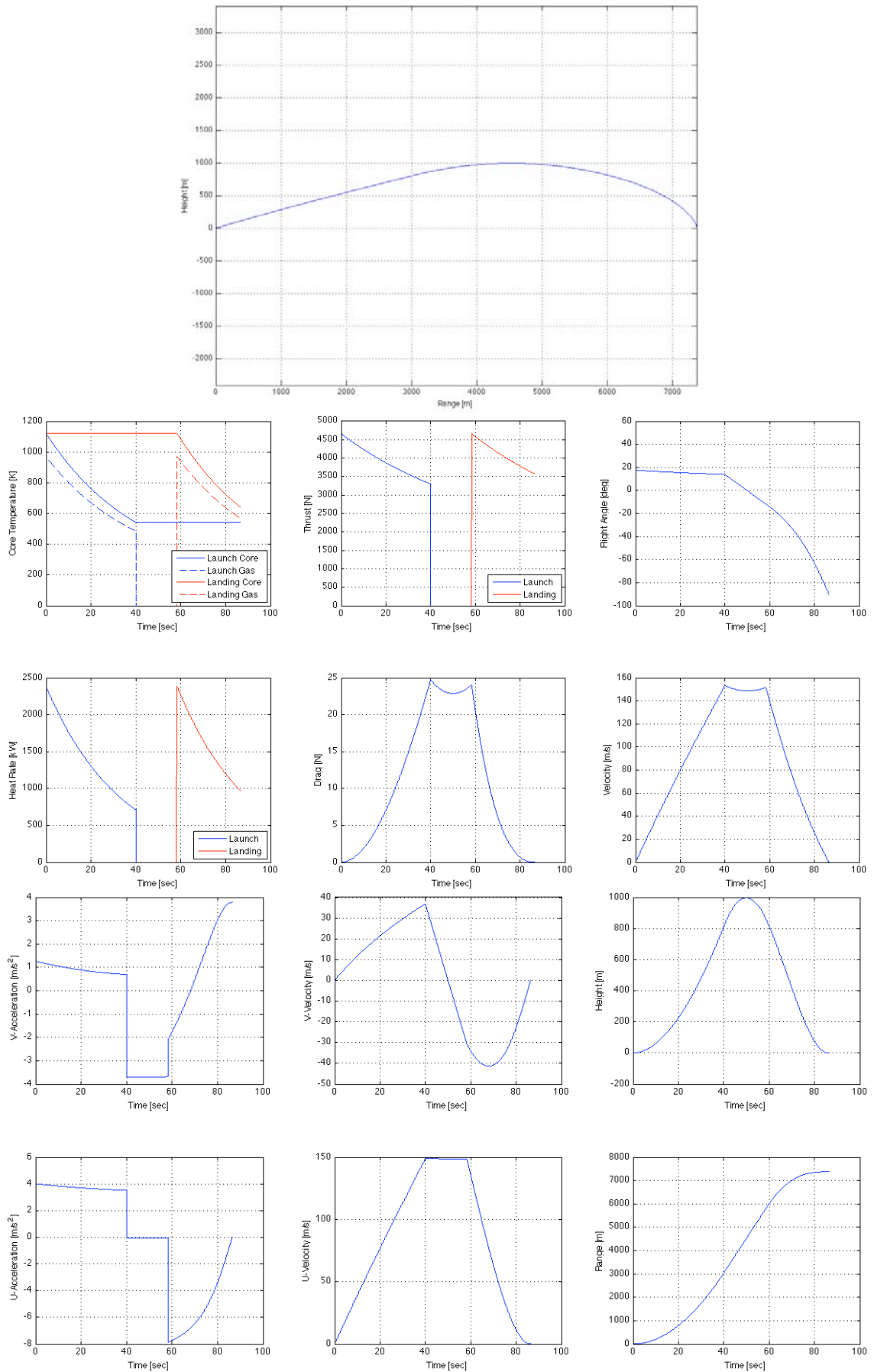


**Figure 7.11:** Performance results for a heat capacitive RTR Mars hopper with a payload mass of 200 kg and 100 MJ of thermal energy storage (Case 1).

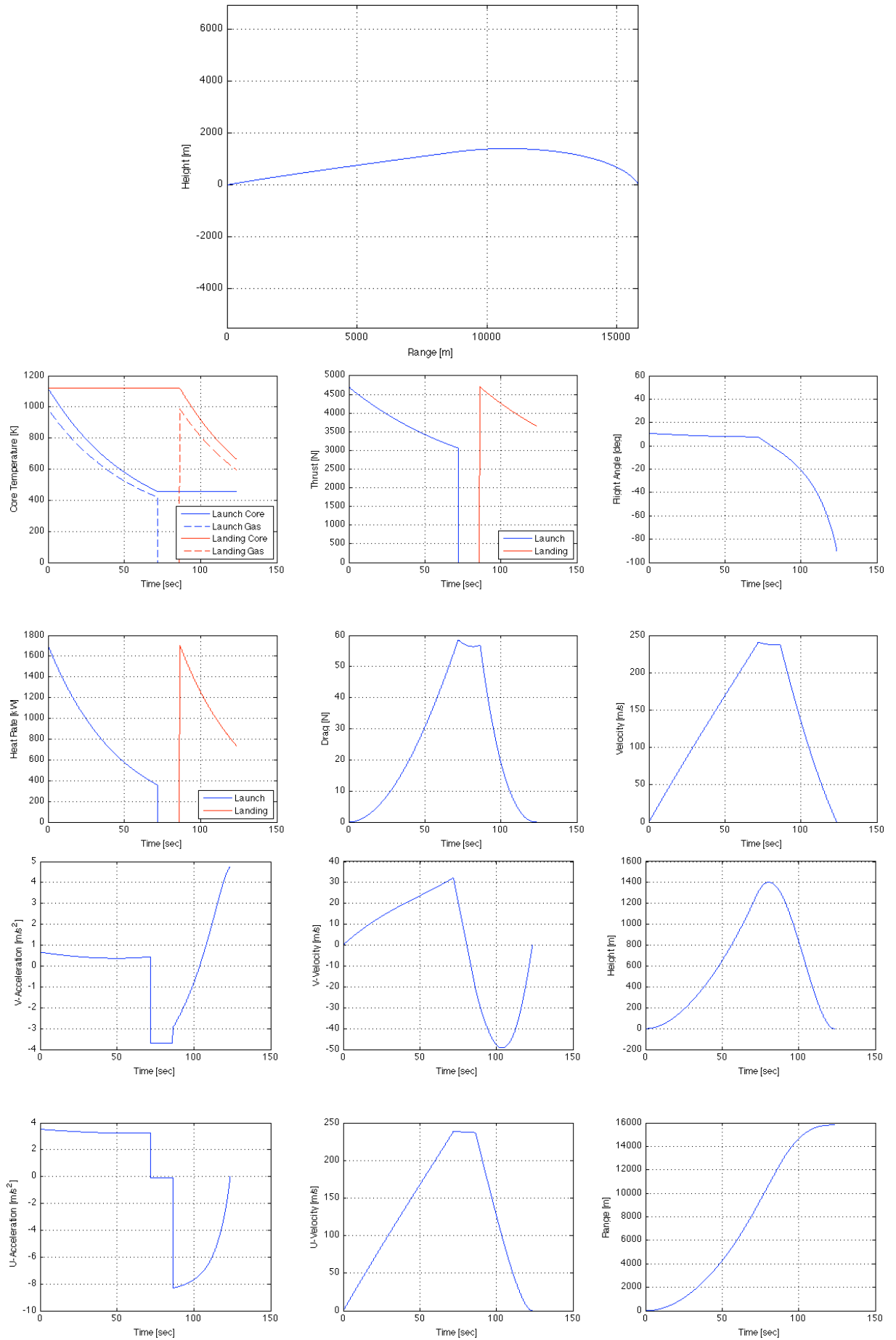


**Figure 7.12:** Performance results for a heat capacitive RTR Mars hopper with a payload mass of 10 kg and 100 MJ of thermal energy storage (Case 2).

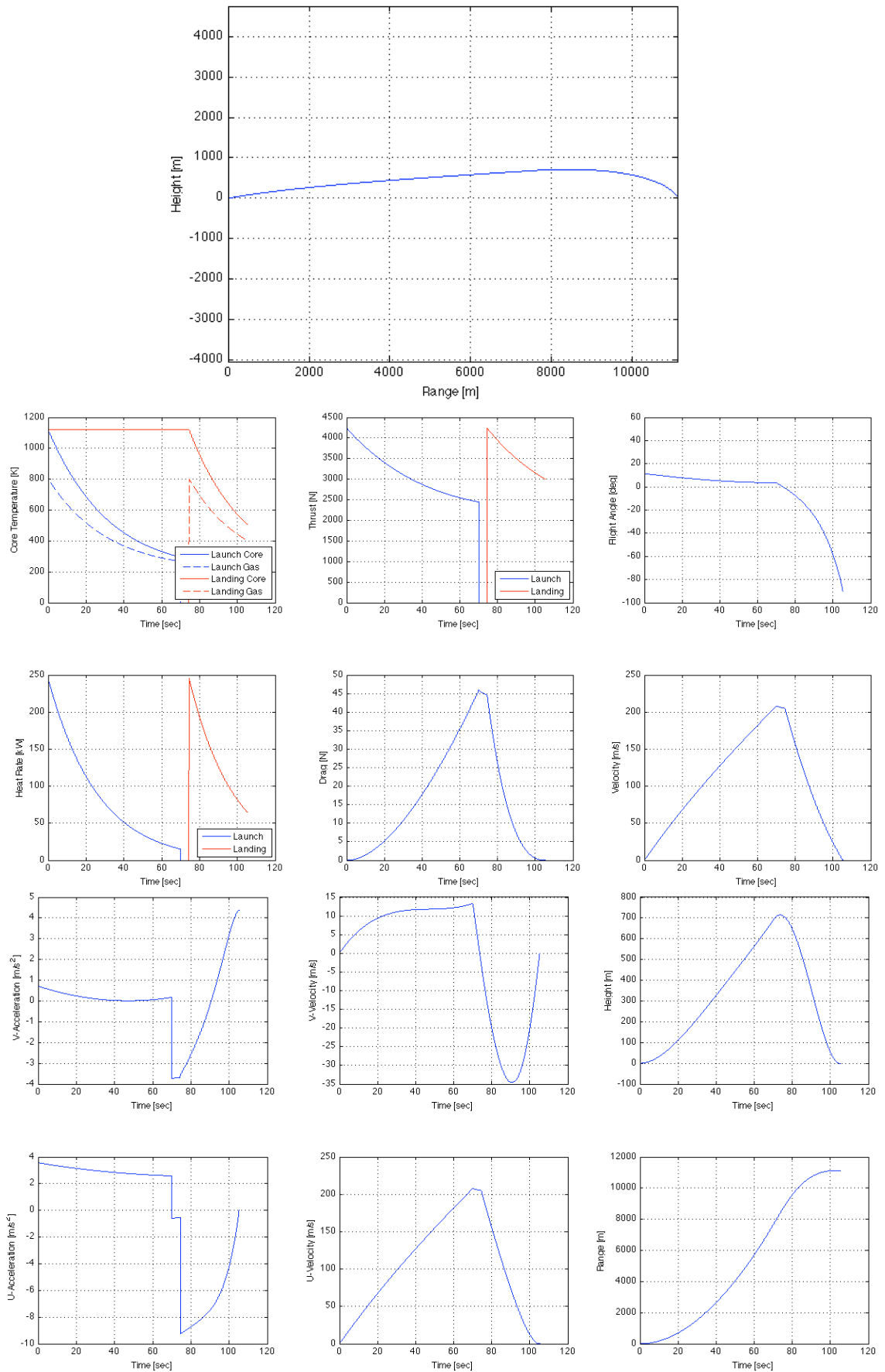


**Figure 7.13:** Performance results for a heat capacitive RTR Mars hopper with a payload mass of 10 kg and 6 MJ of thermal energy storage (Case 3).

The preliminary results presented above indicate that a small, compact systems with a payload of instruments of 10 kg or more can be designed to utilise the in-situ Martian resources to “hop” around the surface via vertical take off and landing under the propulsive power of a heat capacitive Radioisotope Thermal Rocket (RTR). Such a platform may enable high-fidelity data to be acquired at hundreds of sites over a period of a few years. Potentially, this system can travel from the equator to a pole in two years. Thus, a comprehensive set of data using the same instruments can be acquired over much of the surface of Mars. In addition, depositing several of these platforms on Mars may allow the entire surface to be explored within a decade using only a few launches from Earth.

At the time of writing, the author is engaged in a number of proof of concept technology demonstrations for systems and subsystems that may be utilised by a Mars Hopper platform. This work is being performed at Idaho National Laboratory in collaboration with NASA Jet Propulsion Laboratory, NASA Marshall Space Flight Center, Utah State University and Oregon State Universtiy. Demonstration of the RTR core is viewed as a critical development path for escalation of technology readiness level. It is also apparent that given the nature of a beryllium matrix heated by integrated radioisotope heat sources, conventional RPS heat source designs such as the GPHS module are unsuitable for integration due to their low volumetric power density. Thus, the applicability of tungsten cermet isotope encapsulates as described in Chapter 4 is an essential technology development.

### 7.3 Mars sample return via single stage Nuclear Thermal Rocket

The preliminary study of the Mars Hopper concept indicates that a number of samples could be obtained over widely spaced locations in a reasonable period of time. Conceivably 10 samples may be collected over a 150 km range in a period of 10-20 weeks. Alternatively, samples could be collected via rover platforms over extended periods prior to a sample return mission, or a small sample distribution could be obtained from a single mission. The scientific return may be far greater for a large distribution of samples, but this must be considered by mission planners when balancing the economics of the mission.

Regardless of the method of sample collection, the most fundamental challenge presented for a Mars sample return mission is the transportation from the surface of Mars into Mars orbit. The average velocity requirement ( $\Delta v$ ) for injection into a 500 km Martian orbit from the surface is 3.42 km/s [34] and is of the order of the reciprocal landing  $\Delta v$ . It is conceivable that chemical propulsion systems could be utilized to achieve this velocity increment. Unfortunately, chemical propulsion systems imply a particularly large landing mass if the propellants are to be carried from Earth to the Martian surface and, where liquid propellants are concerned, storage for extended periods may present a significant challenge. *In-situ* resource utilization for chemical rocket propellant production has been evaluated by many investigators, most notably Zubrin et al. [35] as a means of reducing the landing mass of a sample return platform on Mars. Such systems not only require propellant compression and storage, but most importantly, rely heavily on an electrochemical plant. Instead, it is proposed that the simple compression system identified for the Mars Hopper concept, be utilized to

liquefy CO<sub>2</sub> as a propellant for a small Nuclear Thermal Rocket (NTR). For CO<sub>2</sub> gas with a ratio of specific heats ( $\gamma$ ) of 1.28 heated in the core of an NTR operating at a temperature of 3000 °C, a characteristic velocity ( $c^*$ ) of 1184.21 ms<sup>-1</sup> can be attained. Since the atmosphere on Mars is approximately 0.6 kPa, it is estimated that a nozzle for an NTR for Mars surface operation can be engineered with a thrust coefficient ( $C_F$ ) of 1.8 with an expansion ratio ( $A_{\text{exit}}/A_{\text{throat}}$ ) of 20 [36]. Using these values for  $c^*$  and  $C_F$ , the specific impulse ( $I_{\text{sp}}$ ) of a CO<sub>2</sub>-NTR is estimated to be of the order 217 seconds. This is comparable to that of a typical solid rocket motor, but has the advantage that its propellant does not need to be carried to the surface, thus saving a considerable quantity of mass.

Based on this initial assessment, the performance of a surface launch mission to Mars orbit via a single stage CO<sub>2</sub> NTR for a payload capsule mass of 50 kg has been evaluated. The masses used for tanks, structures and reactor design were based on an assessment of a tungsten cermet-based NTR system and compared to historical data from the Rover/NERVA [37] and GE 710 [38] NTR and space reactor programs. The results from this study are summarised in Table 7.5.

<b>Component</b>	<b>Mass (kg)</b>
Tankage & Structure	1300
Engine	1750
Sample Payload	10
Sample Capsule	40
CO <sub>2</sub> Propellant	17,700
<b>Core Temperature</b>	
	3000 °C
<b>Burn Time:</b>	191 Seconds
<b>Reactor Power:</b>	398 MW
<b>Mass Flow Rate:</b>	93 kg/s
<b>Tank Volume</b>	22.9 m <sup>3</sup>
<b>Thrust:</b>	200 kN
<b>Exhaust velocity</b>	2132 m/s
<b>I<sub>SP</sub></b>	217 Seconds

**Table 7.5:** CO<sub>2</sub> NTR single stage specifications for Mars surface to 500 km Mars orbit launch.

Mission design parameters can be optimised for any given payload mass and structure configuration, but for a first order estimate, the above example may be used for scaling purposes. Clearly, the limitations for Mars sample return missions are the volume and mass constraints imposed by the Earth departure stage. It is assumed that in any mission where the Mars surface launch stage uses an NTR propulsion system, the same technology will be available for Earth departure. However, its use for Earth departure is likely to be constrained to departure from high altitude orbits (400 – 500 nautical miles) that are stable for approximately 300 years in order to present minimal risk to the Earth’s environment should the reactor fail or malfunction during start-up [39]. Provided that sufficient empty tankage volume can be delivered to the surface of Mars, the use of a single stage NTR system that utilizes atmospheric CO<sub>2</sub> as a propellant is possible for the delivery of payloads to a Mars departure stage in a low Mars orbit. Additionally, mission planners may consider the use of the NTR engine in the surface departure stage to facilitate the Mars surface landing. In this case, the tank may leave Earth filled with propellant (CO<sub>2</sub>) so that it may be used to provide

propellant for the Mars landing manoeuvre and refilled upon safe arrival at the surface of Mars.

In addition to the use of a CO<sub>2</sub> propelled NTR single stage for Mars surface to Mars orbit transfers, mission planners may also consider the provision of propellant for a Mars departure burn given that only around 2.52 km/s  $\Delta V$  is required for such a manoeuvre [34]. Such capability would preclude the requirement for a separate Earth return stage and thus reduce the complexity of on orbit procedures at Mars.

Overall, preliminary studies suggest that the application of nuclear thermal rocket propulsion to missions such as the example considered here appears to offer a significant enabling technology. Clearly NTR propulsion has the breadth and scope to facilitate both manned and robotic missions where in-situ resource utilization is required so as to ensure that a given mission is economically and technologically achievable.

## 7.4 References

- [1] S.D. Howe, R.C. O'Brien, N. Barra, et al. "Returning humans to the moon: comparison of chemical engine and nuclear rocket performance as an earth departure stage". Proceedings of: 2007 Space Nuclear Conference; June 24-28, 2007. American Nuclear Society, ISBN: 0-89448-053-7.
- [2] T. D'Elia, R. Veerapaneni, S.O. Rogers, "Isolation of Microbes from Lake Vostok Accretion Ice". *Applied and Environmental Microbiology*. 74 (2008) 4962-4965.
- [3] J.S. Kargel. "Physical Chemistry Of Ices In The Outer Solar System.". In: Schmitt B., C. De Bergh, M. Festou, eds. *Solar System Ices*. Kluwer Academic Publishers; Dordrecht, The Netherlands: 1998. ISBN: 0-7923-4902-4.
- [4] P. Jenniskens, P. Blake, A. Kouchi. "Amorphous Water Ice". In: Schmitt B., C. De Bergh, M. Festou, eds. *Solar System Ices*. Kluwer Academic Publishers; Dordrecht, The Netherlands: 1998. ISBN: 0-7923-4902-4.
- [5] A. Kouchi, T. Yamamoto, T. Kozasa, T. Koruda, J.M. Greenberg, "Conditions for condensation and preservation of amorphous ice and crystallinity of astrophysical ices". *Astron. Astrophys.* 290 (1994) 1009-1018.

- [6] D.W. James, "The Thermal Diffusivity of Ice and Water Between -40 and +60 C". *Journal of Materials Science*. 3 (1968) 540-543.
- [7] Stefan W. Vogel. "Hot water Drilling - an overview".  
<http://jove.geol.niu.edu/faculty/svogel/Technology/Drilling/HWD-overview.html>.
- [8] G.K.C. Clarke, "Subglacial processes". *Annu. Rev. Earth Planet. Sci.* 33 (2005) 247-276.
- [9] G.S. Boulton, D.L. Dent, E.M. Morris, "Subglacial shearing and crushing, and the role of water pressures in Tills from South-Eat Iceland". *Geografiska Annaler*. 56 (1974) 135-143.
- [10] J. Ahrens et al. "*IceCube Neutrino Telescope Preliminary Design Document*". R 1.24. University of Wisconsin, Madison, WI. October 11th 2001.
- [11] E.S. Robinson, R.M. Potter, B.B. McInteer, J.C. Rowley, D.E. Armstrong, R.L. Mills. "*A Preliminary Study of the Nuclear Subterrene*". LA-4547. Los Alamos Scientific Laboratory, Los Alamos, NM. 1971.
- [12] J.W. Neudecker, A.J. Giger, P.E. Armstrong. "*Design and Development of Prototype Universal Extruding Subterrene Penetrators*". LA-5205-MS. Los Alamos Scientific Laboratory, Los Alamos, NM. March 1973.
- [13] R.J. Hanold. "*Rapid Excavation by Rock Melting - LASL Subterrene Program*". LA-5459-SR. Los Alamos Scientific Laboratory, Los Alamos, NM. 1973.
- [14] W. Zimmerman, S. Bryant, J. Zitzelberger, B. Nesmith. "*A Radioisotope Powered Cryobot for Penetrating the European Ice Shel*". Jet Propulsion Laboratory, California Institute of Technology, Pasadena, CA. 2000.
- [15] W. Zimmerman. "*Extreme Electronics for In-Situ Robotic/Sensing Systems*". 99-2105. Jet Propulsion Laboratory, California Institute of Technology, Pasadena, CA. 1999.
- [16] C.R. Stoker, L. Richter, W.H. Smith, et al. "The Mars Underground Mole (MUM): A subsurface penetration device with in situ infrared reflectance and raman spectroscopic sensing capability". Proceedings of: 6th International Conferene on Mars, 2003; Pasadena, CA.
- [17] D.K. Kotter, S.D. Novack, W.D. Slafer, P. Pinhero. "*Solar Nantenna Electromagnetic Collectors*". INL/CON-08-13925. Idaho National Laboratory, Idaho Falls ID. August 2008.
- [18] R.C. O'Brien, R.M. Ambrosi, N.P. Bannister, S.D. Howe, H.V. Atkinson, "Spark Plasma Sintering of simulated radioisotope materials in tungsten cermet". *Journal of Nuclear Materials*. 393 (2009) 108-113. DOI: [10.1016/j.jnucmat.2009.05.012](https://doi.org/10.1016/j.jnucmat.2009.05.012).
- [19] R.C. O'Brien, R.M. Ambrosi, S.D. Howe, N.P. Bannister, H.V. Atkinson. "Production of safe radioisotope heat sources by Spark Plasma Sintering". Proceedings of: Nuclear and Emerging Technologies for Space (NETS-2009), Paper Number 206155; June 14-19, 2009; Atlanta, GA.
- [20] P.J. Karditsas, M.J. Baptiste. "*Thermal and Structural Properties of Fusion Related Materials*". United Kingdom Atomic Energy Agency (UKAEA - Fusion).
- [21] F.F. Ling, "A Quasi-iterative Method for Computing Interface Temperature Distributions". *Zeitschrift für angewandte Mathematik und Physik*. X (1959) 461-474.
- [22] F.F. Ling, V.C. Mow, "Surface Displacement of a Convective Elastic Half Space Under an Arbitrary Distributed Fast-Moving Heat Source". *Journal of Basic Engineering*. 87 (1965) 729-734.
- [23] S. Fukusako, "Thermophysical Propeties of Ice, Snow, and Sea Ice". *International Journal of Thermophysics*. 11 (1990) 353-372.
- [24] G.A. Soffen, C.W. Snyder, "First Viking mission to Mars". *Science*. 193 (1976) 756-766.

- [25] NASA Jet Propulsion Laboratory. "Phoenix Mars Lander". <http://www.jpl.nasa.gov/news/phoenix/main.php>.
- [26] A. Mishkin, "*Sojourner: An Insider's View of the Mars Pathfinder Mission*". Berkley; 2003. ISBN: 0-425-19199-0.
- [27] NASA Jet Propulsion Laboratory. "The Mars Exploration Rover Mission". <http://www.marsrovers.nasa.gov>.
- [28] C.A. Kuhl. "*Mars Aerial Regional-Scale Environmental Survey (ARES) Coordinate Systems Definitions and Transformations*". NASA/TM-2009-215701. NASA Langley Research Center, Hampton, Virginia. 2009.
- [29] D. Yu, X. W. Lv, W. Bao, Z. Yao, "A Carbon dioxide thermal rocket that utilizes an indigenous resource in raw form for Mars exploration". *J. Aerospace Engineering Part G*. 223 (2009).DOI: 10.1243/09544100JAERO617.
- [30] G.R. Grove, J.A. Powers, C.J. Kershner, T.A. Furtsch, R.H. Steinmeyer. "*Poodle Heat Source Development And Demonstration Test*". MLM-1261. Mound Laboratory, Maimisburg, OH. 1965.
- [31] E.L. Leventhal. "*SNAPOODLE Demonstration Design Study*". AD0475003. TRW Systems Group, Redondo Beach, CA. 1965.
- [32] I.R. Jones, G.E. Austin. "POODLE Radioisotope Propulsion Technology". Proceedings of: Symposium on Radioisotope Applications in Aerospace, 1966.
- [33] D.R. Burgess, "Thermochemical Data". *NIST Chemistry WebBook, NIST Standard Reference Database Number 69*.
- [34] M.J.L. Turner, "*Expedition Mars*". Praxis Publishing Ltd., Chichester; 2004. ISBN: 1-85233-735-4.
- [35] R. Zubrin. "Mars Direct: A Simple, Robust, and Cost Effective Architecture for teh Space Exploration Initiative". Proceedings of: 29th Aerospace Sciences Meeting; 7-10 January, 1991; Reno, NV. AIAA.
- [36] M.J.L. Turner, "*Rocket And Spacecraft Propulsion*". 2<sup>nd</sup> ed. Praxis Publishing Ltd, Chichester; 2005. ISBN: 3-540-22190-5.
- [37] D. Koenig. "*Experience gained from the Space Nuclear Rocket Program (Rover)*". Los Alamos National Laboratory, Los Alamos, NM. May 1986.
- [38] General Electric. "*710 high-temperature gas reactor program summary report. Volume III. Fuel Element development*". General Electric. 1968. Pages: 146. GEMP-600 (Vol.3);.
- [39] D. Buden. "Safety questions relevant to nuclear thermal propulsion". Proceedings of: 9th Symposium on Space Nuclear Power Systems; January 12th - 16th, 1992; Albuquerque, NM.

# 8

## Summary

Since the works of the early space technology pioneers such as Tsiolkovsky, Goddard and Von Braun, phenomenal achievements have been made throughout the space science and engineering community. All of these achievements have been made possible in part through the implementation of chemical propulsion systems. Today, the Space shuttle main engine is seen as the pinnacle of chemical propulsion technology in terms of its efficiency and overall reliability. Unspecific to any given technology, a limit of performance is and must be expected. Thus, it is certainly conceivable that manned or robotic exploration of our solar system, in the context of propulsion, demands a technology that will deliver greater performance than conventional chemical systems. Equally, the ever-increasing demand for electrical power and process energy for robotic and manned missions alike is expected to exceed the capability and capacity of solar and chemical energy sources.

The implementation of nuclear power and propulsion has emerged over the past four decades as mankind's logical progression for exploration of the solar system and beyond. Chapter 2 of this thesis introduced the reader to the historical developments made in the field leading to today's fleet of space nuclear power systems. Chapter 2 also highlights the currently limited availability of  $^{238}\text{Pu}$ , the isotope used by convention for the fuelling of radioisotope power systems. The development of nuclear thermal propulsion technologies is introduced in Chapter 2.

Aside from the socio-political implications attributed to the use of nuclear energy in space, the fundamental challenges that have emerged from this work have placed high demand upon radiation safety and modern materials science and technology. Significantly, the safe handling and encapsulation of radioisotopic materials for milliwatt to kilowatt heat sources, in addition to the production of safe and reliable nuclear fuels for fission reactors is crucial. Equally significant for radioisotope power systems, the energetics and modes of isotope decay in combination with the required thermal output power define the exposure of radiation to the local environment.

The use of radioisotopes whose decay mode is predominantly through the emission of an alpha particle result in the generation of significant volumes of helium gas over the lifetime of a given radioisotope heat source. Helium accumulation and its effects are presented in Chapter 3. The reader was also introduced throughout Chapter 3 to the current methods of isotope encapsulation that have been adopted by both the Russian and U.S. radioisotope power programs [6-8]. Methods of helium ventilation are presented for these conventional designs.

The effect of isotope selection upon dose rate at a distance of 1m from the source was demonstrated in Chapter 4 via the presentation of results obtained by the author through Monte Carlo modelling of several isotopes of interest including  $^{241}\text{Am}$ ,  $^{238}\text{Pu}$ ,  $^{90}\text{Sr}$ ,  $^{208}\text{Po}$  and  $^{210}\text{Po}$  [1]. Modelling was initially performed for substitution of the different isotopes within the General Purpose Heat Source (GPHS) architecture used by the U.S. Department of Energy, and was followed by the adoption of tungsten encapsulated heat source [1]. One particular finding of the modelling studies

demonstrated that the replacement of  $^{238}\text{Pu}$  by  $^{241}\text{Am}$  leads to a mass penalty of the order of 4-5 times that of the  $^{238}\text{Pu}$  GPHS system, but with a reduction in the radiation dose attributed to neutron yields by an order of magnitude, the substitution may be applicable to missions where the source is in the proximity of sensitive electronics or detectors. Other substitutions such as by  $^{210}\text{Po}$ , although attractive for a reduction in local dose rate, their low availability, high production costs and poor chemical stability limit their use to missions of suitable duration and power requirements.

Conversely, certain applications may present the need for a neutron flux that is significantly greater than that produced by conventional radioisotope heat sources. Work performed by the author based on the results in Chapter 4 identified isotopic heat sources [2] that may be used in conjunction with neutron activation analysis experiments [3] whereby the sources are used to provide an incident neutron flux on a sample while delivering electrical power for the operation of detector systems [2].

Examination of blended radioisotopes is considered in Chapter 4 for applications where power densities comparable to  $^{238}\text{Pu}$  sources are required but a penalty in radiation dose can be accepted. Of particular interest to the author are sources composed of a mixture of  $^{241}\text{Am}$ ,  $^{242}\text{Cm}$  and  $^{244}\text{Cm}$ . Such compositions may be obtained in significant quantities [4, 5].

Today, the development of encapsulation methods that prevent the extraction and dispersion of an inventory of radioisotopic materials from an isotopic heat source is increasingly attractive for non-proliferation security and accident protection [9]. The

encapsulation of radioisotopes within a tungsten cermet matrix was first proposed by the author in order to address these concerns [1]. Through the examination of sintering technologies, the author determined that the Spark Plasma Sintering (SPS) technique allows for the production of cermet matrices at greatly reduced temperatures than traditional sintering technologies such as Hot Isostatic Pressing, thus preventing the volatilization of isotope compounds during sintering [1]. Published results produced by the author regarding the experimental demonstration of the SPS production process using CeO<sub>2</sub> as a surrogate for <sup>241</sup>AmO<sub>2</sub> and <sup>238</sup>PuO<sub>2</sub> within tungsten cermets [10] are discussed in Chapter 5.

In the absence of Spark Plasma Sintering capability within a commissioned active hot cell or glove box line, the author was unable to demonstrate the SPS process directly using isotopic compounds. However, under a series of experimental procedures at the Idaho National Laboratory, successful demonstration of the cermet processing temperature response of <sup>241</sup>AmO<sub>2</sub> within tungsten matrices [11]. The results from this experimentation are presented in Chapter 6 of this thesis proving that a stable cermet composition may be produced. Future demonstration of actinide oxide/tungsten cermet fabrication via SPS may be performed by the author following the commissioning of a suitable facility.

The historical demonstration of nuclear thermal propulsion outlined in Chapter 2 highlighted its attributed challenges. Hot hydrogen embrittlement and erosion of nuclear fuel elements in NTP reactors is addressed by the author through the adoption of tungsten cermet fuels for future system designs operating in the fast neutron spectrum [12-14]. Experimental demonstration of tungsten fuel element fabrication is

discussed later in Chapter 5. Here, hexagonal prismatic fuel elements loaded with  $\text{CeO}_2$  to simulate  $\text{UO}_2$  fuel were fabricated via SPS using a die designed and developed by the author. The technique was developed such that circular flow channels could be created through the element while simultaneously producing a fully encapsulated cermet encapsulated in a tungsten or tungsten alloy cladding [12]. The external geometries of the prototype tungsten fuel elements were equal to those developed under the U.S. Rover/NERVA NTP programs [15]. Future development of fuel elements with embedded helical flow channels for the improvement in heat transfer to propellants while minimising element length is also discussed.

As examples of novel mission concepts that may be enabled by nuclear and radioisotope technologies, the author proposes and presents the reader with 3 case studies in Chapter 7. Firstly the reader is presented with a concept in which a radioisotope heat source is used in conjunction with a thermal energy storage device, defined as a heat capacitor, to enable the exploration of subsurface regions of icy planetary bodies such as Europa.

Secondly, using a similar heat capacitor concept, a radioisotope thermal rocket is conceived and used to provide long-range mobility of a Mars science platform, referred to as a Mars Hopper. Using in situ resource utilization techniques, RTR propellants such as  $\text{CO}_2$  are derived from the Mars atmosphere. Such Hopper platforms may be used to determine sites for sampling prior to a Mars sample return mission. Equally, a Hopper platform may be used to collect samples for transfer to an Earth return stage.

Finally, the author presents a concept in which a Nuclear Thermal Rocket engine is used to provide power and thrust for a single stage Mars-Earth sample return spacecraft. The concept presented is capable of lifting multiple kilograms of samples directly from the surface of Mars and transferring itself into an Earth return Hoffman transfer orbit. Again using an abundance of electrical power that may be derived from the reactor core of the NTR engine, in-situ resource utilization techniques are proposed for the isolation and storage of CO<sub>2</sub> from the Mars atmosphere.

Clearly, the scientific return of any given mission is limited by the availability of energy and the efficiency of propulsion and instrumentation. The results presented in this thesis show that nuclear and radioisotope systems can provide an enabling continuous power source for long duration missions while presenting minimal impact upon the local environment.

## References

- [1] R.C. O'Brien, R.M. Ambrosi, N.P. Bannister, S.D. Howe, H.V. Atkinson, "Safe radioisotope thermoelectric generators and heat sources for space applications". *Journal of Nuclear Materials*. 377 (2008) 506-521.
- [2] R.C. O'Brien, R.M. Ambrosi, M.S. Skidmore, N.P. Bannister, S.D. Howe, H.V. Atkinson, "Radioisotope fuels for neutron and heat sources for radioisotope power systems and in-situ planetary science applications". *Applied Radiation and Isotopes*. Article in press (2010).
- [3] M.S. Skidmore, R.M. Ambrosi, R.C. O'Brien, "Neutron sources for in-situ planetary science applications". *Journal of Nuclear Materials*. 608 (2009) 403-409. DOI: [10.1016/j.nima.2009.07.011](https://doi.org/10.1016/j.nima.2009.07.011).
- [4] Revis Services UK LTD, Discussions on the availability of curium isotopic compounds, in private communication to O'Brien R.C., 2010
- [5] S Marschman of Idaho National Laboratory in private communication to O'Brien R.C. 2009
- [6] G.H. Rinehart. "*Lightweight Radioisotope Heater Unit (LWRHU) Production for the Cassini Mission*". LA-13143. Los Alamos National Laboratory, Los Alamos, NM. May 1996.
- [7] G.L. Bennett, J.J. Lombardo, R.J. Hemler, et al. "Mission of Daring: The General-Purpose Heat Source Radioisotope Thermoelectric Generator". Proceedings of: Fourth International Energy Conversion Engineering Conference and Exhibit (IECEC), 2006; San Diego, California. AIAA.
- [8] A.B. Chmielewski, A. Borshchevsky, R. Lange, B Cook. "*A Survey of Current Russian RTG Capabilities*". 94-0898. NASA Jet Propulsion Laboratory, Monterey, California, USA. 1994.
- [9] R.C. O'Brien, R.M. Ambrosi, S.D. Howe, N.P. Bannister, H.V. Atkinson. "Production of safe radioisotope heat sources by Spark Plasma Sintering". Proceedings of: Nuclear and Emerging Technologies for Space (NETS-2009), Paper Number 206155; June 14-19, 2009; Atlanta, GA.
- [10] R.C. O'Brien, R.M. Ambrosi, N.P. Bannister, S.D. Howe, H.V. Atkinson, "Spark Plasma Sintering of simulated radioisotope materials in tungsten cermets". *Journal of Nuclear Materials*. 393 (2009) 108-113. DOI: [10.1016/j.jnucmat.2009.05.012](https://doi.org/10.1016/j.jnucmat.2009.05.012).
- [11] R.C. O'Brien, et al, "Experimental cermet encapsulation of americium oxides within a tungsten matrix under the simulated temperature conditions of Spark Plasma Sintering". *Journal of Nuclear Materials*. Article in Press (2010).
- [12] R.C. O'Brien, R.M. Ambrosi, S.D. Howe, N.P. Bannister, H.V. Atkinson. "Fabrication of prismatic fuel elements for space power and nuclear thermal propulsion reactors by spark plasma sintering". Proceedings of: Nuclear and Emerging Technologies for Space (NETS-2009), Paper Number 206153; June 14-19, 2009; Atlanta, GA.
- [13] S.D. Howe, R.C. O'Brien. "Nuclear Thermal Rockets: History, Benefits and Issues Impacting Future Operations". Proceedings of: 57th Joint Army-Navy-NASA-Air Force (JANNAF) Propulsion Meeting, 2010; Colorado Springs, CO.
- [14] S.D. Howe, R.C. O'Brien, N. Barra, et al. "Returning humans to the moon: comparison of chemical engine and nuclear rocket performance as an earth departure stage". Proceedings of: 2007 Space Nuclear Conference; June 24-28, 2007. American Nuclear Society, ISBN: 0-89448-053-7.
- [15] D. Koenig. "*Experience gained from the Space Nuclear Rocket Program (Rover)*". Los Alamos National Laboratory, Los Alamos, NM. May 1986.

# Appendix A

## Power Conversion Mechanisms

### A.1 Thermoelectric power conversion

RTG systems and some space reactor designs such as the SNAP 10A and BES-5 BUK reactors employ thermoelectric power generators, which produce an electric potential by exploiting the Seebeck effect. The Seebeck effect is observed when a temperature gradient exists across a junction of two different metals or semiconductor elements [1]. The magnitude of the thermoelectric Electro-Motive Force (EMF) across each junction is typically of the order of  $\mu\text{V}$  to several  $\text{mV}$  and is dependant upon junction material selection. An estimate for each junction potential with hot and cold side temperatures ( $T_H$  and  $T_C$  respectively) can be made using Equation A.1. The Seebeck coefficient  $\alpha_{p-n}$  can be defined as the thermoelectric voltage generated across a junction of thermoelectric materials p & n subjected to a junction temperature difference ( $T_H - T_C$ ) and is usually stated in units of  $\mu\text{V}^\circ\text{C}^{-1}$ . For a junction of SiGe, this has been measured to be on average  $135.4\mu\text{V}^\circ\text{C}^{-1}$  [2].

$$V_{\text{junction}} = \int_{T_C}^{T_H} \alpha_{p-n} dT \quad (\text{A.1})$$

**Equation A.1:** Seebeck voltage for a thermoelectric junction p-n with Seebeck coefficient  $\alpha_{p-n}$ .

$$\alpha_{p-n} = |\alpha_p| + |\alpha_n| \quad (\text{A.2})$$

**Equation A.2:** Seebeck coefficient for a p-n junction.

The thermal conversion efficiency of a thermoelectric generator  $\eta_T$  can be defined as the ratio of the electrical power output  $P_e$  to the thermal power input into the generator  $P_{th}$ .

$$\eta_T = P_e / P_{th} \quad (\text{A.3})$$

**Equation A.3:** Thermal conversion efficiency of a thermoelectric generator.

The generator efficiency can be expressed as the ratio of its thermal conversion efficiency to its Carnot efficiency ( $\Delta T/T_H$ ) as shown in Equation A.4 below.

$$\eta_{p-n} = \eta_T / \eta_{CARNOT} = \eta_T T_H / \Delta T \quad (\text{A.4})$$

**Equation A.4:** Junction efficiency of a thermoelectric generator [3].

Three processes constitute and determine the overall efficiency of a thermoelectric junction. These are the Seebeck effect, the Peltier effect and Joule Heating. The Seebeck effect, as discussed above (Equation A.1), results in the production of an EMF at the junction interface, thus forcing a current to flow through the junction. The Peltier effect is significant since the flow of current in a thermoelectric junction results in the evolution of heat that is proportional to the current and the direction of heat flow can be reversed by the reversal of the current. The Peltier coefficient for a p-n thermoelectric junction ( $\pi_{p-n}$ ) is given by the ratio of the Peltier heat evolved ( $Q_p$ ) to the current that flows through the junction ( $I$ ).

$$\pi_{T(p-n)} = -\dot{Q}_p / I \quad (\text{A.5})$$

**Equation A.5:** Definition of the Peltier coefficient for a p-n thermoelectric junction at temperature T [4].

The third process within the thermoelectric junction, Joule Heating or Thomson effect, is significant since the passage of current through the thermoelectric junction results in the evolution of heat. The magnitude of the Joule heating ( $Q_J$ ) is given by the product of the square of the junction current density ( $J$ ), the electrical resistivity of the junction ( $\rho_J$ ) and the length of the thermoelectric element ( $dx$ ). This is given in equation A.6 below.

$$\dot{Q}_J = J^2 \rho dx \quad (\text{A.6})$$

**Equation A.6:** Joule Heat evolved within a thermoelectric junction with a combined p-n junction resistivity  $\rho$ , length  $dx$  and current density  $J$ .

$$\dot{Q} = -\lambda \frac{dT}{dx} \quad (\text{A.7})$$

**Equation A.7:** Fourier's law of heat conduction.

The combination of Fourier's law of heat conduction (Equation A.7), which describes the flow of heat in one dimension along an element with cross sectional area ( $A$ ), length ( $l$ ) and thermal conductivity ( $\lambda$ ) [5], with Equation A.6 allows for the determination of the heat flow at any point along the element between  $x = 0$  (Hot Junction) and  $x = l$  (Cold Junction). Since the heat flux out of a thermoelectric junction must equal the heat input plus joule heating under steady state conditions, equation A.8 must hold.

$$\lambda \left( \frac{d^2 T}{dx^2} \right) + J^2 \rho = 0 \quad (\text{A.8})$$

**Equation A.8:** Joule Heat evolved within a thermoelectric junction

Solving Equation A.8 by setting the x values for the Hot and Cold junction as 0 and l respectively it is possible to determine the temperature T at any point along a given element:

$$T = T_H - \left(\frac{x}{l}\right)\Delta T + \frac{J^2 \rho}{2\lambda} x(l-x) \quad (\text{A.9})$$

**Equation A.9:** Temperature at any given point x along a thermoelectric junction of length l.

Using the relationship in Equation A.9, the Fourier term for the Hot and cold junctions for a thermoelectric junction is given by equations A.10 and A.11 respectively.

$$-A\lambda \left. \frac{dT}{dx} \right|_{x=0} = \frac{A}{l} \lambda \Delta T - \frac{1}{2} I^2 \frac{\rho l}{A} \quad (\text{A.10})$$

**Equation A.10:** Heat flow at Hot Junction of a thermoelectric generator element.

$$-A\lambda \left. \frac{dT}{dx} \right|_{x=l} = \frac{A}{l} \lambda \Delta T + \frac{1}{2} I^2 \frac{\rho l}{A} \quad (\text{A.11})$$

**Equation A.11:** Heat flow at Cold Junction of a thermoelectric generator element.

Equations A.10 and A.11 account for the thermal conduction of a thermoelectric element and joule heating of the element by the Seebeck current. There still remains the final phenomenon of the Peltier effect that must be accounted for. As is provided by Equation A.5, the heat displaced by the Peltier effect is given by Equation A.12 below.

$$\dot{Q}_P = -I\pi_{T(p-n)} = -\alpha_{(p-n)} TI \quad (\text{A.12})$$

**Equation A.12:** Heat flow due to Peltier effect within a p-n thermoelectric junction at temperature T with a Seebeck coefficient  $\alpha_{p-n}$  Angrist, 1971 #147}.

Introducing the terms conductance, K, and element electrical resistance, R, it is possible to relate the thermal input and output power for the junction.

$$K = \frac{\lambda_n A_n}{l_n} + \frac{\lambda_p A_p}{l_p} \quad (\text{A.13})$$

**Equation A.13:** Conductance, K, of a thermoelectric junction with thermal conductivity  $\lambda$ , length l and cross sectional area A for respective p and n type elements.

$$R = \frac{\rho_n l_n}{A_n} + \frac{\rho_p l_p}{A_p} \quad (\text{A.14})$$

**Equation A.14:** Internal resistance, R, of a thermoelectric junction with electrical resistivity  $\rho$ , length l and cross sectional area A for respective p and n type elements.

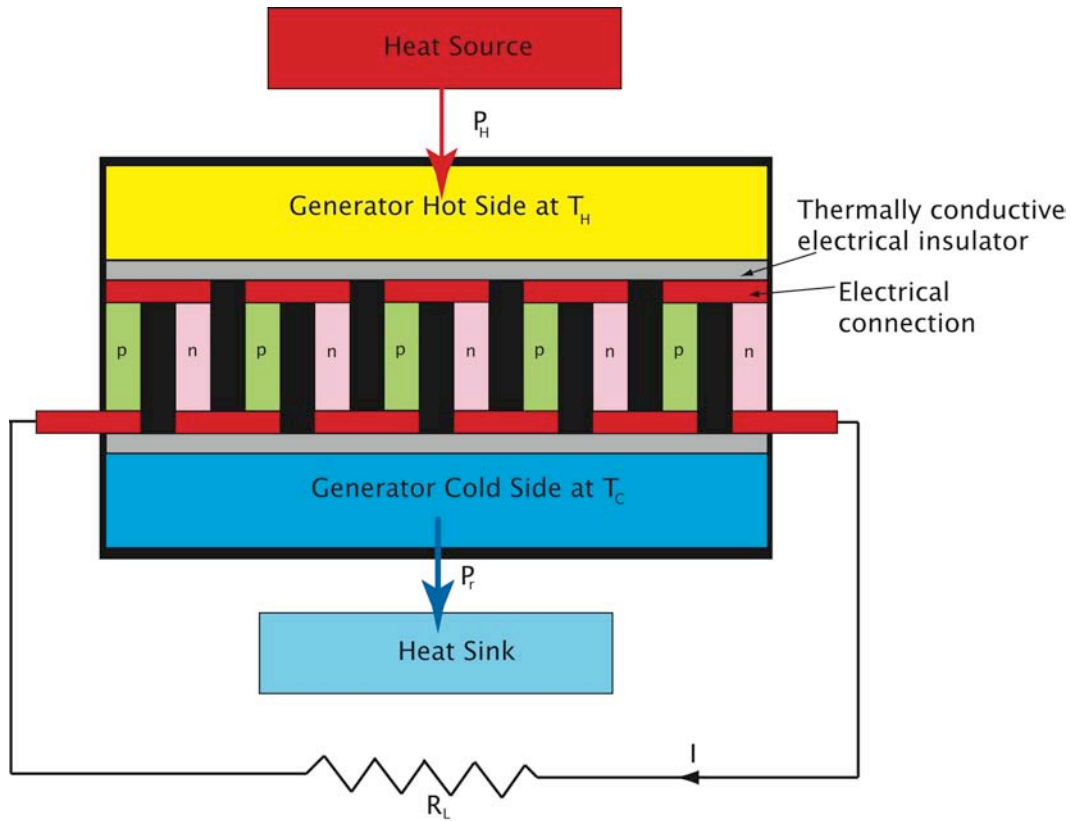
Given that the current flows from the n-type element to the p-type element of a thermoelectric junction, the polarity of the Peltier heat flow in Equation A.12 becomes positive. Therefore we can use the relationships in Equations A.10 to A.14 to determine the heat flow at the hot and cold junctions  $P_H$  and  $P_C$  respectively:

$$P_H = K\Delta T + \alpha_{(p-n)} T_H I - \frac{I^2 R}{2} \quad (\text{A.15})$$

**Equation A.15:** Thermal input power,  $P_H$ , of the hot side of a thermoelectric junction at isothermal temperature  $T_H$  with a Seebeck coefficient  $\alpha_{p-n}$  and internal resistance R.

$$P_C = K\Delta T + \alpha_{(p-n)} T_C I + \frac{I^2 R}{2} \quad (\text{A.16})$$

**Equation A.16:** Thermal output power,  $P_C$ , of the cold side of a thermoelectric junction at isothermal temperature  $T_C$  with a Seebeck coefficient  $\alpha_{p-n}$  and internal resistance R.



**Equation A.1:** Electro-thermal schematic of thermoelectric power generation

In order to minimise the physical thickness of a thermoelectric junction, the p-type and n-type elements of the junction are assembled in a parallel thermal conduction path that is connected electrically in series as illustrated by Figure A.1. Thermoelectric generators typically consist of a multiple number,  $m$ , of thermoelectric junctions that are electrically connected in series in order to produce the required voltage. The generator junctions are typically assembled such that the cold side of the semiconductor element is soldered to a metal cap and the hot side connection is made by compressively loading the element against the hot junction connecting-shoe. Multiple structures can be assembled in the same way [6]. This method of assembly leads to the requirement for the modules to be installed within the RTG system under mechanical compression [6].

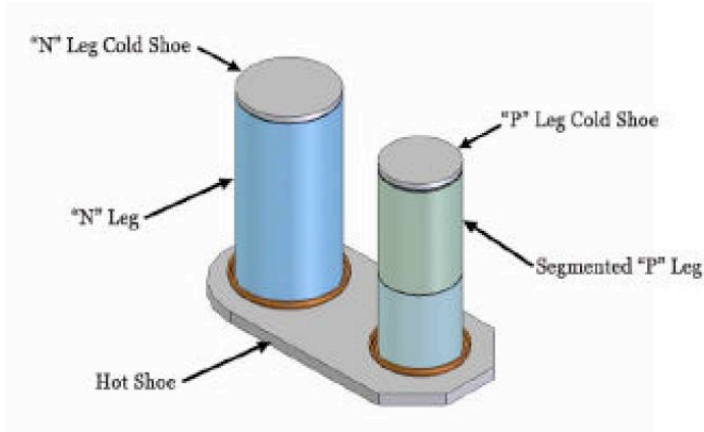


**Figure A.2:** Multi-Mission Radioisotope Thermoelectric Generator (MMRTG) thermoelectric junction. The MMRTG uses 768 thermoelectric junctions [7] composed of PbTe / TAGS (Tellurium-Antimony-Germanium-Silver) [8] in order to generate the required power. Image courtesy of the U.S. Department of Energy.

For a generator comprising of multiple series-connected thermoelectric junctions it is therefore possible to write Equation A.15 as Equation A.17 accounting for the multiplication of the Peltier power term.

$$P_H = K\Delta T + m\alpha_{(p-n)}T_H I - \frac{I^2 R}{2} \quad (\text{A.17})$$

**Equation A.17:** Thermal input power,  $P_H$ , of the hot side of a thermoelectric generator comprising of  $m$  junctions at isothermal temperature  $T_H$ , Seebeck coefficient  $\alpha_{p-n}$ , and with an internal resistance  $R$ .

The generator thermal conversion efficiency can be estimated from Equations A.3 and A.17, and understanding that the electrical output power of the generator is related to the load resistance,  $R_L$ , multiplied by a factor of the square of the current,  $I^2$ . This relationship is written as Equation A.18 below.

$$\eta_T = \frac{I^2 R_L}{P_H} = \frac{I^2 R_L}{K\Delta T + m\alpha_{(p-n)}T_H I - \frac{I^2 R}{2}} \quad (\text{A.18})$$

**Equation A.18:** Thermal conversion efficiency,  $\eta_T$ , of a thermoelectric generator comprising of  $m$  junctions with a hot side temperature  $T_H$ , Seebeck coefficient  $\alpha_{p-n}$ , Load resistance  $R_L$  and with a junction internal resistance  $R$ .

Since the open circuit voltage of a thermoelectric generator is given by the product of the junction Seebeck coefficient  $\alpha_{p-n}$ , the temperature difference between the hot and cold sides of the generator  $\Delta T$  and the number of junctions that are connected electrically in series,  $m$ , we can calculate the electric current drawn from a given generator in Equation A.19;

$$I = \frac{m\alpha_{p-n}\Delta T}{R_L + R} \quad (\text{A.19})$$

**Equation A.19:** Current delivered by a thermoelectric generator comprising of  $m$  junctions with a temperature difference between hot and cold sides  $\Delta T$ , Seebeck coefficient  $\alpha_{p-n}$ , Load resistance  $R_L$  and with a junction internal resistance  $R$ .

It is possible to calculate the maximum efficiency for a given thermoelectric generator. Firstly we must re-arrange Equation A.19 through the substitution of  $R_L$  by:

$$I = \frac{m\alpha_{p-n}\Delta T}{R(1 + \psi)}; \psi = \frac{R_L}{R} \quad (\text{A.20})$$

**Equation A.20:** Current delivered by a thermoelectric generator comprising of  $m$  junctions with a temperature difference between hot and cold sides  $\Delta T$ , Seebeck coefficient  $\alpha_{p-n}$ , Load resistance  $R_L$  and with a junction internal resistance  $R$ .  $\psi$  is the Resistance ratio.

The generator efficiency can be re-arranged in the form of Equation A.21 below:

$$\eta_T = \frac{\psi\Delta T}{[(1 + \psi)T_H] + \left[ \frac{(1 + \psi)^2}{Z} \right] - \left[ \frac{\Delta T}{2} \right]}; Z = \frac{m^2\alpha_{p-n}^2}{RK} \quad (\text{A.21})$$

**Equation A.21:** Thermal efficiency of a thermoelectric generator with a resistance ratio  $\psi$ , hot side temperature  $T_H$ , Temperature difference  $\Delta T$  and figure of merit  $Z$ . The introduced figure of merit is for any generator comprising of  $m$  junctions, with Seebeck coefficient  $\alpha_{p-n}$ , electrical internal resistance  $R$ .

The maximum figure of merit occurs when  $RK$  is minimised. This relationship is determined below:

$$\begin{aligned}
RK &= \lambda_n \rho_n + \lambda_n \rho_p \left( \frac{A_n / l_n}{A_p / l_p} \right) + \lambda_p \rho_n \left( \frac{A_p / l_p}{A_n / l_n} \right) + \lambda_p \rho_p \\
\frac{d}{d \left( \frac{A_n / l_n}{A_p / l_p} \right)} (RK) &= 0 \Rightarrow \left( \frac{A_n / l_n}{A_p / l_p} \right) = \sqrt{\left( \frac{\rho_n \lambda_p}{\rho_p \lambda_n} \right)} \\
(RK)_{\text{Minimum}} &= \left( \sqrt{\lambda_n \rho_n} + \sqrt{\lambda_p \rho_p} \right)^2
\end{aligned}$$

Therefore the maximum figure of merit has the value of:

$$Z_{\text{MAX}} = \frac{m^2 \alpha_{p-n}^2}{\left( \sqrt{\lambda_n \rho_n} + \sqrt{\lambda_p \rho_p} \right)^2} \quad (\text{A.22})$$

**Equation A.22:** Maximum figure of merit for a thermoelectric generator comprising of  $m$  junctions with a Seebeck coefficient  $\alpha_{p-n}$ , electrical resistivity  $\rho$ , and the thermal conductivity  $\lambda$  for respective  $p$  and  $n$  type elements.

$$\eta_T = \frac{\psi \left( \frac{\Delta T}{T_H} \right)}{\left[ (1 + \psi) \right] + \left[ \frac{(1 + \psi)^2}{Z_{\text{MAX}} T_H} \right] - \left[ \frac{\Delta T}{2T_H} \right]} \quad (\text{A.23})$$

**Equation A.22:** Thermal efficiency of a thermoelectric converter with a maximum figure of merit  $Z_{\text{MAX}}$ .

Finally to find the maximum thermal efficiency, we must optimise the resistance ratio  $\psi$  and use the maximum figure of merit  $Z_{\text{MAX}}$ . In order to perform this operation, we take the derivative of Equation A.23 with respect to  $\psi$ , setting the result equal to zero and then rearranging to give  $\psi_{\text{OPT}}$ .

$$\underline{\underline{\psi_{OPT} = \left(1 + Z_{MAX} \left[ \frac{T_C + T_H}{2} \right] \right)^2}} \quad \text{(A.24)}$$

**Equation A.24:** Optimised resistance  $\psi_{OPT}$  ratio for a thermoelectric generator with a hot side temperature  $T_H$  and a cold side temperature  $T_C$  and maximised figure of merit  $Z_{MAX}$ .

$$\underline{\underline{\eta_{MAX} = \left( \frac{\Delta T}{T_H} \right) \frac{(\psi_{OPT} - 1)}{\psi_{OPT} + T_C/T_H}}} \quad \text{(A.25)}$$

**Equation A.25:** Maximum thermal efficiency for a thermoelectric generator with optimised resistance ratio  $\psi_{OPT}$  and geometry, hot side temperature  $T_H$  and a cold side temperature  $T_C$ .

Through the combined application of Equations A.22, A.24 and A.25, it is possible to determine the maximum efficiency achievable by a thermoelectric generator.

RTG systems can exploit conduction, convection or radiative processes to transfer heat to the conversion units. Certain systems may utilise a combination of these methods. One of the main advantages of using radiative transfer in place of conduction or convection is the uniformity of the temperature of the hot junction [6]. The fundamental disadvantage of heat transfer via thermal radiation is the high temperature requirements placed on the heat source.

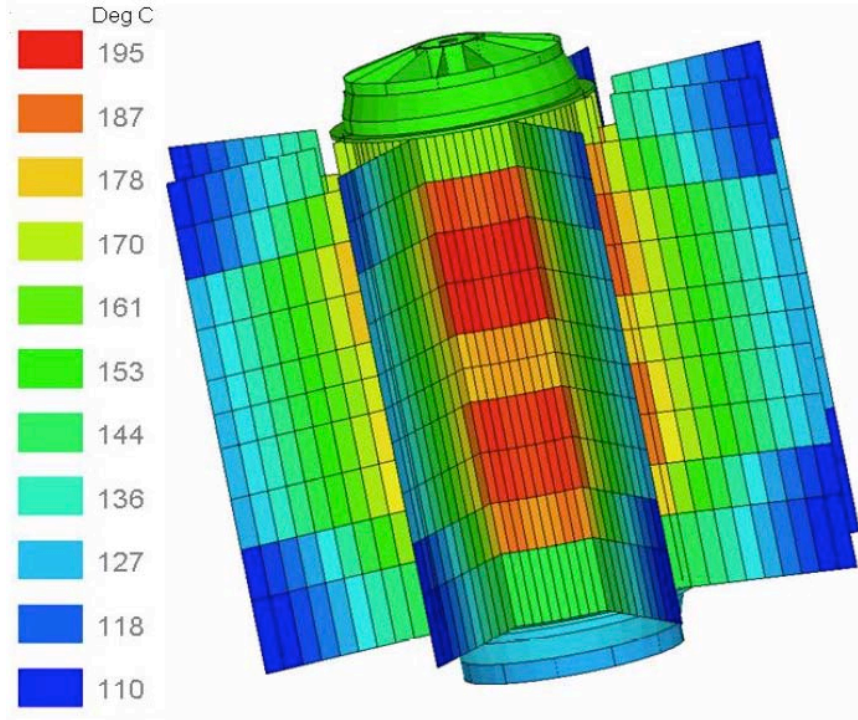


**Figure A.3:** Average external casing and fin temperature for the Multi-Mission Radioisotope Thermoelectric Generator (MMRTG) when operated in the Martian atmosphere [7].

$$P_r = A\varepsilon\sigma_B T^4 \quad (\text{A.26})$$

**Equation A.26:** Stefan-Boltzmann Law for the radiated power of a radiator with surface area  $A$ , emissivity  $\varepsilon$  and temperature  $T$  [9].  $\sigma_B$  is the Boltzmann constant ( $5.6704 \times 10^{-8} \text{ Js}^{-1} \text{ m}^{-2} \text{ K}^{-4}$ ).

Heat rejection from thermoelectric generators for the maintenance of the cold side temperature is typically performed by a finned outer casing. Here, fins act as a radiator; the efficiency of their heat rejection capacity is governed by the Stefan-Boltzmann law (Equation A.26). When operated in an atmosphere, heat is rejected through a combination of radiation, conduction and convection processes. As such, a generator must operate at higher cold side temperatures in vacuum if the same heat rejection capacity as an identical device operating in a gaseous or fluid environment. Alternatively, the design for a generator operating in vacuum may feature increased fin surface area.

As can be appreciated, the material selection for the thermoelectric junction directly drives the operating characteristics of an RTG system. It has been shown that thermoelectric selection drives the requirement for a specific temperature differential  $\Delta T$  for any given level of thermal conversion efficiency  $\eta_T$  (Equation A.25). Equally important to the system efficiency is the heat rejection system. As we have stated that operation in vacuum requires higher cold side temperatures in order to achieve the radiated heat rejection requirements, this also drives the hot side of the generator to higher temperatures in order for a given temperature gradient to be achieved across the junctions. This in turn bears influence upon the material selection for both the composition of the thermoelectric junctions and the nuclear heat source encapsulation.

## A.2 Thermionic power conversion

Thermionic power conversion utilizes the phenomena of thermionic emission of electrons from the surface of a metal cathode maintained at elevated temperatures via collection at a cold or cooler anode. Simple thermionic emission occurs when sufficient energy is supplied to an electron such that it overcomes the ionisation potential of the metal surface. The ionisation potential energy is defined as the Work Function,  $W$ , and is temperature dependant. The temperature dependency of the Work Function arises from the difference in the energy level of the outermost occupied state, or the Fermi energy  $E_F$ . The work Function is defined in equation A.27 and a graphical representation of the thermionic potential is illustrated in Figure A.4.

$$W = U - E_F = U - k_B T \quad (\text{A.27})$$

**Equation A.27:** The work function ( $W$  or  $\phi$ ) for a metal at a given temperature defined as the difference in potential barrier energy  $U$  and the Fermi energy  $E_F$ .  $E_F$  is defined as the product of the Boltzmann constant ( $k_B$ ) and the temperature of the material  $T$  ( $^{\circ}\text{K}$ ).

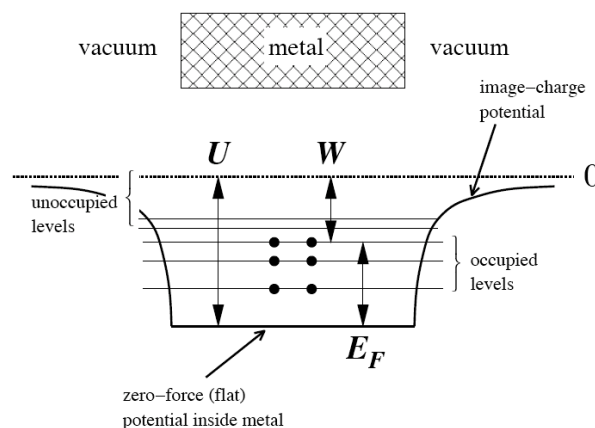


**Figure A.4:** Illustration of the potential barrier  $U$  that must be overcome by an electron emitted via thermionic emission through the provision of thermal energy. The electron energy states that are permissible for occupied and unoccupied levels are illustrated by horizontal lines. Occupying electrons fill the lowest energy levels up to the Fermi energy ( $k_B T$ ). The Work Function ( $W$  or  $\phi$ ) must be overcome via the supply of energy to the electronic in order for thermionic emission / ionisation to occur.

For an energy supply per thermionic electron that exceeds the given work function between the ground state of the outer most occupying electron and zero such as via the elevation of the emitter/cathode to a temperature where  $k_B T$  is greater than the potential barrier  $U$ , the emitted electrons will exhibit the energy difference as kinetic energy. For collection of the emitted charge in a thermionic cell, the anode must absorb the energy of the captured electron and reject it as heat. The rate of heat rejection is in essence a loss from the system and is often referred to as the electron cooling power ( $P_e$ ).

The potential difference between the emitter (cathode) and collector (anode) of a thermionic diode/cell may be determined from the difference in work functions of the emitter and collector divided by  $e$  [10]. This is represented in Equation A.28.

$$V = \frac{(\phi_E - \phi_C)}{e} \quad (\text{A.28})$$

**Equation A.28:** The open cell potential difference,  $V$ , across a thermionic diode where  $\phi_E$  and  $\phi_C$  are the emitter and collector work functions respectively, and  $e$  is the charge on the electron [10].

The current density of emitted thermionic electrons may be calculated via the implementation of the Richardson-Dushman equation [10] as presented as Equation A.29.

$$J_{ES} = A_R T_E^2 e^{\left(\frac{-\phi_E}{k_B T_E}\right)} \quad (\text{A.29})$$

**Equation A.29:** The Richardson-Dushman equation for determination of the saturation current density  $J_{ES}$  for a given cell emitter (cathode) material at temperature  $T_E$  with a work function  $\phi_E$  and Richardson constant  $A_R$  (Amperes.cm<sup>-2</sup>.K<sup>-2</sup>) [10].

Thus, the electrical power generated ( $P_E$ ) may be determined for a simple thermionic diode consisting of an anode and cathode of equal surface area but differing materials and separated within a vacuum. This is presented in Equation A.30. A thermionic cell may therefore be designed for any desired electrical power level by the appropriate selection of emitter and collector materials based on their work functions. Clearly a high power cell can be produced where the current density is low (due to low emitter temperatures) via the selection of emitter and collector materials with the largest possible difference in work functions.

$$P_E = J_{ES} A_S V = \frac{J_{ES} A_S (\phi_E - \phi_C)}{e} \quad (\text{A.30})$$

**Equation A.30:** The electrical power generated by a thermionic diode with saturation current  $J_{ES}$  and equal emitter/collector surface area  $A_S$ .

The thermionic efficiency ( $\eta_{TI}$ ) as with any heat engine is equal to the product of the Carnot efficiency  $\eta_C$  and the intrinsic efficiency of the converter  $\eta_i$  [11]. By consideration of the thermal and electrical cell connections, the overall efficiency relative to the cell driving parameters can be determined through Equation A.31. In practical systems, efficiencies of the order of 27 % have been observed [10, 12, 13].

$$\eta_{TI} = \eta_c \eta_i = \frac{P_E}{P_H} = \frac{J_{ES} V - \left( \frac{J_{ES}^2 \rho}{S} \right)}{P_r + P_c + P_e + P_l} \quad (\text{A.31})$$

**Equation A.31:** The thermionic efficiency  $\eta_{TI}$  [11] where:

- $P_E$  = Electrical output power (W)
- $P_H$  = Thermal input power at cathodic hot side of the converter (W)
- $J_{ES}$  = Converter saturation current density (A/cm<sup>2</sup>)
- $V$  = Thermionic cell/diode voltage (volts)
- $S$  = Ratio of lead area to length per square centimetre of emitter/cathode area (cm/cm-cm<sup>2</sup>)
- $\rho$  = Resistivity of the cathode emitter leads (ohm-cm)
- $P_r$  = Radiation loss from the hot cathode to the cold anode (W)
- $P_c$  = Conduction loss, where present through a working fluid (W)
- $P_e$  = Electron cooling power due to the kinetic energy of the electrons absorbed by the cold anode (W)
- $P_l$  = Thermal losses through conduction along the electrical leads connected to the hot cathode emitter (W)

In the above evaluation we have considered a simple ideal thermionic diode consisting of the emitter and collector separated by a vacuum gap. However, the ideal vacuum thermionic diode performances are difficult to achieve in practice due to space charge accumulation. At high thermionic emission currents, a large net negative charge propagates through the inter-electrode gap and effectively changes the charge distribution within the gap to be significantly negative. This negative space charge accumulation dramatically impacts the performance of the cell since subsequent electrons emitted from the emitter surface are repelled and thus the net current is presented with an internal resistance.

The effect of space charge accumulation can be significantly reduced by either producing a cell with a small inter-electrode void or through the addition of positively charged ions. Both solutions possess significant engineering challenges. Small gaps between different materials are difficult to maintain during thermal transients and the addition of positive ions to the system such as Cs<sup>+</sup> [11] implies the necessity to

significantly elevate the cell operating temperature. For caesium ion use, operational temperatures of the emitter must be driven to the order of 2000 °K [10].

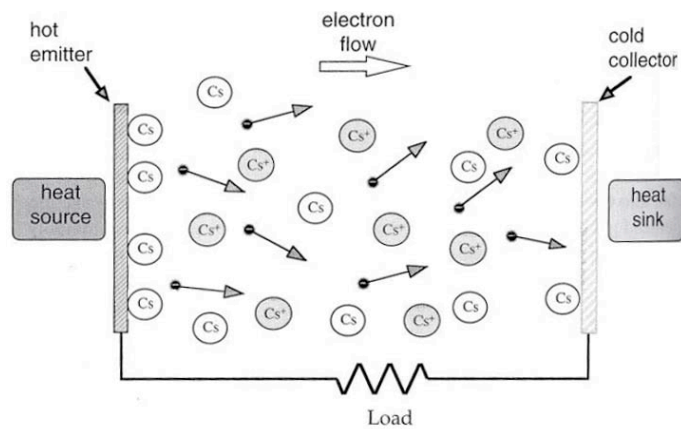


**Figure A.5:** Illustration of the flow of thermionic emission electrons from the cathode emitter to the anode collector. The addition of Cs<sup>+</sup> ions into the inter-electrode gap used to reduce the space charge effect.

The TOPAZ reactors (TOPAZ-I flown & TOPAZ-II ground tested) produced by the Kurchatov Institute of Atomic Energy in the former Soviet Union, as the acronym TOPAZ translated from Russian into English suggests (‘Thermionic Experiment with Conversion in Active Zone’), make use of the thermionic emission phenomena within the core for power conversion. The TOPAZ thermionic converters were integrated within the fuel elements of the reactor. The inter-electrode space charge effect was reduced by the induced flow of Cs<sup>+</sup> vapour. Figure A.6 illustrates the schematic of TOPAZ fuel elements.

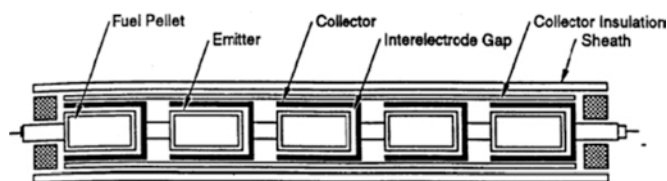


**Figure A.6:** Schematic of TOPAZ space reactor fuel element with integrated thermionic converters [14]. Here high temperature Cs<sup>+</sup> vapour is passed through the inter-electrode gap to reduce the effect of space charge accumulation.

Given the above high temperature requirement for thermionic converter operation, the mechanism is highly suitable to systems that are either rich in thermal power, or scope exists to substantially insulate a small heat source such as a radioisotope heat source [13] so that a sufficiently high hot-side (emitter) temperature can be achieved. For this reason, historical use of thermionic converters for space has focussed upon reactor derived power although some research has evaluated their use within radioisotope power systems [13].

For space reactor systems, radiator area should be minimized in order to reduce its impact upon the specific power density of the overall system. Since the overall operating temperature of the thermionic cell can be elevated, thermionic power conversion is highly suitable to such applications.

### A.3 Direct Charge Conversion

The principle of direct charge conversion is in essence the transfer of the charge of a decay particle such as an electron in the case of  $\beta$  decay to an electrical load. Unfortunately, the maximum theoretical current and hence power for a given generator is limited to the activity of isotope used. Since one ampere is defined as the passage of one coulomb per second through any given conductor, a total of  $6.25 \times 10^{18}$  electrons must be captured each second by a beta-voltaic direct charge converter. Thus a minimum activity of 169 MCi activity is required per ampere, i.e. for a charge collector with 100% efficiency. It is for this reason that the historical development of Beta voltaic cells and batteries has focussed upon very low current applications of the order of  $1 \times 10^{-10}$  A [11]. For space applications, it is therefore assumed that direct charge conversion is not suitable for high power generation, but is suitable for miniaturised subsystems such as clocks or dormant remote sensor applications, despite measured efficiencies of the order of 67% [11].

#### **A.4 Free-Piston Stirling generators**

The Stirling cycle is a perfectly reversible heat engine cycle that can be used to perform work by the transfer of heat from a hot reservoir to a cold reservoir, or can conversely transfer heat by the input of mechanical work. The general Stirling cycle consists of two constant-volume processes and two constant-temperature processes. These conditions are illustrated in Figure A.7.

The cycle commences by the addition of thermal energy from a heat source to a working fluid in a hot expansion space under the conditions of isentropic expansion resulting in the movement of both a heat shuttle displacer and a power piston (See Figure A.7 1-2). When the pressure in the bounce space behind the displacer exceeds the pressure in the expansion space, the displacer (low mass) is pushed back into the expansion space. In doing so, the displacer pushes the working fluid within the expansion space through a baffle regenerator into the cold space ahead of the power piston under ideally isochoric conditions, while thermal energy is transferred from the fluid to the regenerator resulting in a decrease in pressure and temperature (See Figure A.7 2-3). The motion of the larger mass power piston is also retarded by the pressure in the bounce space in addition to a restoring force created by an internal spring. Thus the power piston travel turns through  $180^\circ$  and begins to return to the forward expansion space end of the engine. In doing so, the working fluid in the cold gas space is compressed ideally under isentropic conditions whereby waste heat is rejected from the system at the cold end of the engine. As the power piston reaches the end of its travel (See figure A.7 point 4) the gas in the cold space is fully compressed through the regenerator resulting in the movement of the displacer (See figure A.7 points 4-1)

which in turn forces the remaining working fluid from the cold space under ideally isochoric conditions. In passing through the regenerator baffle, the working fluid is restored to its maximum temperature thus reducing the losses from the system in re-heating the fluid.

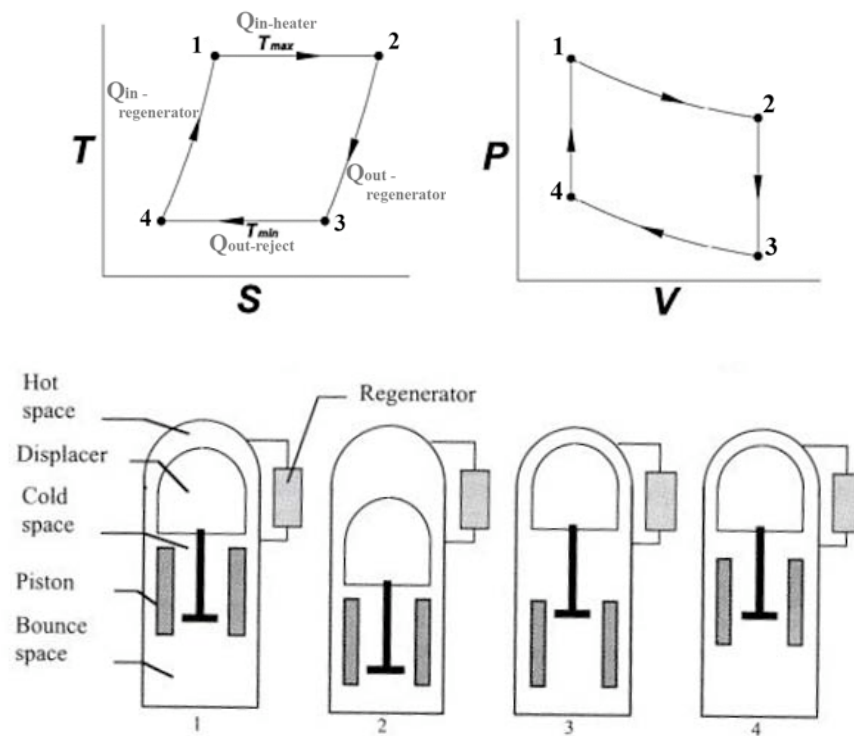


**Figure A.7:** Temperature-Entropy (T-S) and Pressure-Volume (P-V) curves for the reversible Stirling cycle. Also illustrated are the relative positions of the working piston and heat shuttle displacer at each position on the T-S and P-V curves. Image courtesy of NASA.

Carnot postulated that the efficiency of a heat engine is equal to the ratio of the work done by the engine to the thermal energy input  $Q_H$ . The 2<sup>nd</sup> corollary of Carnot states that the efficiency of any reversible heat engine is a function only of the

respective temperatures of the hot and cold reservoirs that can be evaluated by replacing the ratio of heat transfers  $Q_H$  and  $Q_C$  by the ratio of the respective temperatures of those reservoirs. This relationship is represented by Equation A.32 below.

$$\eta_{Carnot} = \frac{W}{Q_H} = \frac{Q_H - Q_C}{Q_H} = 1 - \frac{Q_C}{Q_H} = 1 - \frac{T_C}{T_H} \quad (\text{A.32})$$

**Equation A.32:** The Carnot efficiency of a heat engine and

A Free-Piston Stirling engine, like any traditional Stirling engine, is limited to a maximum efficiency of the Carnot efficiency. Since a Stirling engine is a mechanical heat engine, problems with traditional designs manifest within bearings, crossheads and seals. The Free Piston Stirling (FPS) engine has been developed for high efficiency and low maintenance cooling and electrical power generation applications [15-17]. The characteristics of the FPS design has eliminated many of the mechanical issues. In power conversion operation, a linear alternator is used to convert the harmonic motion of a power piston that is approximately 90 degrees out of phase with a displacer piston. The motion and phase of both pistons is controlled by the attachment of a matching spring (of specific spring constant,  $k$ ) to a given piston mass,  $m$ . Mechanical bearings are eliminated from the FPS engine by the employment of gas bearings. The power piston houses an integral rare earth magnet such as Samarium-Colbolt (SmCo) [15] or Iron-Neodymium-Boron (FeNdB) [15] that is used to induce an a.c. current in a surrounding coil as the piston passes through at a frequency, typically of the order of 50 – 100 Hz [18]. Similarly, the design of FPS engines suggests engine specific powers of the order of 50 – 100 W/kg [18].

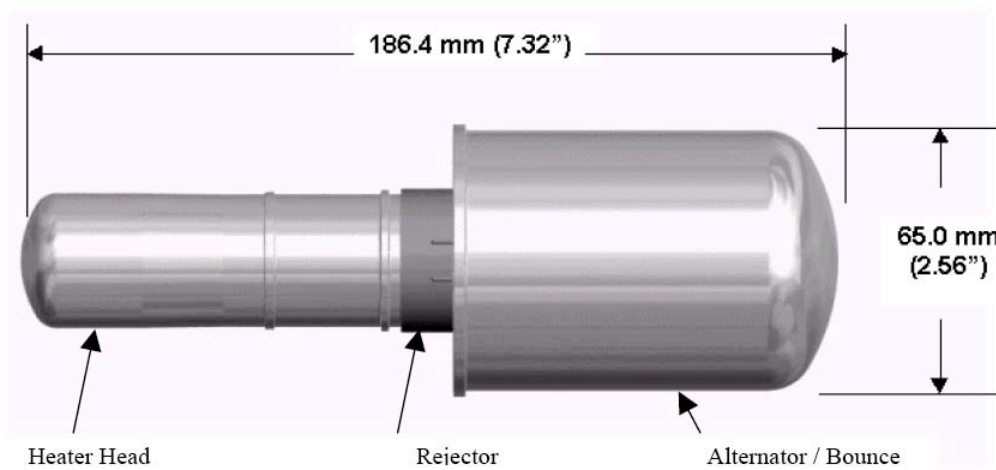
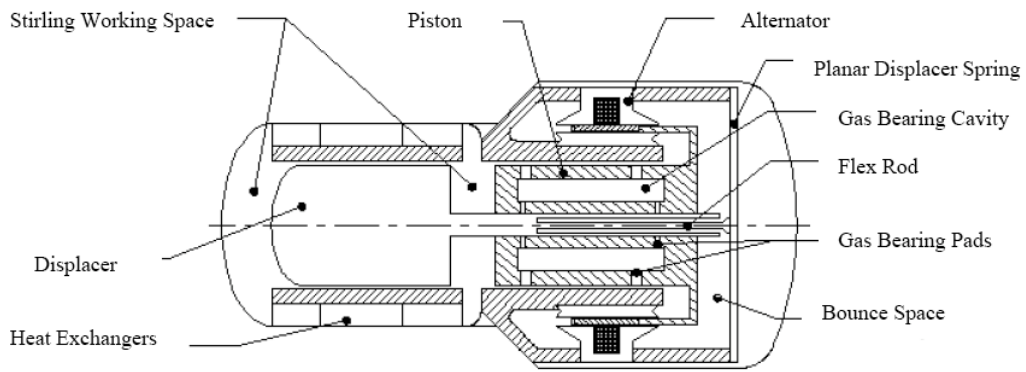


**Figure A.8:** Schematic of a typical Free Piston Stirling engine design. Depicted is the Advanced Stirling Converter (ASC) that will be used by the Advanced Stirling Radioisotope Generator [18].

The thermal efficiency of the ideal Stirling engine as described by Angelo [12] is given in Equation A.33.

$$\eta_{Stirling} = 1 - \frac{T_C}{T_H} \tag{A.33}$$

**Equation A.33:** efficiency of the ideal Stirling engine (Zero convert loss) where  $T_H$  is the hot head temperature and  $T_C$  is the heat rejection temperature.

In consideration of the practical or effective efficiency of a Stirling engine, multiple losses must be accounted for in addition to the Carnot efficiency ratio of engine efficiency to its Carnot efficiency,  $C$ . It should be noted that the Carnot efficiency ratio that relates the efficiency of the expansion, compression and any thermal regeneration of the working fluid to the Carnot efficiency ( $\Delta T/T_H$ ), is practically demonstrated to values of 0.6 to around 0.8. The losses of primary concern are attributed to the heater efficiency  $\eta_H$ , mechanical efficiency  $\eta_M$ , and alternator efficiency  $\eta_A$ . The heater efficiency is a measure of the fraction of thermal energy supplied from a heat source to the engine that is transferred to the working fluid. The mechanical efficiency may be used as a measure of the fraction of the energy released in the expansion of the working fluid that is translated into shaft power in the power piston. Finally, the alternator efficiency is related to the amount of energy that is converted from shaft power to electrical current via induction in the coils of the linear alternator. These considerations may be related algebraically in Equation A.34.

$$\eta_{eff} = \left(1 - \frac{T_C}{T_H}\right) C \eta_M \eta_A \quad (\text{A.34})$$

**Equation A.34:** The effective efficiency of a Free Piston Stirling engine where  $T_H$  is the hot head temperature,  $T_C$  is the heat rejection temperature.  $C$ ,  $\eta_M$  and  $\eta_C$  are the Carnot efficiency ratio, and the mechanical and alternator efficiencies respectively.

William Beale, the founder of Sunpower inc, now manufacturer of the Advanced Stirling Converter for the Advanced Stirling Radioisotope Generator, determined an empirical relationship between the engine power of a Stirling engine and various design parameters. In doing so, he noted that a common constant for a given engine design was present within this relationship. This constant became known as the Beale Number [19]. This relationship is presented in Equation A.35 below.

$$\frac{P}{p_{ave} f V_0} = N_B \quad (\text{A.35})$$

**Equation A.35:** The definition of the Beale Number,  $N_B$ , through its first order relationship to the power of an engine  $P$  in Watts, the average cycle pressure  $p_{ave}$ , in bar, the cycle frequency  $f$  in Hz, and the stroke displacement of the power piston  $V_0$  in  $\text{cm}^3$  [19].

It should be noted that although the Beale Number varies with design and operating temperatures [19], for most designs of Stirling engine operating between 800 and 1000 °K,  $N_B$  typically lies within the range of 0.011 and 0.015 [19]. Understanding this, a first order approximation for the design of a free piston engine may be determined. Work undertaken by William R. Martini in 1979 resulted in the production of a computational code for second order determination of the performance of Stirling engines [20]. The work presented by Martini considers the thermodynamics of each stage in the Stirling cycle in addition to losses and regeneration mechanisms that may be employed in order to minimise the energy that would otherwise be lost to the restoration of the working fluid to the hot head temperature  $T_H$  after return from a previous cycle.

Since the efficiency of a FPS engine is driven most fundamentally by the magnitude of the temperature gradient between hot end and rejection ends of the system, designs have focussed on the maximisation of these values. In doing so, multiple engineering challenges have been presented to developers, most notably in terms of material selection for each component. As is evident from Equation A.29, the power output of a given design is very much dependant upon its average operating pressure  $p_{ave}$ . Through the use of high operating pressures, the output power of an engine, and therefore its efficiency may be optimised. The use of high pressure helium

as a working fluid implies a high degree of quality in seals and indeed in material strengths. Equally, obvious losses such as conduction through the walls of the engine along the temperature gradient between hot and cold ends drives a designer to thin sections of materials. Thus, careful selection of materials for components is vital. Extensive testing of many components including hot head casings, pistons, displacers and regenerators have been performed by researchers at the NASA Glenn Research Center in support of the ASRG Advanced Stirling Converter [21-23]. Material creep and swelling is of particular significance. Specifically, nickel based alloy components have been developed for the ASC hot end and displacer piston in order to minimise the effect of creep [22].

The oscillatory nature of the Free Piston Stirling engine design presents an important consideration for space systems that may be sensitive to vibration and noise. Equally, a spacecraft that contains moving parts will ultimately enter modes of rotation unless control or dampening mechanisms are adopted. As a solution to this problem, a tuned harmonic dampener may be applied to the outside of an FPS engine casing that reacts to the vibrations generated, thus dampening the net effect. Alternatively, two FPS engines may be connected in a configuration referred to as dual opposed such as the scheme adopted by the Advanced Stirling Radioisotope Generator [24]. In the dual opposed configuration, the engines are rotated through 180 degrees to one another such that their operation mutually counteracts the vibrations generated by the counterpart engine.

The typical efficiency achieved by FPS engines is of the order 27 – 30 % [22]. Clearly the use of FPS technology for radioisotope power systems is highly advantageous where the reduction in consumption of isotopic material is concerned for a given electrical power requirement, when compared to that of a similar RTG system. This is extremely important where large powers are demanded for flagship class space missions and with the current low availability of  $^{238}\text{Pu}$  (see Chapter 1). However, the introduction of moving components to an RPS presents a potential increase in failure probability for the system. Where the failure of a single thermoelectric junction in an RTG may not result in significant loss of power from a parallel arrangement of junctions, the failure of a Stirling engine would almost certainly result in severe power limitations or in the worst case, termination of a mission. For this reason, the work undertaken at NASA Glenn has examined the failure modes of the system and has driven the design of the ASC to mitigate risk of failure for extended lifetimes of operation [24] and under various impact conditions and exposure to sources of vibration [25].

Overall, the research undertaken within the Free Piston Stirling engine community has demonstrated applicability of the cycle to output powers in the range of mW to kW. Since the operation of a generator requires a temperature gradient and not a specific range of temperatures for maximum efficiency, the cycle can be easily applied to the low power (mW) class generation system or high power (kW) generation in general via simple scaling [20].

## **A.5 Thermoacoustic & Thermoacoustic MHD power conversion**

The Thermoacoustic engine is similar to a Stirling engine in terms of the use of a working gas to transfer expansion energy to a piston in an overall thermodynamic cycle equivalent to the Stirling cycle, although the way in which the gas cycle physically functions differs significantly. Here, the amplitude of standing waves within a gas bearing resonant cavity results in the compression and expansion at tuned nodes. Pressure waves that are formed out of phase of the standing waves result in the displacement of working fluid parallel to the temperature gradient that is established between the hot and cold ends of the heat engine [26]. This displacement of the working fluid acts as a shuttle for energy between the hot and cold ends of the system, similar to the displacer mechanism in a FPS engine.

The expansion of the working fluid may be coupled via one or more mechanisms for conversion of its energy to mechanical or electrical power. In the case of a mechanical engine, energy may be extracted from the working fluid through the interface of a free-floating piston, which in turn may be coupled to a mechanical motion translator or drive wheel. Electrical power may be derived from the mechanical motion of a piston, as in the case of the Free Piston Stirling engine, which houses an integral permanent magnet for the induction of current in a surrounding coil. Such a route to conversion introduced, as we have seen for the FPS engine, multiple losses and inefficiencies to the system. The use of piezoelectric materials for the coupling of fluid expansion to the production of electrical power may be useful in the maximisation of efficiency for miniaturised systems [27].

The phenomena of magnetohydrodynamics (MHD) [28] may be exploited in conjunction with the operation of a thermoacoustic cavity provided that an electrically conductive working fluid employed [29]. Here, thin walled electrodes are mounted orthogonally to a position in the resonant cavity where a magnetic field is passed perpendicularly to the axis of working fluid flow (See Figure A.9). As the working fluid passes through the active MHD cell region of the cavity, an electromotive force is produced. This in turn may be used to provide electrical power to a given load. Typically, gases such as caesium vapour is used as the working fluid due to its ionisation at moderate temperatures. Unfortunately since the cold end of the engine must operate above the ionisation temperature of the working fluid, the hot end must be driven to very high temperatures. This presents significant challenges to system design with respect to material selection and performance.

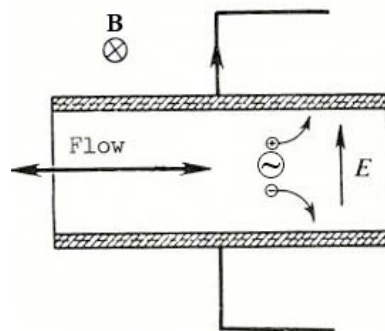


**Figure A.9:** Cross sectional schematic of a MHD converter.

Although thermoacoustic systems are in the early stages of development for power conversion, it is anticipated that their use for RPS may be exploited. For space reactor systems, their use is somewhat more attractive given that significantly high temperatures can be achieved, and the reduction or elimination of moving components is highly desirable at high temperature when considering operational lifetime and reliability.

## A.6 The Brayton Cycle

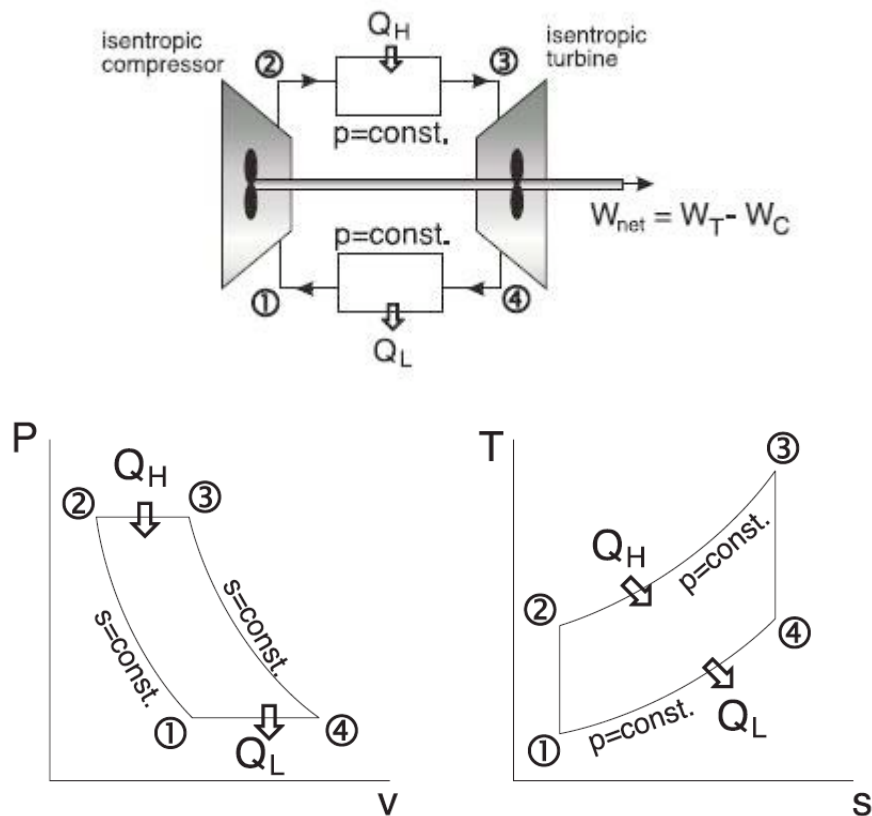


**Figure A.10:** The closed Brayton cycle. The net or shaft rotational power for the cycle ( $W_{net}$ ) is presented as the difference in the power derived by the turbine ( $W_T$ ) and the power consumed by the compressor ( $W_C$ ) in compressing a working fluid. Also illustrated are the Temperature – Entropy (T-S) and Pressure – Volume (P-V) diagrams for each stage of the cycle.

The closed Brayton cycle takes place in four stages. Firstly, a working fluid such as He is compressed under isothermal conditions via a turbo compressor (See Figure A.10 points 1-2). Secondly, heat is added under isobaric conditions to a working fluid within a heat exchanger (See Figure A.10 points 2-3). Thirdly, the working fluid is expanded isentropically through a turbine that translates energy from the working fluid into kinetic energy or shaft power (See Figure A.10 points 3-4). Finally, the working fluid is cooled using a cold heat exchanger or radiator under isobaric conditions prior to re-circulation through the compressor stage (See Figure A.10 points 4-1).

The net work output of a Brayton cycle is embedded within rotational shaft power. Since the power derived by the turbine at the aft end of the cycle is used in part to recompress the working fluid prior to recirculation, the net work output is equal to the difference between the work produced by the turbine and the work used by the compressor. This is illustrated in Figure A.10 above. Based on this it is possible to determine the efficiency of an ideal Brayton cycle.

$$W_{net} = W_T - W_C \quad (\text{A.36})$$

**Equation A.36:** The net work done by the Brayton cycle.  $W_T$  is the power derived by the turbine and  $W_C$  is the power consumed by the compressor.

$$\eta_{cycle} = \frac{W_{net}}{W_{in}} = \frac{W_T - W_C}{W_{in}} \quad (\text{A.37})$$

**Equation A.37:** The efficiency of the ideal Brayton cycle where  $W_{in}$  is equal to the thermal input power of the cycle or the heat source output power.

If we consider the net work done by the cycle and the thermal input power  $W_{in}$  with respect to the specific mass flow rate we can express this function in terms of specific enthalpy:

$$W_{net} = h_{T-in} - h_{T-exit} - h_{C-exit} + h_{C-in} \quad (\text{A.38})$$

**Equation A.38:** The net work done by the Brayton cycle where  $h_{T-in}$  is the specific enthalpy of the working fluid as it enters the turbine,  $h_{T-exit}$  is the energy per mass flow rate of the working fluid as it is rejected from the turbine,  $h_{C-exit}$  is the energy per mass flow rate of the working fluid as it exits the compressor, and  $h_{C-in}$  is the energy per mass flow rate of the working fluid as it enters the compressor.

$$W_{in-net} = h_{T-in} - h_{C-exit} \quad (\text{A.39})$$

**Equation A.39:** The net heat input per mass flow rate of the ideal Brayton cycle with respect to the specific enthalpies of the turbine inlet stage and compressor exit stage.

$$\eta = 1 - \frac{h_{T-exit} - h_{C-in}}{h_{T-in} - h_{C-exit}} \quad (\text{A.40})$$

**Equation A.40:** The net work done by the Brayton cycle where  $h_{T-in}$  is the specific enthalpy of the working fluid as it enters the turbine,  $h_{T-exit}$  is the specific enthalpy of the working fluid as it is rejected from the turbine,  $h_{C-exit}$  is specific enthalpy of the working fluid as it exits the compressor, and  $h_{C-in}$  is the specific enthalpy of the working fluid as it enters the compressor.

Equation A.40 above describes the efficiency of the ideal Brayton cycle with respect to the enthalpy of the working fluid per unit mass flow rate at critical points in the cycle. Thus, the enthalpy may be interchanged with temperature through the division of energy by the specific heat capacity of the working fluid  $C_p$ . Therefore the efficiency of the system may be related to the operating temperatures throughout the cycle and is presented in Equation A.41 below.

$$\eta = 1 - \frac{T_{T-exit} - T_{C-in}}{T_{T-in} - T_{C-exit}} \quad (\text{A.41})$$

**Equation A.41:** The efficiency of the ideal Brayton cycle where  $T_{T-in}$  is the temperature of the working fluid as it enters the turbine,  $T_{T-exit}$  is the temperature of the working fluid as it is rejected from the turbine,  $T_{C-exit}$  is the temperature of the working fluid as it exits the compressor, and  $T_{C-in}$  is the temperature of the working fluid as it enters the compressor.

Since the processes of compression in the compressor and expansion in the turbine are isentropic, and the heating and cooling processes are isobaric, it is possible the turbine and compressor inlet and exit temperature ratios to their pressure equivalent ratios by implementation of the ratio of specific heats ( $\gamma$ ) such that Equation A.42 and A.43 hold.

$$\frac{T_{C-exit}}{T_{C-in}} = \left( \frac{P_{C-exit}}{P_{C-in}} \right)^{\frac{\gamma-1}{\gamma}} \quad (\text{A.42})$$

**Equation A.42:** reciprocal pressure ratios for the turbine inlet and outlet temperature ratio.

$$\frac{T_{T-exit}}{T_{T-in}} = \left( \frac{P_{T-exit}}{P_{T-in}} \right)^{\frac{\gamma-1}{\gamma}} = \left( \frac{P_{C-in}}{P_{C-exit}} \right)^{\frac{\gamma-1}{\gamma}} \quad (\text{A.43})$$

**Equation A.43:** reciprocal pressure ratios for the turbine inlet and outlet temperature ratio.

By substitution of the temperature ratios in Equation A.41 with the pressure ratios defined in Equations A.42 and A.43, it is possible to determine the efficiency of the ideal Brayton cycle with respect to pressure. This is defined by Equation A.44.

$$\eta = 1 - \left( \frac{P_{C-in}}{P_{C-exit}} \right)^{\frac{\gamma-1}{\gamma}} \quad \text{or} \quad \eta = 1 - \left( \frac{P_{T-exit}}{P_{T-in}} \right)^{\frac{\gamma-1}{\gamma}} \quad (\text{A.44})$$

**Equation A.44:** The efficiency of the ideal Brayton cycle with respect to cycle pressures.

$$r_p = \frac{P_{C-exit}}{P_{C-in}} = \frac{P_{T-in}}{P_{T-exit}} \quad (\text{A.45})$$

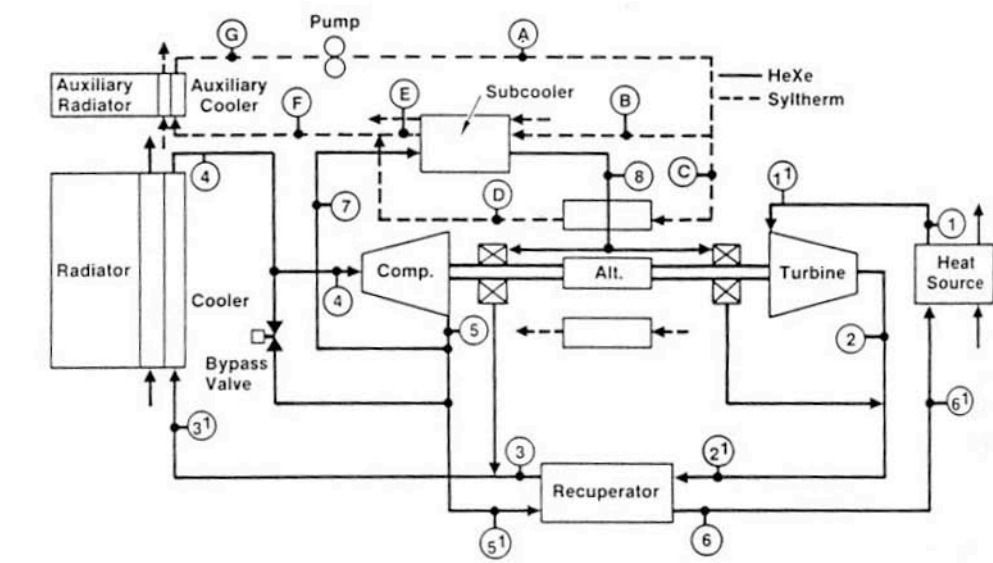
**Equation A.45:** The pressure ratio  $r_p$  for the ideal Brayton cycle.

For cycle design purposes, the overall pressure ratio  $r_p$  is often discussed and is defined by Equation A.45. Clearly the two definitions of the pressure ratio in Equation A.45 are the inverse of the ratios of the ratios within Equation A.44. Thus, we may define the efficiency in terms of the overall pressure ratio in Equation A.46. It should therefore be noted that as the pressure ratio  $r_p$  increases, the efficiency tends towards 1.

$$\eta = 1 - \left( \frac{1}{r_p} \right)^{\frac{\gamma-1}{\gamma}} \quad (\text{A.46})$$

**Equation A.44:** The efficiency of the ideal Brayton cycle with respect to the overall cycle pressure ratio  $r_p$ .

The closed Brayton cycle has been examined for many terrestrial and space power applications including a miniaturised system developed by NASA called Mini-BRU [30]. The Mini-BRU was designed to deliver kWe power conversion for large radioisotope and small reactor systems [30, 31]. Later work performed by NASA in partnership with the U.S. Department of Energy resulted in the evolution of the Mini-BRU designs for use in 1-10 kWe systems under the Dynamic Isotope Power System (DIPS) program [32, 33].



State point	Location	Temperature (K)	Pressure (psia)	Mass flow (gm/sec)
1	Heat source outlet	1038	52.55	306.4
1'	Turbine inlet	1033	52.49	306.4
2	Turbine outlet	861	31.27	306.4
2'	Lo-P recuperator in	852	31.26	311.6
3	Lo-P recuperator out	417	30.99	311.6
3'	Gas cooler in	419	30.95	317.9
4	Gas cooler out	290	30.34	317.9
4'	Compressor inlet	290	30.31	317.9
5	Compressor outlet	384	53.86	317.9
5'	Hi-P recuperator in	384	53.79	306.4
6	Hi-P recuperator out	826	53.10	306.4
6'	Heat source inlet	826	53.04	306.4
7	Bleed flow out	384	53.86	15.86
8	Bleed flow to TAC	337	53.84	15.86
A	Pump outlet	337	-	12.68
B	Bleed cooler inlet	337	-	3.05
C	TAC inlet	337	-	9.63
D	TAC outlet	365	-	9.63
E	Bleed cooler out	367	-	3.05
F	Cooler inlet	366	-	12.68
G	Cooler outlet	336	-	12.68

Net power = 6 kWe; TAC speed = 49,632 RPM; He-Xe molecular weight = 61.7

Figure A.11: Schematic of the NASA DIPS 6kWe Brayton conversion system [34].

As is evident in Figure A.11, practical Brayton systems are often significantly more complicated than 4 basic components. Typically, intercoolers and recuperators/regenerators are used to ensure that various processes are held at temperatures where components such as alternators operate efficiently and to recover heat that would otherwise be rejected from the system as waste, thus improving the overall efficiency. Figure A.12 illustrates the implementation of a thermal regenerator to transfer heat from the working fluid as it leaves the outlet of the turbine to the working fluid as it exits the pressure prior to the main heat source heat exchanger. Waste heat rejection radiators typically constitute a significant fraction of the total conversion system mass. Volumetrically, radiators are also most dominant.

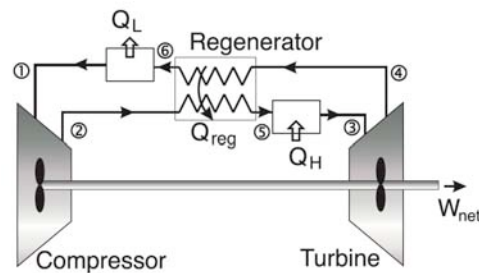


**Figure A.12:** Schematic of a Brayton cycle with regeneration stage (points 5 and 6).

Overall the efficiency of the ideal Brayton cycle may be maximised through the following design criteria:

1. Maximisation of the turbine inlet temperature such as via heat source power selection, limited by maximum creep resistant temperature.
2. Maximisation of heat rejection from the working fluid between the exit of the turbine and the inlet of the compressor.
3. Minimisation of the temperature of the working fluid at the exit plane of the compressor by providing sufficient cooling of the compressor assembly to compensate the adiabatic compression process.
4. Recuperate heat from the working fluid upon exiting the turbine prior to cooling. This recovers heat that would otherwise be rejected.

Since the Brayton requires the turbine inlet temperature to be as high as possible in order to maximise the overall efficiency, careful selection is required for materials such as for the blades of the turbo machinery in order to prevent creep that would otherwise lead to fatigue and reduced lifetime. In practical systems, reduction of thermal losses is challenging. Turbine Efficiency must also be considered and due to manufacturing constraints, turbine efficiency is typically lower for small compact and low power levels. Thus, for low power systems such losses are generally more detrimental to the overall system performance despite operation at high temperature.

At the heat rejection side of the cycle, the radiators must be sized appropriately such that the required power to be radiated is achieved while minimising the radiator outlet temperature (see Equation A.26) since, as we determine in Equation A.41, doing so results in a greater overall efficiency.

## A.7 The Rankine Cycle

Today, the Rankine cycle is the most commonly used power conversion cycle. Its use is also the most common method of refrigeration. Its use is exemplified in the form of the thermodynamic steam cycle used within commercial power plants worldwide. Although the steam cycle is not ideal for space applications due to the relatively low cycle and rejection temperatures, the cycle can be designed to function at higher temperatures through careful selection of the working fluid.

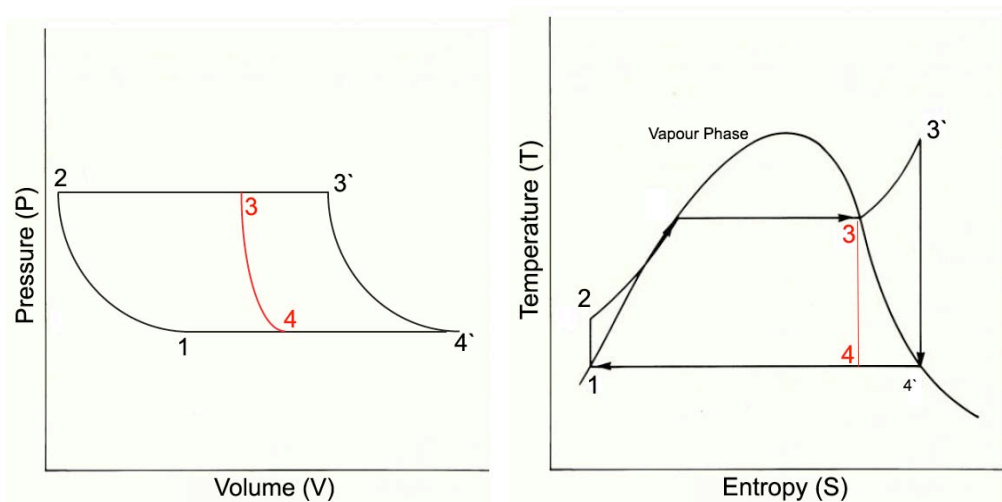


**Figure A.13:** The pressure-volume (P-V) and temperature-Entropy (T-S) diagrams for the basic Rankine cycle (1,2,3,4) and the superheated Rankine cycle (1,2,3',4').

The Rankine cycle is similar to the Brayton cycle since a turbine is used to extract power from a working fluid that is heated by a heat source such as a fission reactor or radioisotope source. The fundamental difference between the Brayton cycle and Rankine cycle is that the working fluid of the Rankine cycle is purposefully subjected to phase changes from liquid to gas within a boiler followed by condensation after passage through the power turbine. In doing so, the size and mass of the heat exchangers and radiators can be minimized.

The ideal Rankine cycle is composed of 4 basic stages. An initial isentropic compression is performed via a pump where the working fluid is in a pre-cooled liquid state (See Figure A.12 1-2). As the fluid leaves the pump, its temperature is greater than its inlet temperature. Once compressed, the fluid is passed to a boiler where sufficient thermal energy is transferred to the working fluid under isobaric conditions such that the liquid undergoes a phase change into vapour (See Figure A.12 2-3). The vaporised fluid is expanded isentropically through a turbine and the energy released is translated into shaft power (See Figure A.12 3-4). Prior to recycling the fluid, it is condensed under isothermal conditions (See Figure A.12 4-1). A jet condenser is commonly used for isothermal condensation [33].

Since the Rankine cycle is an extension to the Carnot heat engine, the efficiency may be prescribed as defined in Equation A.41 where the Brayton compressor inlet and outlet conditions may be substituted by those for the Rankine Pump.

The Pressure-Volume and Temperature-Entropy diagrams illustrated in Figure A.12 display the superheated Rankine cycle in between the prime points (3' and 4'). The Superheated Rankine cycle allows the working fluid to be heated beyond its vapour phase at the corresponding boiling temperature. In doing so, the Carnot efficiency is improved (see Equation A.32).

Figures A.14 to 1.16 below illustrate examples of Rankine cycles that have been examined for operation within the space environment. Typical temperatures and pressures are also presented.

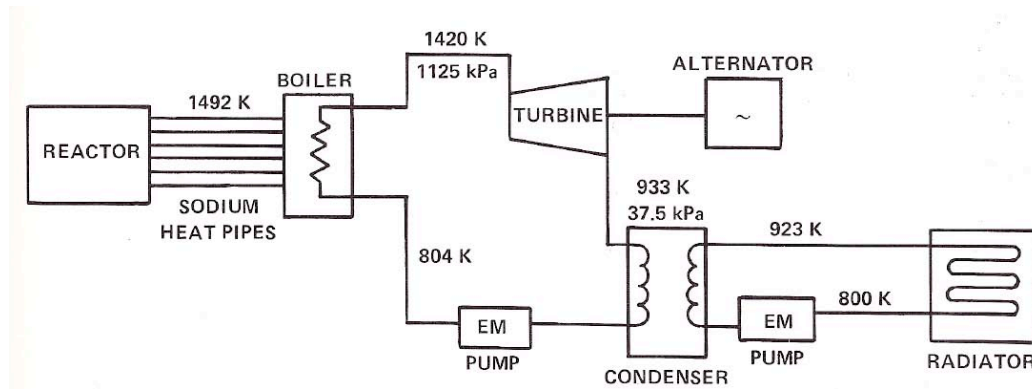


**Figure A.14:** Example of a proposed potassium Rankine cycle for power conversion from a space reactor [35].

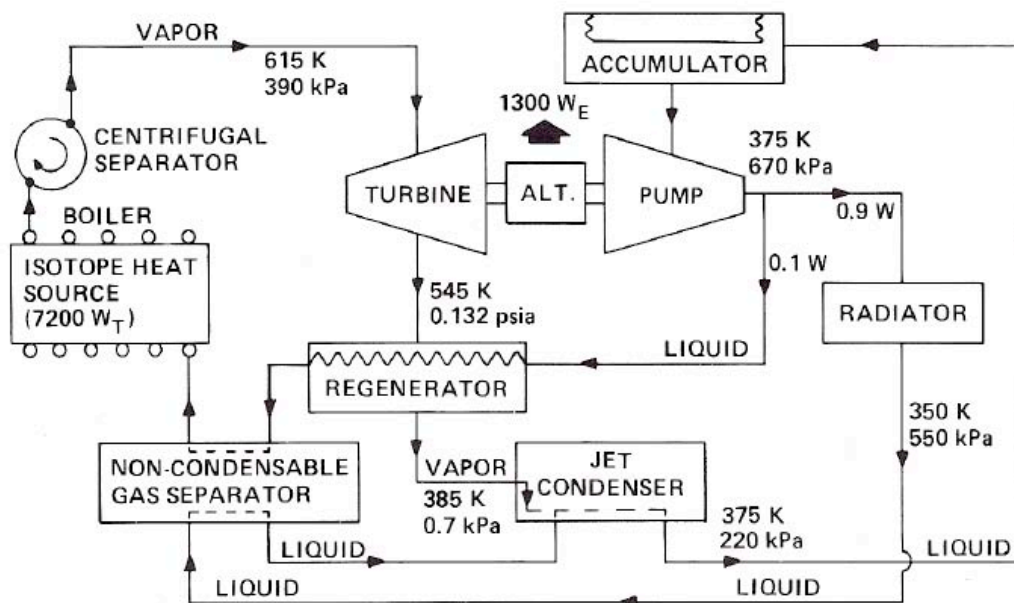


**Figure A.15:** Typical operating conditions for an organic Rankine cycle generator developed under the U.S. Dynamic Isotope Powers Systems program [36] interfaced with a Multi-Hundred Watt type radioisotope heat source [37].

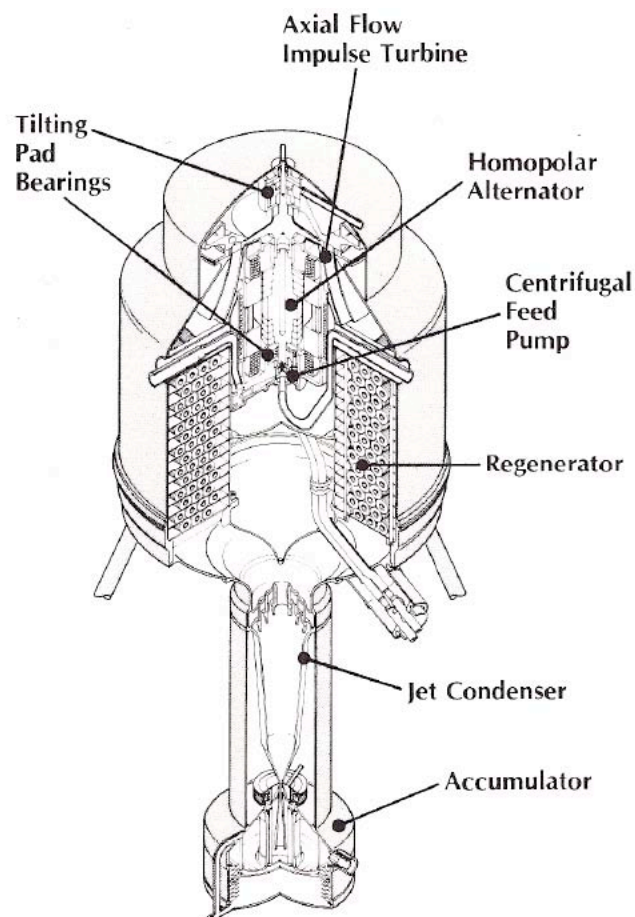
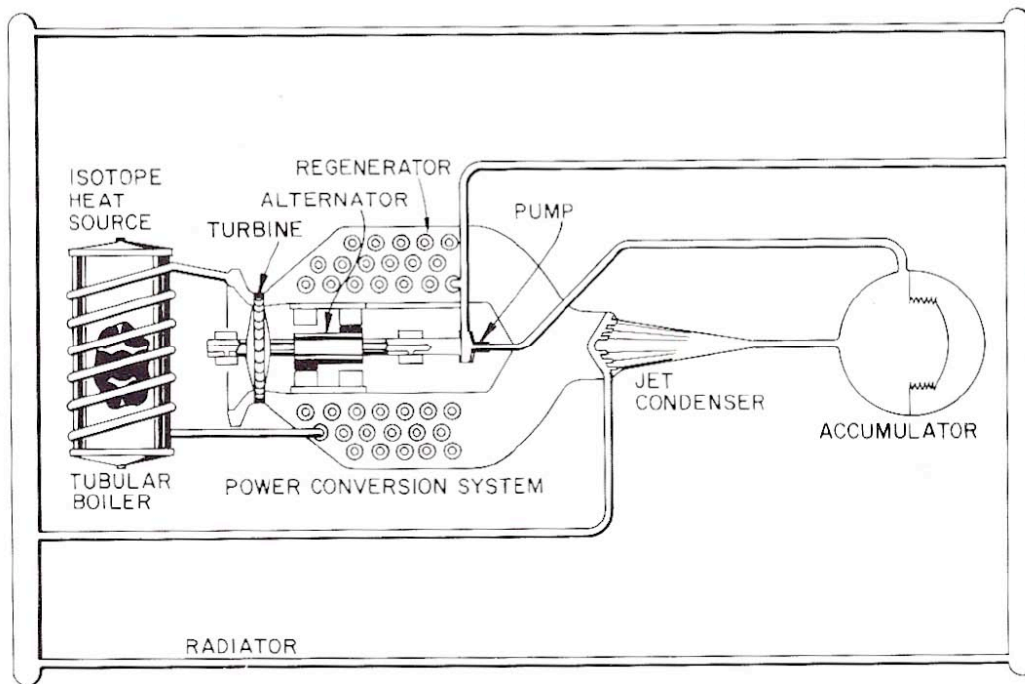


**Figure A.16:** Schematic of the components of an organic fluid Rankine power converter interfaced with a Multi-Hundred Watt radioisotope heat source considered by the Dynamic Isotope Power System (DIPS) study. [35]

## A.9 References

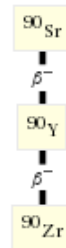
- [1] C.P. Bankston, K.L. Atkins, E.F. Mastal, D.G. McConnell, "Technology development issues in space nuclear power for planetary exploration". *Acta Astronautica*. 24 (1991) 161-170  
DOI: [10.1016/0094-576\(91\)90163-Y](https://doi.org/10.1016/0094-576(91)90163-Y).
- [2] Y. Zhamd, G. Zeng, R. Singh, et al. "Measurement of Seebeck coefficient perpendicular to SiGe superlattice Thermoelectrics". Proceedings of: ICT '02. Twenty-First International Conference on Thermoelectrics, 2002.
- [3] S.W. Angrist, "*Direct Energy Conversion*". 2<sup>nd</sup> ed. Allyn and Bacon Inc., Boston, MA; 1971.
- [4] R. Decher, "*Direct Energy Conversion: Fundamentals of Electric Power Production*". Oxford University Press Inc., New York; 1997. ISBN: 0-19-509572-3.
- [5] S. Sieniutycz, A. De Vos, "*Thermodynamics of Energy Conversion and Transport*". Springer-Verlag, New York; 2000. ISBN: 0-387-98938-2.
- [6] J. Kaye, J.A. Welsh, (Eds), "*Direct Conversion of Heat to Electricity*". John Wiley, New York; 1960.
- [7] A.V. Von Arx. "MMRTG Heat Rejection Summary". Proceedings of: STAIF 2006 - 23rd Symposium on Space Nuclear Power and Propulsion; 12-16 February, 2006 ISBN: 0-7354-0305-8.
- [8] F. Ritz, C.E. Peterson. "Multi-Mission Radioisotope Thermoelectric Generator (MMRTG) Program Overview". Proceedings of: 2004 IEEE Aerospace Conference, 2004; Big Sky, MT ISBN: 0-7803-8 155-6.
- [9] P.W. Fortescue, J.P.W. Stark, G.G. Swinerd, "*Spacecraft Systems Engineering*". 3<sup>rd</sup> ed. John Wiley & Sons Ltd., Chichester. ISBN: 0-471-61951-5.
- [10] F.G. Baksht, G.A. Dyuzhev, A.M. Martsinovsky, et al., "*Thermionic Converters And Low-Temperature Plasma*". U.S. Department of Energy Technical Information Center; 1978. ISBN: 0-87079-301-2.
- [11] W. R. Corliss, Harvey D. G., "*Radioisotopic Power Generation*". Prentice-Hall, New Jersey; 1964.
- [12] J. A. Angelo, D. Burden, "*Space Nuclear Power*". Krieger Publishing, Malabar, FL.; 1985. ISBN: 0-89464-000-3.
- [13] G. Miskolczy, Lieb D.P. "Radioisotope thermionic converters for space applications". Proceedings of: 25th International Energy Conversion Engineering Conference, IECEC-90, 1990 ISBN: 0-8169-0490-1.
- [14] V.P. Nikitin, B.G. Ogloblin, E.N. Sokolov, et al., ""YENISEI" SPACE NUCLEAR POWER SYSTEM". *Atomnaya Energiya*. 88 (2000) 95-108.
- [15] J.G. Schreiber. "*Assessment of the Free-Piston Stirling Converter as a Long Life Power Converter for Space*". NASA/TM-2001-210604. NASA Glenn Research Center, Cleveland, Ohio. 2000.
- [16] S.M. Geng, L.S. Mason, R.W. Dyson, L.B. Penswick. "*Overview of Multi-Kilowatt Free-Piston Stirling Power Conversion Research at Glenn Research Center*". NASA/TM-2008-215061. 2008.
- [17] J. Chan, G.J. Wood, J.G. Schreiber. "*Development of Advanced Stirling Radioisotope Generator for Space Exploration*". NASA/TM-2007-214806. 2007.
- [18] J.G. Wood, C. Carroll, L.B. Penswick. "Advanced 80 W<sub>e</sub> Stirling Converter Development Progress". Proceedings of: Space Technology and Applications International Forum - STAIF, 2005; Albuquerque, NM. American Institute of Physics, ISBN: 0-7354-0230-2.

- [19] G. Walker. "Elementary Design Guidelines for Stirling Engines". Proceedings of: Intersociety Energy Conversion Engineering Conference (IECEC); August 5th - 10th, 1979.
- [20] W.R. Martini, B.A. Ross. "An Isothermal Second Order Stirling Engine Calculation Method". Proceedings of: Intersociety Energy Conversion Engineering Conference (IECEC), 1979.
- [21] J.G. Schreiber, L.G. Thieme. "GRC Supporting Technology for NASA's Advanced Stirling Radioisotope Generator (ASRG)". Proceedings of: Space Technology Applications and International Forum (STAIF 2008); February 10-14, 2008; Albuquerque, NM.
- [22] R.K. Shalturns, W.A. Wong. "*Advanced Stirling Technology Development at NASA Glenn Research Center*". NASA/TM-2007-214930. NASA Glenn Research Center, Cleveland, OH. 2007.
- [23] S.M. Oriti, G.M. Blaze. "*Advanced Stirling Converter Testing at NASA Glenn Research Center*". NASA/TM-2007-215010. NASA Glenn Research Center, Cleveland, OH. 2007.
- [24] H. Chuong, R. Fernandez. "Advanced Stirling Radioisotope Generator: Design Processes, Reliability Analyses Impact, and Extended Operation Tests.". Proceedings of: Space Technology and Applications International Forum (STAIF 2008); February 10-14, 2008; Albuquerque, NM.
- [25] A. Shah, I. Korovaichuk, S.M. Geng, J.G. Schreiber. "*Reliability of Radioisotope Stirling Converter Linear Alternator*". NASA/TM--2006-213636. NASA Glenn Research Center, Cleveland, Ohio. 2006.
- [26] S.L. Garret, "Thermoacoustic engines and refrigerators". *Am. J. Phys.* 72 (2004) 11 -17.
- [27] R.M. Keolian, K.J. Bastyr. "Thermoacoustic Piezoelectric Generator (Patent WO/2005/022606)", 2005.
- [28] D.J. Cerini. "*Liquid Metal MHD Power Conversion*". *JPL Quarterly Technical Review, Volume 1*. April 1971.
- [29] A.A. Castrejón-Pita, G. Huelsz, "Heat-to-electricity thermoacoustic-magnetohydrodynamic conversion". *Appl. Phys. Lett.* 90 (2007).
- [30] R.D. Gable, H.J. Lloyd. "*Space power application of the all purpose mini-Brayton rotating unit / Mini-BRU*". 19750061947. NASA. 1975.
- [31] A.G. Birchenough. "*The 2kW Mini-BRU Electrical Controls Concept and Transient Performance*". NASA/TM-2006-214043. NASA Glenn Research Center, Cleveland, Ohio. 2006.
- [32] M.E. Hunt, "High efficiency dynamic radioisotope power systems for space exploration - a status report". *IEEE Aerospace and Electronic Systems Magazine.* (1993) 18-23. DOI: 10.1109/62.246037.
- [33] A.G. Stadnik. "DIPS power conversion cycle selection". Proceedings of: Energy Conversion Engineering Conference IECEC-89, 1989; Washington D.C.
- [34] Rocket Dyne Division. "*Dynamic Isotope Power Subsystem Engineering Unit Flight System Design Report*". ER-00021. Rockwell International, Canoga Park, CA. 1988.
- [35] D. Buden, et al. "*Selection of Power Plant Elements for Future Reactor Space Electric Power Systems*". LA-7858. Los Alamos National Laboratory, Los Alamos, NM. September 1979.
- [36] G.L. Sorenson, R.E. Niggemann, E.C. Krueger, R.C. Brouns, F.A. Russo. "Status Report of the Dynamic Isotope Power System". Proceedings of: Intersociety Energy Conversion Engineering Conference, 1979.
- [37] G.L. Bennett. "Space nuclear power: opening the final frontier". Proceedings of: Fourth International Energy Conversion Engineering Conference and Exhibit (IECEC), 2006; San Diego, California. AIAA.

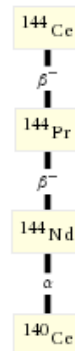
# Appendix B

## Decay Chains for radioisotopes considered for space applications

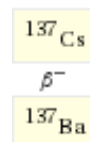
### B1. $^{90}\text{Sr}$ Beta decay chain



### B2. $^{144}\text{Ce}$ Beta decay chain



### B3. $^{137}\text{Cs}$ Beta decay chain



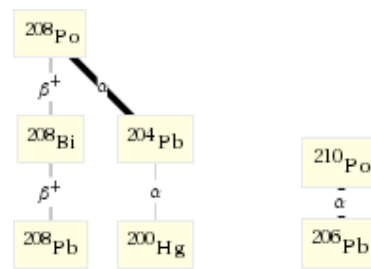








**B8.  $^{208}\text{Po}$  &  $^{210}\text{Po}$  decay chains**



**B9.  $^{241}\text{Am}$  Decay Chain**

